Rotating Torsion Balance Tests of the Weak Equivalence Principle

Todd A. Wagner

A dissertation
submitted in partial fulfillment of the
requirements for the degree of

Doctor of Philosophy

University of Washington

2014

Reading Committee:

Jens H. Gundlach, Chair

Stephan Schlamminger

Alejandro Garcia

Program Authorized to Offer Degree:
Physics

University of Washington

Abstract

Rotating Torsion Balance Tests of the Weak Equivalence Principle

Todd A. Wagner

Chair of the Supervisory Committee:
Professor Jens H. Gundlach
Physics

We used a rotating torsion balance to make the most precise laboratory search for equivalence-principle violation. We used a beryllium-aluminum composition dipole to complement our previous measurement with a beryllium-titanium composition dipole. We improved the tilt stability of the apparatus and reduced the temperature gradient feed-through to improve the uncertainty by 30% compared to our beryllium-titanium result. Using the beryllium-aluminum test bodies, we found $\eta_{\oplus} = (-1.3 \pm 1.2) \times 10^{-13}$. The combined limits using both test bodies pairs generally limit any new equivalence-principle-violating force that couples to ordinary neutral matter. We also measured test-bodies with compositions that mimic the difference in composition between the earth and moon to provide a model-independent weak equivalence principle limit of $\eta_{\mathrm{CD}} = (1.2 \pm 1.1) \times 10^{-13}$ for comparison with lunar laser ranging strong equivalence principle measurements. The combined lunar laser ranging and weak equivalence principle measurements limit equivalence-principle violation for gravitational binding energy to $\lesssim 6 \times 10^{-4}$ at 1-σ.

TABLE OF CONTENTS

LIST OF FIGURES

LIST OF TABLES

ACKNOWLEDGMENTS

Perhaps it is more common to write literature or poetry for those we love, but I present this scientific work to my wife, Michelle, as a symbol of my love for her.

I could not have completed this without the insight and support of the Eöt-Wash group. In particular, I would like to thank Stephan Schlamminger, Jens Gundlach, Eric Adelberger, and Erik Swanson. Stephan Schlamminger spent many hours working with me on the apparatus and discussing measurements, physics, and life. My adviser, Jens Gundlach, offered needed support and tried to keep me focused on goals. Eric Adelberger always challenged me to improve and to focus on the most important part of a problem. Erik Swanson kindly shared his detailed knowledge of the data acquisition system and apparatus electronics. Many thanks to all of the graduate students and post-docs for insightful problem solving and advice.

Chapter 1

INTRODUCTION

Galileo experimentally verified the universality of free fall – that the gravitational acceleration of a point test body is independent of its composition – around 1600. In modern language we consider the universality of free fall as a consequence of the equivalence principle – the equivalence of gravitational mass and inertial mass. Our precision torsion balance experiments maintain the universality of free fall as the most precisely tested prediction of the equivalence principle. Our multiple test body pairs and multiple sources allow our measurements to strongly constrain new non-gravitational interactions with a broad range of couplings to ordinary neutral matter.

Modern physics consists of two main theories that describe the four fundamental interactions. General relativity describes gravitational phenomena and the standard model describes the nuclear forces and electromagnetism. Both theories successfully describe the experiments and observations made to test them. One question of modern physics is whether these two theories can be joined under a single framework that also solves issues such as neutrino oscillations, galactic rotation curves, vacuum energy density, and the homogeneity of the cosmic microwave background. Precision tests of fundamental principles provide one of the most versatile tools to search for clues to a more complete understanding of the laws of physics.

General relativity accurately describes gravitational phenomena as a classical (non-quantum) theory; however, in the context of quantum theories, it can be considered as an effective field theory with physics of the underlying theory suppressed by the Planck mass [41]. While our measurements are still far from probing the Planck scale, they require any new framework, such as string theory, to closely reproduce the predictions of general relativity. An alternative interpretation assumes that the equivalence principle is exact, and equivalence principle experiments search for new forces.

Torsion balances serve as excellent equipment for testing the equivalence principle because the fiber provides an extremely weak spring but only twists when the forces on the test bodies act in different directions. Because a uniform gravitational field accelerates all test bodies identically, our torsion balance achieved the remarkable differential acceleration sensitivity of $\Delta a/a \sim 10^{-13}$. The torsion balance geometry allows long integration times because the test bodies are continuously suspended, but it requires a modulated source in the horizontal direction. The rotation of the Earth naturally modulates the position of the sun. We also rotated the apparatus to modulate the horizontal gravitational acceleration of earth. Rotating the torsion pendulum had several additional advantages. First, the horizontal gravitational acceleration at Seattle's latitude is 1.68 $\mathrm{cm\,s^{-2}}$ or almost 3 times the acceleration toward the sun of 0.6 $\mathrm{cm\,s^{-2}}$. Second, our sources included the local topography and variations in the mass distribution of the earth, which let us set limits on the strength of new forces with interaction ranges greater than a meter. Third, our control of the rotation rate and direction improved our detection and measurement of systematic effects.

We tested the equivalence principle using three different test body composition pairs towards four different sources. Our results limit equivalence-principle violation on ordinary neutral matter towards ordinary matter, dark matter, and due to a preferred reference frame. Multiple test body pairs and sources expand the constraints on equivalence-principle violation to any new vector charge coupled to the protons, neutrons, or electrons in our test bodies. One test body set mimics the differences in the earth's and moon's compositions, which improves the limit on equivalence-principle violation for gravitational binding energy when combined with lunar laser ranging equivalence principle results. Our results are the most precise laboratory measurements of the equivalence principle.

Chapter 2

THE EQUIVALENCE PRINCIPLE

Einstein's general theory of relativity successfully describes known gravitational phenomena. Tests consistent with general relativity include laboratory experiments comparing the free fall of individual atoms, prediction of orbits within our solar system, binary pulsar energy loss matching gravitational radiation, and the deflection of light by distant galaxies. The parametrized-post-Newtonian formalism (PPN) is a linearized extension of general relativity for weak gravitational fields [134]. PPN includes parameters for possible gravitational effects beyond those predicted by general relativity and provides a framework to compare tests of gravity in the weak gravitational field of our solar system. Limits on the PPN parameters all agree with general relativity with precisions ranging from 2% for the violation of momentum conservation parameter ζ_1 using a bound on the Nordtvedt effect to better than 4×10^{-20} on the preferred-frame effect parameter α_3 from pulsar acceleration measurements (most of the parameters from [134] are consistent with general relativity at the level of $10^{-3} \sim 10^{-4}$) [133]. Binary star systems with at least one pulsar provide excellent tests of general relativity for strong gravitational fields. The Hulse-Taylor binary pulsar PSR B1913+16 provides strong evidence for the gravitational wave radiation predicted by general relativity. The ratio of the change in the orbital period to that predicted by general relativity due to gravitational radiation is 0.997 ± 0.002 [131]. Despite the success of general relativity many cosmological phenomena with gravitational consequences remain to be explained, such as the inflation of the early universe, the characteristics of dark matter, and the accelerating expansion of the universe.

While equivalence principle experiments take their name from testing a fundamental aspect of gravity, an equivalence principle experiment may also be characterized as a search for new forces. String theory is one attempt to join all the forces in a unified quantum framework, but it also predicts equivalence-principle violations due to new fields such as the

dilaton. Theoretical explanations for inflation, dark energy, and dark matter also commonly introduce new fields. Equivalence principle experiments provide one method to search for signs of these hypothesized fields. The matter couplings of hypothetical new fields can be parametrized by a Yukawa potential as described below in section 2.2. The experimental bounds from equivalence principle tests and astronomical observations often exclude or restrict the parameter space for the hypothetical fields. The chameleon method [72] is one way to avoid equivalence principle derived limits on a scalar field. The chameleon method causes the scalar field to acquire a mass based on the local energy density. This effectively limits the interaction between bulk materials to a small skin depth, but allows long-range interactions where the matter density is small. Chameleon fields may evade bounds set by equivalence principle experiments while still affecting galactic and cosmological structure. However, short-range, gravitational inverse-square-law tests may detect any such chameleon fields.

2.1 Equivalence Principle Defined

The universality of free fall is a precisely tested empirical fact determined by experiments and astronomical observations. The universality of free fall (UFF) states that a free test body in an uniform gravitational field experiences acceleration independent of its mass, composition, or internal structure. The qualification "free test body" means that the body is not acted on by other forces, while the qualification "uniform gravitational field" means that gravitational tidal effects are negligible. Several different equivalence principles exist in the literature to explain the universality of free fall as a consequence of gravitational theory and to differentiate between experimental tests. Our experiments keep the universality of free fall the most precisely tested consequence of the equivalence principle.

The Newtonian version of the equivalence principle equates inertial mass m_i and gravitational mass m_g. This differs dramatically from other forces, where the acceleration of a body depends separately on its charge and mass (e.g., a proton and a positron experience different accelerations in an electric field because they have different masses even though they possess the same electric charge). In Newtonian mechanics the universality of free fall arises from comparing Newton's second law (equation 2.1) with the gravitational inverse

square law (equation 2.2).

$$\mathbf{F} = \quad m_i \mathbf{a} \tag{2.1}$$

$$\mathbf{F} = -\frac{GMm_g}{r^2}\,\hat{\mathbf{r}} \tag{2.2}$$

The Newtonian equivalence principle requires that $m_i = m_g$, which results in a body's acceleration being independent of its mass. Both Galileo and Newton observed this long ago, but Baron Roland von Eötvös began the systematic investigation for different materials [49].

Einstein realized that the laws of physics should be the same regardless of the coordinates of the experiment [47]. Einstein's equivalence principle guided the formation of general relativity and states that an uniform gravitational field and an uniformly accelerated system are equivalent. General relativity describes gravity in non-uniform fields, so modern statements of the equivalence principle attempt to generalize by requiring uniformity only for some small region [133, 22, 99]. Following Will [133] the Einstein equivalence principle has three logical parts:

Weak equivalence principle (WEP) A freely-falling, non-gravitationally bound "test body" follows a path independent of its structure or composition. A "test body" must be sufficiently small that it is not affected by gravity gradients and "freely-falling" means not acted on by other forces.

Local Lorentz invariance (LLI) Any non-gravitational experiment is independent of the velocity of the freely-falling frame in which it is performed.

Local position invariance (LPI) Any non-gravitational experiment is independent of the location and time at which it is performed.

The strong equivalence principle extends the provisions of the Einstein equivalence principle to include gravitational experiments as well. In the context of experiments, the strong equivalence principle relates to equivalence principle tests using bodies that have appreciable gravitational binding energy, such as planetary bodies; whereas, the test bodies used in weak equivalence principle experiments are typically laboratory sized, with insignificant gravitational binding energy.

Strong equivalence principle (SEP) A freely-falling – including gravitationally bound – "test body" follows a path independent of its structure or composition.

Local Lorentz invariance (LLI) An experiment is independent of the velocity of the freely-falling frame in which it is performed.

Local position invariance (LPI) An experiments is independent of the location at which it is performed.

2.2 Models for Equivalence-Principle Violation

Tests of the weak equivalence principle are typically null tests because they compare the gravitational acceleration of different materials, which the equivalence principle requires to be the same. Several different ways to express equivalence principle results exist in the literature. The simplest comparison takes the ratio of the difference in the acceleration of two different materials, A and B, to their average acceleration a toward a source. This comparison is commonly denoted with the Eötvös parameter η:

$$\eta = \frac{\Delta a}{a} = 2\frac{a_A - a_B}{|a_A + a_B|} \tag{2.3}$$

The mean acceleration $a = |a_A + a_B|/2$ must be measured or otherwise determined separately for torsion balance experiments. Torsion pendulums are inherently sensitive only to the differential acceleration of the test bodies in the horizontal plane.

While the Eötvös parameter readily shows the precision of an experiment and whether an equivalence-principle violation occurs, it does not fully utilize the information an experiment can provide. The Yukawa potential is a theoretically motivated model that incorporates the main features of equivalence principle tests:

1. defined distance between a source and a test body
2. specific compositions for a source and test body
3. effects are empirically weak compared to gravity

The Yukawa potential arises in theories from the quantum exchange of a massive boson. It provides a model for the parametrization of equivalence principle experiments.

$$V(r) = -G\frac{m_T m_S}{r}\left[1 + \tilde{\alpha}\left(\frac{\tilde{q}_T}{\mu_T}\right)\left(\frac{\tilde{q}_S}{\mu_S}\right)e^{-r/\lambda}\right] \tag{2.4}$$

In the Yukawa model for an equivalence-principle violation, $\tilde{\alpha}$ gives the strength of a Yukawa interaction relative to that of gravity, $(\tilde{q}/\mu)$ defines the property of a material ("charge") per unit of mass that relates to an interaction, and λ controls the range of the interaction. The remaining parameters define the mass of the bodies m and the distance between them r similar to the gravitational inverse-square law. For equivalence principle experiments, we explicitly parametrize a property of the bodies $(\tilde{q}/\mu)$ in contrast to the parametrization typically used for tests of the gravitational inverse-square law where $\alpha = \tilde{\alpha}(\tilde{q}/\mu)_T(\tilde{q}/\mu)_S$. Inverse-square-law experiments may be interpreted as equivalence principle tests; however, inverse-square-law tests have good sensitivity only for ranges λ approximately equal to the distance between the two bodies used for the experiment. In contrast to inverse-square-law experiments, equivalence principle experiments measure the difference in acceleration of two materials towards a source, which results in the following form for the Yukawa parametrization:

$$\tilde{V}(r) = \tilde{\alpha}\left(\Delta\frac{\tilde{q}}{\mu}\right)_T\left(\frac{\tilde{q}_S}{\mu_S}\right)G\frac{m_T m_S}{r}e^{-r/\lambda} \tag{2.5}$$

$$\left(\Delta\frac{\tilde{q}}{\mu}\right)_T = \left[\left(\frac{\tilde{q}_A}{\mu_A}\right) - \left(\frac{\tilde{q}_B}{\mu_B}\right)\right] \tag{2.6}$$

where $m_T = m_A = m_B$ assumes a design where the masses of the different test body materials are equal. This form can be related back to the Eötvös parameter to give

$$\eta = \tilde{\alpha}\left(\Delta\frac{\tilde{q}}{\mu}\right)_T\left(\frac{\tilde{q}_S}{\mu_S}\right)\left(1+\frac{r}{\lambda}\right)e^{-r/\lambda}, \tag{2.7}$$

for $\tilde{\alpha} \ll 1$.

The Yukawa parametrization interprets an equivalence-principle violation as being due to a new force-carrying boson coupling to the "charge" $\tilde{q}$ with a boson mass m_b giving a Compton wavelength of $\lambda = \hbar/(m_b c)$. The coupling constant for the new interaction $\tilde{g}$ relates to $\tilde{\alpha}$ through the Yukawa potential:

$$V(r) = \mp\frac{\tilde{g}^2}{4\pi}\frac{\Delta\tilde{q}_A\tilde{q}_B}{r}e^{-r/\lambda} \tag{2.8}$$

where the – and + refer to scalar and vector interactions, respectively. Resulting in

$$\tilde{\alpha} = \pm\frac{\tilde{g}^2}{4\pi G u^2}, \tag{2.9}$$

where u is an atomic mass unit.

2.2.1 Charge Parametrization

The choice of "charge" per atomic mass unit for an equivalence-principle-violating interaction is selected by $(\tilde{q}/\mu)$. The quotes around "charge" indicate that it is a property of the body that is different from electric charge. The quotes are dropped through the remainder of this work for readability. Any new interaction with ordinary matter would couple to some combination of the protons, neutrons, or electrons composing the material. The torsion balance experiments described in this work used neutral matter, which prevents them from distinguishing between new interactions coupled to protons or electrons. When considering vector interactions between neutral matter, we can parametrize the charge as due to interactions with the neutrons N or the protons and electrons Z using the parameter $\tilde{\psi}$ constrained to $-\pi/2 < \tilde{\psi} \leqslant \pi/2$:

$$\begin{aligned} \tilde{q} &= Z\cos\tilde{\psi} + N\sin\tilde{\psi}, \\ &\text{where for neutral matter } \tan\tilde{\psi} = \frac{\tilde{g}_n}{\tilde{g}_{e^-} + \tilde{g}_p}. \end{aligned} \tag{2.10}$$

For any given Z and N, there exists a value $\tilde{\psi}'$ for which $\tilde{q}$ is zero, resulting in no sensitivity to a force with that charge:

$$\tan\left(\tilde{\psi}'\right) = -\frac{Z}{N} \tag{2.11}$$

Fischbach introduced an alternate basis for charge parametrization Θ_5 when he reanalyzed the Eötvös experiment [52] as possible evidence for a "fifth force" coupled to baryon number B, where lepton number L was the other charge. Charges associated with the known forces have conservation laws, so conserved quantities with no associated symmetry are plausible candidates for the charge of a hypothetical new force. Both baryon number and lepton number are conserved to a very high level, but are not associated with symmetries:

$$q_5 = B\cos\Theta_5 + L\sin\Theta_5 \tag{2.12}$$

Other theoretically motivated choices for charges include $B - L$ and Z. $B - L$ remains conserved in supersymmetric theories where B and L are not conserved individually. An axion or axion-like particle would interact through the electromagnetic force and thus couple to Z, though likely masses for the axion of ~ 1 meV are better constrained by gravitational

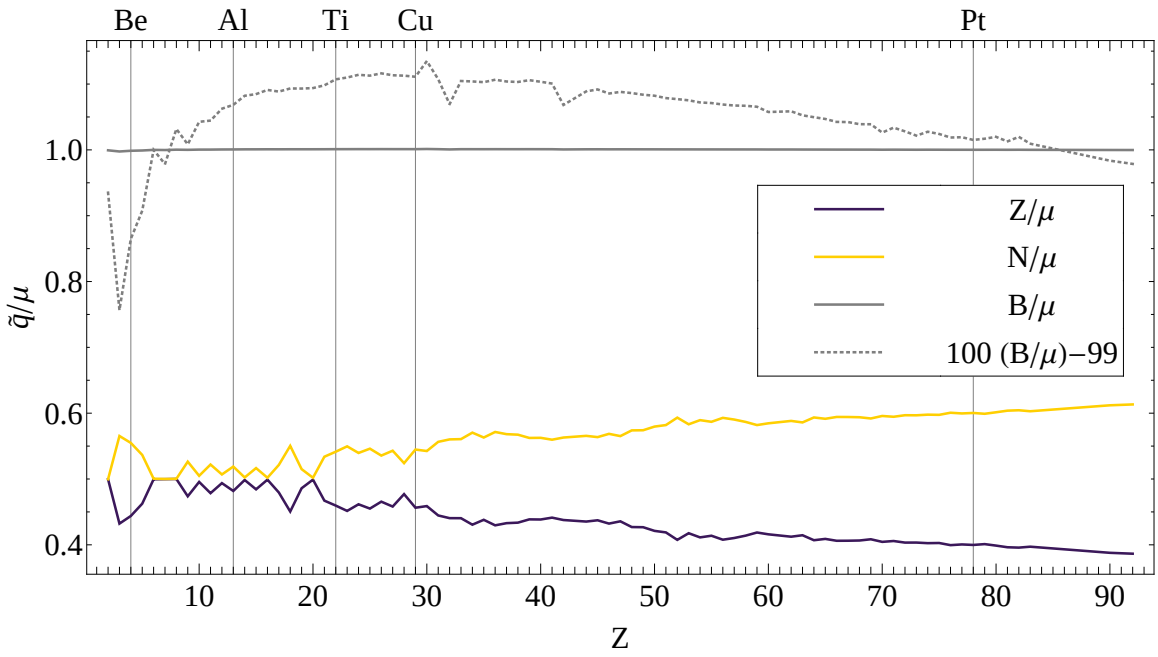

Figure 2.1: Variation of Z/μ ($\tilde{\psi} = 0°$), N/μ ($\tilde{\psi} = 90°$), and B/μ (proportional to q/μ with $\tilde{\psi} = 45°$) for the stable elements, excepting hydrogen. Because $B = N + Z$ and $(B/\mu) \approx 1$ for all elements, the N/μ and Z/μ lines mirror each other about 1/2.

inverse-square-law tests with small separations [43]. Values for Z/μ, N/μ and B/μ for the stable elements are shown in figure 2.1. The parametrization for charge in equations 2.10 and 2.12 are exact for vector charges, which are conserved, but provide only an approximation in the case of scalar charges, which require detailed field theoretic calculations to determine the exact charge for each material. A model for scalar charges related to the dilaton is described in section 2.3.

Calculations of charges for a particular isotope are straightforward, but many elements have more than one stable isotope. In this case the reported charge is the natural-abundance weighted-average of the charge $\tilde{q}$ divided by the atomic mass for the element (which is the natural-abundance weighted-average of the isotope masses). More complicated compounds and mixtures are computed in a similar manner, where the weighted average for the compound mass is explicitly computed for the denominator.

2.3 Dilatons

The dilaton arises naturally in string theory as the scalar partner to the graviton. Since the scalar and tensor forms couple differently to matter, the dilaton violates the equivalence principle. Kaplan and Wise [68] find that the composition-independent gluon field dominates the dilaton coupling for ordinary matter with a strength between $\mathcal{O}(1) \sim \mathcal{O}(10^3)$ times gravity. The remaining equivalence-principle-violating contribution gives a differential acceleration between protons and neutrons of $\sim 0.3\%$ of the total dilaton acceleration. Since observations find no evidence for such a force, it is generally assumed that the dilaton acquires a mass, which limits the range of its interactions.

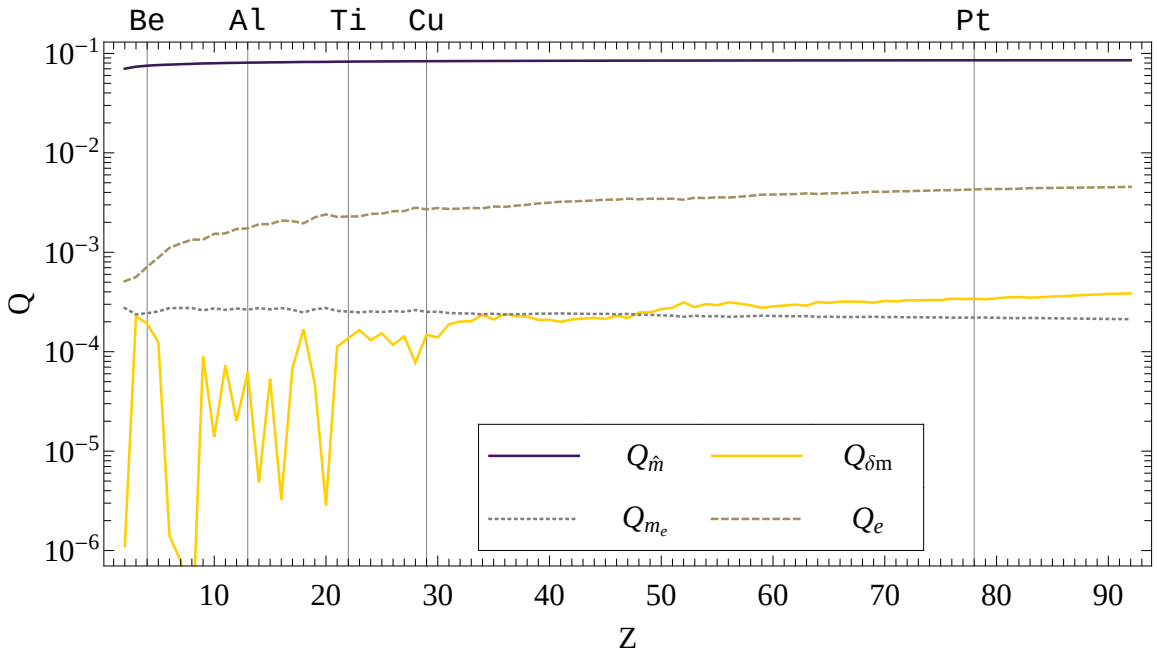

Figure 2.2: Variation of the dilaton charge parameters for the stable elements, excepting hydrogen. $Q_{\hat{m}}$ is associated with the average light quark mass, $Q_{\delta m}$ with the difference in light quark mass, Q_{m_e} with the electron mass, and Q_e with the electromagnetic field strength.

Damour and Donoghue developed a model for scalar charges due to a massless dilaton [37]. In contrast to Kaplan and Wise, they use the dominant coupling due to the gluon field as a free parameter – assuming only that it is the largest contribution to the total dilaton

coupling. They determine equivalence-principle-violating contributions to the dilaton coupling due to the average of the up and down quark masses $d_{\hat{m}}$, the difference in the up and down quark masses $d_{\delta m}$, the mass of the electron d_{m_e}, and the electromagnetic field strength d_e, while assuming that the dominant dilaton coupling due to the gluons d_g does not violate the equivalence principle. Equivalence principle tests place limits on combinations of the dilaton coupling parameters for a light dilaton ($\lambda \gg 1\text{AU}$). The charge parametrizations Q for each coupling are

$$Q_{\hat{m}} = \left(\frac{B}{\mu}\right)\left[0.093 - \frac{0.036}{B^{1/3}} - 0.020\frac{(B-2Z)^2}{B^2} - 1.4\times10^{-4}\frac{Z\,(Z-1)}{B^{4/3}}\right] \tag{2.13}$$

$$Q_{\delta m} = \left(\frac{B}{\mu}\right)\left[0.0017\frac{B-2Z}{B}\right] \tag{2.14}$$

$$Q_{m_e} = \left(\frac{B}{\mu}\right)\left[5.5\times10^{-4}\frac{Z}{B}\right] \tag{2.15}$$

$$Q_e = \left(\frac{B}{\mu}\right)10^{-4}\left[-1.4 + 8.2\frac{Z}{B} + 7.7\frac{Z\,(Z-1)}{B^{4/3}}\right], \tag{2.16}$$

where $B = Z + N$ is the atomic mass number (equivalent to baryon number) and Z is the proton number. The dilaton charges for the stable elements are plotted in figure 2.2. The relationship between the couplings and η is

$$\begin{aligned}\eta &\simeq d_g\left[\left(d_{\hat{m}} - d_g\right)\Delta Q_{\hat{m}} + \left(d_{\delta m} - d_g\right)\Delta Q_{\delta m} + \left(d_{m_e} - d_g\right)\Delta Q_{m_e} + d_e\Delta Q_e\right] \\ &\equiv D_{\hat{m}}\Delta Q_{\hat{m}} + D_{\delta m}\Delta Q_{\delta m} + D_{m_e}\Delta Q_{m_e} + D_e\Delta Q_e,\end{aligned} \tag{2.17}$$

where ΔQ gives the difference in charge for the test bodies and the D couplings are defined similar to [37], but without absorbing approximately constant terms from the charge definitions into them. The overall factor of d_g comes from the source, since the gluon contribution (which does not violate the equivalence principle) is assumed to dominate other contributions. The dilaton coupling to other components of the source gives second order effects, which are dropped here following Damour and Donoghue [37]. In contrast to the charge parametrization in equation 2.10 that requires two test body pairs, four different test body pairs are required to independently constrain the D couplings. However, since the contributions for $D_{\hat{m}}$ and D_e dominate, Damour and Donoghue recommend that current experiments set limits on this linear combination.

2.4 Strong Equivalence Principle and Lunar Laser Ranging

Since Apollo 11 astronauts placed the first retro-reflector array on the moon in 1969, observatories have been measuring the distance from the earth to the moon with lunar laser ranging (LLR). Lunar laser ranging measures the round-trip time-of-flight for laser pulses traveling from an earth observatory to the moon and back. The laser is reflected by the retro-reflectors on the moon, but the majority of the light is lost as the beam diverges over the long journey. Advances in techniques and measuring equipment allows the APOLLO project to measure the distance between the earth and moon with millimeter precision on a regular basis [90]. These measurements result in a precise knowledge of the orbit of the moon. Lunar laser ranging tests a broad range of phenomena due to general relativity and the arrangement of the matter in the earth and moon [138, 97] and provides several separate tests of the equivalence principle:

1. An anomalous precession of the moon's orbit around earth [3]
2. A difference in the way the earth and moon fall toward the sun [95]
3. A difference in the way the earth and moon fall toward the center of the galaxy [98]

Current Lunar laser ranging results give $\eta_{LLR} = (-0.8 \pm 1.3) \times 10^{-13}$ for the earth and moon falling towards the sun [137], $\eta_{LLR}^{gal} \leqslant 1.3 \times 10^{-6}$ toward the center of the galaxy [98], and an anomalous precession of the moon's orbit relative to the general relativity prediction of $K_{\rm gp} = (-0.0005 \pm 0.0047)$ [127]. The anomalous precession result also limits equivalence-principle violation through equation 38 of Adelberger, Heckel and Nelson [3]:

$$\frac{\delta\omega}{\omega} = \frac{\alpha}{2}\left(\frac{a}{\lambda}\right)^2 e^{-a/\lambda}, \tag{2.18}$$

where ω is the moon's orbital period, a is the mean earth-moon distance, and the anomalous precession $\delta\omega$ is the relative precession $K_{\rm gp}$ times the general relativity prediction of 19.2 mas y^{-1}. The strongest limit due to the anomalous precession occurs at a range $\lambda = (a/2)$ and results in $\alpha = (-0.2 \pm 1.9) \times 10^{-11}$.

Lunar laser ranging tests of the equivalence principle could see a violation due to either (or both) the composition or the gravitational binding energy difference between the earth

and moon [96]. It has even been proposed that a scalar field with a charge closely tied to the gravitational binding energy could cancel a contribution due to a vector field with a charge based on the body's composition [93]. To address this ambiguity, we performed laboratory experiments using test bodies that match the earth's and moon's compositions, but have no appreciable gravitational binding energy [13]. The combined laboratory and lunar laser ranging results set a 1-σ limit on the equivalence principle for gravitational binding energy by itself of $|\eta_{grav}| \leqslant 1.3 \times 10^{-3}$ prior to our current experiment [13]. Due to improvements in lunar laser ranging by the APOLLO collaboration, this thesis includes results using an improved laboratory measurement to complement the expected improvement in lunar laser ranging equivalence principle results.

The gravitational binding energy of an object is given by the sum of the potential of all the point-wise pairs making up the object:

$$E_{grav} = \iint \frac{G\,\rho(\mathbf{r})\rho(\mathbf{r'})}{|\mathbf{r}-\mathbf{r'}|} d^3r\, d^3r', \tag{2.19}$$

where ρ is the density of the object. The earth's gravitational binding energy as a fraction of total mass (using Dziewonski and Anderson's density model of the earth [45]) is $E^{\oplus}_{grav}/m_{\oplus} \approx -4.6 \times 10^{-10}$, while that of the moon (using Weber *et als.* density model of the moon [130]) is $E^{\leftmoon}_{grav}/m_{\leftmoon} \approx -0.2 \times 10^{-10}$. While small, these contributions are substantially larger than that of a laboratory test body and are greater than the experimental sensitivity of $\sim 10^{-13}$. For comparison, the fraction of gravitational binding energy in one of the test bodies used in the Eöt-Wash equivalence principle tests is $E^{TB}_{grav}/m_{TB} \sim 10^{-28}$.

2.4.1 Dark Matter

Measurements of the cosmic microwave background, gravitational lensing of distant galaxies, observations of merging galaxies and the discrepancy between the mass of luminous matter and the orbital velocity of stars far from the center of their galaxy all provide evidence for dark matter. Measurements of the cosmic microwave background predict that dark matter makes up 23% of the mass of the universe [65]. Currently, dark matter has only been observed through its gravitational interaction with ordinary matter. However, it is possible that dark matter candidates, such as weakly-interacting massive particles

(WIMPS) [117] or axions [102], have non-gravitational interactions with ordinary matter. Weak equivalence principle tests constrain non-gravitational dark matter interactions both directly, through searches for an equivalence-principle violation towards the dark matter in our galaxy, and indirectly, through an additional force between neutral ordinary matter due to virtual quantum loops involving dark matter [23]. The indirect limits are much stronger than the direct limits because the acceleration of the earth or sun are $\sim 10^{-2}$ $\mathrm{m\,s^{-2}}$ while the acceleration of our solar system toward the center of our galaxy is inferred to be $a_{gal} = (2.3 \pm 0.3) \times 10^{-10}$ $\mathrm{m\,s^{-2}}$. Measurement of our solar system's velocity with respect to distant quasars agree with measurements of the proper motion of and distance to Sagittarius A* at the center of the Milky Way [105] to determine a_{gal}. The indirect limits require a model for the non-gravitational force, while the direct limits require only an estimate of the dark matter contribution to the acceleration.

Non-gravitational interactions between neutral ordinary matter and galactic dark matter would appear as an equivalence-principle-violating acceleration towards the center of the Milky Way. Dark matter has been estimated to make up $f_{DM} \approx 25\%$ of the mass inside the sun's orbit of the Milky Way galaxy [121]. This results in

$$\eta_{DM} = \frac{\Delta a_{gal}}{f_{DM} a_{gal}}. \tag{2.20}$$

In order to relate this to astrophysical observables, the composition of the test bodies pairs can be taken into account to set limits on the non-gravitational acceleration of neutral hydrogen. Using equation 2.10 to adjust from the test-body-pair composition to that of hydrogen gives

$$\delta a_{DM} = \Delta a_{gal} \left(\frac{\tilde{q}}{\mu}\right)_H \left[\Delta \left(\frac{\tilde{q}}{\mu}\right)_T\right]^{-1}, \tag{2.21}$$

which can then be compared to the inferred total acceleration due to dark matter $a_{DM} = f_{DM} a_{gal}$ to give

$$\frac{\delta a^H_{DM}\left(\tilde{\psi}\right)}{f_{DM} a_{gal}} = \frac{\Delta a_{gal}}{f_{DM} a_{gal}} \frac{\left[\left(\frac{Z}{\mu}\right)_H \cos\tilde{\psi} + \left(\frac{N}{\mu}\right)_H \sin\tilde{\psi}\right]}{\left[\left(\Delta\frac{Z}{\mu}\right)_T \cos\tilde{\psi} + \left(\Delta\frac{N}{\mu}\right)_T \sin\tilde{\psi}\right]}. \tag{2.22}$$

Using a measured deuterium-to-hydrogen ratio in interstellar gas of $2.3^{+1.5}_{-1.3} \times 10^{-5}$ [108]

gives the following charges for interstellar hydrogen:

$$\left(\frac{Z}{\mu}\right)_H = 0.992213 \qquad \left(\frac{N}{\mu}\right)_H = 2.3 \times 10^{-5}$$

Weak equivalence principle tests relate to interactions between ordinary matter and dark matter where a new force couples directly only to dark matter, but dark matter may have non-gravitational interactions with Standard Model particles (e.g., Higgs or weak interactions) [17, 23, 24]. A new force in the dark sector then induces a force between ordinary matter through quantum corrections involving virtual dark matter. Improvements to weak equivalence principle experiments, astrophysical observations (such as [71, 16]), direct dark matter detection experiments (such as CDMS [30], XENON [33], CoGeNT [32], etc.), and Higgs physics from the Large Hadron Collider will elucidate the properties of dark matter and possible dark sector forces.

2.4.2 Antimatter

The AEgIS collaboration [42] is attempting the technically challenging task of an equivalence principle test between antihydrogen $\bar{\mathrm{H}}$ and hydrogen H. Advances in the creation and trapping of low-temperature antihydrogen creates possibilities for precision spectroscopy tests of CPT and tests of the equivalence principle between anti-matter and matter. Previous attempts to compare the gravitational acceleration of antimatter with that of matter [139] used charged particles (positrons and electrons), which resulted in experimental difficulties that precluded a conclusive measurement [93]. However, several arguments suggest that existing limits from differences in ordinary matter require extremely high precision from an antimatter-matter experiment to set new limits. A difference in the forces acting on matter and on antimatter would require either a new vector interaction or a violation of CPT symmetry for gravity. Vector interactions are precisely modeled using the Yukawa force with the vector charge parametrized by $\tilde{\psi}$. Since the vector charges vary across the periodic table, albeit about three orders of magnitude smaller than that for $H - \bar{H}$, any vector interaction is tightly constrained by precision weak equivalence principle tests with ordinary matter. In the case of both a new scalar interaction and a new vector interaction, it is conceivable that the couplings could coincide or be forced by a symmetry to nearly can-

cel. This proposed cancellation cannot be exact because the vector and scalar interactions transform differently under Lorentz boosts.

For a vector charge the Lorentz invariant is the charge Q given by

$$Q = \int j^0 dV = \int \gamma j_r^0 \frac{dV_r}{\gamma} = \int j_r^0 dV_r \tag{2.23}$$

$$\gamma = \frac{1}{\sqrt{1-\frac{v^2}{c^2}}} \tag{2.24}$$

where j^0 is the 0 component of the vector current, dV is the volume element, v is the velocity relative to the rest frame, and the subscript r represents the rest frame for the charge. In contrast for a scalar interaction the charge density ρ is Lorentz invariant and the charge Q' obtains a factor of γ^{-1} compared to the vector charge:

$$Q' = \int \rho dV = \int \rho_r \frac{dV_r}{\gamma} \tag{2.25}$$

This different velocity dependence of the vector and scalar charge along with the relativistic nature of the nucleons limits cancellation between a vector and a scalar to $\sim 10^{-3}$ in ordinary nuclei [7].

2.4.3 CPT, Lorentz symmetry and the equivalence principle

Requiring energy conservation leads to quantitative relationships between the equivalence principle and preferred-location and preferred-frame effects that would arise if Lorentz symmetry were violated [57]. Similarly, violations of CPT result in Lorentz violation [55]. These relationships allow comparisons between different experiments testing these fundamental postulates of our physical theories. The standard model extension [73] expands the standard model of particle physics to systematically parametrize the effects of violating CPT and Lorentz symmetries. Due to the strong relationships between CPT, Lorentz invariance and the weak equivalence principle, many of the parameters that arise in the standard model extension for violations in the gravitational sector are accessible to weak equivalence principle experiments.

Considering the energy contributions to a composite structure illustrates the interdependence of the weak equivalence principle, preferred location effects and Lorentz invariance. The standard model extension provides a more complete examination of the effects of CPT

or Lorentz violation, but the large number of coefficients involved in characterizing the different violations reduces its effectiveness for conceptual understanding. To conceptually illustrate the relationships between preferred locations, preferred frames and the weak equivalence principle, I summarize part of Haugan's energy conservation argument [57]. Haugan presents a relationship for the energy of a composite body in an external gravitational potential. The energy relationship is derived from a Lagrangian constructed in the semi-conservative parametrized post-Newtonian framework to ensure conservation of energy.

$$E_c = \left[m_R - E_B\left(\mathbf{x}, \mathbf{v}\right)\right] - m_R U\left(\mathbf{x}\right) + \frac{1}{2} m_R \mathbf{v}^2 + \mathcal{O}\left(m_0 U^2, m_0 \mathbf{v}^4, m_0 U \mathbf{v}^2\right) \tag{2.26}$$

$$E_B\left(\mathbf{x}, \mathbf{v}\right) = \delta m_P^{ij} U^{ij}\left(\mathbf{x}\right) - \frac{1}{2} \delta m_I^{ij} v^i v^j \tag{2.27}$$

The rest mass of the composite body m_R includes the constituent masses and the portion of the binding energy that follows the equivalence principle, while $E_B\left(\mathbf{x}, \mathbf{v}\right)$ includes the equivalence-principle-violating portions to a consistent order, $\mathbf{x}$ and $\mathbf{v}$ are quasi-Newtonian coordinates of the center of mass, and $U\left(\mathbf{x}\right)$ is the external gravitational potential. The binding energy term E_B includes the anomalous passive gravitational mass δm_P^{ij} of the internal components coupling to the gravitational field U^{ij} with $U = U^{ii}$ and the anomalous kinetic energy due to the internal inertial masses encoded by the δm_I^{ij} and their center of mass velocities v^i. The position and velocity dependence of these terms indicates their relationship to preferred frame and location effects, as can be shown by relating the energy of a body allowed to freely fall a small distance. The acceleration of the body is

$$a^k \approx g^k + \left(\frac{\delta m_P^{ij}}{m_R}\right) \frac{\partial U^{ij}}{\partial x^k} - \left(\frac{\delta m_I^{kj}}{m_R}\right) g^j, \tag{2.28}$$

where $\mathbf{g} \equiv \nabla U$ and $\mathbf{a} \approx \mathbf{g}$ to first order was used in the last term on the right-hand side. The resulting acceleration includes the acceleration $\mathbf{g}$, which respects the equivalence principle, a location dependent portion indicating a preferred-location effect, and a preferred-frame effect due to the anomalous inertial mass coupling to changes in velocity. The total energy consists of the kinetic energy, the internal binding energy, and the external potential energy. If the internal binding energy changes due to different locations or frames, then either the

interaction energy with the external potential (e.g., an anomalous gravitational redshift) or the kinetic energy (an additional acceleration) must change to maintain energy conservation.

This argument on the basis of energy conservation generalizes to any theory that results in changing mass or binding energy of a composite object. An additional interesting case is varying fundamental constants. The fundamental constants control the binding energy content of composite bodies. If a fundamental constant were to vary, a violation of the weak equivalence principle occurs due to the different changes in the binding energy contributions to mass for different elements. Many theories introduce a cosmological scalar that affects fundamental constants, so limits on the variations of the fundamental constants due to a cosmological scalar field [40] provide a different perspective on equivalence-principle violation by scalar fields.

Chapter 3

TORSION BALANCES

Torsion balances permit extremely sensitive equivalence principle experiments due to two main properties. The first and most important property is that torsion balances only experience an angular deflection about the fiber axis (twist) due to forces acting on the test bodies in different directions. The second property is that a thin fiber provides an extremely weak spring for twists, which allows deflections by extremely weak forces. Figure 3.1 illustrates a simple torsion pendulum consisting of two test bodies separated by a rigid rod and supported by a fiber near the center. In a static configuration using an idealized, perfectly flexible fiber, a torque about the vertical will only occur if the forces acting on the test bodies have different vector directions. To see this, define "down" by the sum of all forces acting on the pendulum in static equilibrium, except for the fiber tension, which defines "up". Define a second axis $\hat{\mathbf{x}}$ as perpendicular to both the rod supporting the test bodies $(\mathbf{r}_B - \mathbf{r}_A)$ and the fiber $\hat{\mathbf{z}}$, and the final axis $\hat{\mathbf{y}}$ mutually perpendicular to the first two (coincident with the rod if the pendulum hangs level):

$$\hat{\mathbf{z}} = -\frac{\mathbf{F}_A + \mathbf{F}_B}{|\,\mathbf{F}_A + \mathbf{F}_B|} \tag{3.1}$$

$$\hat{\mathbf{x}} = \frac{(\mathbf{r}_B - \mathbf{r}_A)}{|\,\mathbf{r}_B - \mathbf{r}_A|} \times \hat{\mathbf{z}} \tag{3.2}$$

$$\hat{\mathbf{y}} = \hat{\mathbf{z}} \times \hat{\mathbf{x}} \tag{3.3}$$

Then the torque about the fiber τ_z is

$$\begin{aligned} \tau_z &= \hat{\mathbf{z}} \cdot (\mathbf{r}_A \times \mathbf{F}_A + \mathbf{r}_B \times \mathbf{F}_B) \\ &= \frac{(\mathbf{r}_B - \mathbf{r}_A) \cdot \mathbf{F}_A \times \mathbf{F}_B}{|\,\mathbf{F}_A + \mathbf{F}_B|}, \end{aligned} \tag{3.4}$$

where $\mathbf{r}_A$ and $\mathbf{F}_A$ give the position of and total force on test body A and likewise for B. Equation 3.4 generalizes to more test bodies (or pendulum parts) by summing the triple products of the difference in position of each pair of test bodies and the forces acting on

those test bodies. A torsion balance only twists if the forces acting on the test bodies act in different directions. It is this principle of torsion balances that allows an apparatus to achieve a measurement sensitivity independent of the mass and positioning tolerances of the test bodies. However, these tolerances result in sensitivity to gravity gradients, which are a leading systematic effect.

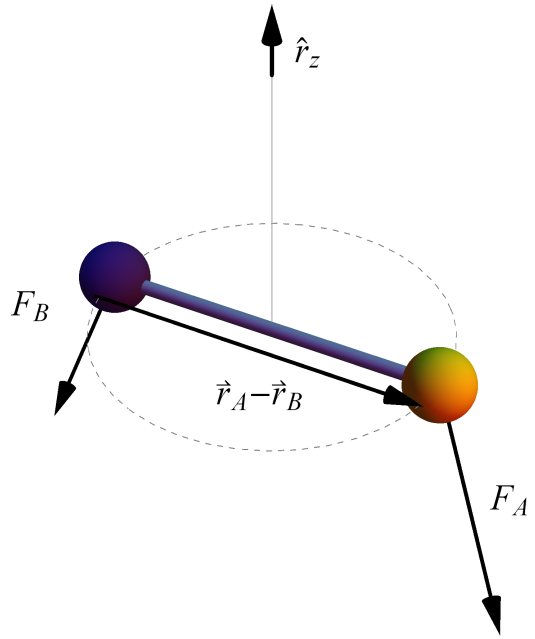

Figure 3.1: A torsion pendulum experiences a torque about the fiber axis only due to differences in the directions of the forces $\mathbf{F}_A$ and $\mathbf{F}_B$ acting on the test bodies.

The other components of the torque on the pendulum are

$$\begin{aligned}\tau_x &= \hat{\mathbf{x}} \cdot (\mathbf{r}_A \times \mathbf{F}_A + \mathbf{r}_B \times \mathbf{F}_B) \\ &= (\mathbf{r}_A \cdot \hat{\mathbf{y}})(\mathbf{F}_A \cdot \hat{\mathbf{z}}) + (\mathbf{r}_B \cdot \hat{\mathbf{y}})(\mathbf{F}_B \cdot \hat{\mathbf{z}}) + [(\mathbf{r}_B - \mathbf{r}_A) \cdot \hat{\mathbf{z}}](\mathbf{F}_A \cdot \hat{\mathbf{y}}) \quad \text{and} \qquad (3.5) \\ \tau_y &= \hat{\mathbf{y}} \cdot (\mathbf{r}_A \times \mathbf{F}_A + \mathbf{r}_B \times \mathbf{F}_B) \\ &= [(\mathbf{r}_B - \mathbf{r}_A) \cdot \hat{\mathbf{z}}](\mathbf{F}_A \cdot \hat{\mathbf{x}}) \qquad (3.6)\end{aligned}$$

where the condition of zero net force in the horizontal directions $(\mathbf{F}_A \cdot \hat{\mathbf{x}}) = -(\mathbf{F}_B \cdot \hat{\mathbf{x}})$ and $(\mathbf{F}_A \cdot \hat{\mathbf{y}}) = -(\mathbf{F}_B \cdot \hat{\mathbf{y}})$, restricting the pendulum rod to lie in the $z-y$ plane, and an idealized

perfectly flexible fiber were used. If the pendulum rod is level, then the terms proportional to $(\mathbf{r}_B - \mathbf{r}_A) \cdot \hat{\mathbf{z}}$ also vanish, so good tolerances in the torsion balance construction reduce gravity gradient systematic effects by allowing the pendulum to rest in a level orientation (see section 7.1). The other terms in τ_x relate to the center of mass resting under the fiber attachment point as can be seen by considering the case of $\tau_x = 0$ with only gravity.

3.1 Experimental Harmonic Oscillator with Noise

The differential equations for a harmonic oscillator provide a good model for a torsion balance. Here I present the equations to provide consistent notation and to introduce the fundamental noise floor that a torsion balance faces due to thermal noise in the fiber. A more thorough treatment of noise in a torsion oscillator and other mechanical systems can be found in Saulson [112]. Ritter and Gillies [54] have an illustrative discussion on coupling horizontal seismic noise into the torsion mode.

A torsion balance can be modeled by the differential equation

$$M\ddot{\theta}(t) + f\dot{\theta}(t) + \kappa\left(1 + \frac{i}{Q_i}\right)\theta(t) = \tau(t), \tag{3.7}$$

where M is the moment of inertia of the torsion pendulum, f characterizes velocity damping and gives a quality factor $Q_v = M\omega_0/f$, κ is the torsion constant, Q_i is the quality factor for damping internal to the fiber and $\tau(t)$ describes all external torques. The quality factor indicates the number of oscillations for the damping to reduce the pendulum amplitude by $e^{-\pi}$.

In the undamped case where $f \to 0$ and $Q_i \to \infty$

$$\ddot{\theta}(t) + \omega_0^2\theta(t) = \frac{\tau(t)}{M}, \tag{3.8}$$

and $\omega_0 = \kappa/M$ gives the undamped frequency of oscillation for the system.

A high Q torsion pendulum operated under high vacuum is most commonly limited by internal damping in the torsion fiber. Internal damping in the fiber is modeled using an imaginary contribution to the torsion constant with a magnitude inversely related to Q_i. Though Q_i may be frequency dependent, the frequency dependence is empirically weak for many materials [112]. Velocity damping may also contribute to noise, possibly through gas

or eddy-current damping, but a good design and low vacuum pressure can substantially reduce these effects. The transfer function $\mathcal{R}(\omega)$ models the torsion pendulum's response to torques. Solving the differential equation using a Fourier series expansion for $\tau(t)$ allows us to determine the transfer functions for both internal and velocity damping:

$$\mathcal{R}(\omega) \equiv \frac{\tilde{\theta}(\omega)}{\tilde{\tau}(\omega)} \tag{3.9}$$

$$\mathcal{R}_{\text{internal}}(\omega) = \frac{1/\kappa}{\left(1-\omega^2/\omega_0^2\right)+i/Q_i} \tag{3.10}$$

$$\mathcal{R}_{\text{velocity}}(\omega) = \frac{1/\kappa}{\left(1-\omega^2/\omega_0^2\right)+i\omega/\left(\omega_0 Q_v\right)} \tag{3.11}$$

The fluctuation-dissipation theorem [21] gives the thermal noise floor based on the transfer functions for these common forms of damping in a torsion pendulum. The fluctuation-dissipation theorem provides a quantitative relationship between dissipation in a system and the random fluctuations (noise) of the measured quantity:

$$\tau^2(\omega) = 4k_B T X(\omega), \tag{3.12}$$

where k_B is Boltzmann's constant, T is the temperature, and $X(\omega) = \text{Re}\left(1/[i\omega\mathcal{R}]\right)$ is the generalized (real) resistance of the mechanical system, in this case, the torsion oscillator. In the internally damped case $X_{\text{internal}}(\omega) = \kappa/(\omega Q_i)$ and in the velocity damped case $X_{\text{velocity}}(\omega) = f$. Putting this together with the transfer function leads to predictions for the thermal noise spectrum of the twist angle for a torsion pendulum:

$$\theta^2_{\text{internal}}(\omega) = \frac{4k_B T}{\kappa\omega Q_i}\frac{1}{\left(1-\omega^2/\omega_0^2\right)^2 - 1/Q_i^2} \tag{3.13}$$

$$\theta^2_{\text{velocity}}(\omega) = \frac{4k_B T}{\kappa\omega_0 Q_v}\frac{1}{\left(1-\omega^2/\omega_0^2\right)^2 - \left(\omega/\left(\omega_0 Q_v\right)\right)^2} \tag{3.14}$$

For the experiments discussed here, the main difference in the noise predictions is the direct dependence of the internal damping noise on $1/\omega$ as shown in figure 3.2.

One may question how valid a one dimensional model can be for a complex 3D object suspended by a non-ideal wire from a point that must be mechanically defined on a rotating platform. In principle there could be 8 or more modes of the system beyond their common motion together, such as the wobble of the pendulum, swing, bounce, guitar string, and of

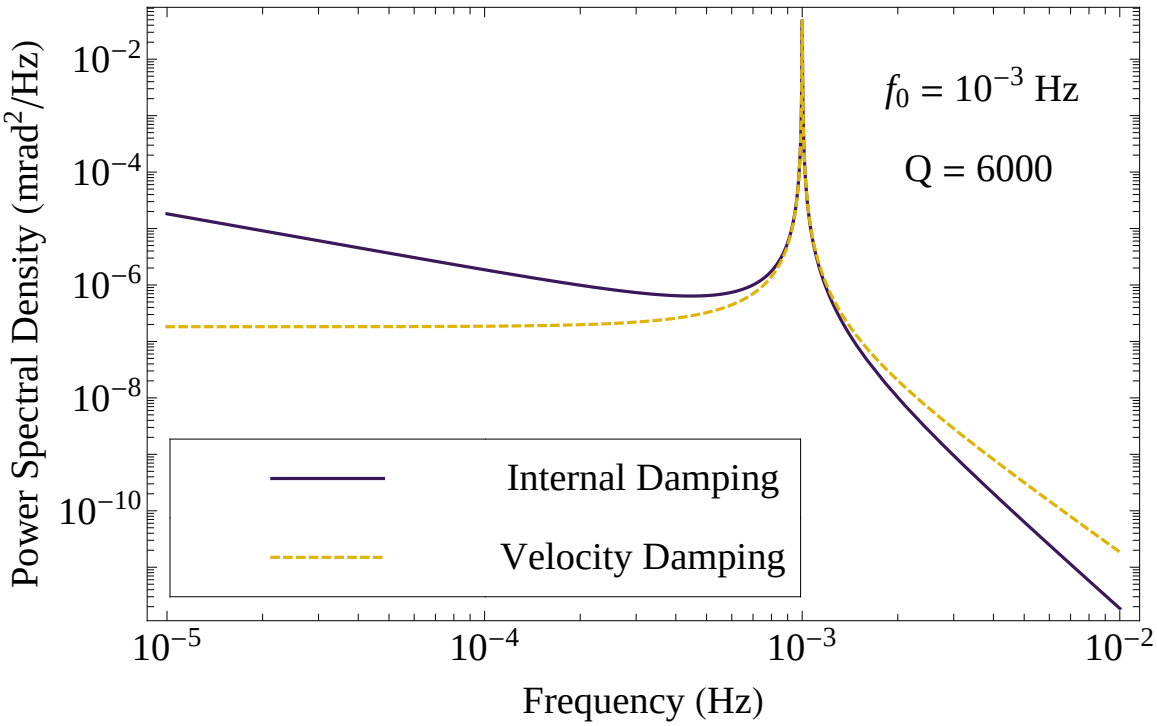

Figure 3.2: Comparison of the power spectral density for internal damping versus velocity damping of a torsion oscillator's twist.

course the torsion mode. In table 3.1 the frequencies of the various modes are approximated. The apparatus is designed to damp and isolate these other modes from the torsion mode as described in section 5.2. The important feature is that the torsion mode is well separated in frequency from all of the other modes. Since all of the other (non-torsion) modes are much higher in frequency, a design including physical damping of the unwanted modes substantially reduces the energy available to couple into the torsion mode. Furthermore, the large frequency separation allows straightforward extraction of the torsion mode during data analysis.

Additional noise sources, such as seismic motion, changes in gravity gradients, tilts and thermal motion of the apparatus, have other functional dependencies, with both $1/\omega$ $(1/f)$ and $1/\omega^2$ $(1/f^2)$ being common [54].

Table 3.1: Functional dependence of the pendulum mode frequencies on mechanical parameters and estimated values for our torsion balance. Numerical factors are omitted. E is Young's modulus for the fiber, ρ is the fiber density, d is the fiber diameter, l is the fiber length, $\kappa \propto d^4/l$ is the torsional fiber constant, m is the pendulum mass, h is the pendulum height, M_z is the pendulum's moment of inertia about the fiber axis, M_h is the pendulum's moment of inertia about an axis in the horizontal plane, k_d is the vertical damper spring constant, and g is earth's gravitational acceleration.

Pendulum Mode	Functional Form	Estimated Frequency (Hz)
Guitar	$\sqrt{mg/(\rho d^2 l^2)}$	10
Bounce	$\sqrt{Ed^2/(ml)}$	10
Bounce (Damper)	$\sqrt{k_d/m}$	1
Wobble	$\sqrt{hmg/M_h}$	1
Swing	$\sqrt{g/l}$	5×10^{-1}
Torsion	$\sqrt{\kappa/M_z}$	1×10^{-3}

3.2 Multipole Formalism

The torsion pendulum responds to differences in the direction of the forces on the test bodies. Unfortunately, gravity gradients have this characteristic, making them an important systematic effect to understand. The cylindrical symmetry of our torsion balances makes the multipole expansion of the gravitational field particularly useful for characterizing the gravity gradient coupling with the pendulum. A review of the multipole formalism in the context of torsion pendulums is presented here (see references [44, 123, 124] for further details). An expansion of the gravitational potential V_N between two extended bodies (defined by functions of their density ρ_p and ρ_s for the pendulum and surrounding masses, respectively) using the spherical harmonics Y_ℓ^m as basis functions provides the form for the gravitational interactions and can be separated into those affecting each harmonic of the

turntable rotation frequency:

$$V_N = -\int_{pend}\int_{source} G\,\frac{\rho_p(\mathbf{r}')\rho_s(\mathbf{r})}{|\mathbf{r}-\mathbf{r}'|}\,d^3r\;d^3r' \tag{3.15}$$

$$= -4\pi G\sum_{\ell=0}^{\infty}\frac{1}{2\ell+1}\sum_{m=-\ell}^{\ell} q_{\ell m}Q_{\ell m} \tag{3.16}$$

$$q_{\ell m} = \int_{pend} \rho_p(\mathbf{r}')\;r'^{\ell}\;Y_\ell^{m*}(\hat{\mathbf{r}}\,')\;d^3r' \tag{3.17}$$

$$Q_{\ell m} = \int_{source} \rho_s(\mathbf{r})\;r^{-(\ell+1)}Y_\ell^m(\hat{\mathbf{r}}\,)\;d^3r \tag{3.18}$$

With inner moments $q_{\ell m}$ and outer fields $Q_{\ell m}$ defined to separate the pendulum's configuration from that of the laboratory environment. Calculations of $q_{\ell m}$ and $Q_{\ell m}$ are easiest in a body fixed frame, which is typically the same as the laboratory frame for the environmental model. A transformation from the body fixed frame of the pendulum in the rotating apparatus to the the laboratory frame involves a rotation giving $\bar{q}_{\ell m} = q_{\ell m}e^{-im\phi_{\rm TT}}$, where $\phi_{\rm TT}$ is the angle of the turntable with respect to the laboratory frame.

The torque about the fiber (calculated in the laboratory frame) is defined as

$$\begin{aligned}\tau_Z &= -\frac{\partial}{\partial\phi}V_N \\ &= -4\pi iG\sum_{\ell=0}^{\infty}\frac{1}{2\ell+1}\sum_{m=-\ell}^{\ell} m\;q_{\ell m}Q_{\ell m}e^{-im\phi_{\rm TT}} \\ &= 4\pi iG\sum_{\ell=0}^{\infty}\frac{1}{2\ell+1}\sum_{m=1}^{\ell} m\;\left(q_{\ell m}^*Q_{\ell m}^*e^{im\phi_{\rm TT}} - q_{\ell m}Q_{\ell m}e^{-im\phi_{\rm TT}}\right),\end{aligned} \tag{3.19}$$

where $q_{\ell,-m} = (-1)^m q_{\ell m}^*$ and likewise for $Q_{\ell m}$. Taking a specific term in the sum and separating the moments and exponential into real and imaginary components, the torque for a given gravitational coupling can be written as

$$\begin{aligned}\tau_{\ell m}^{\rm grav} &= 8\pi G\frac{m}{2\ell+1} \\ &\quad\{\sin(m\phi)\left[\mathrm{Im}\left(Q_{\ell m}\right)\mathrm{Im}\left(q_{\ell m}\right) - \mathrm{Re}\left(Q_{\ell m}\right)\mathrm{Re}\left(q_{\ell m}\right)\right] \\ &\quad + \cos(m\phi)\left[\mathrm{Im}\left(Q_{\ell m}\right)\mathrm{Re}\left(q_{\ell m}\right) + \mathrm{Re}\left(Q_{\ell m}\right)\mathrm{Im}\left(q_{\ell m}\right)\right]\}.\end{aligned} \tag{3.20}$$

This form shows the relationship to the two Fourier components for a given m that are determined from the pendulum twist using the appropriate transfer function. In fact, the

measured pendulum twist was used to determine unknown gravity gradient moments and fields. The $m = 0$ moments are cylindrically symmetric and produce no change with the turntable rotation, though tilts of vertical can rotate them into moments with different m. The $\ell = 1,\ m = 1$ moment also must vanish for a torsion balance. The force due to the bending of the fiber is much smaller than that due to gravity, the center of mass of a stationary torsion pendulum lies directly below the attachment point, so that the integrals over x' and y' in equation 3.21 are zero.

$$q_{11} = \int\limits_{pend} \rho_p(\mathbf{r}') \left[-\sqrt{\frac{3}{8\pi}} \left(x' + i\, y' \right) \right] dx'\, dy'\, dz' \tag{3.21}$$

The q_{21} is the leading moment that may introduce a twist at the equivalence-principle-violation signal frequency. Figure 3.3 illustrates the qualitative shapes of the spherical harmonics up to $\ell = 4$.

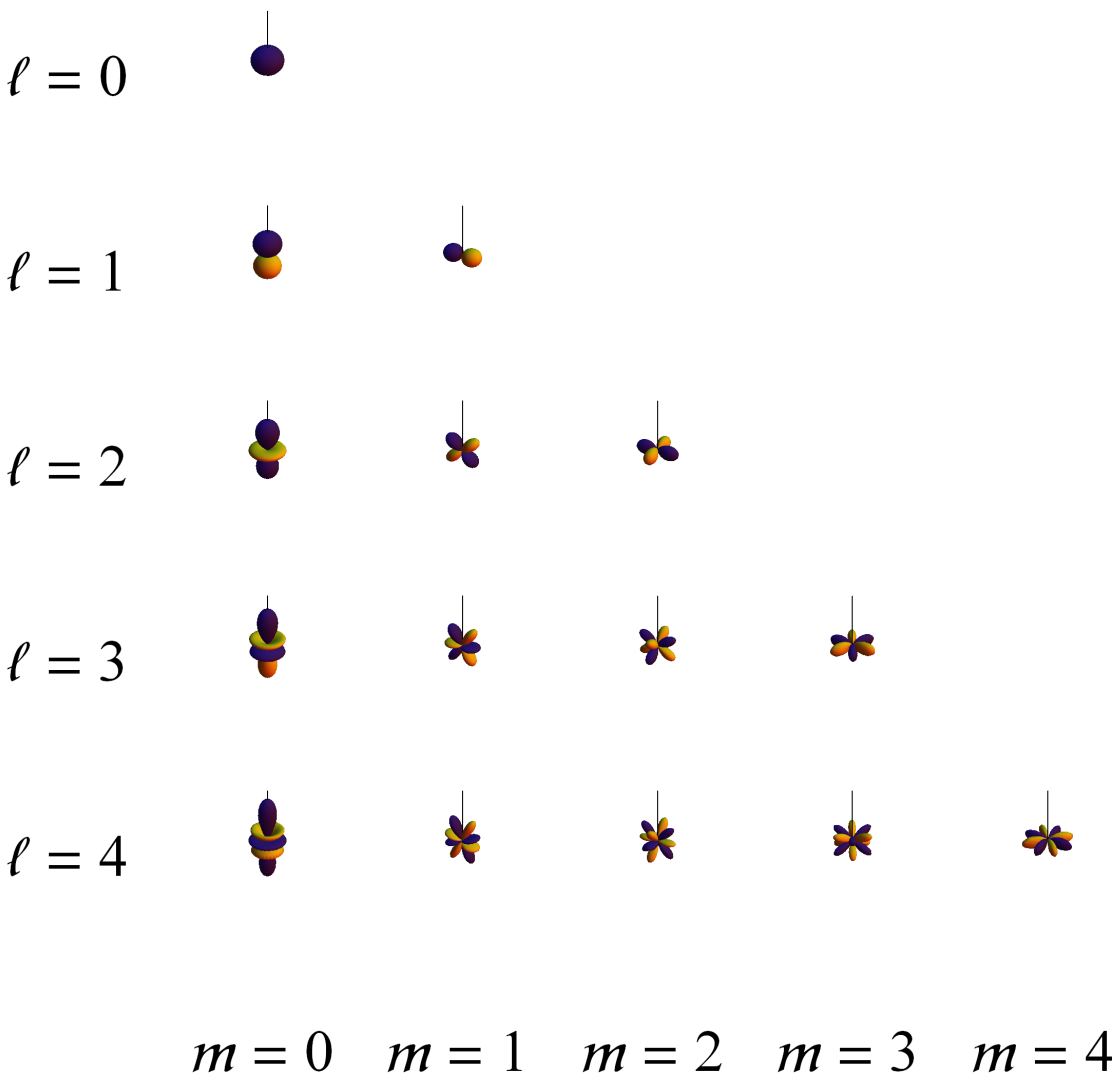

Figure 3.3: Representations of the spherical harmonics. The gravitational multipole moment corresponding to the illustrated spherical harmonic has high density in the gold regions and low density in the purple regions. Note that for $\ell = 1, m = 1$, the arrangement is unphysical for a torsion pendulum as described in the text.

Chapter 4

SIGNAL SOURCES

Our experiment relies on measuring the differential acceleration of the test bodies towards a source. We use sources such as the earth, sun, and center of the galaxy. While the test body charges can be chosen to maximize a particular charge difference, our sources have fixed compositions. Within the Yukawa framework (see section 2.2), a particular choice of charge or interaction range for an equivalence-principle-violating interaction can render an experiment insensitive. Fortunately, each of our sources has a unique composition that differs from the others. In the case of the galaxy, we utilize the large fraction of the mass due to dark matter to search for non-gravitational interactions between ordinary neutral matter and dark matter. For unknown forces with ranges greater than 1 AU, the substantially different compositions of the earth (mostly oxygen, magnesium, and silicon) and sun (hydrogen) provide strong limits on any possible charge described by equation 2.10. Because of the inverse-square relationship between the gravitational force and distance, using the earth gives an inherently stronger source than using the sun (e.g., in experiments by Roll, Krotkov and Dicke [109] and Braginsky and Panov [18, 19]). Using the earth as a source also probes violations of the equivalence principle at shorter ranges. Our apparatus sets the best limits on equivalence principle violation for ranges as short as 0.2 meters. The source model explained in this chapter expands the applicability of previous source models (developed by Su and Choi [123, 28]) into the previously unmodeled range from 20 km to 1000 km. We incorporated a detailed model for the composition and local density variations of the earth to create the source model for these intermediate ranges.

This chapter is divided into two main parts: In the first part, a general framework describing sources using the Yukawa parametrization is presented along with a detailed characterization of the earth as a source. In the second part, several astronomical sources that could provide insight into unknown physics are discussed.

4.1 Whole Earth Source Model

A rotating torsion balance enables the earth to be used as a source by modulating any equivalence-principle-violating signal at the apparatus's rotation frequency. The horizontal gravitational acceleration $a_\perp$ due to the entire earth is equal to the centrifugal acceleration a_c due to earth's rotation:

$$a_c = \Omega_\oplus^2 R_\oplus \cos\vartheta \tag{4.1}$$

$$a_\perp = a_c \sin\vartheta = \frac{\Omega_\oplus^2 R_\oplus \sin(2\vartheta)}{2} \tag{4.2}$$

The horizontal gravitational acceleration depends on earth's rotation frequency $\Omega_\oplus$, earth's radius $R_\oplus$, and the experiment's latitude ϑ. The torsion balance for our experiment is in Seattle, Washington at a latitude of 47.7° N, which corresponds to $a_\perp = 1.68 \times 10^{-2}\ \mathrm{m\,s^{-2}}$. However, the earth is inhomogeneous, so for ranges less than the diameter of the earth the details of earth's structure must be incorporated. We updated and extended the model developed by Su [123, 124] and modified by Choi [28] for this apparatus with recent geophysical data to model the entire earth with appropriate detail.

Two general types of models were included in our source integration: Local models impose an approximate rectangular coordinate system near the apparatus, where the curvature of the earth contributes minimally. Global models are inherently tied to earth's curved surface and often use angular coordinates of latitude and longitude. For both model types, the pendulum position was transformed into the model's horizontal and vertical datum (see appendix A.2). The pendulum position was always centered in the grid to prevent asymmetries in the grid from contributing to the calculations. The sole exception to locating the pendulum at the center of the grid occurred during the terrain integrations. The pendulum was located at the center of the terrain grid, but the surface rock density was interpolated from the regional density model [120], which used a different grid. However, the model's surface density remains constant in the apparatus locale and increases only slowly going into nearby mountain ranges.

Many different geophysical features contribute to the overall model. The apparatus is located underground with a hill rising immediately to the west of the laboratory. The

Puget Sound basin to the west and the Cascade mountains to the east are the largest terrain features impacting the model. The local subsurface density consists of a bowl of bedrock containing less dense sediments. At depths of 20 km, the bedrock underlying the Cascades is more dense towards the east and south, due to the subduction of the Juan de Fuca plate under the North American plate. In fact, the Juan de Fuca plate extends substantially down into the mantle east of the apparatus's location. Over the longest ranges, hydrostatic equilibrium for earth requires the east-west components to be relatively balanced, while the ellipsoidal shape of the earth produces a steady accumulation in the source integral to the north that balances the centrifugal force of earth's rotation.

We parametrize charge in our source model using baryon number and lepton number (see section 2.2) for consistency with the previous models by Su [123, 124] and Choi [28]. Among common materials baryon number per mass differs by less than about 0.5% and lepton number per mass differs by less than about 10%, as shown in table 4.2. Since density varies by factors of two or more, the source model primarily accounts for density variations, while assuming uniform composition of water, earth's crust, mantle, and core. An example illustrating the greater importance of density is the shift from land to water: The lepton number changes by 20% compared to a density change of more than 200%. Within the crust and mantle, the variation in lepton number is smaller, but substantial density changes still occur (e.g., between a subducted plate and surrounding mantle material). The primary contribution to the source acceleration comes from the density variations obtained from the different geophysical models.

Due to the different region covered by each geophysical model, several different underlying models were incorporated into a composite source acceleration model for our apparatus. Terrain was modeled in three parts: First, Choi's model of the laboratory and local terrain based on measurements and architectural and site plans for the CENPA laboratory covers distances up to 180 m [28]. Second, the PSDEM2005 digital elevation model (DEM) for the Puget Sound region includes terrain elevation and bathymetry for distances up to 24 km [51]. Third, NOAA's Coastal Relief Model provides terrain and bathymetry data extending out to 91 km [94]. We used the surface density from a USGS tomographic density model for all the terrain integrations [120]. In addition, the subsurface density from the

Table 4.1: Enumeration of the individual geophysical models and their applicable range. Models are listed multiple times when the integration was performed with different grid sizes. The range indicates the distance to the inner and outer edge of the model. MULTI is a program that computes the source acceleration based on a model built of primitive solids. DEM is a digital elevation model that describes the height of terrain. Density refers to a model for the density of the earth.

Model	Type	Range (m)		Grid Size (m)
		Inner	Outer	
CENPA Building [28]	MULTI	0	60	Dynamic†
Lab Site Plans [28]	DEM	0	20	0.2083
Lab Site Plans [28]	DEM	20	60	1.25
Lab Site Plans [28]	DEM	60	180	3.75
PSDEM2005 [51]	DEM	180	600	9.14
PSDEM2005 [51]	DEM	600	1800	27.4
PSDEM2005 [51]	DEM	1800	6000	82.3
PSDEM2005 [51]	DEM	6000	2.38×10^4	246.9
Coastal Relief [94]	DEM	2.38×10^4	9.10×10^4	$558^{\ddagger}$
Cascadia Density [120]	Density	0	9.10×10^4	2.00×10^3
Global Sediment [75]	Density	0	Crust	1°
CRUST 2.0 [15]	DEM & Density	0	Crust	2°
STB00D [118]	Density	0	Mantle	$\approx 12^{\circ}$*
PREM [45]	Density	0	Depth Only	Polynomials

† Grid was dynamically determined as part of the numerical integration performed by the MULTI program.

‡ Coastal Relief data was interpolated onto a rectangular grid from a 3 arcsec angular grid.

* Uses spherical harmonics with $\ell, m \leqslant 31$.

Table 4.2: The charge per mass used in the combined model for different parts of the earth.

Source composition	Z/μ	N/μ	B/μ
Fresh water [77] in [82]	0.5551	0.4443	0.9994
Puget sound 3.0 % salinity [56]	0.5529	0.4466	0.9995
Sea water 3.5% salinity [87]	0.5523	0.4472	0.9994
Crust [111]	0.4950	0.5056	1.0006
Mantle [80]	0.4954	0.5052	1.0006
Core [66]	0.4690	0.5321	1.0012

USGS density model was included to a depth of 60 km. A global crust (primarily CRUST 2.0 and related work [74]) and a mantle density model (STB00D) [45, 15, 118] provided the subsurface density for distances greater than about 90 km. The global model used an angular grid size of of 1° ($\sim$100 km near our apparatus) in both latitude and longitude, which provided only a slight overlap with the regional terrain models. The lack of overlap between the regional models (Coastal Relief and Cascadia Density) with the global crust model leads to greater uncertainty (a total uncertainty of $\sim$25%) in the source acceleration for 200 km $< \lambda <$ 600 km. The greater uncertainty arises because the grid size of the global crust model is comparable to λ for these ranges and contributes greater than 1/3 of the source acceleration magnitude.

4.1.1 Source Model Integration

It simplifies the calculation of limits on hypothetical interactions to separate the Yukawa force expression into a source part and a pendulum part. The source part can be separately calculated and further subdivided by the available models (laboratory, local terrain, local crustal structure, and entire earth). We rearrange the terms in the Yukawa parametrization

of an equivalence-principle violation from equation 2.5:

$$\tilde{V}(r) = \tilde{\alpha} \underbrace{\left[\left(\Delta\frac{\tilde{q}}{\mu}\right)_T m_T\right]}_{pendulum} \underbrace{G\left(\frac{\tilde{q}_S}{\mu_S}m_S\right)\frac{e^{-r/\lambda}}{r}}_{source}$$

For clarity, we determine the source strength in one dimension. Appendix A provides details on the integration in three dimensions. Differentiating the Yukawa potential for two point bodies $\tilde{V}$ with respect to the separation distance r gives the force:

$$\begin{aligned}\tilde{F} &= -\frac{\partial}{\partial r}\tilde{V} \\ &= \tilde{\alpha}\left[\left(\Delta\frac{\tilde{q}}{\mu}\right)_T m_T\right] \underbrace{G\left(\frac{\tilde{q}_S}{\mu_S}m_S\right)\left(\frac{1}{\lambda}+\frac{1}{r}\right)\frac{e^{-r/\lambda}}{r}}_{\text{point source acceleration}},\end{aligned} \tag{4.3}$$

where the last part of the expression is the acceleration of a test body due to a point source. For an extended source obeying superposition, the integral of the point source acceleration over the extended body gives the total source acceleration a_S (the acceleration experienced for unity $\tilde{\alpha}$ and test body charge):

$$a_S = G\int_{source}\left(\frac{\tilde{q}_S}{\mu_S}(r)\rho_S(r)\right)\left(\frac{1}{\lambda}+\frac{1}{r}\right)\frac{e^{-r/\lambda}}{r}dr, \tag{4.4}$$

where the source mass was replaced with the position dependent source density $\rho_S(r)$ and the charge per mass may also depend on the position r.

Combining the modeled source acceleration and the measured differential acceleration Δa gives the strength of a force compared to gravity $\tilde{\alpha}$ for a given choice of charge and range for the hypothetical interaction:

$$\tilde{\alpha} = \frac{\Delta a}{\left(\Delta\frac{\tilde{q}}{\mu}\right)_T a_S\left(\frac{\tilde{q}_S}{\mu_S},\lambda\right)} \tag{4.5}$$

We integrated the 3-dimensional versions of equation 4.4 over each model for selected values of λ. For each model, we estimated the minimum and maximum values of λ needed

to achieve a desired tolerance of 1% assuming constant density:

$$\frac{\int_{r=r_{min}}^{\infty} \frac{e^{-r/\lambda_{min}}}{r} dV}{\int_{r=0}^{\infty} \frac{e^{-r/\lambda_{min}}}{r} dV} = (1 + \frac{r_{min}}{\lambda_{min}}) e^{-r_{min}/\lambda_{min}} = \text{desired tolerance} \tag{4.6}$$

$$\frac{\int_{r=0}^{r_{max}} \frac{e^{-r/\lambda_{max}}}{r} dV}{\int_{r=0}^{\infty} \frac{e^{-r/\lambda_{max}}}{r} dV} = 1 - (1 + \frac{r_{max}}{\lambda_{max}}) e^{-r_{max}/\lambda_{max}} = \text{desired tolerance} \tag{4.7}$$

$$\tag{4.8}$$

Using a tolerance of 1% results in $\lambda_{min} \approx r_{min}/6$ and $\lambda_{max} \approx 6 \times r_{max}$ for each constituent model, where r_{min} is the distance from the apparatus to the nearest grid point in the model and r_{max} is the distance to the furthest grid point in the model. After the initial integration for all constituent models was completed over the estimated domain for λ, we selected additional λ for constituent models until we met the tolerance goal.

The relative size of the grid spacing δr to λ contributes significantly to the integration uncertainty if the grid is too coarse. We selected the grid spacing for the regional models so $\delta r \leqslant r_{min}/20$, which ensured that λ was larger than the grid spacing at all distances. The global models instead have $\delta r \sim \lambda_{min}$ because the global crust model used a 1° ~100 km grid, while the regional density model only extends beyond the Cascadia subduction zone (~100 km east of Seattle). The global model has increased uncertainty for $\lambda < 350$ km, but the overall uncertainty is likely less than 25% as discussed below in section 4.1.4.

Two three-dimensional coordinate systems were used for integration: Regional models used a local Cartesian coordinate system oriented as East-North-Up with the origin at the apparatus location, which included the curvature of the earth. Global models used latitude, longitude and elevation measured from the World Geodetic System of 1984 (WGS84) reference ellipsoid defined below by equation 4.9. At Seattle's latitude a $1^\circ \times 1^\circ$ grid box corresponds to 75 km × 111 km in the east-west and north-south directions, respectively. However, the northern edge is 1.4 km shorter than the southern edge. Models were converted into the integration coordinate systems as necessary. We used linear interpolation to align points from a model's coordinate system in the integration coordinate system. Linear

interpolation "flattens" models slightly because the interpolated value must be between the original values. To limit computational time, some high resolution terrain models were averaged to a lower resolution where the detail was small compared to the relevant range for λ.

The numerical integration was performed using the Mathematica [140] numerical integration function NIntegrate. The AccuracyGoal option was set to require at least 10^{-12} accuracy of individual integrations. Some zero or near zero values failed to meet the 10^{-12} accuracy criteria. These values generally occurred due to symmetry cancellations or to locations where the Yukawa integrand was near the integration numerical precision.

4.1.2 Composition of the Earth

Earth's bulk composition is fairly well agreed upon; however, several questions affecting the charge parametrization (equation 2.10) remain, including the light element composition of the outer core, the identification of chemical or phase changes that result in mantle sound velocity discontinuities, and the mapping of detailed inhomogeneous structure. In our source acceleration model, density uncertainties dominate the bulk composition uncertainty estimated as $\lesssim 1\%$. To give an idea of the maximum charge difference that could be found in a detailed inhomogeneous model, pure natural gas would have $Z/\mu \sim 0.527$ and $N/\mu \sim 0.473$, whereas iron ore would have $Z/\mu \sim 0.476$ and $N/\mu \sim 0.525$, with a difference of $\Delta(Z/\mu) \sim 0.051$ and $\Delta(N/\mu) \sim -0.052$ or about 10%. Differences between rock types result in typical charge variations of about $\sim$0.1% for Z/μ and N/μ. Due to the larger density uncertainty, we neglected the composition dependence on location (surface position or depth) within the crust, mantle or core, but the existing rock categorization in the CRUST model [74] makes this a future possibility. Table 4.2 summarizes the charge values we adopted. We used Rudnick and Gao's 2003 [111] bulk crust composition, Lyubetskaya and Korenaga's [80] composition for the mantle, and the Javoy *et al.* [66] model with silicon and oxygen as the primary light elements for the core composition. Appendix A.4 includes a comparison of the adopted models with other models of earth's composition.

4.1.3 Combined Source Model

Both terrain and density variations in the earth's crust contribute to the source integral with terrain contributions dominating for smaller λ and the density variations in the earth's interior becoming comparably important for larger λ. Earth's elliptical shape dominates the north-south component for $\lambda \gtrsim 1000$ km, but at shorter distances (all distances for the east-west component) both crustal variation and terrain make significant contributions. Due to intense research into earthquakes (Seismic Hazards Investigations in Puget Sound [129]) and modeling earth's interior (Reference Earth Model [74]), there has been a substantial increase in the detail of geophysical models, which allows us to extend our source integration to include 20 km $< \lambda <$ 200 km.

Laboratory Model

The laboratory building, including large equipment in the same room as the apparatus, was modeled by Choi [28]. The model accounts for the walls and dirt covering of the entire CENPA building and certain features of the room where the apparatus is located, including a large cyclotron magnet, excavation under the magnet, a crane, support structure for the apparatus, and a pond over the room. Both the composition charge-to-mass ratio and density were included explicitly in the model. The terrain was manually digitized from the CENPA laboratory site plans, which have a two foot contour interval and a scale of 1:600. The integration results of Choi were directly incorporated into the composite model without any reprocessing. The laboratory model provides the dominant contribution for $\lambda \lesssim 500$ m due to the apparatus's location in a buried laboratory with a hill rising immediately to the west.

The building model and terrain located within 180 meters of the apparatus were also used to model the gravity gradients. The calculated Q_{21} and Q_{31} agree with the measured values to about 10%, indicating that the model provides a good representation of the local mass distribution.

Terrain Model

The PSDEM2005 [51] and Coastal Relief [94] digital elevation models provided terrain elevation and bathymetry information out to 91 km. We separated the terrain model into different regions (see table 4.3) for the numerical integration. Figures 4.1 and 4.2 show the terrain from the PSDEM2005 [51] and Coastal Relief [94] models, respectively. A USGS density model for the Cascadia subduction zone [120] provided location dependent densities, which replace the bedrock map used by Su and Choi (see section 4.1.3). The surface density ranges from $2.0 - 2.4\ \mathrm{g\,cm^{-3}}$ out to 24 km and up to $2.8\ \mathrm{g\,cm^{-3}}$ over the entire region. The surface density is typically $2.0\ \mathrm{g\,cm^{-3}}$ within the Puget Sound basin and increases in the Olympic and Cascade mountain ranges. The terrain integration used the PSDEM2005 grid spacing within the East-North-Up integration coordinate system, which resulted in a small amount of interpolation as the model's projective coordinate system and the 3D integration coordinate system diverge with distance from the apparatus. The Coastal Relief model was interpolated onto a rectangular grid for integration. The Coastal Relief elevation data is relative to the 1996 Earth Gravity Model (EGM96) [76], but deviations from the reference ellipsoid were ignored as they are smaller than a few cm in the integration region.

Table 4.3: The domain of the different models used for terrain.

Model	Domain	Format	Horizontal Datum	Vertical Datum
CENPA Plans	< 180 m	2 ft contours, manually digitized	WSPN[a]	City of Seattle
PSDEM2005	< 23784 m	30 ft grid	WSPN[a]	NAVD88[b]
Coastal Relief	< 91 km	3 arcsec grid	WGS84[c e]	EGM96[d e]
Global sediment	Entire earth	1° grid	WGS84[c]	Sea Level

[a] Washington State Plane - North

[b] North America Vertical Datum of 1988

[c] World Geodetic System of 1984

[d] Earth Gravity Model of 1996

[e] The Coastal Relief Model is a composite model from different origins and may have additional uncertainty related to this.

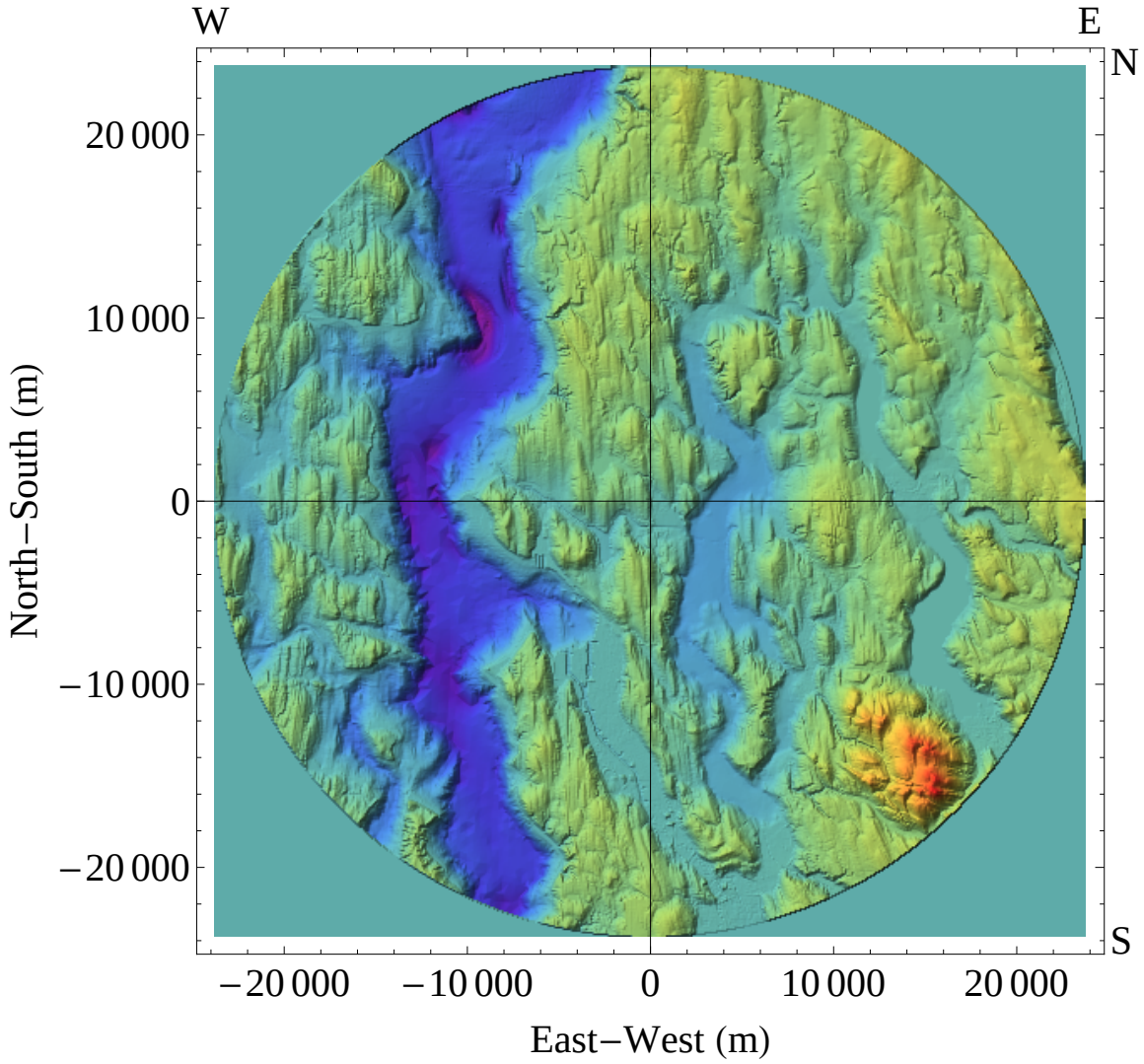

Figure 4.1: Terrain extracted from the PSDEM2005 model, centered on the pendulum's location.

The PSDEM2005 model [51] covers much of the Puget Sound region, but the eastern edge is 24 km from the apparatus's location. The closest edge of a model was used to limit its applicable region, since density differences between opposite directions result in the source acceleration. PSDEM2005 has a grid size of 30 feet (9.14 m) and a vertical resolution of 1 foot. However, it is a composite model with vertical accuracy of less than 2 feet for LIDAR data and as much as 50 feet for portions derived from USGS elevation maps. The

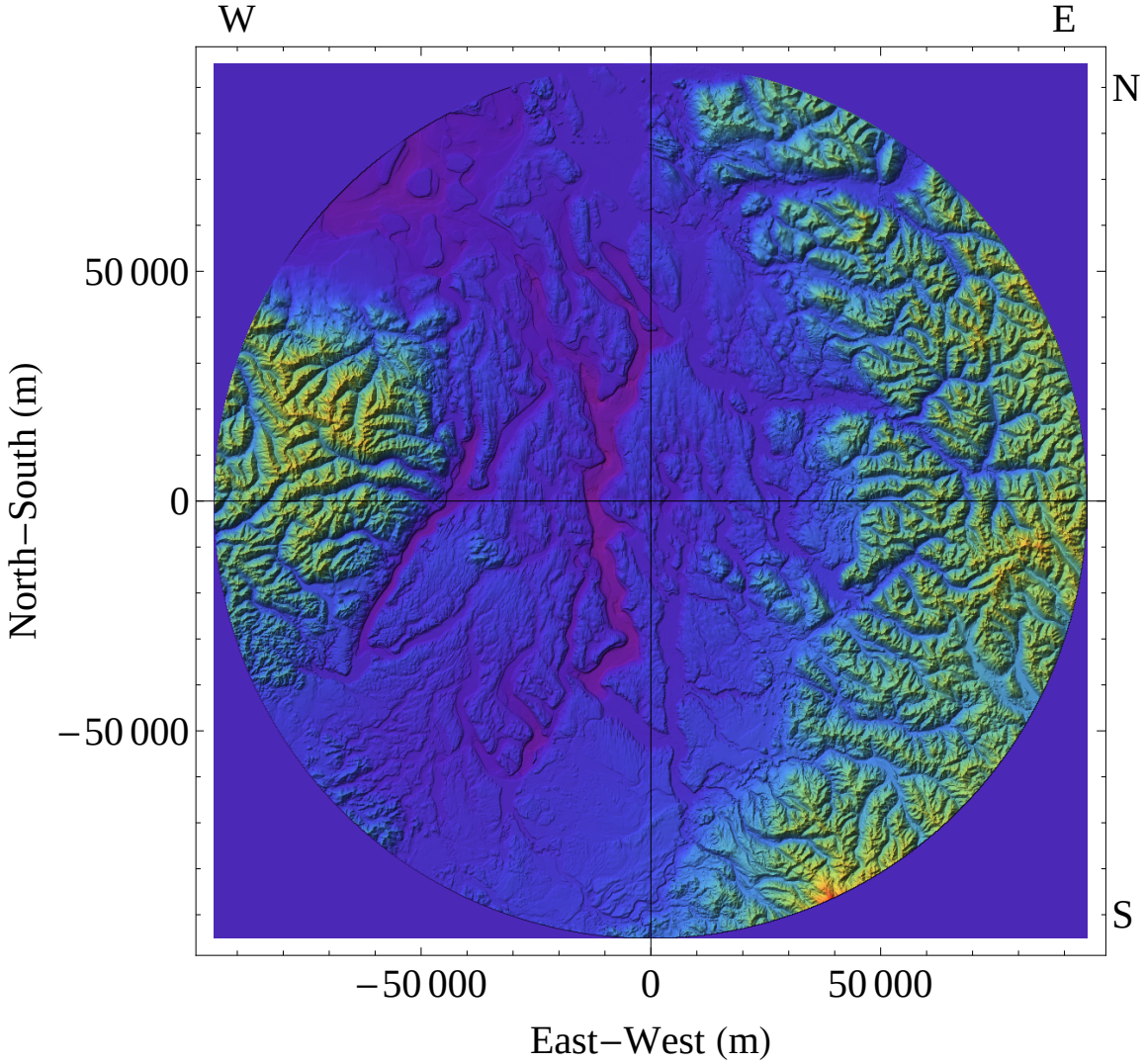

Figure 4.2: Terrain extracted from NOAA's Coastal Relief model, centered on the pendulum's location.

largest part of the terrain data used for the source integration came from LIDAR data. Terrain immediately surrounding Lake Sammamish and roughly the North-East quadrant located further than the far shore of Lake Washington were derived from USGS elevation maps. A comparison with Choi's terrain model [123, 28], interpolated from 25 foot (7.6 m) contour lines, shows a RMS variation of about 3 meters over a 1400 m by 1400 m square centered on the apparatus site (see figure 4.3).

The Coastal Relief model [94] covers the entire coastal region of the United States. The Coastal Relief model is on a 3 arcsecond grid, which corresponds to a resolution of ∼90 m. We used this terrain model to extend the terrain integration from 24 km to 91 km for consistency with the region covered by the USGS Cascadia density model.

The terrain source region includes two major bodies of water, Lake Washington and Puget Sound, for which constant surface elevations were assumed. Lake Washington and connected water was assigned an elevation 6.1 m above US Army Corps of Engineers Datum (COED), though the US Army Corps of Engineers maintained the lake level between 6.1 and 6.7 m above the COED with seasonal adjustments [26, 128]. A slope of ≈ 0.1 m from the ends of the lake to the locks into Puget Sound was also ignored as negligible. Tides were not incorporated into our model, and Mean Sea Level (MSL) was used for the Puget Sound water level. Tidal levels in Puget Sound range over 3.5 m at Tidal Station 94A near the Hiram M. Chittenden Locks (the Puget Sound tidal station closest to the apparatus). A pond over the laboratory was included in the model from Choi [28]. All other bodies of water were considered to have negligible contributions.

USGS Cascadia Subduction Zone Density Model

We used a USGS density model of the Cascadia subduction zone (USGS Cascadia density model) [120] to incorporate the local geology into the source model. The Puget Sound region has complex geology, with low density sediments, higher density bedrock, and several faults. The seismic wave velocity and the rock density fall along curves for different classes of rocks [20]. The USGS Cascadia density model used seismic wave travel times from 220 monitoring stations in the Pacific Northwest to construct a detailed, three-dimensional model of the

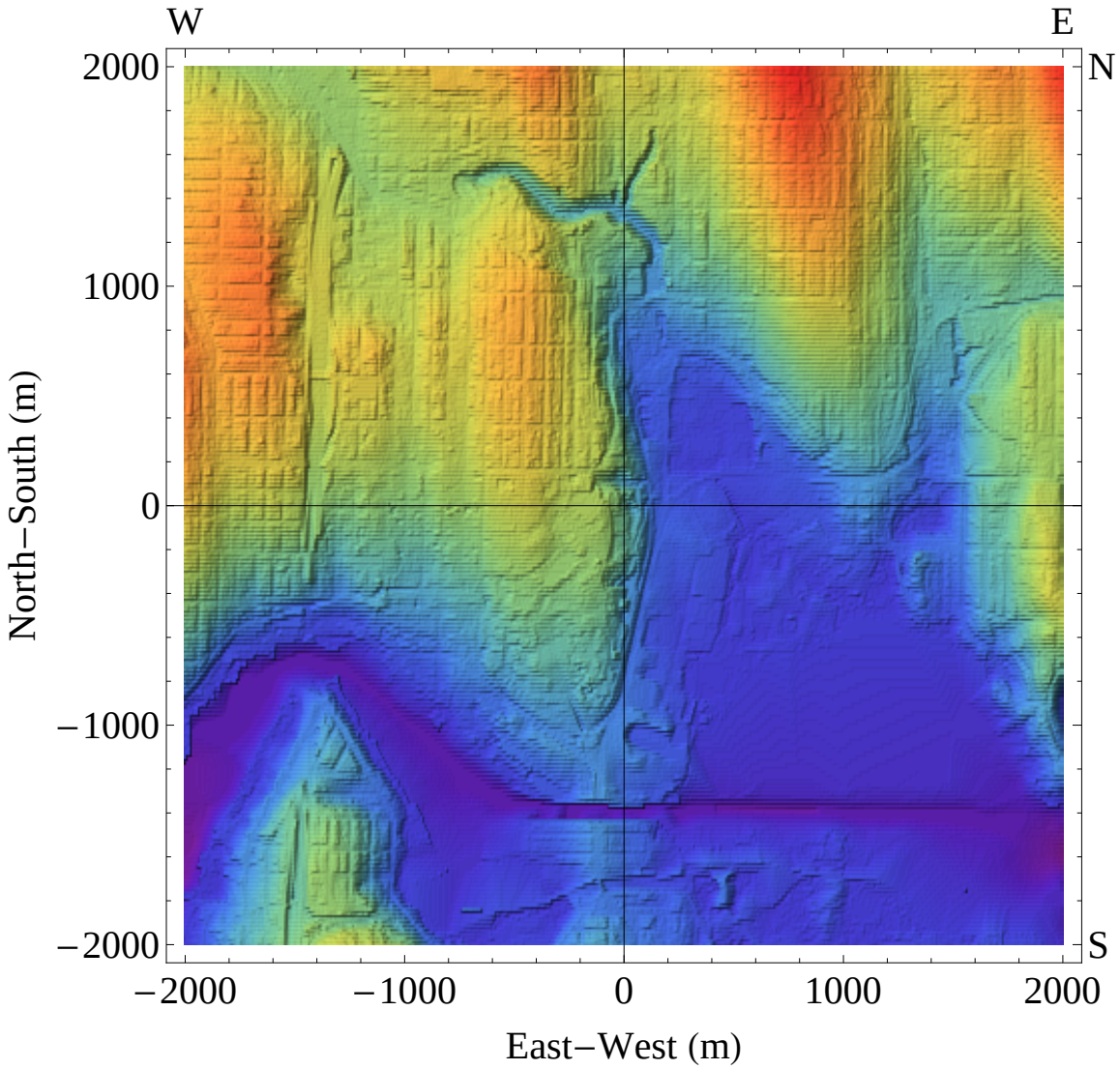

Figure 4.3: Detail of terrain extracted from the PSDEM2005 model, centered on the pendulum's location.

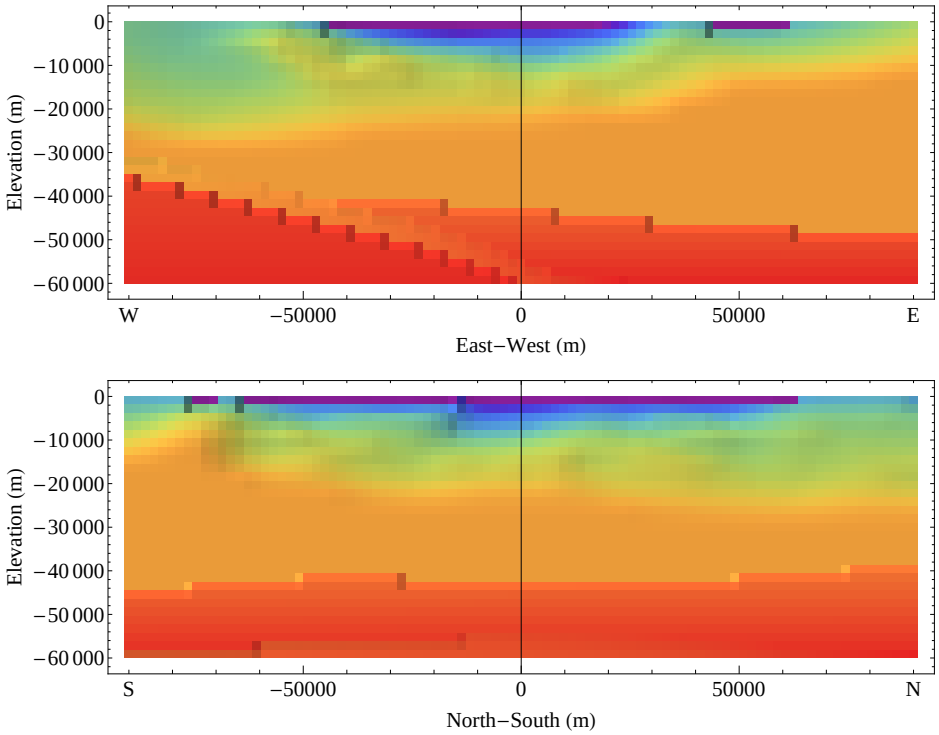

Figure 4.4: Cross sections of the local density model in the east-west and north-south directions from the apparatus's location. Positive directions indicate north and east from the apparatus. Density increases from 2.0 g cm^{-3} (purple) to 3.4 g cm^{-3} (red).

regional density. The density model has a grid size of 2000 m and extends 91 km from the apparatus, limited by the edge to the east which was nearest to the apparatus. The density ranges from $2.0 - 2.8$ g cm^{-3} at the surface and increased with depth to a maximum of 3.4 g cm^{-3}. The USGS Cascadia density model does not include the Puget Sound or other inland water, but it does include the Pacific Ocean. The source acceleration model included Puget Sound and Lake Washington through the terrain model. Figure 4.4 shows a low density sediment bowl near the surface and a slope down from west to east below 40 km (due to the subduction of the Juan de Fuca plate) in cross-sections of the USGS Cascadia density model.

Whole Earth Source Model

At ranges greater than 5000 km, a layered ellipsoid model of earth describes the relevant density variations well [123, 28]. To extend the utility of this model to shorter distances, the density variations of earth's crust and mantle must be taken into account. Four separate geophysical models of the earth were combined to include these density variations. The Preliminary Reference Earth Model (PREM) [45] is a radially layered spherical model of the earth that gives the density as polynomial functions of normalized radius. Following Su's work [123], this model was deformed onto the WGS84 reference ellipsoid. The PREM density functions provide the density for earth's core and the vertical density for the mantle. The STB00D model from Steinberger [118] provided variations of the PREM density in terms of latitude, longitude, and depth (specified as spherical harmonics for $\ell \leqslant 31$ with modified depths to important mantle boundary layers). Global models of earth's crust and sediments from the Reference Earth Model [74] replace the uniform PREM crust density. Many geophysical models include wave propagation speeds, but relatively few explicitly include density. The availability of high-order gravitational field data from satellite measurements will likely result in future models explicitly using gravitational data to independently constrain density, which will result in better models for equivalence principle experiments. However, the models reasonably describe earth's density variation, which should be sufficient to meet the current goal of expanding the source model to all relevant λ.

Table 4.4: Geophysical models contributing to the whole earth source integration.

Model	Type	Spacial Parametrization
Global Sediment [75]	3 layers of sediment	1° grid
CRUST 2.0 [15]	8 layers of crust	2° grid
STB00D [118]	45 layers of mantle	spherical harmonics $\ell \leqslant 31$
PREM [45]	8 radial polynomials	radial only

The WGS84 reference ellipsoid provides the coordinate basis for the whole earth source model. Geoid variations from the reference ellipsoid may reach 200 m, but these were not included in the source model because they are small compared to the distances of > 100 km relevant for the global source acceleration. Earth's radius $R_\oplus$ as a function of latitude ϑ defines the ellipsoid:

$$R_\oplus(\vartheta) = \frac{a}{\sqrt{1 - \epsilon^2 \cos^2(\vartheta)}}, \tag{4.9}$$

where $a = 6356752$ m is earth's semi-minor axis and $\epsilon^2 = 0.00669438$ is earth's eccentricity squared [63]. All elevations and depths for the integration were with respect to the surface of the WGS84 reference ellipsoid. The source integration of the crust, mantle and core were conducted independently. Each integration for the whole earth model was performed in spherical coordinates for functional simplicity. The final integration result was rotated to local horizontal coordinates based on the tangent to the reference ellipsoid at the apparatus's latitude. The applied rotation was 3.3 mrad at 47.5°N latitude for the grid center point.

The sediment model includes the ocean depth and three layers of sediment on a one-degree grid in latitude and longitude. It provides the elevation, thickness and density of each of the layers. The CRUST 2.0 model provides density, thickness, and propagation speeds of seismic waves on a two-degree grid for 8 layers, including ice cap thickness, ocean depth, two sediment layers, three crystalline crust layers and the uppermost mantle. The source model integration for the crust was performed over each $1^\circ \times 1^\circ$ grid region using the elevation or ocean depth from the sediment model and replacing the two sediment layers of the CRUST 2.0 model with the three sediment model layers to span the entire thickness of the crust from earth's surface into the uppermost mantle. The integration over the entire crust took about 6 CPU-hours for each value of λ.

The STB00D mantle model explicitly provides density based on the history of slab subduction into the mantle. It provides density variations in terms of spherical harmonics up to $\ell = 31$ relative to the PREM radial density value in 45 layers. The uppermost layer was excluded in favor of the CRUST 2.0 model upper mantle value, which had a higher resolution. Integration was performed over the spherical harmonics and PREM radial density function for each individual layer.

Earth's core was assumed to be a symmetric ellipsoid with radial density variation given by the PREM. Integration over the core, mantle and crust were performed with the same integration functions, but with different functions providing the density. The integration for earth's core was performed as a single numerical integration.

Complete Earth Model

We combined the individual model integrations into a complete earth source model covering the entire range from $\lambda = 1$ m to $\lambda \gg R_{\oplus}$. The overall magnitude and direction of the source model horizontal acceleration, along with the component model contributions, are shown in figure 4.5. The direction plot for the horizontal source acceleration has a complex dependance on terrain and crustal and mantle geology as local hills, Lake Washington, Puget Sound, the Cascade Mountains, the Pacific Ocean, the subducting Juan de Fuca plate, and variations in the mantle depth and density contribute to the integration. The source acceleration in the down direction, which we created for verification and for comparison with drop type experiments, increases steadily until the entire earth has been included. The complete combined model values are listed in appendix A.

The downward source acceleration should increase with increasing λ until the entire earth has been included, because there is a density asymmetry between the earth and the surrounding space. Figure 4.6 shows the downward acceleration increasing steadily, but with slight deviations from a straight line around 2 km and 50 km. The deviation for $\lambda \sim 2$ km is near the grid resolution of the USGS Cascadia density model. The deviation for $\lambda \sim 50$ km could be due to either the resolution of the global model or the density change between the crust and mantle. Higher resolution regional and global subsurface density models would help, but this model substantially improves upon previous models by addressing the difficult intermediate range between where local terrain and where global structure dominate the model.

The east-west direction of the model (shown in figure 4.7) has the most complex behavior. For $\lambda \sim R_{\oplus}$ hydrostatic equilibrium of the earth implies that the source acceleration should be zero; however, at shorter ranges clear asymmetries exist, such as between the Pacific

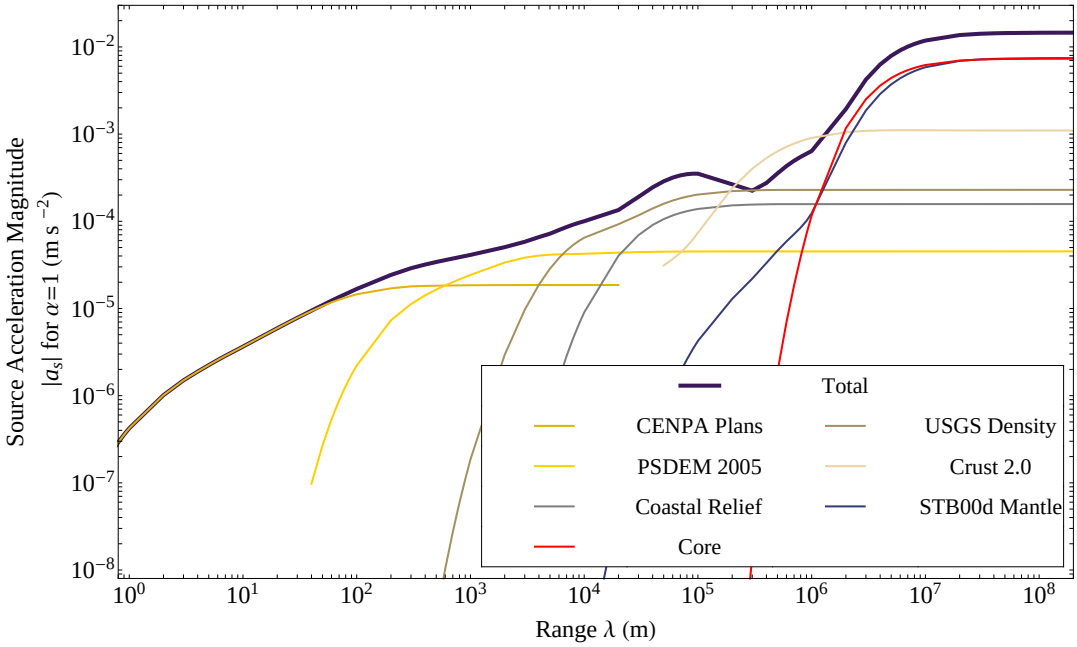

(a) Source model acceleration magnitude

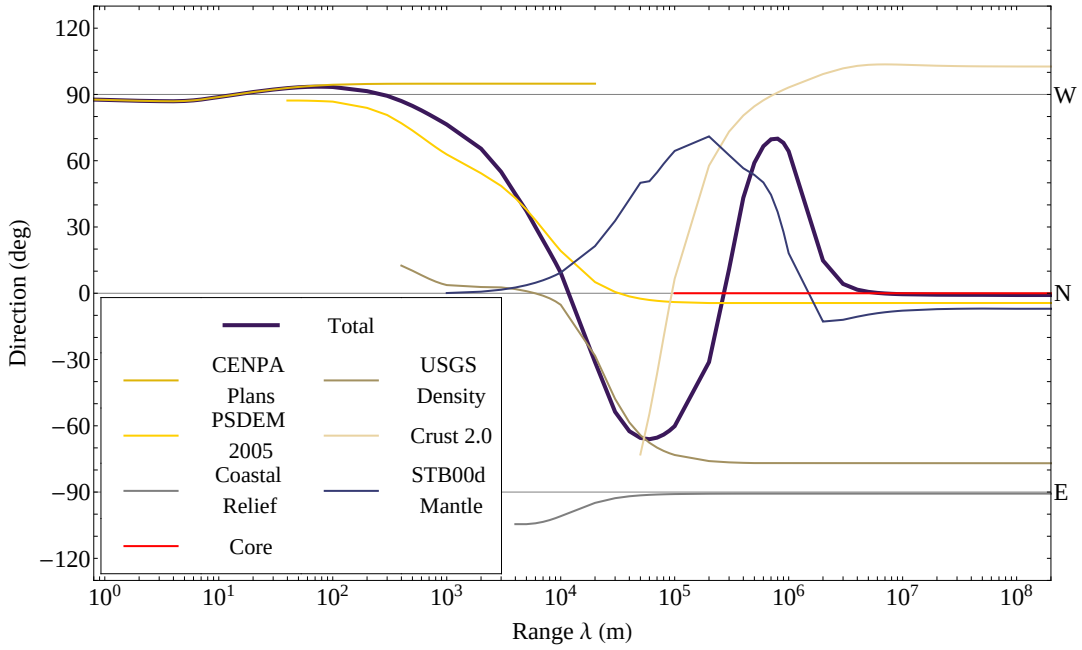

(b) Source model acceleration direction

Figure 4.5: Frame (a) shows the magnitude and frame (b) the direction of the total source acceleration and contributions from individual models.

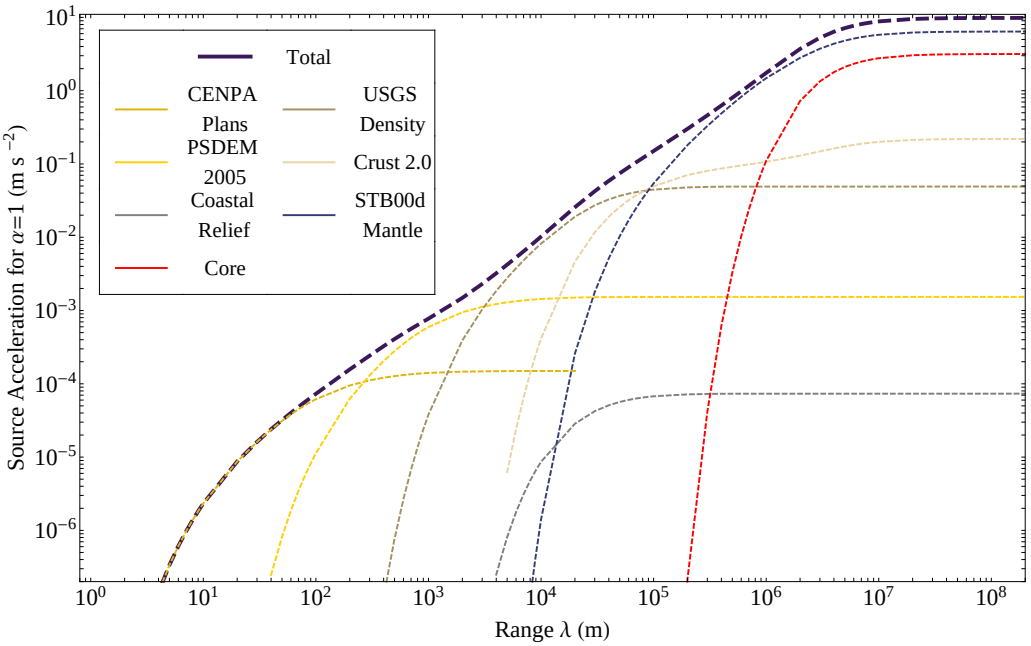

Figure 4.6: Source integration in the Down direction with contributions from individual models.

Ocean and North America or between Puget Sound and the Cascade mountain foothills. Hydrostatic equilibrium means that the large-scale crustal and mantle contributions should cancel and the long-range source acceleration should be similar to the source acceleration due to local terrain. Figure 4.7 shows multiple reversals of the source acceleration's direction: For $\lambda < 20$ km, the density asymmetry between a hill immediately to the west of the laboratory and the shoreline of Lake Washington to the east produces the westerly source acceleration observed. In the range 20 km $< \lambda <$ 200 km, the Puget Sound basin to the west (see figure 4.1), a subsurface low-density sediment bowl that extends more to the south and west of the apparatus's location (see figure 4.4), and the beginning of the Cascade Mountains to the east contribute to the easterly source acceleration. The next reversal has a source acceleration to the west again for 200 km $< \lambda <$ 6000 km, due to the density difference between the continental plate to the east and the thinner oceanic crust and mantle to the west. Oceanic crust is generally thinner and denser than continental crust and results in the underlying mantle being closer to the surface. Figure 4.9 shows the complete extent of

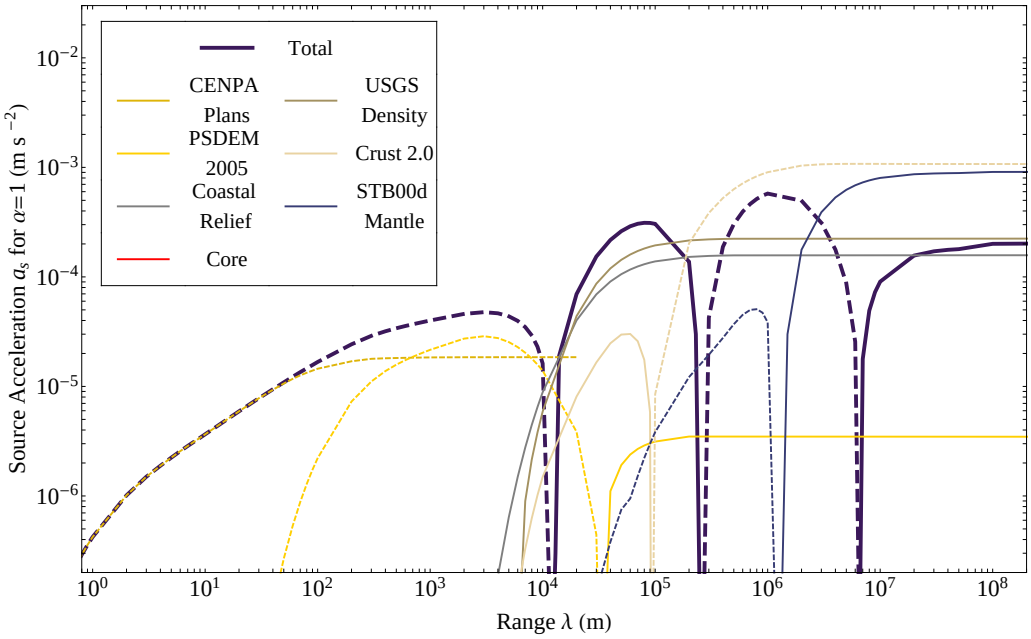

Figure 4.7: Source integration in the East-West direction with contributions from individual models. Solid lines indicate a source acceleration towards east and dashed lines indicate a source acceleration towards west.

the USGS Cascadia density model to illustrate the density difference between the oceanic crust to the west and the continental crust to the east. Note that the full extent of the USGS Cascadia density model corroborates the global sediment and CRUST 2.0 models that actually provide the density values used in this range. Finally, on the scale of the entire earth, the hydrostatic equilibrium requires the the underlying mantle cancels the large-scale crustal density asymmetry, leaving only the small-scale density asymmetry due to the rigid nature of the crust.

The north-south component of the source acceleration model, shown in figure 4.8, results in the strongest long-range limits on $\tilde{\alpha}$ due to the horizontal gravitational acceleration to the north that counteracts the centrifugal acceleration from earth's rotation. At the shortest ranges ($\lambda < 200$ m) the source acceleration reverses from north to south due to the hillside that the laboratory room is dug into and a substantial ravine about 20 m north of the laboratory building. Terrain features, predominantly hills to the north and a waterway to

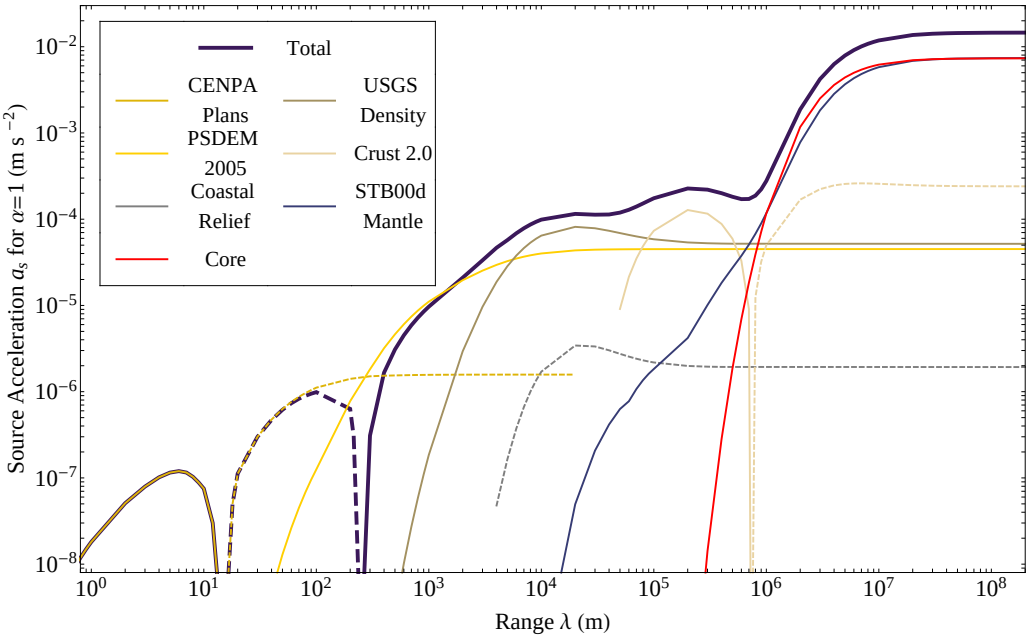

Figure 4.8: Source integration in the North-South direction with contributions from individual models. Solid lines indicate a source acceleration towards north and dashed lines indicate a source acceleration towards south.

the south dominate the source acceleration out to a few km, at which point the subsurface density contributes comparably with the terrain. The main local subsurface feature is the low-density sediment bowl that extends to the south and west of the laboratory site. Near $\lambda = 200$ km a bump in the magnitude of the north source acceleration occurs due to the detailed location of the Juan de Fuca plate, with some of the asymmetry visible in figure 4.9. The eastern edge of the Juan de Fuca plate extends roughly south-east from Vancouver Island, curving to mostly south following the Cascade mountains, and heading slightly back west towards the Pacific coast south of Seattle. For $\lambda > 200$ m the source acceleration gradually accumulates to the north, with a dramatic increase beyond $\sim 10^6$ m as the mantle and core are included due to earth's ellipticity.

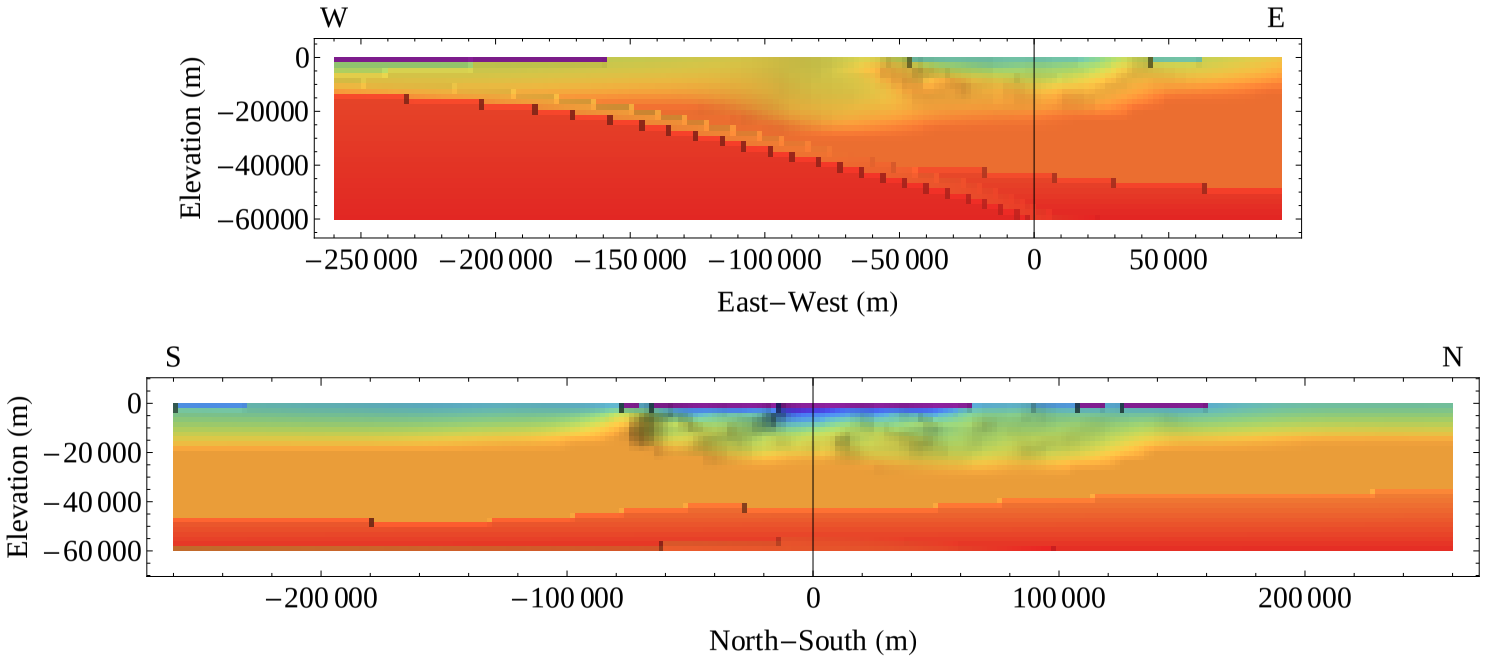

Figure 4.9: Cross sections in the east-west and north-south directions centered on the apparatus's location. Positive directions indicate north and east from the apparatus. Density increases from water at 1 g cm^{-3} (purple) to 3.4 g cm^{-3} (red).

4.1.4 Source model uncertainties

The dominant uncertainties in the source model come from the geophysical models for density, which can have localized density uncertainties of ∼25% in the mantle [88]. We estimated that uncertainties from composition, elevation models, coordinate system transforms, and numerical integration were typically less than a few percent. We verified our model by comparing certain regions where we can independently estimate the value and by comparison between different models covering the same region. At the shortest distances ($\lesssim$100 m), our computed gravity gradients were within 10% of the measured gravity gradients [28]. At the longest distances ($\sim R_\oplus$), our results follow the expectation that the earth is in hydrostatic equilibrium, and the horizontal gravitational acceleration toward north equals the centrifugal acceleration from earth's rotation. Due to a lack of good uncertainty estimates for the underlying models we used in the source acceleration, we did not use any model uncertainty to compute our limits on α. The inclusion of source acceleration uncertainties could change limits significantly ($> 10\%$) only in the difficult region 10 km $< \lambda <$ 1000 km.

Table 4.5: A comparison of results from different terrain models for $\lambda \to \infty$.

Model	Comparison Range	East-West ($\mathrm{m\,s^{-2}}$)	North-South ($\mathrm{m\,s^{-2}}$)
Choi [28]	0 - 180 m	-1.44×10^{-5}	-1.85×10^{-6}
PSDEM2005 [51]	0 - 180 m	-1.33×10^{-5}	-9.14×10^{-7}
PSDEM2005 [51]	6 - 24 km	4.05×10^{-5}	1.80×10^{-5}
Coastal Relief [94]	6 - 24 km	3.96×10^{-5}	1.75×10^{-5}
Su Bedrock [123]	0 - 20 km	7.90×10^{-6}	3.16×10^{-5}
USGS Density [120]	0 - 20 km	9.46×10^{-6}	1.04×10^{-5}

The composition and elevation model uncertainties were negligible compared to the density model uncertainties. Composition charge differences arise primarily between rock and water, with the little composition variation between different types of rock (e.g., comparing

the crust and mantle compositions gives a charge difference ∼0.1%). The digital elevation models accurately depict terrain and water depth with more detail than could be accommodated by the numerical integration at all $\lambda > 600$ m. In the local region, overlap of different terrain models occurred, so we compared the different models as summarized in table 4.5. Choi and PSDEM2005 agreed to about 10% on the overall magnitude, but have a direction difference of about 30°. The direction difference arises at the shortest ranges ($\lambda \lesssim 10$ m), where the PSDEM2005 model lacks resolution. Choi also computed the Q_{21} gravity gradient from the model and found agreement within 10% of the measured value [28]. The PSDEM2005 and Coastal Relief terrain models agreed within 2%, while each model was derived from different measurements with the exception of some Puget Sound bathymetry.

The subsurface density models used sound speed as a proxy for the density with constraints by geological considerations and gravitational measurements. Mooney and Kaban [88] estimate 0.05 g cm^{-3} ($\sim 1\%$) as the density uncertainty for our global crust model, 25% uncertainty in mantle density anomalies for poorly studied regions, and about onhalf that for well studied regions. Our source acceleration from the mantle, crust, and USGS Cascadia density models cancel in the east-west direction for $\lambda >> R_{\oplus}$ to better than 10%, leaving a long-range east-west component approximately equal to that of the local terrain (i.e., "crustal density variations within sedimentary basins and the crystalline crust are compensated in the uppermost mantle." [88]). The density of the USGS Cascadia density model has a typical standard deviation $< 3.5\%$ for each layer. A maximum standard deviation of 12% occurred for the surface layer, due to an asymmetric bimodal distribution, where about half the grid locations had a constrained density of 2.0 g cm^{-3} and half had a typical (approximately Gaussian) distribution of densities with a mean of 2.5 g cm^{-3}.

Comparison of different models over the same range permits some estimate of the uncertainty. We had only one density model for the local region, but we compared it to the previously used bedrock map. These two models include slightly different information: the bedrock map provides the depth of the sediment layer with a 418 m horizontal grid spacing and $\sim$ 25 m vertical resolution (better resolution for shallower bedrock), while the density model provides density on a 2 km grid in both vertical and horizontal directions. The

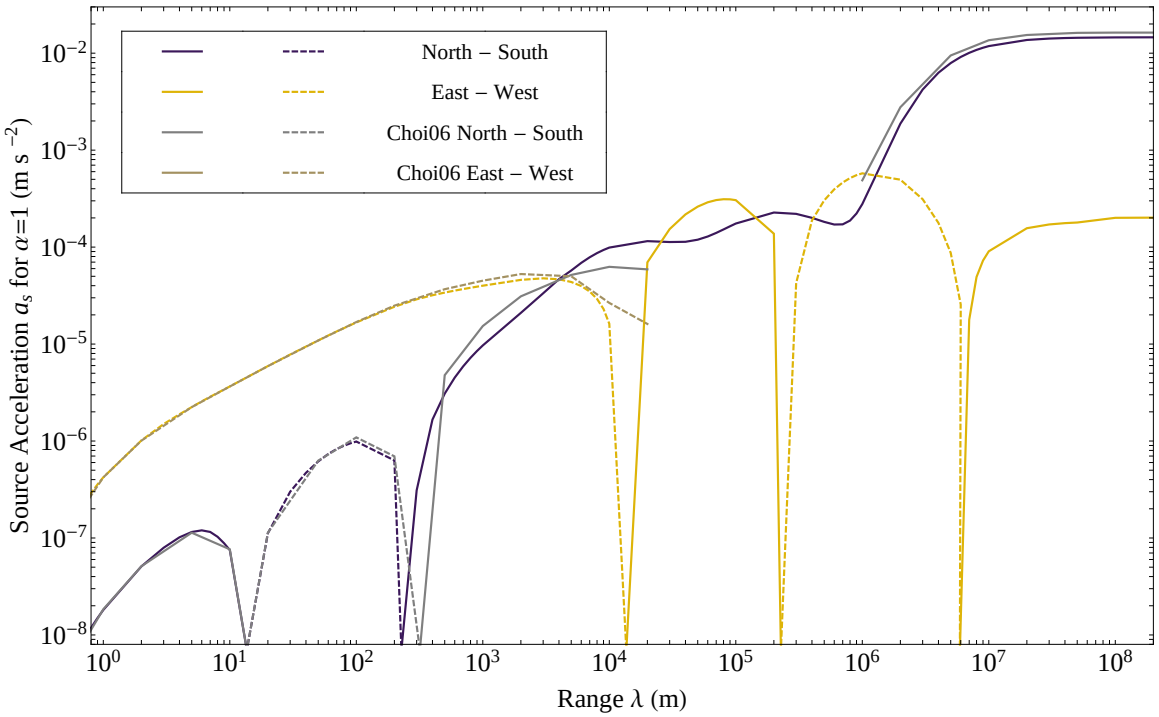

Figure 4.10: Comparison of our horizontal source acceleration model with that of Choi [28]. Solid lines indicate a source acceleration towards north or east and dashed lines indicate a source acceleration towards south or west. Ranges at which direction changed between east and west or north and south were interpolated.

bedrock provides a factor of 3 larger signal to the north partially due to the grid differences. We compare our composite model with the previous model by Choi [28] in figure 4.10. The two models use entirely different data sources for distances greater than 180 m.

4.2 Astronomical Sources

Astronomical sources complement earth-fixed sources with different compositions and modulation periods. An equivalence-principle-violating signal due to an astronomical source is modulated by the relative motion of the laboratory and the astronomical body with daily (either sidereal or solar) and yearly periods. While many systematic effects have a period of a solar day, the combination of a rotating turntable and daily modulation reduces most systematic effects compared to earth-fixed sources. We analyzed our data toward three

astronomical sources: The sun's hydrogen composition differs substantially from earth's composition, which we use to eliminate the source composition insensitivity that arises from using a single source (see equation 2.10). The galaxy's substantial dark-matter fraction (∼25% of its mass) allows us to investigate non-gravitational interactions between dark matter and ordinary matter. The cosmic microwave background is the most plausible preferred frame in the universe, so any preferred-frame effects should be examined with respect to it.

4.2.1 The Sun

Our rotating torsion balance has a greater intrinsic sensitivity to lab-fixed equivalence-principle-violating signals because the horizontal acceleration due to earth's gravity is 1.68 cm s^{-2} at the apparatus's latitude, whereas the gravitational acceleration due to the sun is 0.6 cm s^{-2}. However, the sun consists primarily of hydrogen, which gives it a charge $\left(\frac{L}{\mu}\right)_H \approx 1$, roughly two times greater than common earth-based sources. The signal modulation due to the rotation of the earth and its orbit around the sun leads to reduced systematic effects compared to a laboratory-fixed signal. The combination of charge and reduced systematic effects make the sun and earth nearly equivalent sources for $\tilde{q} = L$. Additionally, since the long-range earth signal is toward north and the modulated sun signal is predominantly east-west, the correlation between these measurements is small, allowing a combined result.

A specific question we addressed with our torsion balance test with earth- and moon-like materials is "Does a composition dependent violation of the equivalence principle exist at a level that would be detected by lunar laser ranging?" Due to the compositional similarity of earth's mantle and the moon, we used test bodies that enhanced the composition difference between the earth and moon to achieve greater sensitivity to any composition dependent equivalence-principle violation. Moon-mantle test bodies were designed to mimic the composition of the moon (or earth's mantle). Earth-core test bodies were designed to mimic the composition of earth's core. The compositions of the earth, moon, and test bodies (see section 5.1.1) are summarized in table 4.6.

Table 4.6: Charges for the sun, earth, moon and earth-core-like and moon-mantle-like test bodies. The sun's composition comes from Asplund *et al.* [11]. The moon's composition comes from Longhi [78]. Earth's composition is described in section 4.1.2 and the test body composition is described in section 5.1.3.

Body	Z/μ	N/μ	B/μ
Sun	0.8516	0.1427	0.9943
Earth Core	0.4690	0.5321	1.0012
Earth Mantle	0.4954	0.5052	1.0006
Moon	0.4956	0.5050	1.0006
Earth Core Test Body	0.4661	0.5351	1.0012
Moon-Mantle Test Body	0.4984	0.5022	1.0006

The moon-mantle and earth-core test bodies enhanced the composition difference between the earth and moon. The composition of the earth and moon equal the composition of the test bodies weighted by the fraction of the total mass. Defining the non-iron or mantle fraction as $f = (mantle\ mass)/(total\ mass)$, then the iron or core fraction is $(1 - f)$. Since the moon has a a small iron content the moon's iron mass fraction is $f_{\leftmoon} = 0.059$, while earth's iron mass fraction is $f_{\oplus} = 0.387$. The composition of our test bodies yields a factor 4 enhancement of any composition dependent equivalence-principle violation measured by our torsion balance compared to that experienced by the earth and moon falling towards the sun.

$$\begin{aligned} \tilde{q}_{\leftmoon} &= \tilde{q}_{\mathrm{MM}} f_{\leftmoon} + (1 - f_{\leftmoon})\tilde{q}_{\mathrm{C}} \\ \tilde{q}_{\oplus} &= \tilde{q}_{MM} f_{\oplus} + (1 - f_{\oplus})\tilde{q}_{\mathrm{C}} \\ \frac{\Delta\tilde{q}_{\mathrm{lab}}}{\Delta\tilde{q}_{\mathrm{LLR}}} &= \frac{\tilde{q}_{\mathrm{MM}} - \tilde{q}_{\mathrm{C}}}{\tilde{q}_{\leftmoon} - \tilde{q}_{\oplus}} = \frac{1}{f_{\oplus} - f_{\leftmoon}} = 3.76 \end{aligned} \tag{4.10}$$

The charge $\tilde{q}_{MM}$ corresponds to the moon-mantle test bodies and $\tilde{q}_C$ to the earth-core test bodies.

4.2.2 Center of the Galaxy and Dark Matter

Observations of the Cosmic Microwave Background and the rotation curves of galaxies indicate that there is a large amount of dark matter that interacts gravitationally with ordinary matter. The Milky Way galaxy provides a source of dark matter for us, since about 25% of the mass enclosed by our sun's orbit of the Milky Way is likely due to dark matter [121]. A search for an equivalence-principle violation in the direction of the center of the galaxy provides a model independent test for non-gravitational interactions between ordinary neutral matter and dark matter. We note that non-gravitational interactions between ordinary matter and dark matter would also likely produce second-order forces between ordinary matter [23]. Due to the much greater precision of the equivalence principle results between ordinary matter, the limit on second-order forces results in a more stringent limit than that of the test towards the galactic center for some dark matter models, such as weakly-interacting massive particles (WIMPS). Nevertheless, the model-independence of this test provides strong grounds for including the galaxy's dark matter as a source.

The acceleration of a test body towards the center of the Milky Way is made up of the acceleration due to ordinary matter a_{OM} and the acceleration due to dark matter a_{DM}. If the dark matter acceleration has a non-gravitational component as shown in figure 4.11, then $\Delta a \approx \Delta a_{\mathrm{DM}}$ since there are strong limits on the differential acceleration due to ordinary matter. The total acceleration of our solar system towards the center of the galaxy $a = v^2/R = 1.9 \times 10^{-10}$ m s^{-2}, where $v = (219 \pm 20)$ km s^{-1} is the velocity of our solar system about the center and $R = (8.0 \pm 0.5)$ kpc $= (2.5 \pm 0.2) \times 10^{17}$ km [106]. Stubbs gives a range with the lowest value $a_{\mathrm{DM}} = 4.8 \times 10^{-11}$ m s^{-2} [121]. This results in the ratio of mass of dark matter to regular matter enclosed by our solar system's orbit of $\sim$25%. The galactic center is located at a right ascension of 17.761 hours and declination of -29.008° (J2000) [12].

4.2.3 Cosmic Microwave Background Frame

Lorentz invariance and the equivalence principle are closely related in general relativity. Violations of one often lead to a violation of the other as discussed in section 2.4.3. The

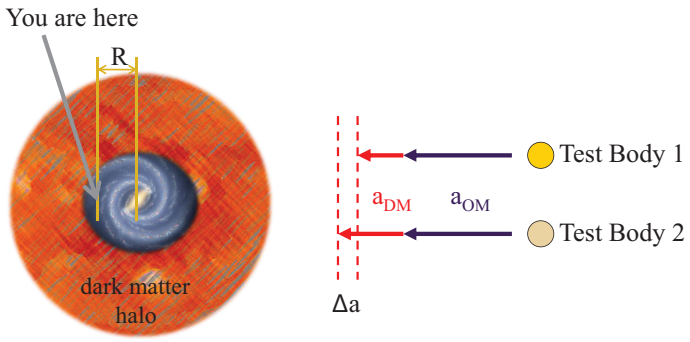

Figure 4.11: Our solar system falls towards the center of the galaxy due to both ordinary and dark matter. A non-gravitational force between dark matter and our test bodies would result in a differential acceleration Δa.

cosmic microwave background (CMB) is a plausible preferred frame for the universe, so any violations of the equivalence principle related to a preferred frame could have a relationship with this direction. We fit for an equivalence-principle-violation oriented with the CMB frame. The CMB dipole is located at a right ascension of 11.20 hours and declination of -6.93° (J2000) [65].

Chapter 5

APPARATUS

Our torsion balance hung inside a vacuum chamber suspended from an air-bearing turntable. The turntable enabled the smooth rotation of the apparatus, which places any equivalence-principle-violating signal at the turntable's rotation frequency. Figure 5.1 shows a schematic cross-section of the apparatus. Many different sensors measured temperature, tilt, pressure, and positions. A laser-beam reflected from one of four pendulum mirrors onto a position sensitive photo-detector is used to measure the angular deflection about the fiber axis or pendulum twist. A thin fiber suspended the pendulum and provided a weak restoring force for the twist. A fiber positioning stage attached at the top of the fiber and controlled the vertical and horizontal position and the rotation of the pendulum within the apparatus. Magnetic and thermal shields surrounded the pendulum to isolate it from ambient changes. Large masses placed about the pendulum's position reduced laboratory gravity gradients by at least two orders of magnitude. The apparatus sat less than 1 m from an external laboratory wall buried into a hillside, which was the dominant short-range source in our search for new forces weaker than gravity.

The apparatus rested on a concrete platform constructed between the wall of the laboratory and the magnet of a decommissioned cyclotron. An insulating enclosure entirely contained the apparatus. The laboratory room is circular and the apparatus's enclosure extended from the laboratory wall towards the center of the room in a trapezoidal shape with width of about 2 meters. The entire structure extended from the floor up past the supporting platform for a total height of about 7 m. The concrete platform divided the enclosure into an upper portion, where the air-bearing and stationary wiring were accessed, and a lower portion, where the vacuum chamber and gravity gradient compensators were located.

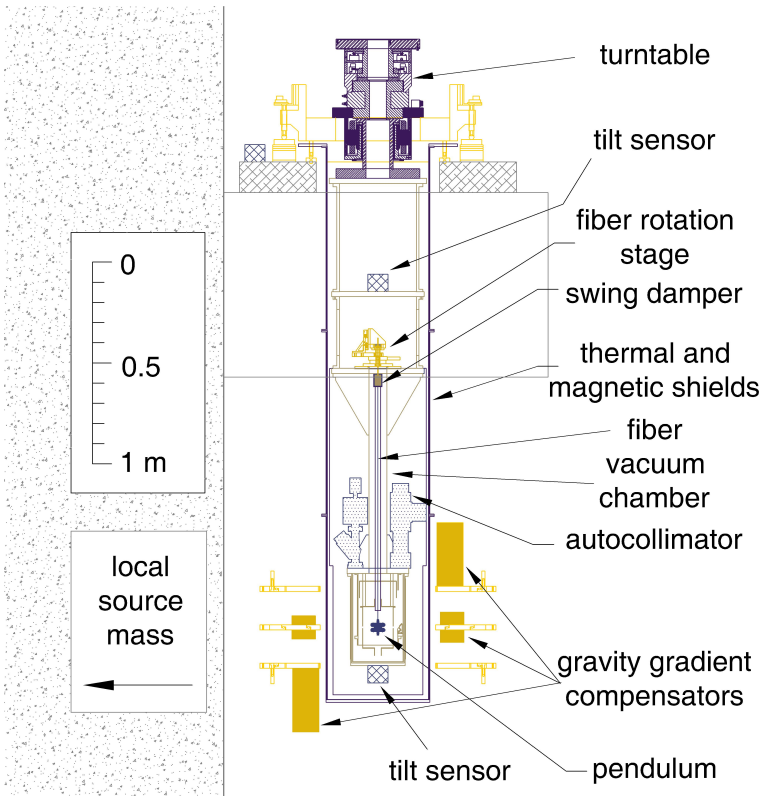

Figure 5.1: Schematic diagram of the apparatus. A torsion pendulum enclosed in a vacuum chamber hung from an air-bearing turntable. Environmental sensors helped discriminate systematic effects from an equivalence-principle-violation. Passive thermal and magnetic shielding enclosed the vacuum chamber, and gravity gradient compensators reduced the Q_{21}, Q_{22}, and Q_{31} gravity gradients.

5.1 Pendulums

We used three separate pendulums for our equivalence principle experiments. Two of the pendulums were configured with a composition dipole and one with large gravity gradient moments. The composition dipole pendulums —the eight test-body pendulum and the earth-moon pendulum— were designed for two separate goals. The eight-test-body pendulum achieved good sensitivity for any unknown charge (see section 2.2.1) using the earth as a source. In contrast, the earth-moon pendulum addressed the ambiguity of whether an equivalence-principle violation in the lunar laser ranging tests of the strong equivalence principle would be due to composition or gravitational binding energy differences. Each of the three pendulums weighed 70 g, or a little more than half the expected fiber breaking strength. Each pendulum had four mirrors for the angular position readout and was coated with an optically thick layer ($\gtrsim$ 200 nm) of gold to eliminate work function differences in electrostatic interactions with the apparatus. The surrounding shield and support structure were similarly gold coated. Table 5.1 compares the physical properties of the pendulums. A copper fiber screw threaded into the upper post of the pendulums and crimped to the fiber to provide a uniform mounting method and to allow us to easily exchange pendulums. A design tradeoff between differential acceleration sensitivity and gravity gradient moments occurs through their shared dependence on the pendulum's lever arm. The eight-test-body pendulum had a smaller lever arm for reduced gravity gradient sensitivity, while the earth-moon pendulum had a larger lever arm at the expense of greater gravity gradient sensitivity. The daily modulation of any signal towards the sun ameliorated the earth-moon pendulum's greater gravity gradient sensitivity. The eight-test-body pendulum achieved its best sensitivity using earth as a source in the laboratory frame, where gravity gradient systematic effects were substantial.

An autocollimating angular position readout determined the pendulum's angular position by reflecting a laser beam off one pendulum mirror onto a position sensitive photodetector. Four mirrors on each pendulum allowed the four different orientations of the pendulum with respect to the apparatus shown in figure 5.2. Using opposite orientations allowed systematic effects that are fixed to the apparatus to be separated from effects that

Table 5.1: Physical properties of the pendulums in different operating configurations. The flat mirror configuration included fixed optics that reflected the laser off the pendulum twice, doubling the optical readout angle sensitivity compared to the corner mirror configuration, which used a single reflection.

Pendulum Configuration		Mass (g)	Moment of Inertia (g cm^2)	Mirror
8-test-body	Be-Ti	69.8	378.9	Flat
8-test-body	Be-Al	70.1	378.0	Flat
Earth-moon		71.3	570.99	Corner
Gradiometer	q_{21}	69.1	493.8	Flat
Gradiometer	q_{31}	69.1	493.8	Flat
Gradiometer	q_{41}	69.1	437.2	Flat

followed the pendulum orientation. This separation improved our ability to identify and understand systematic effects and to minimize their effect upon our results. The composition dipole orientation $\phi_{\rm d}$ in the laboratory frame is given by

$$\phi_{\rm d} = \phi_{\rm TT} \pm \phi_{\rm f}, \tag{5.1}$$

where the turntable angle $\phi_{\rm TT}$ increases west from north and the pendulum frame (or mirror) angle $\phi_{\rm f}$ increases in a clockwise direction as viewed from the top. The composition dipole was defined as positive when the beryllium or earth-core test bodies were oriented about the 0° mirror on the pendulum frame and as negative when they were oriented about the 180° mirror. The eight-test-body pendulum and gradiometer pendulum had flat mirrors that were used with a fixed mirror assembly to achieve two reflections of the laser beam off the pendulum mirror. The earth-moon pendulum had a corner mirror and used a single reflection for the angular position measurement. The optical path is further described in section 5.4.

The composition dipole pendulums' designs specifically addressed coupling of the leading gravity gradient moments to the local environment by maintaining a high degree of symmetry. The $\ell \geqslant 2,\ m = 1$ moments directly produce a systematic signal at the mea-

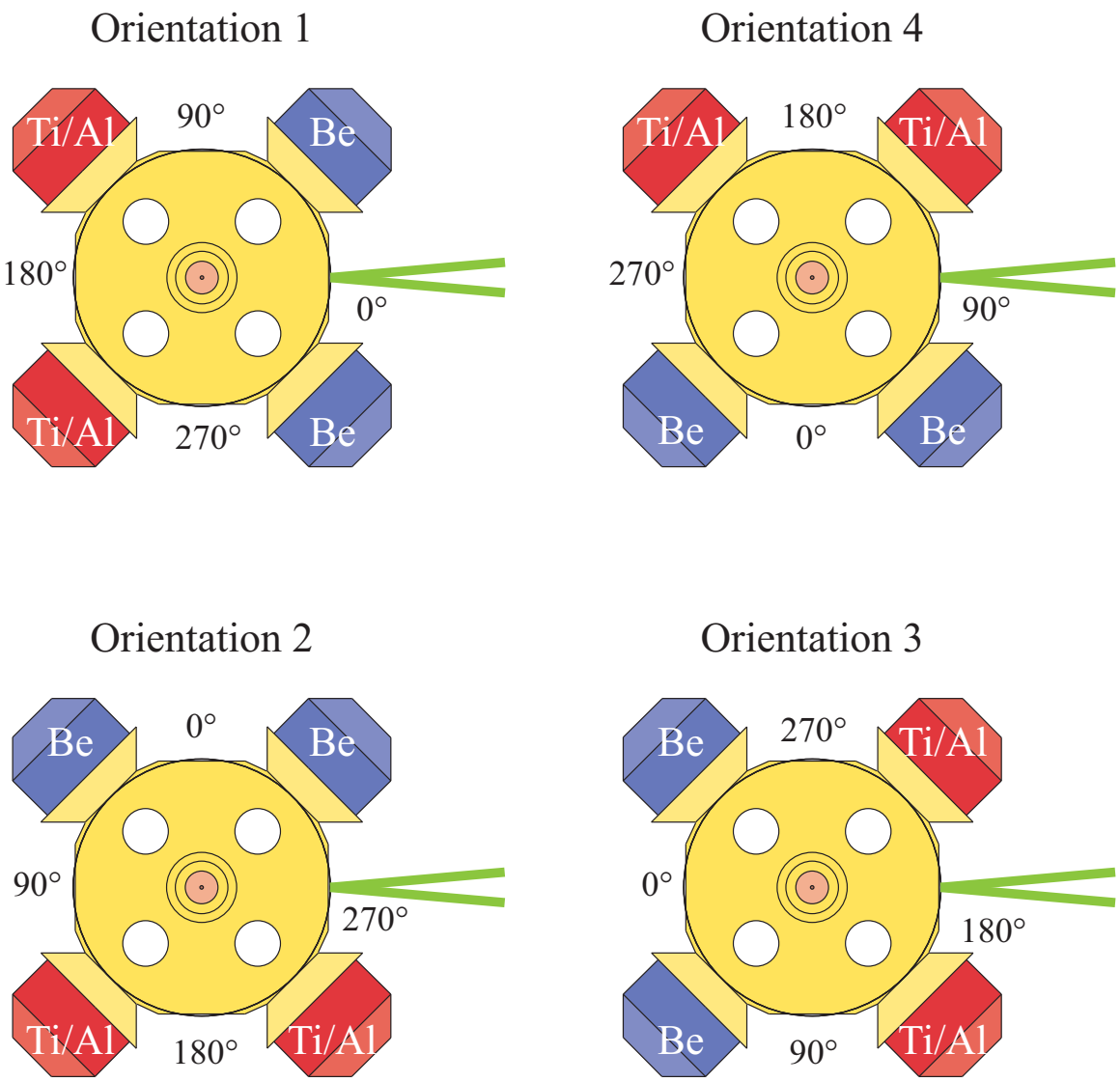

Figure 5.2: Four possible orientations of the pendulum with respect to the apparatus. The test bodies may also be exchanged with respect to the pendulum frame to separate systematic effects that follow the pendulum frame from an equivalence-principle violation that tracks the test bodies. All orientations shown have the composition dipole aligned with the 0° mirror. Ti / Al means either titanium or aluminum test bodies were installed on the pendulum.

surement frequency. The $\ell \leqslant 1$ moments cannot produce a twist of the pendulum due to the properties of a torsion balance (see section 3.2). Moments for $\ell < 6$ and all m, except for the q_{44} and some $m = 0$ moments on the earth-moon pendulum, were also minimized because small tilts of the pendulum rotate these moments into the $m = 1$ moments [124]. In practice, small tilts arise due to imperfections in the suspension or construction tolerances. The q_{44} moment was unconstrained due to the choice of four-fold axial symmetry as a primary pendulum symmetry. We adjusted the q_{21} moment with tuning screws in the upper and lower posts.

Table 5.4 shows the computed moments for the eight-test-body configurations along with those of the earth-moon pendulum. While the table lists values for the $\ell = 1,\ m = 1$ moment, this moment can not be realized when the pendulum is suspended. The formalism from D'Urso and Adelberger [44] for translating moments can be used to estimate the combined tilt and translation of the pendulum that results in the elimination of this moment. As an example, rotating the beryllium-aluminum configuration so that the q_{11} moment is entirely in the q_{10} gives a tilt of $\sim 0.5^\circ$. This would result in a q_{21} $\approx$0.04 g cm^2, compared to the measured value of ≈ 0.06 g cm^2 prior to adjusting the tuning screws. For this measurement the tuning screws were only roughly in their neutral positions and could have contributed the difference from this simple estimate. The large q_{51} values for the eight-test-body configurations come from a limitation in the model software where the mirror cutout could not be accurately modeled. The actual geometry differs slightly from the model geometry.

The composition dipole pendulums had two radial perpendicular holes on both the upper and lower posts. Set screws, called tuning screws, within these holes were used to reduce the q_{21} moment of the pendulums. The design of these pendulums specifically attempted to minimize the $m = 1$ gravitational moments of the pendulums, which may produce signals at the turntable rotation frequency; however, imperfections such as machining tolerances, suspension tilts, and variations in the density of materials may introduce small gravitational moments. The set screws in the eight-test-body pendulum seated against each other to prevent them from moving. A solid central post in the earth-moon pendulum prevented the set screws from being seated against each other, and some small changes to the gravitational

moments of this pendulum were observed as shown in section 7.1. The tuning screws were adjusted every time a composition dipole pendulum was installed in the apparatus.

5.1.1 Composition Dipole Selection

Any complete test of the equivalence principle must use two different test body pairs falling toward two different sources. Each material or material combination has a charge given by equation 2.10 to which it is completely insensitive. For any particular theory, there will likely be a choice of materials that maximize the predicted charge difference. However, a general test should use two pairs of materials that differ substantially in $\Delta\left(Z/\mu\right)$ and $\Delta\left(N/\mu\right)$. Table 5.2 lists charges for some materials used in current or proposed equivalence principle experiments.

Table 5.2: Charges for selected materials used in existing or proposed experiments. Z/μ, N/μ, and B/μ are the vector charges described by equation 2.10. $Q_{\hat{m}}$, Q_e, $Q_{\delta m}$, Q_{m_e} are the dilaton charge parameters given in equation 2.13.

Material	Z/μ	N/μ	B/μ	$Q_{\hat{m}}$	Q_e	$Q_{\delta m}$	Q_{m_e}
$(CH_2)_n$	0.5703	0.4285	0.99888	0.0714	0.00105	-0.000237	0.000313
Be	0.4438	0.5548	0.99865	0.0753	0.00072	0.000191	0.000244
Al	0.4818	0.5188	1.00068	0.0808	0.00174	0.000062	0.000265
Ti	0.4596	0.5415	1.00107	0.0827	0.00229	0.000137	0.000253
Cu	0.4564	0.5447	1.00111	0.0835	0.00270	0.000148	0.000251
Au	0.4011	0.5991	1.00017	0.0853	0.00433	0.000336	0.000221
Pt	0.3998	0.6003	1.00015	0.0853	0.00428	0.000341	0.000220

The pendulum materials must also meet other experimental requirements. For a torsion pendulum, the test bodies must be accurately positioned and not allow motion during measurements. Movement of a test body changes the coupling to gravity gradient fields, one of the leading systematic effects. We constructed the pendulums from non-magnetic materials, such as aluminum, titanium, beryllium, quartz, stainless steel and gold. Ther-

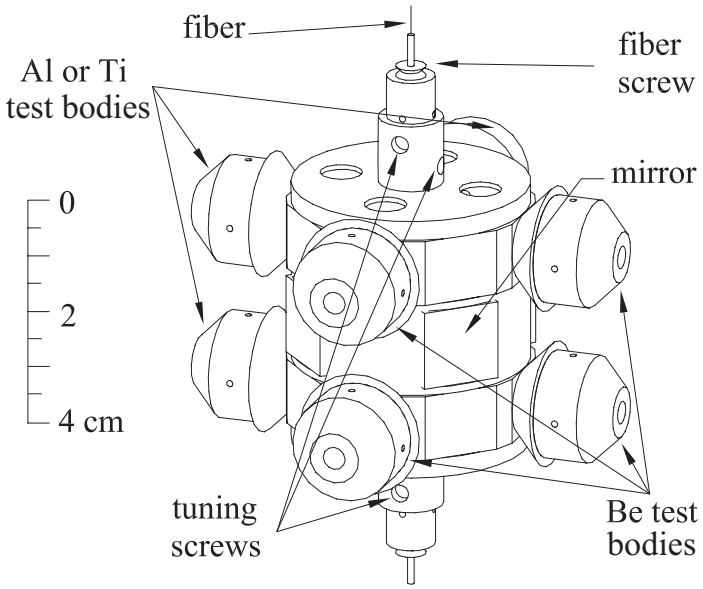

Figure 5.3: Schematic drawing of the eight test-body pendulum. Four test bodies were beryllium and four were either aluminum or titanium. Screws held the test bodies in cylindrical cups and allowed them to be exchanged with respect to the pendulum frame to remove systematic effects. Four mirrors allowed the pendulum to be positioned in four different orientations with respect to the apparatus. The tuning screws in the upper and lower support allowed small changes to the q_{21} moment.

mal stability prevents the test bodies them from deforming or creeping when the vacuum chamber is heated during pump-down, which was necessary to reach lower pressures and minimize drifts in the fiber. The materials should not out-gas under vacuum and should be conductive. Conductivity prevents electrostatic interactions with the apparatus from overwhelming the weak signal of an equivalence-principle violation. Outgassing would increase the noise or induce a systematic effect, particularly if it were different for the different materials.

5.1.2 Eight Test-Body Pendulum

Figure 5.3 shows the primary features of the eight test-body pendulum. The pendulum frame held eight test bodies (four each of two different compositions) with four-fold azimuthal symmetry and top-bottom reflection symmetry. Eight test bodies gave the pendu-

lum more closely matched symmetry between the torsion axis and the other primary axes. The test body mounting system resulted in a larger lever arm for the test body mass and allowed easy exchange of test bodies, while minimizing the largest diameter of the pendulum frame. Four flat mirrors allowed for measurement of the angular position. The fiber crimped to a fiber screw that inserts into the upper post. Both the upper and lower post had two orthogonal through-holes for reducing or "tuning" the q_{21} moment of the pendulum.

Beryllium and either titanium or aluminum were used for the composition dipole. Each test body had a cylindrical center section with truncated cones tapering away at each end. One truncated cone fit securely into a matching cup on the pendulum frame. A titanium screw through the axis of each test body attached it to the frame. This attachment method allowed the test bodies to be moved with respect to the pendulum frame and consistently positioned. Each test body weighed 4.8408 ± 0.0002 g. The test body and pendulum weights were corrected for their buoyancy in air. The higher density test bodies (aluminum and titanium) had hollow interiors, which reduced their volume and hence their buoyancy. The beryllium test bodies were solid, while the aluminum and titanium test bodies were hollow due to their larger densities. In the beryllium-aluminum configuration the pendulum weighed 70.0890 g while in the beryllium-titanium configuration it weighed 69.8203 g. The difference in weight came from exchanging the titanium tuning screws with copper screws in the lower stem for the beryllium-aluminum configuration to reduce a residual q_{21} moment greater than the adjustment range provided by the titanium screws.

5.1.3 Earth-Moon Pendulum

The earth-moon pendulum held four cylindrical test bodies between two horizontal trays as shown in figure 5.4. The pendulum incorporated four-fold azimuthal symmetry and top-bottom reflection symmetry. The lower tray supported the test bodies and was fixed to the center post. The upper tray slid along the post to allow the test body positions to be interchanged with respect to the frame. The cylindrical test bodies were composed of two half cylinders glued to a central spacer. Each test body weighed 10.0787 g, and the entire pendulum weighed 71.3053 g (weights are corrected for buoyancy in air). Disks near the top

Table 5.3: Comparison of the moon's, earth's mantle's, earth's core's, and the test body's compositions. The moon's composition comes from Longhi [78] as reviewed by Longhi [79]. Earth's mantle composition is from Lyubetskaya [80] and earth's core composition is from Bardo [14]. Percentages refer to the percent weight contribution to the overall composition. Values are listed as "excluding iron (including iron)" for the moon and mantle.

Element	Moon [79]		Mantle [80]		Moon-Mantle Test Body	Core [14]	Earth-Core Test Body
Si	24.4%	(21.5%)	24.0%	(21.1%)	39%	2.8%	0.4%
Al	2.4%	(2.1%)	2.1%	(1.9%)			
Mg	26.1%	(23.1%)	26.6%	(23.4%)	16%		
Fe	0%	(5.9%)	0%	(6.22%)		87.0%	72%
Ni			0.2%	(0.2%)		5.0%	9%
Cr	0.4%	(0.3%)	0.3%	(0.3%)			17%
Ca	2.6%	(2.3%)	2.3%	(2.0%)			
O	50.3%	(44.5%)	50.5%	(44.4%)	44%	5.3%	
Z/μ	0.4975	(0.4956)	0.4974	(0.4954)	0.4984	0.4690	0.4661
N/μ	0.5031	(0.5050)	0.5031	(0.5052)	0.5022	0.5321	0.5351

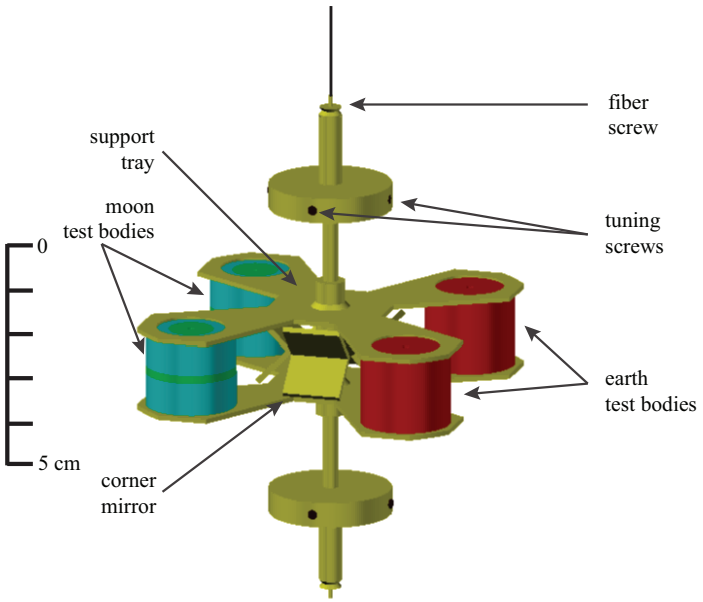

Figure 5.4: Schematic drawing of the earth-moon pendulum. Two test bodies mimicked the composition of earth's core and two mimicked the composition of the moon and earth's mantle. Cylindrical indentations in the horizontal trays positioned the test bodies. The upper tray slid along the post to allow repositioning of the test bodies.

and bottom of the central post had two orthogonal holes, which each held a pair of #4-40 set screws. The lower holes had copper set screws used for coarse determination of the q_{21} moment, while the upper holes had aluminum set screws for fine adjustments. The design incorporated a large lever arm of 2.44 cm to increase sensitivity to differential accelerations of the test bodies.

The test bodies for the earth-moon pendulum were chosen to closely match the bulk composition of the moon / earth's mantle and the earth's core (see table 5.3). The two earth-core test bodies were made of stainless steel to model the earth's core composition. The two moon-mantle test bodies were made of quartz with magnesium inserts to give them a composition similar to the moon's and to the earth's mantle. The similar composition of earth's mantle and the moon allows a factor of $\sim$4 (see equation 4.10) enhancement of the composition difference for a laboratory test in comparison to the effect on the earth-moon system. The enhancement arises because earth has a large core and the moon's composition

is similar to that of earth's mantle.

Due to the iron content of the earth-core test bodies, each test body was degaussed inside the outer stationary magnetic shield until the residual magnetic field was less than 5×10^{-8} T. The test body magnetic field was measured by a fluxgate magnetometer across a ∼2 mm plastic spacer with the test body placed on the spacer in multiple orientations.

5.1.4 Gradiometer Pendulum

The gradiometer pendulum frame supported 16 titanium spheres in conical cutouts on four flat aluminum disks. The conical cutouts precisely positioned the spheres to create reproducible gravity gradient moments. Each disk had eight cutouts around its edge. The top and bottom plates each had an additional eight cutouts near the central spindle. A model of the gradiometer pendulum with the balls arranged to produce a large q_{21} is depicted in figure 5.5. The spheres were arranged to give the pendulum a large q_{21}, q_{31}, or q_{41} moment, with other moments remaining small. Table 5.5 enumerates the calculated moments in the different configurations. The gradiometer pendulum had four flat mirrors that allowed different orientations of the pendulum with respect to the apparatus. It weighed 69.062 g with the 16 titanium spheres installed and each sphere weighed 0.795 g. The support frame and mirrors were coated with gold, but the titanium spheres were uncoated. The amplitude of the twist signal for the interaction of the main pendulum moment with the ambient gravity gradients were ∼900 μrad for the q_{21} and ∼1 μrad for the q_{31}. In contrast, the equivalence principle pendulums produced signals of at most a few nrad after we minimized the q_{21} moment with the tuning screws.

Table 5.4: Calculated moments using measured values for parts of the constructed equivalence principle pendulums for $\ell < 7$. Moments for $\ell < 2$ or $m = 0$ can not produce a twist of the torsion pendulum, but see the text for a discussion on interpreting the $\ell = 1,\ m = 1$ moments. A — denotes values less than 10^{-5}.

Multipole Moment (ℓ, m)	Be-Ti	Be-Al	earth-moon
(0,0) (g)	19.7	19.8	20.1
(1,0) (g cm)	—	-0.343	-1.15
(1,1) (g cm)	-4.8×10^{-3}	-2.74×10^{-3}	$-9.94 \times 10^{-4} - i\ 8.95 \times 10^{-3}$
(2,0) (g cm^2)	-3.43	-2.27	-8.48
(2,1) (g cm^2)	—	—	—
(2,2) (g cm^2)	—	—	$4.09 \times 10^{-3} - i\ 1.03 \times 10^{-3}$
(3,0) (g cm^3)	—	-3.71	-18.5
(3,1) (g cm^3)	**0.186**	$\mathbf{9.50^{-2}}$	$\mathbf{7.79 \times 10^{-2} + i\ 2.68 \times 10^{-3}}$
(3,2) (g cm^3)	—	$i\ 9.33 \times 10^{-4}$	—
(3,3) (g cm^3)	0.278	0.144	$(1.23 + i\ 1.44) \times 10^{-3}$
(4,0) (g cm^4)	-35.9	-24.1	4.54×10^3
(4,1) (g cm^4)	—	—	—
(4,2) (g cm^4)	$i\ 0.129$	$i\ 0.119$	$-1.14 \times 10^{-3} + i\ 4.15 \times 10^{-4}$
(4,3) (g cm^4)	—	—	—
(4,4) (g cm^4)	-9.34×10^2	-9.35×10^2	-2.72×10^3
(5,0) (g cm^5)	—	-33.8	-1.91×10^2
(5,1) (g cm^5)	-3.44×10^6	-3.44×10^6	$-2.64 + i\ 1.24$
(5,2) (g cm^5)	—	0.0649	—
(5,3) (g cm^5)	-2.19	-1.10	-1.97
(5,4) (g cm^5)	—	-2.30×10^{-4}	$1.06 + i\ 1.74$
(5,5) (g cm^5)	6.99	3.59	$(94.4 + i1.4) \times 10^{-4}$
(6,0) (g cm^6)	1.63×10^4	1.64×10^4	2.48×10^4
(6,1) (g cm^6)	$-i\ 6.98 \times 10^6$	$-i\ 6.98 \times 10^6$	—
(6,2) (g cm^6)	$i\ 4.64$	$i\ 4.29$	-3.27
(6,3) (g cm^6)	—	—	—
(6,4) (g cm^6)	-7.10×10^3	-7.10×10^3	2.56×10^4
(6,5) (g cm^6)	—	—	—
(6,6) (g cm^6)	—	—	$(-8.8 + i28.4) \times 10^{-5}$

Table 5.5: Calculated moments for the q_{21}, q_{31}, and q_{41} configurations of the gradiometer pendulum for $\ell < 7$. Moments for $m = 0$ can not produce a twist of the torsion pendulum. A — denotes values less than 10^{-5}.

Multipole Moment (ℓ, m)	q_{21}	q_{31}	q_{41}
(0,0) (g)	20.7	20.7	20.7
(1,0) (g cm)	4.46	4.46	4.46
(1,1) (g cm)	—	—	—
(2,0) (g cm^2)	8.11×10^{-2}	8.11×10^{-2}	17.9
(2,1) (g cm^2)	**35.685**	—	-4.01×10^{-3}
(2,2) (g cm^2)	—	—	—
(3,0) (g cm^3)	58.3	58.3	73.2
(3,1) (g cm^3)	28.0	**104.92**	-3.15×10^{-3}
(3,2) (g cm^3)	—	—	—
(3,3) (g cm^3)	—	—	—
(4,0) (g cm^4)	-1.61×10^3	-1.61×10^3	-8.06×10^2
(4,1) (g cm^4)	-1.69×10^2	1.08×10^2	**280.72**
(4,2) (g cm^4)	—	—	—
(4,3) (g cm^4)	-2.40×10^2	—	53.3
(4,4) (g cm^4)	9.09	9.09	9.09
(5,0) (g cm^5)	4.27×10^2	4.27×10^2	1.47×10^3
(5,1) (g cm^5)	-2.28×10^2	-1.45×10^3	3.57×10^2
(5,2) (g cm^5)	—	—	—
(5,3) (g cm^5)	-2.49×10^2	-9.31×10^2	55.3
(5,4) (g cm^5)	—	—	—
(5,5) (g cm^5)	—	—	—
(6,0) (g cm^6)	1.54×10^4	1.54×10^4	1.41×10^4
(6,1) (g cm^6)	-5.69×10^3	-2.26×10^3	-2.70×10^2
(6,2) (g cm^6)	—	—	—
(6,3) (g cm^6)	-1.81×10^3	-1.24×10^4	-8.88×10^2
(6,4) (g cm^6)	2.05×10^3	2.05×10^3	2.05×10^3
(6,5) (g cm^6)	3.21×10^3	—	-7.92×10^2
(6,6) (g cm^6)	—	—	—

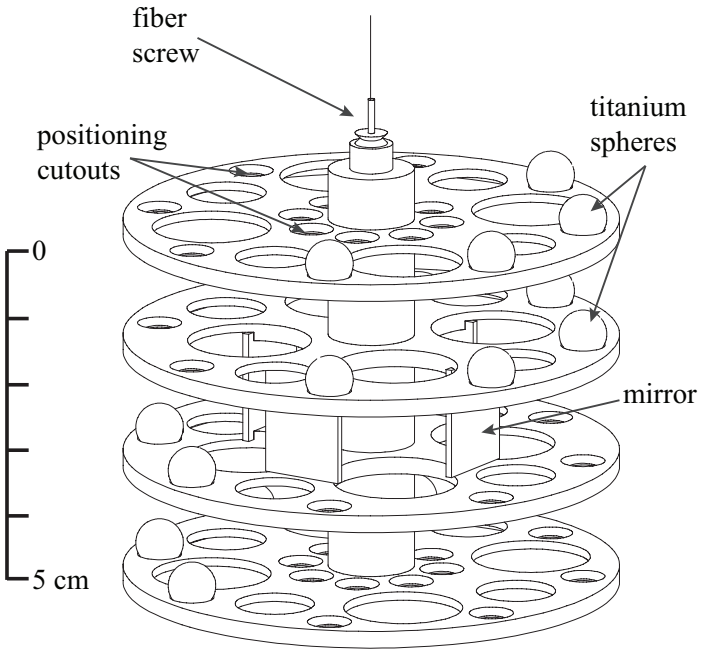

Figure 5.5: Schematic drawing of the gradiometer pendulum in the q_{21} configuration. The small holes in the disks precisely positioned the titanium spheres. The spheres were arranged to produce large q_{21} (shown), q_{31}, or q_{41} moments to measure the corresponding environmental field moments. The four mirrors allowed four different orientations with respect to the apparatus.

5.2 Suspension

The pendulum suspension positioned the pendulum fiber attachment to within 25 μm of a desired position and isolated the torsion mode from vibrations of the apparatus. The fiber positioning stage allowed translations and horizontal rotation. A vibration damper used eddy currents in a copper slug to rapidly damp vibrations of the upper fiber attachment point without significantly affecting the torsion mode. A two-section, 1 m long, tungsten fiber attached to the damper and suspended the pendulum. The frequency separation of the torsion mode $\sim$mHz from the damped, high-frequency modes of the fiber and suspension $\gtrsim$Hz effectively isolated the torsion mode.

Each fiber was about 107 cm long and consisted of a short ($\sim$3 cm long, 50 μm thick) upper pre-hanger and a long ($\sim$104 cm long, 20 μm thick) section with a small torsional restoring constant κ. The upper pre-hanger section was more uniformly round than the thinner, long fiber, due to manufacturing constraints. A round fiber cross-section prevents tilt-dependent excursions of the pendulum (see section 7.2). Three separate fibers were used, one with the beryllium-aluminum composition dipole configurations and two with the earth-moon pendulum. Each fiber had a typical resistance of $\sim$200 Ω, which we used to determine when the pendulum was in contact with a support within the apparatus. The height at which the pendulum and apparatus were no longer in electrical contact defined the reference position for the pendulum height. From the reference position, we raised the pendulum stage a predetermined distance to the operating position. At the operating position, the optics aligned with the pendulum's mirror and the center of mass of the pendulum corresponded to the center of the gravity gradient compensators. The (innermost magnetic) shield and support structure in the immediate vicinity of the pendulum were all gold coated. The gold coating reduces electric fields due to different materials having different work functions. Even with the gold coating a small shift in the pendulum period of $\sim$1 s occurred when the support structure was removed; however, we observed no difference in noise at the turntable rotation frequency.

The fiber used for the beryllium-aluminum and the first earth-moon fiber (fibers A and B, respectively) underwent a heating process. We attached electrodes to the fiber screws

at each end and hung the fiber in a glass vacuum chamber evacuated to $\lesssim 10^{-3}$ Pa. We increased the voltage across the fiber in 10 V steps up to 65 V, held the maximum voltage for a few minutes, then decreased the voltage in steps. Table 5.8 shows data for fiber A, which is typical of the fibers that underwent the heating procedure. At the maximum voltage, the fiber glowed a bright light orange color, which roughly indicates a temperature of ∼1200 K. Estimates based on the resistivity of the fiber imply a slightly higher temperature of ∼1450 K. The heating process made the surface of the fiber much shinier. The measured Q of fiber A was higher than that of all other fibers, but fiber C does not substantially differ from the fiber used for the beryllium-titanium composition dipole ($Q \sim 5400$) that did not undergo the heating process. The difference in Q could arise from the heating process, the quality of the wire section (though all fibers were created from the same spool of wire), or the quality of the crimp connections. The heating process may clean the surface of the fiber and possibly recrystallize the tungsten. Tungsten recrystallizes above temperatures of 1425 K [114], with the process occurring faster are higher temperatures. Many fibers were made using the heating procedure and broke during the installation process, some unable to support a 70 g test weight. This apparent reduction in breaking strength could be due to recrystallization occurring, a thinning of the fiber at a hot spot, or a mechanical defect introduced by handling during the mounting of the fiber screws or the heating process. The expected breaking strength for a 20 μm diameter work hardened tungsten fiber is about 130 g. The fibers required extremely delicate handling to prevent kinks, which cause them to break when loaded.

The damper consisted of an aluminum post with a copper slug pressed onto it. The rod hung from three beryllium-copper leaf springs. A screw through a disk uniformly clamped the three leaf springs to the top of the post. The copper slug was centered within a magnet encased in an iron flux return. The magnet induced eddy currents in the copper slug as it moved to damp the swing and bounce, while the cylindrical symmetry and stiff structure minimized any effect on the torsion mode. The leaf springs together with the mass of the pendulum had a bounce mode period of ≈1 Hz. The damper mounted on a polished steel shaft that exited the vacuum through a vertical bellows and an O-ring seal. Clamps outside the vacuum held the shaft to three orthogonal linear positioning stages. Screws

Table 5.6: Summary of fiber measurements. All fibers were constructed from the same spool of 0.8 mil tungsten wire. The earth-moon pendulum was taller than the eight-test-body pendulum, requiring a shorter fiber.

Fiber	Date			Thickness (μm)	Length (mm)	Pre-hanger length (mm)
A	7/10/2006	-	6/20/2007	20.3	1078	45
B	8/7/2007	-	11/24/2008	20.3	1064	25
C	5/15/2009	-	2/14/2011	20.3	1064	—[†]

[†] The pre-hanger length was not recorded, but was typically $2 - 5$ cm.

Table 5.7: Summary of each fiber's torsion constant κ, Q, and the maximum heating current.

Fiber	κ (nN m)	Q	Max Current (mA)
A	2.42	6700 ± 300	3.0
B	2.41	5280 ± 120	3.5
C	2.43	3800 ± 150	—

pressed against the shaft allowed small position adjustments and were used to reduce the run-out (horizontal movement of the fiber at different rotation angles) of the rotation stage to $\lesssim 50$ μm. Motors moved the assembly vertically and rotated it horizontally. The positioning stage also allowed translations in the two horizontal directions, which we used to align the fiber axis with the rotation axis of the apparatus to $\lesssim 50$ μm. The rotation stage run-out and alignment of the fiber with the rotation axis were done during the installation of each new fiber. The fiber and damper were electrically isolated from the rest of the apparatus, but grounded with a wire attached to the rotating shaft during operation.

Table 5.8: Typical data recorded during the heating process for a tungsten fiber.

Time (s)	Voltage (V)	Current (mA)	Computed Resistivity (10^{-7} Ω m)	Estimated Temperature (K)
	0	0		293
30	10	16.7	1.9	500
30	20	26.4	2.4	600
30	30	34.2	2.8	1100
60	40	40.2	3.0	1330 (red)
60	50	46.1	3.5	1050 (red/orange)
60	60	50.3	3.8	1430 (orange)
500	65	53.1	3.9	1460 (light orange)

5.3 Turntable

The vacuum chamber hung from a custom built air-bearing turntable (Professional Instruments Block-Head Model 10BR-AL). An eddy-current motor maintained a constant rotation speed through feedback to a 36000 lines per revolution rotary encoder (Heidenhain Model ERO 725). Two Peavy PV-500 Power Amplifiers sourced the three phases needed to drive the eddy-current motor. Transformers isolated the amplifiers from the motor drive coils. A Scott-T produced the three phase signals using two quadrature reference phases and a drive signal output by the data-acquisition system digital signal processor. The digital signal processor used a proportional-integral-derivative (PID) loop to control the rotation speed. The maximum rotation speed was $\sim$25 mrad s^{-1}. A slip-ring made the electrical transition between the laboratory and the rotating turntable.

The turntable maintained a constant speed using two read-heads oriented 180° apart on the rotary encoder to measure the turntable orientation. We averaged the two read-heads to reduce the effects of encoder inhomogeneity on the rotation rate. Through measurements of the pendulum at various turntable rotation rates, we determined that the rotation rate had variations at harmonics of the turntable rotation frequency. The first through ninth

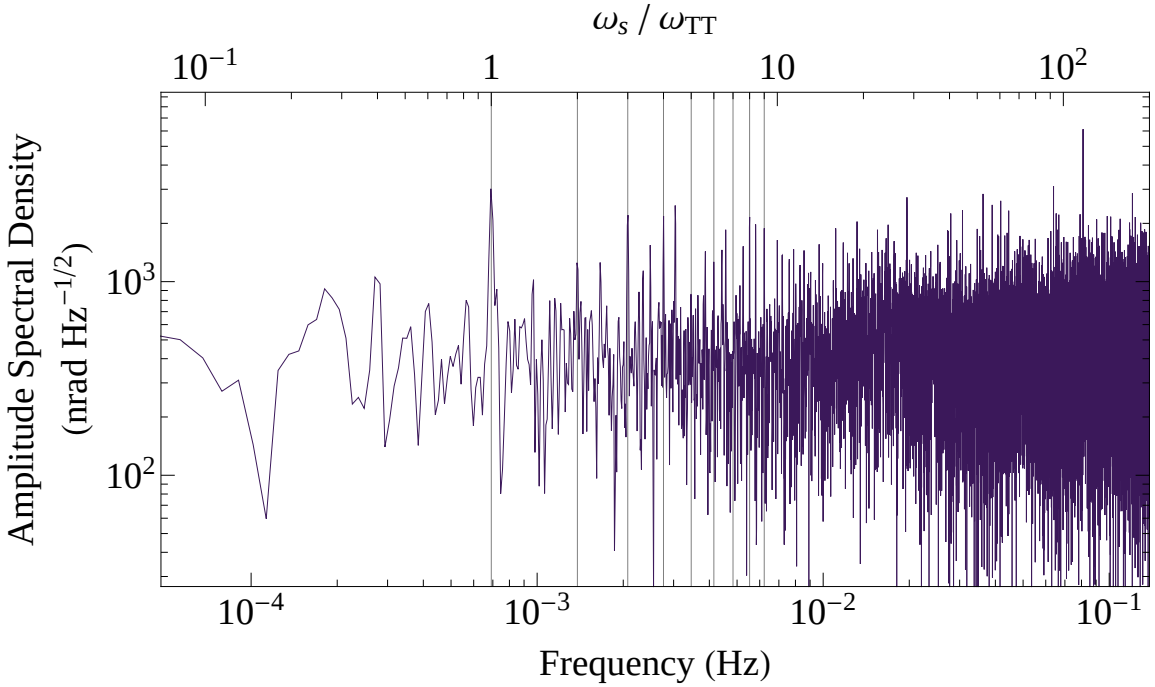

Figure 5.6: Amplitude noise density for the turntable control loop error signal. The peaks at harmonics one through nine (marked with grid-lines) correspond to corrections applied by the turntable control loop to account for encoder variations.

harmonics were corrected in the digital signal processor drive code and correspond to peaks in the noise spectrum shown in figure 5.6 (see section 7.5). We selected the drive speed based on the pendulum frequency ω_0 using two criteria: the pendulum oscillation was out-of-phase on consecutive turntable rotations and the least common multiple of the pendulum period and the turntable period was a small integer. The majority of data was taken with two turntable rotations commensurate with three pendulum oscillations. A smaller group of data using the earth-moon pendulum was taken with two turntable rotations equal to one pendulum oscillation. Pendulum twist calibrations and investigation of turntable rotation inhomogeneities were the only situations the turntable was run at different speeds. Analog feedback to a shadow detector drove the slip-ring at the same rate as the turntable to prevent the cables from producing a variable torque on the turntable. The shadow detector consisted of a LED and a photo-detector with the edge of a 180° cylindrical ridge casting

the shadow. A mechanical switch stopped the turntable if the slip-ring and turntable were out of alignment.

5.4 Angular Position Readout

An autocollimating angular position readout (autocollimator for short) measured the pendulum's twist angle in the apparatus's rotating frame. Figure 5.7 shows a schematic diagram of our autocollimator. A laser diode (Mitsubishi ML64114R) produced the beam, which passed through a 350 μm diameter collimating hole. The beam then passed through a polarizing beam splitter followed by a quarter wave plate and a 300 mm focal length lens. For the eight-test body and gradiometer pendulums, the beam reflected from a mirror to the pendulum, off a stationary corner mirror to a second reflection off the pendulum, then returned to the polarizing beam splitter via the lens and quarter wave plate. For the earth-moon pendulum, there was a single 45° mirror and a corner mirror on the pendulum returned the beam. The returning beam was transmitted through the polarizing beam splitter onto a position sensitive photo-detector (UDT SL3-2). The two mirror geometries are shown in figure 5.8. The dynamic range for this geometry allowed angles up to 2.6 μrad for a double bounce off the pendulum or 5.2 μrad for a single bounce off the earth-moon pendulum.

The position sensitive photo-detector output a current from each end that depended on the position of the beam on the detector. An analog circuit combined the currents from both ends to produce signals proportional to the difference ΔI and to the sum ΣI of the currents. The ratio $(\Delta I)/(\Sigma I)$ was proportional to the linear position on the detector. A function generator (Stanford Research DS340) modulated the laser at 142 Hz, which allowed two lock-in amplifiers (Stanford Research SR830) to amplify the difference and sum signals. Both lock-in amplifiers were typically configured with a 3 s low-pass filter at 12 dB/octave, a synchronous filter, and optionally a digital notch filter at 60 Hz. The synchronous filter removes harmonics of the lock-in frequency by averaging the digitized points over one period of the primary frequency. The digital notch filter removes noise due to electrical circuit interference; however, our lock-in reference frequency was sufficiently removed from the line frequency that this filter did not improve the signal [116]. The data acquisition system digitized the signal and quadrature components of the lock-in outputs

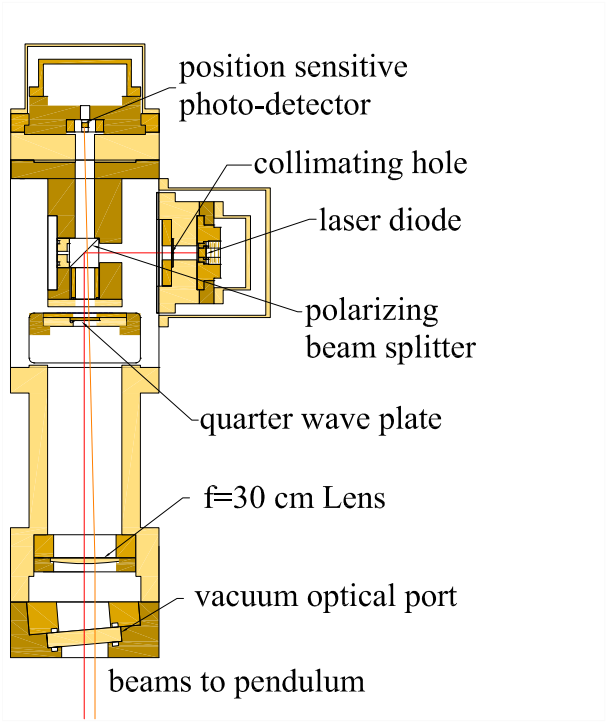

Figure 5.7: Schematic diagram of the autocollimator showing the major features. A laser diode produced a beam that was directed to the pendulum via a polarizing beam splitter and other optics. The beam returned after reflecting off the pendulum and was transmitted onto a position sensitive detector.

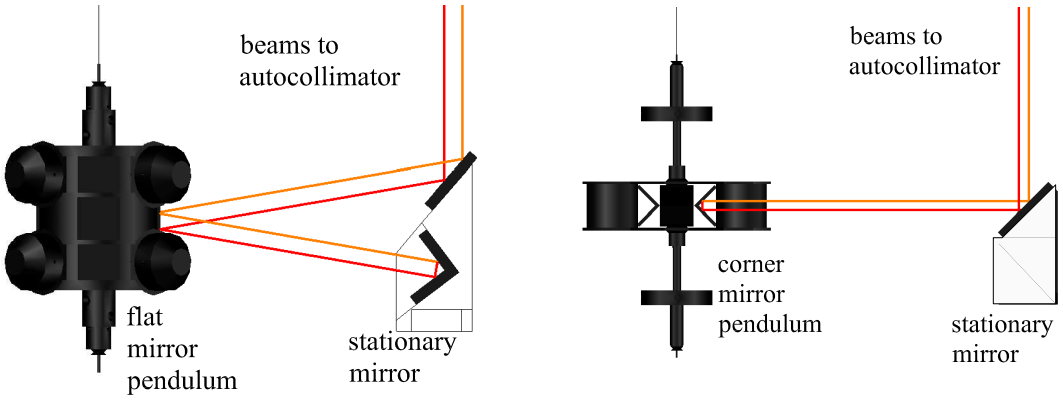

(a) Illustration of the beam path with a double bounce off a flat mirror on the pendulum.

(b) Illustration of the beam path with a corner mirror on the pendulum.

Figure 5.8: Diagram of the beam paths for the two different pendulum configurations. Dimensions are not to scale.

for both the ΔI and ΣI signals.

The the laser-beam's position on the photo-detector produces two output currents. The ratio of the difference ΔI and sum ΣI of the detector currents is proportional to the pendulum twist:

$$\begin{aligned}\theta &= \frac{1}{2}\arctan\left(k\frac{\Delta I}{\Sigma I + I_L}\right) \\ &\approx \frac{1}{2}\left(k'\frac{\Delta I}{\Sigma I}\right) - \frac{1}{6}\left(k'\frac{\Delta I}{\Sigma I}\right)^3 + \mathcal{O}\left[\left(\frac{\Delta I}{\Sigma I}\right)^5\right],\end{aligned} \tag{5.2}$$

where k and k' are calibration factors and I_L is an uniform leakage current (absorbed into the definition of k'). Any leakage current arising consistently across the detector results in only a calibration change while not affecting the linearity.

Using an autocollimator configuration sensitive to the polarization of the light permitted a low noise readout and minimized the effects of stray reflections. A sample noise trace using a stationary mirror as a reflector, both with and without the turntable rotating, is compared to the pendulum noise in figure 5.9. The data presented in this plot was all taken using the eight test-body pendulum. The pendulum was used as a stationary mirror by placing in on an aluminum spacer of the proper height.

5.5 Vacuum System

A vacuum chamber with a typical pressure between 4×10^{-5} Pa and 8×10^{-5} Pa enclosed the torsion balance. The vacuum chamber consisted of a vertical column that housed the fiber, a lower can that held the pendulum, and a top plate that supported the fiber positioning stage. An optical vacuum window allowed the optical readout of the pendulum angle and a sliding O-ring seal permitted rotations of the pendulum. A copper shroud surrounded the fiber inside the vacuum chamber and covered about 80% of its length. During the earth-moon portion of the experiment, small transient pressure increases resulted in a redesign of the vacuum chamber column and seals. The new design reduced the number of seals, more reliably compressed several larger O-rings, and increased the stiffness of the column.

An ion pump (Varian StarCell VacIon Plus 20 Model 919-0235) maintained the pressure of the vacuum chamber while the apparatus rotated. The ion pump could maintain vacuum

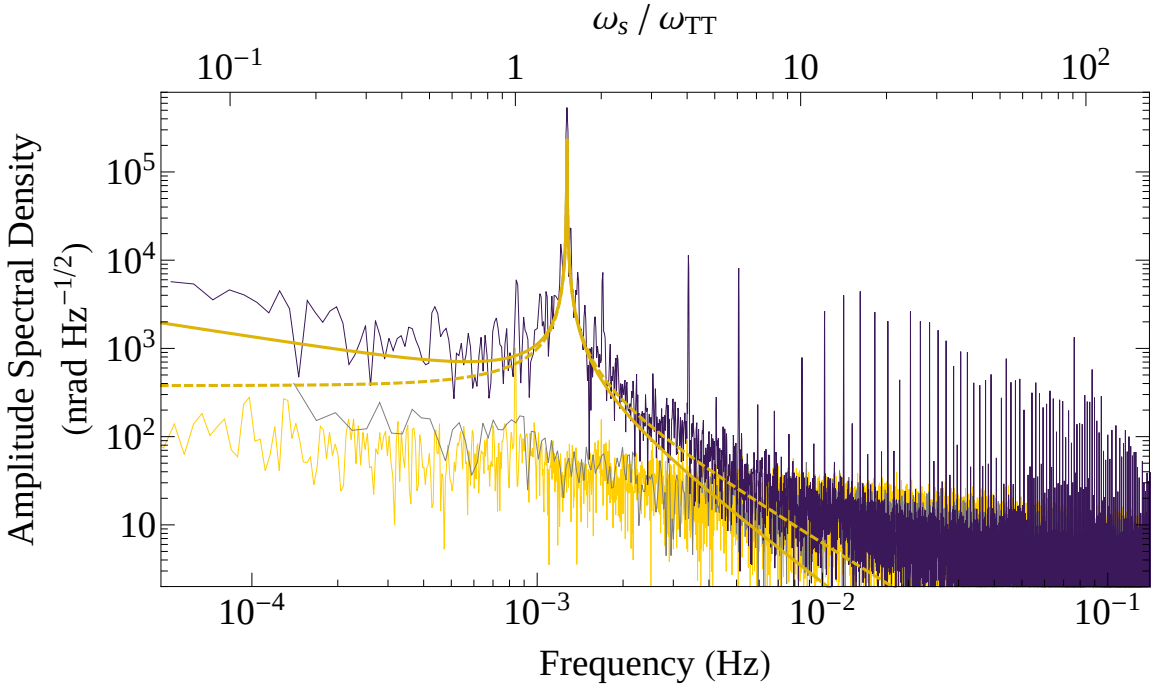

Figure 5.9: Displacement angle power spectral density of the apparatus in different configurations. The uppermost noise spectrum (purple) was taken with the turntable rotating and the pendulum suspended. The solid gold and dashed gold lines indicate the theoretical prediction for noise due to damping internal to the fiber and velocity damping, respectively, both with Q=6000. The two lower traces were taken with the pendulum resting on a spacer to determine readout noise. The gray trace was taken with the turntable feedback holding the turntable at a fixed position. The yellow trace, which shows harmonics of the turntable rotation frequency, had the turntable rotating at the normal rate.

pressure within our operating range for many months at a time, but needed an additional pump to initially evacuate the vacuum vessel. To evacuate the chamber, we connected a turbomolecular pump to the vessel through a vacuum bellows valve. During evacuation of the air, we heated the vacuum chamber to ∼60°C and a copper shroud surrounding the fiber to ∼80°C. Resistive heater tapes were wrapped around the exterior of the vacuum chamber to heat it. The shroud incorporated tubing that carried hot air through it. Heating the fiber greatly reduced the drift of the pendulum equilibrium position after the apparatus had cooled. When the typical chamber pressures were reached after pumping for up to two days with the turbomolecular pump, the ion pump was started. After ensuring proper operation

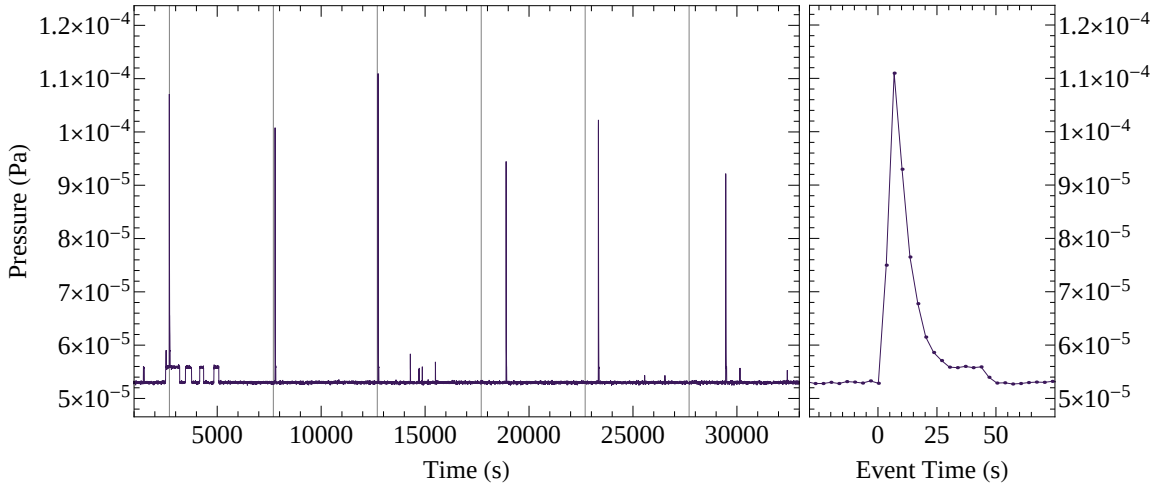

Figure 5.10: Example of transient pressure events that resulted in increased noise in the earth-moon pendulum angle. Grid lines aligned with the first event and spaced every 5000 s illustrate the regularity of the events. The right segment expands the pressure increase near 12700 s to reveal the rapid rise followed by pumping back to the base pressure. The points indicate the recorded measurements with the line as a guide for the eye. Transient pressure events correlated with changes in the pendulum's twist.

of the ion pump, a valve sealed the apparatus from the turbomolecular pump, which was then disconnected.

The ion pump also output a voltage V related to the pressure p by

$$p(V) = c_0 10^{c_1 V}, \tag{5.3}$$

where c_n are calibration coefficients.

During the experiment using the earth-moon pendulum, the pendulum angle noise was about 3 times greater than during the eight-test-body pendulum measurements, which operated near the thermal noise limit of the fiber. Transient events in the pendulum twist correlated with fast rises in the ion pump pressure from the base pressure $\sim 5 \times 10^{-5}$ Pa to $\sim 10^{-4}$ Pa followed by a decrease to the base pressure within about 20 s. These transient events occurred regularly roughly every 5000 s as shown in figure 5.10. Similar events occurred during the measurements with the eight-test-body pendulum, but had a negligible effect upon the pendulum twist. We made a concerted effort to locate the source and to reduce the effects of the pressure events upon the pendulum. A grounded screen was

inserted between the ion pump and the pendulum, all O-rings were cleaned or replaced and static O-ring seats were vented. The pressure events were determined to be actual gas releases rather than an ion pump phenomenon by pumping on the apparatus with a turbomolecular pump (which exhibited similar events) and pumping on an isolated volume with the ion pump (which had no transient events). Unfortunately, the specific seals causing the events could not be determined. Sliding seals between the column and support plates were suspected since these seals required clearance between the surfaces for installation and potentially compressed the O-rings asymmetrically.

We redesigned the vacuum chamber (shown in figure 5.11) to eliminate the sliding O-ring seals, improve mechanical stiffness and reduce sensitivity to temperature gradients, while minimizing other changes to the apparatus. Two sliding O-ring seals on the central column were replaced with more reliable compression O-ring seals. The sliding seals were compressed radially between the outer wall of the column and the inner face of a cylindrical hole in each of the upper and lower plates. We replaced these seals with axial compression of seals against the face of a new thicker column. The new column, machined from a 6 inch diameter aluminum holobar, has walls a factor of six thicker, and the thickness of the triangular structural supports doubled. These changes resulted in more than an order of magnitude increase in the stiffness of the vacuum chamber column. The seal between the column and the fiber positioning stage was separated from structural support of the column. The fiber support stage now rests on top of the column, which extends through the upper support plate with a small gap around it to reduce thermal coupling. We previously determined that the top support plate was the location of the apparatus's greatest sensitivity to temperature gradients. The outer surface of the column attaches to eight triangular support pieces that structurally connect the column to the supporting apparatus above and to the lower vacuum chamber below. To accommodate the ion pump and autocollimator, the column has a square cross-section through its lower-middle portion. The redesigned vacuum chamber reduced both the typical frequency (by more than a factor of 4) and maximum pressure rise of the transient pressure increases, but some still occurred (see section 6.5).

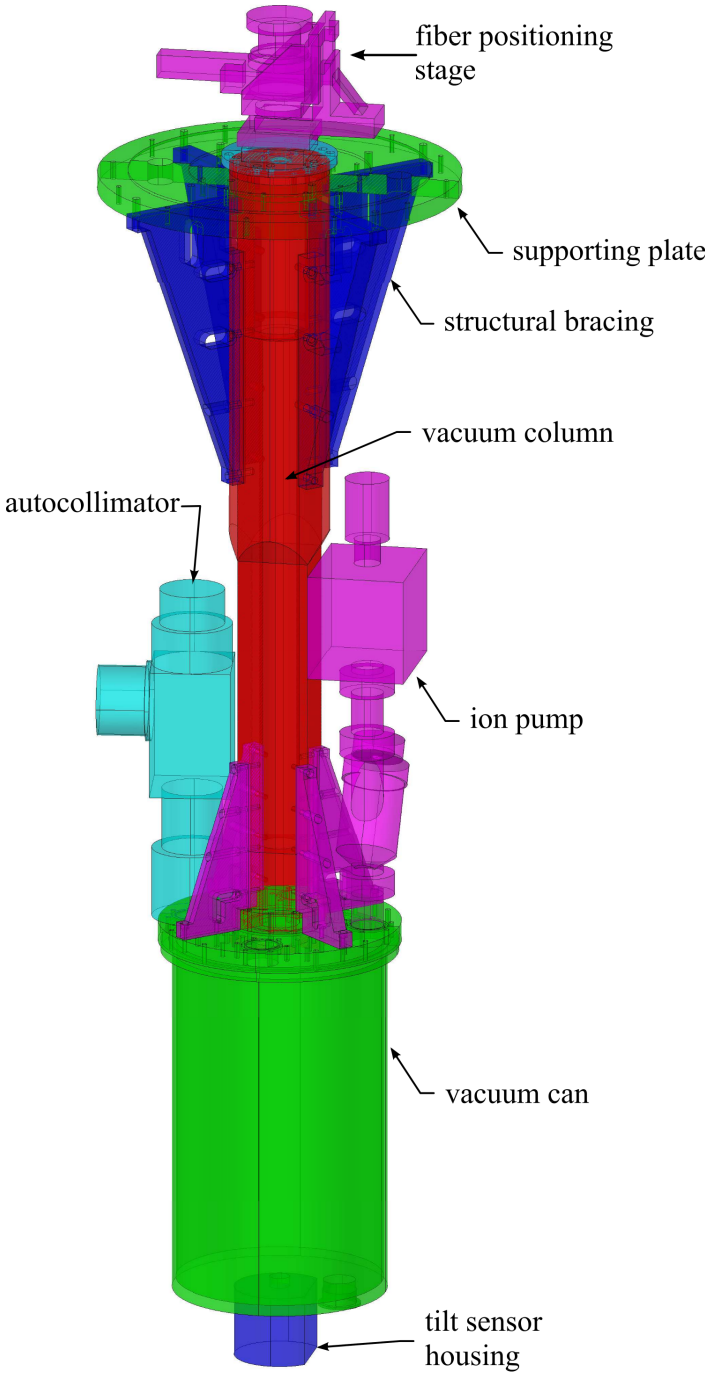

Figure 5.11: Rendering of the improved apparatus vacuum chamber. The triangular pieces attached to the column provide structural support. The square cross-section of the middle portion of the column accommodated the ion pump and autocollimator. The column passed through the upper supporting plate to directly support the fiber positioning stage.

5.6 Temperature Sensors and Shielding

Temperature plays an important role in any sensitive mechanical experiment because it can produce displacements and tilts, induce stress, and relates to noise through the fluctuation-dissipation theorem. Thermal effects due to changes in the mean temperature and to temperature gradients across the apparatus result in systematic effects for measurements with a torsion pendulum. Due to the rotation of our apparatus in a temperature stabilized enclosure, temperature gradients were the dominant source of systematic effects. We located the apparatus in an insulated enclosure within a temperature controlled room. Thermistors measured the temperature at 22 locations in and around the apparatus. Two pairs of thermistors measured the difference in temperature across the rotating thermal shield of the apparatus, which we used to determine the sensitivity of the apparatus to temperature gradients. Ten temperature sensors recorded the absolute temperature and six recorded temperature gradients around our apparatus. Four absolute temperature sensors and four differential temperature sensors were mounted on the rotating part of the apparatus. The remaining sensors measured temperatures within the enclosure, the room, and a water bath for the leveling feedback as enumerated in table 5.9.

Foam insulation supported by wood framing entirely enclosed the apparatus. Two-inch thick foam insulated the walls, ceiling, and floor of the enclosure. Within the upper section, an additional hexagonal foam structure enclosed the air-bearing and tilt leveling legs. Fans within the structure mixed the air to maintain a uniform temperature. The structure extended 20 cm from either side of the concrete platform to mix air between the upper and lower sections of the enclosure.

Two thermal shields attached to the apparatus to minimize temperature gradients. An outer, stationary, thermal shield consisted of an aluminum cylinder with insulation covering the exterior (one layer of the magnetic shielding was laminated to the inside of the aluminum cylinder). A second uninsulated aluminum cylinder rotated with the apparatus separated from the outer shield by a $\sim$1 cm air gap. The high thermal conductivity of the aluminum minimized gradients across the cylinders.

The temperature sensors were negative temperature coefficient thermistors (YSI 44006)

Table 5.9: Temperature sensor locations on the apparatus. The first eight sensors were located on the rotating part of the apparatus, while the second eight sensors were fixed in the laboratory.

Temperature Sensor Location	Type of Sensor
Upper tilt sensor	Absolute
Vacuum chamber column	Absolute
Autocollimator	Absolute
Lower tilt sensors	Absolute
Rotating temperature shield	Radial differential
Rotating temperature shield 90°	Radial differential
Vacuum chamber column	Radial differential
Vacuum chamber column	Vertical differential
Air-bearing turntable	Absolute
Concrete support bridge	Absolute
Stationary thermal shield (South side)	Absolute
Stationary thermal shield (Bottom)	Absolute
Room outside apparatus enclosure	Absolute
Tilt feedback temperature bath	Absolute
Stationary thermal shield	East-West Differential
Turntable air-bearing output	Absolute

with a resistance of 10 kΩ at 25°C. The voltage across the thermistors was measured using balanced Wheatstone bridges. Each bridge consisted of a thermistor (or two for a differential measurement) and resistance matched low temperature coefficient resistors. The difference in voltage between the thermistor and the reference branch (or between the two thermistors for a differential setup) was amplified with an instrumentation amplifier and converted to a current for transmission to the data acquisition system. The 16 temperature sensors were

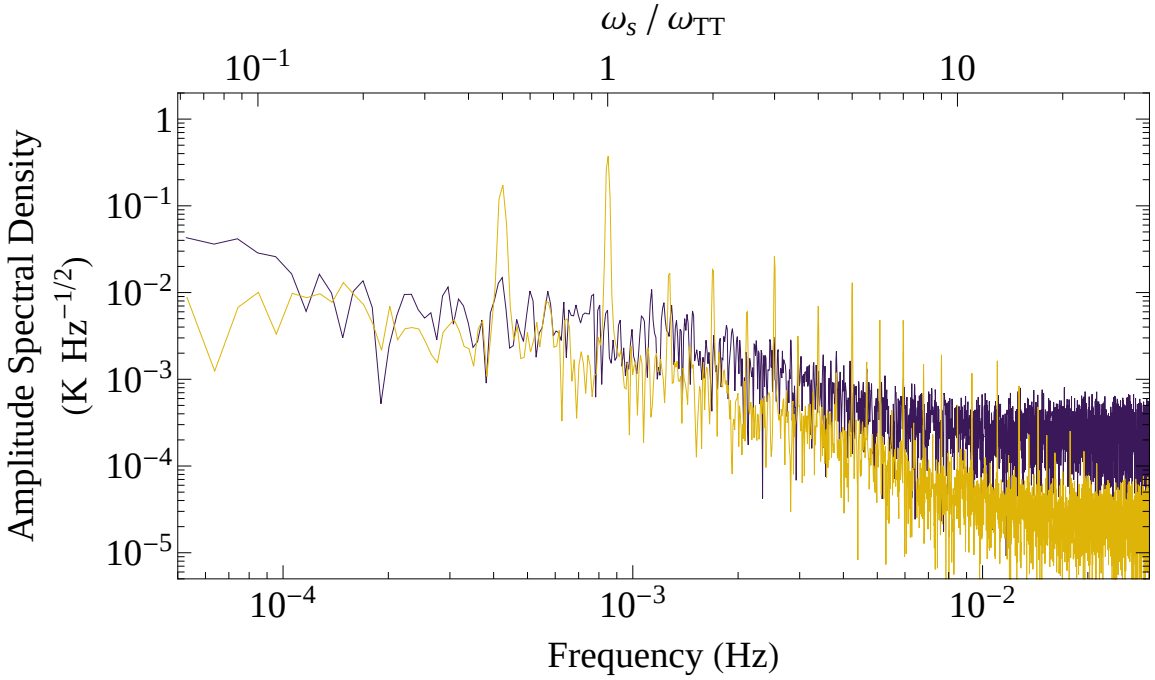

Figure 5.12: Comparison of temperature noise for differential sensor on outside of rotating thermal shield (yellow) and absolute sensor inside thermal shield (purple). The difference in noise at low frequencies in the differential sensor arises due to the rejection of temperature changes common to both sensors. The lower noise floor at high frequencies is due to the higher gain the differential temperature sensors can use due to their insensitivity to the absolute temperature. The absolute temperature sensor shows very little indication of the temperature variation at harmonics of the turntable rotation frequency, which demonstrates the effectiveness of the thermal shielding. The peak at $\omega_s/\omega_{TT} = 1/2$ occurs due to the turntable tilt feedback loop as described in the text.

multiplexed into a single digitization channel that was read multiple times to maintain the same sample rate as the other sensors. The circuit diagram is shown in figure 5.13. The differential measurements reduced sensitivity to the absolute temperature, which allowed the sensors to remain in range with an order of magnitude larger gain. Figure 5.12 compares a differential temperature sensor located on the outer surface of the rotating shield with the temperature sensor on the autocollimator inside the rotating thermal shield. The lack of peaks at turntable harmonics in the trace for the temperature sensor inside the rotating thermal shield demonstrates their effectiveness at equalizing temperature gradients. The

peak at $\omega_s/\omega_{TT} = 1/2$ in the differential sensor arises from a tilt feedback loop correction applied at this frequency. The tilt adjustments changed the separation between the rotating shield (and the attached differential temperature sensors) and the stationary shield.

We determined the temperature from a thermistor's resistance using the Steinhart-Hart equation [119]:

$$\frac{1}{T} = a + b\log(R) + c[\log(R)]^3, \tag{5.4}$$

where T is the temperature, neglecting self-heating effects, R is the thermistor resistance and a, b, and c are coefficients determined through calibration to a laboratory thermometer at multiple temperature points in the desired range. The amplified voltage from the Wheatstone bridge was proportional to the thermistor resistance. The differential temperature sensors were modeled using the derivative of equation 5.4:

$$-\frac{\mathbf{d}T}{T^2} = \mathbf{d}a(T) + \log(R)\mathbf{d}b(T) + [\log(R)]^3\mathbf{d}c(T) + \underbrace{b(T)\frac{\mathbf{d}R}{R} + 3c(T)[\log(R)]^2\frac{\mathbf{d}R}{R}}_{\text{bridge}} \tag{5.5}$$

While the coefficients vary depending on the calibration range chosen, the bridge circuit is sensitive primarily to $\mathbf{d}R/R$, the portion of the equation designated as *bridge*. In addition, the differential temperature sensor measurements were most important during the equivalence principle data collection, when the enclosure temperature was stabilized to within a few tenths of a degree over a period of weeks. Since the bridge portion of the equation is essentially in the measured quantity, we use a linear polynomial to calibrate the differential temperature sensors.

We maintained a constant temperature in the laboratory room using a heat exchanger (MagicAire 60-BVW/BVX-A) with the temperature controlled by a Neslab HX-300. The Neslab HX-300 had a remote temperature probe located in the airstream near the center of the room. This setup maintained the enclosure air temperature within 300 mK of the mean over the two weeks of a typical measurement set.

5.7 Tilt Sensors and Leveling

Three pairs of orthogonal tilt sensors (Applied Geomechanics Model 755) measured the tilt of the apparatus. Two pairs of tilt sensors were installed on the rotation axis, with one

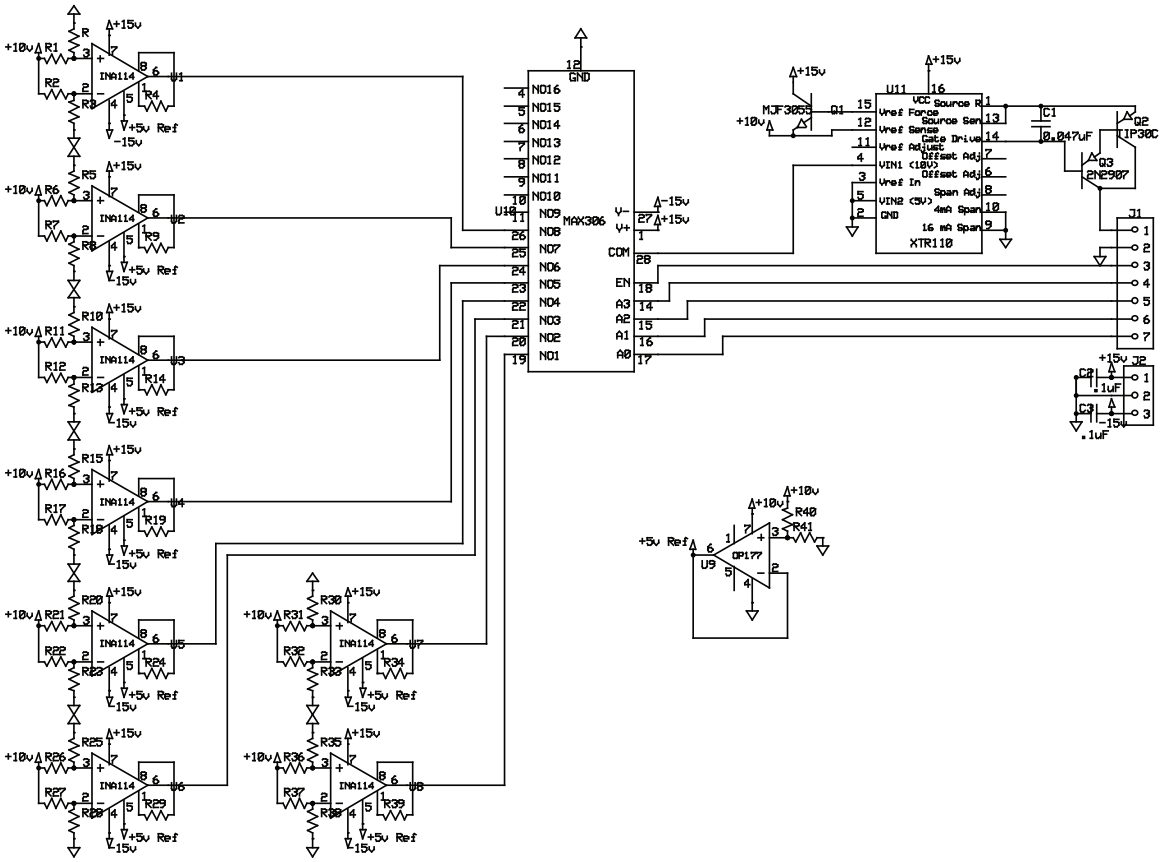

Figure 5.13: Circuit schematic for the temperature sensors. Each grouping of resistors with an instrumentation amplifier (INA114) made one temperature channel. For an absolute temperature channel, the resistor connecting the inverting amplifier input to ground was a thermistor connected by appropriate cabling. For a differential temperature channel, the two thermistors connected the two amplifier inputs to ground. The amplifier gain restricted the temperature range to $23^\circ - 27^\circ$C for the absolute temperature sensors and to 0.5°C for the differential sensors, which generally sufficed in our temperature controlled room and provided good sensitivity. The multiplexed temperature channels were recorded by the data acquisition system.

1.71 m above the pendulum and the second 0.20 m below the pendulum. The third pair of tilt sensors were installed on the stationary platform that supports the turntable. A feedback loop using the rotating tilt sensors aligned the rotation axis with vertical to within a few nanoradians. Two linear variable displacement transducers (LVDT) measured the separation between the concrete platform and the turntable base for coarse leveling of the turntable and calibration of the rotating tilt sensors.

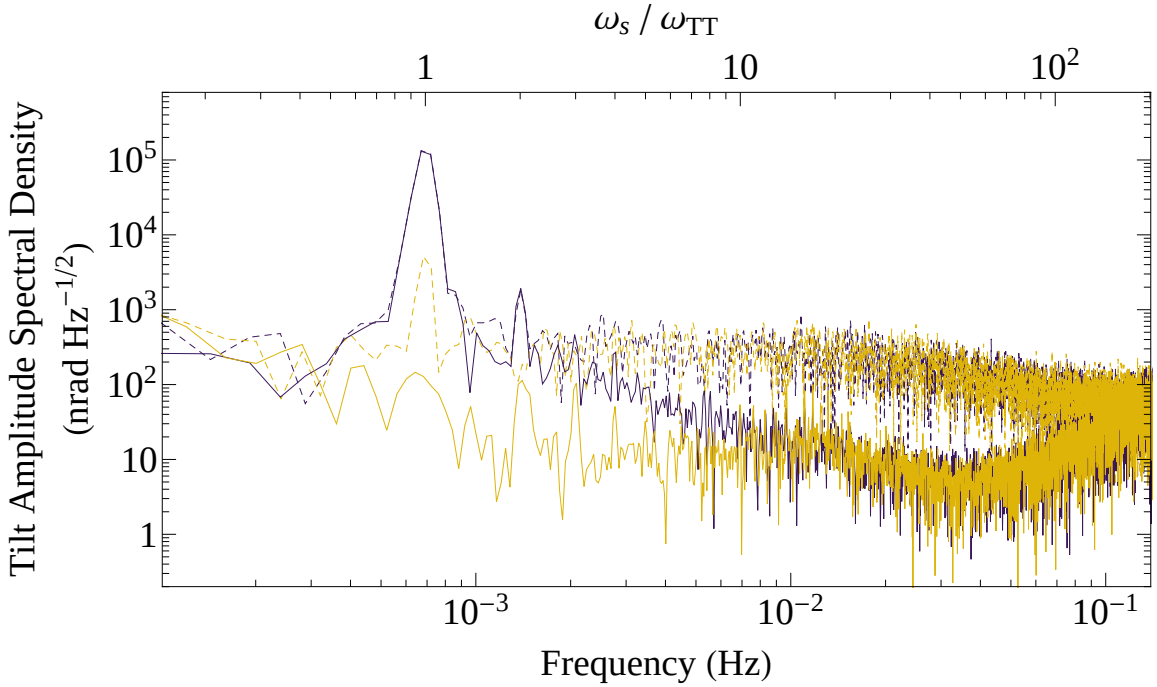

Figure 5.14: Tilt noise amplitude spectral density for an upper (solid lines) and a lower (dashed lines) tilt sensor. A longer cable connecting the lower tilt sensor to the amplifier resulted in greater noise. The gold lines were taken with the leveling feedback on and the purple lines with the feedback off.

Placing the tilt sensors on the rotating apparatus reduced the tilt sensors sensitivity to zero-point drift. Figure 5.14 compares the noise from our tilt sensors with the leveling feedback on and off. The two tilt sensor pairs on the rotating apparatus had a sensitivity difference due to the length of wiring between the sensor and its amplifier electronics. The tilt sensor pair above the pendulum had wiring $\sim$20 cm long, while the wiring for the lower tilt sensors was $\sim$2 m long. We used a grounded shield on the longer wiring, but the

difference was still appreciable. A low-pass filter with a 30 s time constant was enabled on the signal conditioning amplifier boxes.

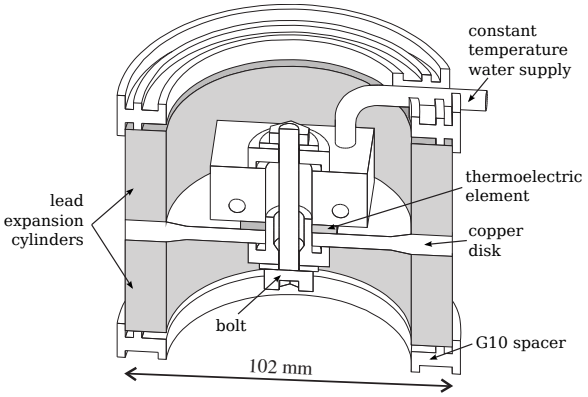

Figure 5.15: Schematic diagram of a leg used to control the tilt of the apparatus. A thermoelectric element between a constant temperature bath and a thermally conducting copper disk controlled the heat flow into the leg. Thermal expansion of the lead cylinders resulted in small height changes that a control system used to level the apparatus. Insulation, including G10 spacers and foam wrapping (not shown), thermally isolated the leg from the environment.

Three short legs supported the turntable base above a concrete platform. The height of two of the legs could be adjusted to level the turntable. Lead screws driven by stepper motors on two of the legs allowed coarse leveling of the turntable. The fine adjustments were accomplished using small displacements from controlled thermal expansion. The legs and feedback loop were developed by Ulrich Schmidt and described in appendix B of Heckel *et al.* [59]. The legs consisted of a thermoelectric element connected to a copper piece inset between two lead cylinders, see figure 5.15. The thermoelectric element also maintained contact, through a brass block, with constant temperature water flowing through it. A flow-through water bath with a temperature controller (Polyscience VWR 1165) maintained the flow of water to the legs. Each leg was entirely wrapped in foam insulation and separated from the platform and base by insulating G10 spacers. A feedback loop used the tilt sensors to control the thermoelectric elements via two power supplies (Kepco BOP 20-5M), one for each leg. The water bath was kept at a constant temperature of 24.3°C, slightly cooler than the room air temperature. The LVDTs and tilt sensors were calibrated using tilts of

the turntable with respect to the platform. The LVDT calibrations were made to a dial indicator referenced to the same surfaces and the tilts were calculated using the apparatus geometry and the dial indicator readings.

The tilt control loop transformed the signal from the tilt sensors into the laboratory frame and determined the height adjustment necessary at each of the two thermal legs to null the tilt. In addition, the Fourier components of the tilt signal were monitored to remove zero drift of the sensor from the feedback output. The zero adjustment occurred over half a turntable revolution every two turntable revolutions. A simple thermal model included the heat flux from the thermoelectric element, the thermal resistance of the copper and thermoelectric element, and the heat capacity of the copper disk and lead cylinders. The control loop solved this thermal model using stored Fourier series coefficients specific to the legs to find the heat flux needed to produce the desired height adjustment. The data collection loop and the tilt feedback loop both relied upon the data acquisition system sampling rate. This rate was typically increased when the pendulum was rotated and damped. The change in the sampling rate caused the leveling feedback loop to reset. It took up to a few hours for the loop to redetermine the zero-point. The data acquisition system code was updated between the beryllium-titanium and beryllium-aluminum data sets to reduce the effects of sample rate changes on the zero-point.

5.8 Magnetic Field Sensors and Shielding

Four layers of magnetic shielding reduced the ambient magnetic field to minimize magnetic forces acting on the pendulum. Two layers of high magnetic permeability metal (Magnetic Shield Corporation CO-NETIC AA alloy) were located inside the vacuum, one layer rotated with the apparatus, and the outermost layer remained stationary.

The large stationary shield consisted of two segments 0.9 m tall and 0.5 m in diameter along with a cap that fit snugly within the bottom segment. The top segment attached to an aluminum cylinder of the same dimensions to enclose the uppermost part of the apparatus. The two segments of the stationary magnetic shield were marked to permit removal and reattachment in the same orientation. A 35 cm tall magnetic shield tightly wrapped the outside of the vacuum can containing the pendulum. A magnetic shield with a closed bottom

(44 cm tall with a diameter of 25 cm) rested on insulating spacers that held it ∼1 mm from the inside vacuum can wall. A single conductor grounded the shield to the vacuum can. The innermost magnetic shield entirely enclosed the pendulum. It was 20 cm tall with a diameter of 15 cm and had small openings for the fiber, autocollimator and pumping. This innermost magnetic shield was gold-coated to provide an uniform electrostatic potential along with attenuation of the magnetic field. The stationary magnetic shield was degaussed in place and reduced the ambient magnetic field to $< 2.5 \times 10^{-6}$ T inside the shield. The three rotating magnetic shields were degaussed inside the stationary magnetic shield.

During the earth-moon pendulum measurements, a fluxgate magnetometer probe was installed inside the outermost, stationary magnetic shield. The iron content of the earth-core test bodies led us to monitor the magnetic environment while using the earth-moon pendulum. We measured the magnetic field to account for the effect of the daily variation (≈20 nT at our location) of the ambient magnetic field. Earth's magnetic field varies daily, primarily due to the dependence of the ionosphere's conductance on solar radiation [60].

5.9 Data Acquisition and Control System

The data acquisition and control system (DAQ) consisted of a computer (Pentium II running National Instruments LabWindows based software), a digital signal processor (Spectrum Signal Processing AM/D16SA Burr-Brown ADC/DAC), an analog to digital converter (Analogic Corporation LSDAS-16), and various signal conditioning electronics. The data acquisition system digitized analog signals from the optical position readout, turntable angle encoder, and the environmental sensors and recorded the values every ≈3 s. The recorded sensor data was written to a structured binary file for each run. The data acquisition system also executed control loops and performed other automated control of the apparatus. The turntable and tilt feedback are described further in their respective sections 5.3 and 5.7.

A slip ring allowed electrical signals to pass between the data acquisition system and electronics on the rotating turntable. The signals from the autocollimator, tilt sensors, and turntable angular encoder used balanced lines for transmission from the apparatus to the data acquisition system. The temperature sensors transmitted a current based upon the measurement, which was converted to a voltage across a reference resistor for digitization.

The data acquisition system had 20 channels of 16 bit analog to digital converters. Four channels were associated with the DSP (Spectrum Signal Processing AM/D16SA Burr-Brown ADC/DAC) and had a maximum sampling rate of 200 kS/s. The remaining 16 channels were digitized via an Analogic Corporation LSDAS-16 analog to digital converter with a maximum aggregate sampling rate of 50 kS/s. The typical sampling rate was between 3 and 20 Hz for each sensor. The digitization rate was set so an integer number of digitized measurements averaged to a single sample record. Because limited digitization frequencies were available, the actual sample recording interval differed slightly from the requested sample recording interval.

The data acquisition system controlled the fiber positioning and coarse tilt adjustment stepper motors. The system allowed simple backlash corrections, synchronization of the fiber rotation with the turntable rotation speed, and automated damping of the torsion oscillation.

The data acquisition system user interface simplified common activities, such as calibrating the pendulum twist, coarse leveling of the turntable, changing the turntable rotation rate while keeping the pendulum amplitude small, rotating the pendulum with respect to the apparatus, and scheduling data recording. The implementation of scheduling for data collection increased the data coverage and permitted defined run times, since we were was no longer required to manually set up data recording. Using the scheduler we set a run length of 98400 s, including the time taken to rotate to a new mirror and damp the pendulum oscillation.

5.10 Gravity Gradient Compensation

Gravitational coupling between environmental gradients and the moments of the pendulum produced the largest systematic effect. We constructed a set of masses, called compensators, with supporting structures around the apparatus to minimize the strength of the Q_{21}, Q_{22}, and Q_{31} components of the field. The local gravity gradient field was relatively strong because the laboratory was buried into the side of a hill.

The Q_{21} compensation mass consisted of trapezoidal blocks of lead installed in two rectangular semi-tori with an inner radius of 35.1 cm and an outer radius of 44.8 cm. The

semi-tori were positioned such that the center of mass of each is located on a line, 45° from vertical, that passed through the pendulum position. The lead massed 858 kg and reduced the Q_{21} field from 1.74 g cm^{-3} to $\lesssim$ 0.02 g cm^{-3}. The Q_{22} compensation mass was constructed of lead in four quarter cylinders with an inner radius of 29.2 cm and an outer radius of 42.2 cm, with pairs mounted to the top and bottom of the supporting plate, which was positioned at the same height as the pendulum. The pairs were positioned with their center of mass rotated 180° from each other about the apparatus rotation axis giving the necessary 2-fold symmetry. In all, the Q_{22} compensator massed 208 kg and reduced the Q_{22} field from 0.77 g cm^{-3} to $\lesssim$ 0.08 g cm^{-3}. The Q_{31} compensation mass was 5.5 kg made of 12 pairs of aluminum blocks and four rectangular lead bars placed along an arc with an inner radius of 28.6 cm and an outer radius of 32.4 cm. The aluminum blocks were arranged equally spaced through 165° of arc on the same support plate as the Q_{22} compensator, but with a smaller radius. Two lead bars connected both the top and bottom of the middle two pairs of aluminum blocks. The Q_{31} compensator reduced the field from 1.06×10^{-3} g cm^{-4} to $\lesssim 3 \times 10^{-5}$ g cm^{-4}. The compensator masses in their compensating positions are illustrated in figure 5.17. The supporting plates were removed in the figure to clearly show the compensating mass arrangement.

Four independently rotatable platters (entirely separate from the rotating apparatus) were incorporated into the three plates that support the compensator masses. One rotatable platter supported each of the upper Q_{21} half, the lower Q_{21} half, the Q_{22}, and the Q_{31} compensators. The rotatable platters for the Q_{22} and Q_{31} are incorporated into the same support plate. During equivalence principle data taking the compensators were positioned to minimize the gravity gradient field at the pendulum's position. To measure the effects of gravity gradients on the pendulum, we took measurements with each compensator at multiple angles to separate the ambient field from the compensator field. These measurements were the basis of the gravity gradient systematic studies described in section 7.1. The combined environment and compensator fields are described by

$$\bar{Q}_{\ell m} = \bar{Q}^{\rm env}_{\ell m} + Q^{\rm comp}_{\ell m} e^{im\alpha_{\ell m}} \tag{5.6}$$

where the barred fields are in the laboratory frame, the unbarred are in body fixed coor-

dinates and $\alpha_{\ell m}$ measures the angles between the body-fixed compensator frames and the laboratory frame. The body-fixed frames were defined as the frame in which the primary compensator moment was entirely positive and real. Since $|Q_{\ell m}^{\rm env}| \approx \left|Q_{\ell m}^{\rm comp}\right|$, rotating the compensator can change a moment from nearly zero to about twice the environmental field. To create a large Q_{31} field for measuring the equivalence principle pendulums' small q_{31} moment, the two semi-torus sections of the Q_{21} compensator were rotated to the same side of the apparatus to create a $Q_{31} = 2.62 \times 10^{-2}$ (20 times larger than that of the Q_{31} compensator), with no other large $m = 1$ moments. In this configuration it did not reduce the environmental Q_{21} and also had a small Q_{33}.

The separate support plates were rigidly fixed together, so that they cannot move with respect to each other except for the rotations of the platters. The compensators were kinematically centered on the pendulum's location through slide attachments to vertical supports. Three lead screws linked by a motorized chain drive provided vertical movement of the compensators with a positioning resolution of 0.127 mm. The vertical movement allowed access to the pendulum, installation of the thermal and magnetic shields, and adjustment of the compensator position with changes to the apparatus.

simple thermal model

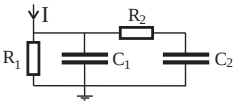

I : heat flux peltier element
C_1 : heat capacity copper disk
C_2 : heat capacity lead rings
R_1 : heat resistance peltier element
R_2 : heat reststance copper disk

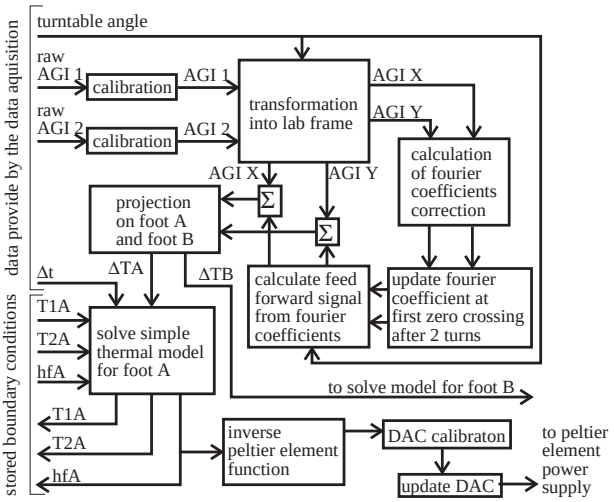

Figure 5.16: Flow diagram of the control loop for the tilt feedback. A simple model for the thermal expansion includes input heat flux, thermal resistance of the thermoelectric element and copper disk, and heat capacity of the copper disk and lead cylinders.

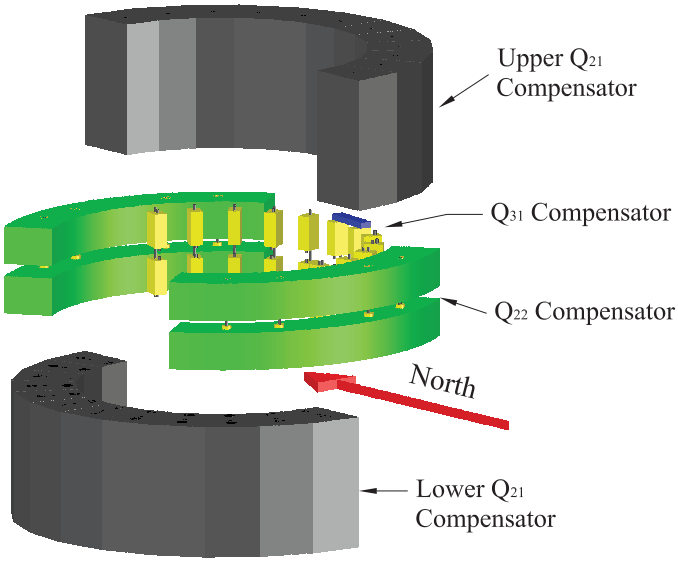

Figure 5.17: Schematic drawing of the Q_{21} (black), Q_{22} (green), and Q_{31} (yellow and blue) gravity gradient compensators. The Q_{21} compensator masses were located on two independent turntables mounted symmetrically about the vertical pendulum position. The Q_{22} and Q_{31} were each on concentric turntables vertically centered on the pendulum position. The arrow indicates the direction of North when the compensators were in their maximally compensating positions. The platters, turntables and supporting structure were removed in the figure to clearly show the compensators' mass arrangements.

Table 5.10: Calculated moments for the gravity gradient compensators with $\ell < 5$. Each compensator was named by the moment it was designed to cancel. Moments for $\ell < 2$ or $m = 0$ can not produce a twist of the torsion pendulum. A — denotes values less than 10^{-5}. Seasonal variations of the environmental gravity gradients limit cancellation to a percent.

Multipole Moment (ℓ, m)	Q_{21}	Q_{22}	Q_{31}	Q_{31} by Q_{21}
(0,0) (g cm^{-1})	4.88×10^3	1.45×10^3	50.1	4.88×10^3
(1,0) (g cm^{-2})	—	—	—	—
(1,1) (g cm^{-2})	—	—	$-i$ 1.32	i 57.3
(2,0) (g cm^{-3})	0.747	-0.955	-5.25×10^{-2}	0.747
(2,1) (g cm^{-3})	$\boldsymbol{i}$ **1.74**	—	—	—
(2,2) (g cm^{-3})	—	$\boldsymbol{i}$ **0.774**	-7.51×10^{-3}	—
(3,0) (g cm^{-4})	—	—	—	—
(3,1) (g cm^{-4})	—	—	$\boldsymbol{i\, 1.06 \times 10^{-3}}$	$\boldsymbol{i\, 2.62 \times 10^{-2}}$
(3,2) (g cm^{-4})	—	—	—	—
(3,3) (g cm^{-4})	—	—	$-i$ 2.24×10^{-4}	i 5.94×10^{-3}
(4,0) (g cm^{-5})	-1.04×10^{-3}	5.28×10^{-4}	4.29×10^{-5}	-1.04×10^{-3}
(4,1) (g cm^{-5})	—	—	—	—
(4,2) (g cm^{-5})	—	$-i$ 3.69×10^{-4}	—	—
(4,3) (g cm^{-5})	2.41×10^{-4}	—	—	—
(4,4) (g cm^{-5})	—	—	—	—

Chapter 6

DATA ANALYSIS

We collected data using two different composition dipoles from 2006 to 2011 as summarized in table 6.1. Our data acquisition system recorded the pendulum twist signal along with the turntable angle, 6 tilt sensors, 16 temperature sensors, pressure, and a few sensors related to the tilt and turntable feedback loops. We used the auxiliary sensors to ensure the quality of the data and investigate systematic uncertainties.

We fit segments of the pendulum twist data for a signal at the turntable frequency, which includes any equivalence-principle violation along with systematic effects. Each segment included two full turntable rotations over about 40 minutes. The mean and standard deviation of all the segment fit parameter results in each run determined the lab-fixed signal. We alternated the pendulum orientation between daily data runs. Local systematic effects were greatly reduced by taking two differences: First, apparatus-fixed systematic effects were removed by taking the difference between data collected on the 0° and 180° or 90° and 270° mirror pairs. Second, pendulum frame and suspension related systematic effects were removed by taking the difference between data collected with the composition dipole direction exchanged with respect to the pendulum frame. For signals toward the sun, dark matter and cosmic microwave background dipole, we fit the pendulum twist towards the position of each astrophysical source projected onto the local horizontal plane. The astrophysical-source fit model included terms for apparatus-fixed systematic effects. Pendulum frame and suspension systematic effects were removed by taking the difference between data collected with the beryllium-aluminum and aluminum-beryllium configurations. We did not exchange the test bodies on the earth-moon pendulum because it was difficult to accurately position them on the pendulum frame. The analysis process steps are summarized in the flow chart shown in figure 6.1.

We separate the data into different sets as part of our analysis. The list here summarizes

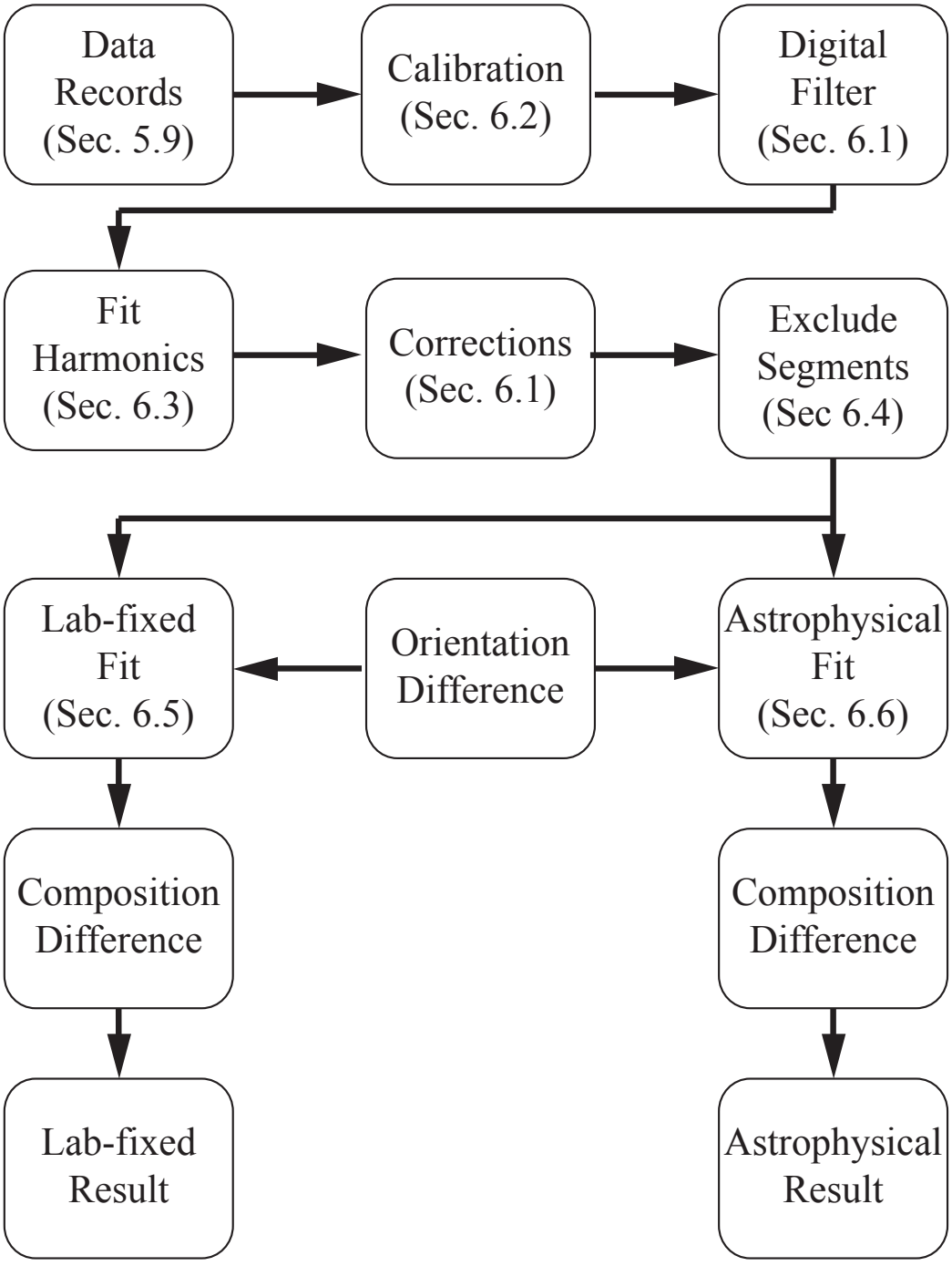

Figure 6.1: Flow diagram of the data analysis process.

Table 6.1: Summary of data collected using the beryllium-aluminum and earth-moon pendulums. The exclusion percentages were larger for the earth-moon pendulum due to greater sensitivity to pressure spikes as described in section 6.5.

Composition Dipole	Date			Fiber	Data Hours	Percent Excluded
Be-Al	7/31/2006	-	1/25/2007	A	1497	20.4%
Al-Be	2/20/2007	-	5/8/2007	A	914	13.3%
Earth-Moon	2/8/2008	-	11/24/2008	B	3197	52.7%
Earth-Moon	9/11/2009	-	2/14/2011	C	5491	21.7%

the terminology that we use to distinguish the different groupings:

Segment Set of consecutive data points (typically two turntable rotations long) that were fit to find the twist of the pendulum at harmonics of the turntable rotation frequency.

Run Continuous collection of data (typically for about 27 hours) with the pendulum in a particular orientation with respect to the apparatus. An equivalence principle data run included about 30 segments.

Group Set of runs collected to measure either a systematic effect or the equivalence principle. Groups of equivalence principle runs were taken with the pendulum in opposite orientations on consecutive runs (orientations 1 and 3 or 2 and 4 as shown in figure 5.2).

Configuration All equivalence principle groups with the test bodies in the same orientation with respect to the pendulum frame. The three configurations were beryllium-aluminum, aluminum-beryllium, and earth-moon.

6.1 Signal Processing

The measured pendulum twist differs from the actual twist due to signal processing during data acquisition and analysis. Signal processing for the pendulum twist included a lock-in amplifier, data acquisition system digitization and averaging, and a two-point digital filter to remove the pendulum oscillation. We analytically computed the attenuation effect for each filter and applied corrections to the harmonic fit Fourier coefficients (see section 6.3). We used the internal damping transfer function (equation 3.10) to model the pendulum's twist angle response to a torque. The predicted noise spectrum from internal damping plus the autocollimator noise matches well with our measured twist noise spectrum as shown in figure 5.9.

6.1.1 Low-pass filters

Low-pass filters separate desired signals from unwanted, high-frequency noise, but also attenuate and phase-shift the signals that pass through. The lock-in amplifiers for the difference and sum of the photo-sensor outputs each used a 2-pole, 3 s time constant low-pass filter to remove the laser modulation (see section 5.4). The tilt sensor electronics included a 1-pole low-pass filter with a 30 s time constant for each tilt sensor.

We modeled the transfer function $\mathcal{R}_{\text{low}}$ of an order p low-pass filter as

$$\mathcal{R}_{\text{low}}(\omega) = \left(\frac{1}{1 + i\omega\tau}\right)^{p}, \tag{6.1}$$

where ω is the signal frequency and τ is the filter time constant.

6.1.2 Data averaging

The data acquisition system averaged N data points sampled at a frequency ω_a to produce a single record. Averaging attenuates the amplitude of signals since values at an extremum are averaged with data points not at the extremum. For an average taken symmetrically about the mean of the sample times:

$$\mathcal{R}_{\text{avg}}(\omega) = \frac{1}{N}\csc\left(\frac{\pi\omega}{\omega_a}\right)\sin\left(\frac{\pi\omega N}{\omega_a}\right) \tag{6.2}$$

6.1.3 *Two-point digital filter*

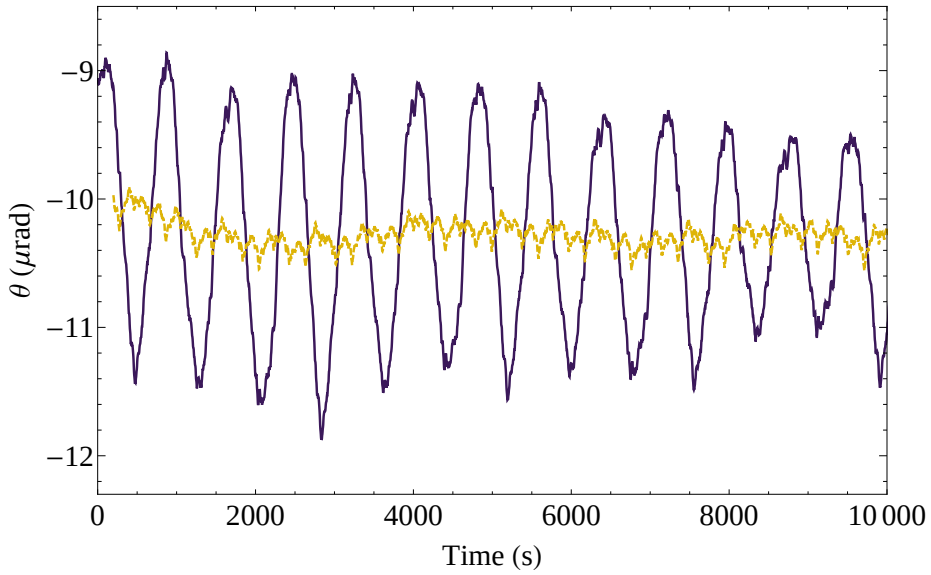

Figure 6.2: A two-point digital filter removed the pendulum's torsion oscillation. The solid purple line shows the recorded data for the pendulum twist. The dashed gold line shows the output of the two-point digital filter. The filtered output begins a quarter pendulum period after the first recorded data point.

The pendulum's torsion oscillation had an amplitude of ∼100 μrad after our automated damping process (see section 5.9). We removed the torsion oscillation with a two-point filter that averaged points separated by half of the pendulum period $T_0 = 2\pi/\omega_0$:

$$\theta_{2\text{pt}}(t) = \frac{1}{2}\left[\theta(t + \frac{T_0}{4}) + \theta(t - \frac{T_0}{4})\right] \tag{6.3}$$

We recorded an integer number of data points (72×4) each pendulum period T_0, which resulted in a sample interval between 2.7 s and 3.4 s and minimized interpolation for the two-point filter. The two-point filter reduced the torsion mode amplitude by at least 30 dB.

The two-point filter attenuated signals at frequency ω, which we corrected using the following transfer function:

$$\mathcal{R}_{2\text{pt}}(\omega) = \cos\left(\frac{\pi\omega}{2\omega_0}\right) \tag{6.4}$$

The two-point filter correlates data by including each recorded data point in two different filtered points. We modeled the covariance $U_{k\ell}$ between two segments k and ℓ due to the

two-point filter:

$$U_{k\ell} = \frac{\sigma^2}{M^2}\Big[\delta_{k\ell}(M-\beta) + (\delta_{k,\ell-1} + \delta_{k,\ell+1})\frac{\beta}{2}\Big], \tag{6.5}$$

where M is the number of data points in a segment, σ^2 is the variance for a single data point, β is the number of data points in the filter interval $T_0/4$, and δ is the Kronecker delta. A derivation of the two-point-filter covariance model is in appendix B. The effect of the two-point-filter correlation on the lab-fixed analysis was to increase the statistical uncertainty by 4.4%.

6.1.4 Attenuation Correction

The product of the transfer functions for the filters and the pendulum (see equation 3.10) with the twist Fourier coefficients determined the torque Fourier coefficients:

$$\tilde{\tau}(\omega) = \mathcal{R}^{-1}_{\text{internal}}(\omega)\,\mathcal{R}^{-1}_{\text{2pt}}(\omega)\,\mathcal{R}^{-1}_{\text{avg}}(\omega)\,\mathcal{R}^{-1}_{\text{low}}(\omega)\,\tilde{\theta}(\omega) \tag{6.6}$$

Table 6.2 enumerates typical values of the attenuation corrections for the pendulum's Fourier coefficients at the turntable rotation frequency.

Table 6.2: Attenuation corrections to the turntable rotation frequency Fourier coefficients for the beryllium-aluminum data. The magnitude scales the Fourier coefficients and the phase indicates the rotation angle that mixes the sin and cos coefficients.

	Magnitude	Phase (deg)
Pendulum	1.79994	−0.018
Averaging	0.99999	0.000
Two-point filter	0.50002	0.000
Low-pass filter	0.99975	−1.831
Total	**0.89977**	**−1.849**

6.2 Calibration

Each sensor was calibrated using known signals that spanned the sensor's range. In contrast to most of the sensors, which maintained the same calibration values, the twist calibration depended on the pendulum and fiber. We calibrated the pendulum twist angle each time we changed the pendulum configuration by measuring the amplitude change due to a rapid change in the turntable rotation velocity.

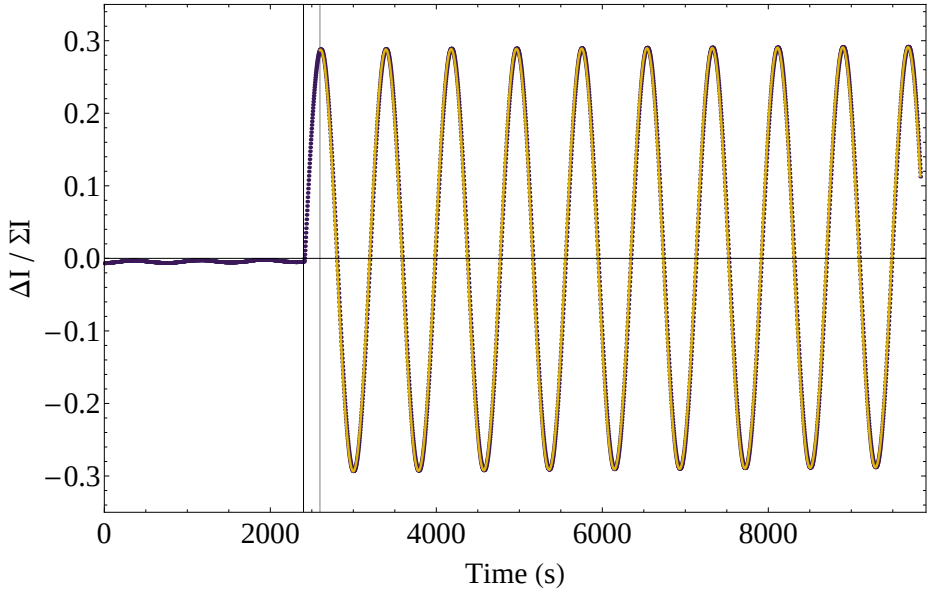

Figure 6.3: Calibration of the pendulum twist using an abrupt change in the turntable rotation velocity at 2400 s by 3 μrad s^{-1} and the resulting change in the pendulum twist amplitude. The decay of the oscillation amplitude after the change determines the Q.

The autocollimator used a linear photo-detector to measure the position of the beam spot from a laser diode reflected off a pendulum mirror as described in section 5.4. Reflections off surfaces other than the pendulum mirror or mismatched gains between the sum and difference amplifier circuits for the photo-detector may result in a position dependent twist calibration. Without any position dependence, equation 5.2 predicts $a_1 = -a_3/3$ and all other coefficients are zero. To account for a position dependent calibration, we modeled the twist with a fourth-order polynomial in the ratio of the difference to the sum of the

photo-detector currents $\Delta I/\Sigma I$:

$$\theta = a_0 + a_1\left(\frac{\Delta I}{\Sigma I}\right) + a_2\left(\frac{\Delta I}{\Sigma I}\right)^2 + a_3\left(\frac{\Delta I}{\Sigma I}\right)^3 + a_4\left(\frac{\Delta I}{\Sigma I}\right)^4 \tag{6.7}$$

A calibration run had three sections as shown by the trace of the pendulum oscillation in figure 6.3: First, the twist was damped to an amplitude of $\lesssim 100$ μrad, which was measured for at least one complete oscillation. Second, the turntable rotation velocity was abruptly changed, typically by 3 μrad s^{-1}. Using the turntable speed change to stop the turntable prevented turntable rotation rate variations from affecting the calibration. However, calibration measurements with a small velocity change to the typical rotation rate ($\sim$5 mrad s^{-1}) yielded equivalent calibrations. Third, the pendulum twist was measured for many oscillations after the speed change to accurately determine the pendulum period and Q in addition to the calibration terms. We denote the fit coefficients from before the speed change with $<$ and after the speed change with $>$. To determine the values of the calibration coefficients a_i, we iterated a multi-step fitting process that used the amplitude change in the torsion oscillation from the rapid turntable rotation speed change: First, we performed a nonlinear fit to the twist $\theta^>$ following the turntable speed change Δv at time t_0:

$$\theta^> = c_0^> + c_1^> t + \left[d_s^> \sin(\omega_0 t) + d_c^> \cos(\omega_0 t)\right] e^{-(t-t_0)/T}, \tag{6.8}$$

where ω_0 is the torsion frequency, $d_s^>$ and $d_c^>$ are the sinusoidal amplitude terms, $c_0^>$ is a constant offset, $c_1^>$ is a linear drift, and T is the damping time constant that determines $Q = T\omega_0/2$. Second, we performed a linear fit of the initial pendulum twist $\theta^<$ with ω_0 determined by the nonlinear fit:

$$\theta^< = c_0^< + c_1^< t + (d_s^< \sin(\omega_0 t) + d_c^< \cos(\omega_0 t)) \tag{6.9}$$

Third, the residuals from the nonlinear fit as a function of $\theta^>$ (shown in figure 6.4) were fit to the calibration polynomial 6.7. The calibration coefficients were updated using

$$a_n = (a_n - a_n')\sqrt{\frac{\left[\tilde{d}_s^< + \frac{\Delta v}{\omega_0}\cos(\omega_0 t_0)\right]^2 + \left[\tilde{d}_c^< - \frac{\Delta v}{\omega_0}\sin(\omega_0 t_0)\right]^2}{(\tilde{d}_s^>)^2 + (\tilde{d}_c^>)^2}}, \tag{6.10}$$

where $\tilde{d}^{<}$ and $\tilde{d}^{>}$ are the attenuation-corrected amplitude coefficients from before and after the turntable velocity change and a'_n are the residual fit coefficients. The amplitude coefficients $\tilde{d}$ were corrected for the effects of the lock-in amplifiers using equation 6.1. Our initial calibration used the coefficients predicted for the photo-detector (equation 5.2): $\theta = (\Delta I/\Sigma I) - (\Delta I/\Sigma I)^3/3$. Additional iterations were performed until the fit coefficients stopped changing.

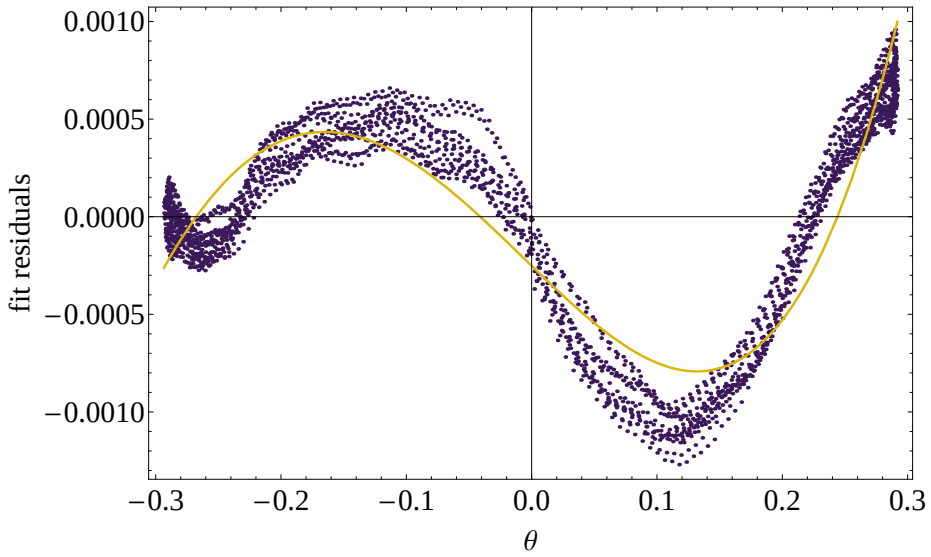

Figure 6.4: The first iteration residuals from the damped exponential fit plotted against the value of θ. The initial choice of calibration coefficients gives $\theta = \Delta I/\Sigma I - (\Delta I/\Sigma I)^3/3$ as shown in this plot, but later iterations converge on the conversion to radians.

6.3 Harmonic Coefficient Fits

We fit segments of the filtered data for harmonics of the turntable rotation frequency ω_{TT}. A lab-fixed equivalence-principle-violating signal would occur at the turntable rotation frequency. We set the turntable rotation speed so that two turntable rotations corresponded to three torsion oscillations, which made the fit to turntable harmonics orthogonal to the pendulum oscillation for segments including an even number of turntable rotations. To reduce the amount of data discarded due to disturbances, we used segments that included two

Table 6.3: Summary of pendulum twist calibration results. The beryllium-aluminum configuration included a double bounce of the laser-beam off the mirror that accounts for the factor of 2 difference in the a_1 coefficient for the earth-moon pendulum.

Date	Configuration (Mirror)	ω_0 (s^{-1})	a_1	a_2	a_3	a_4
9/8/2006	Be-Al (90°)	786.480 ± 0.009	1.300	−0.0031	−0.0637	−0.0790
11/9/2006	Be-Al (0°)	786.464 ± 0.007	1.325	0.0316	−0.1950	−0.5192
3/13/2007	Al-Be (90°)	786.498 ± 0.007	1.305	−0.0014	−0.1293	−0.1008
1/31/2008	EM (270°)	964.332 ± 0.004	2.604	0.0406	−0.0034	−0.4131
5/23/2008	EM (90°)	964.415 ± 0.005	2.600	0.0947	−0.1763	−1.2678
8/12/2008	EM (0°)	964.426 ± 0.004	2.647	0.2457	−1.3685	−1.4731
8/11/2009	EM (270°)	961.705 ± 0.007	2.648	−0.0332	−1.3528	−1.8010

turntable rotations. The filtered data for each segment was fit using the following model:

$$\begin{aligned} \theta_{\mathrm{2pt}}(\phi_{\mathrm{TT}}) &= \sum_m \left[\tilde{\theta}^c_m \cos(m\phi_{\mathrm{TT}}) - \tilde{\theta}^s_m \sin(m\phi_{\mathrm{TT}})\right] + \sum_n c_n P_n(\phi_{\mathrm{norm}}) \\ \phi_{\mathrm{norm}} &= \frac{2\phi_{\mathrm{TT}} - (\max(\phi_{\mathrm{TT}}) + \min(\phi_{\mathrm{TT}}))}{\max(\phi_{\mathrm{TT}}) - \min(\phi_{\mathrm{TT}})} \end{aligned} \tag{6.11}$$

The turntable angle is ϕ_{TT}, $\tilde{\theta}^s_m$ and $\tilde{\theta}^c_m$ are the Fourier coefficients of the twist for harmonics $m \in \{1/2, 1, 3/2, 2, 3, 4, 6, 8, 12, 16\}$, c_n is the nth drift coefficient, and P_n are Legendre polynomials for $n \in \{0, 1\}$. The normalized turntable angle ϕ_{norm} is the map of the recorded turntable angle onto the interval [-1,1]. The harmonic functions of $-\sin(m\phi_{\mathrm{TT}})$ and $\cos(m\phi_{\mathrm{TT}})$ correspond to torques where the potential energy was minimized toward the north and west respectively for the 0° pendulum orientation.

The first harmonic coefficients $\tilde{\theta}_1$ include any equivalence-principle-violating signal along with systematic effects at the turntable rotation rate. Other harmonic coefficients include effects that contribute to systematic uncertainties, such as residual pendulum oscillation (i.e., amplitude for $m = 3/2$ not removed by the two-point digital filter), turntable rotation irregularities, and gravity gradient coupling. The $m = 1/2$ harmonic corresponds to the

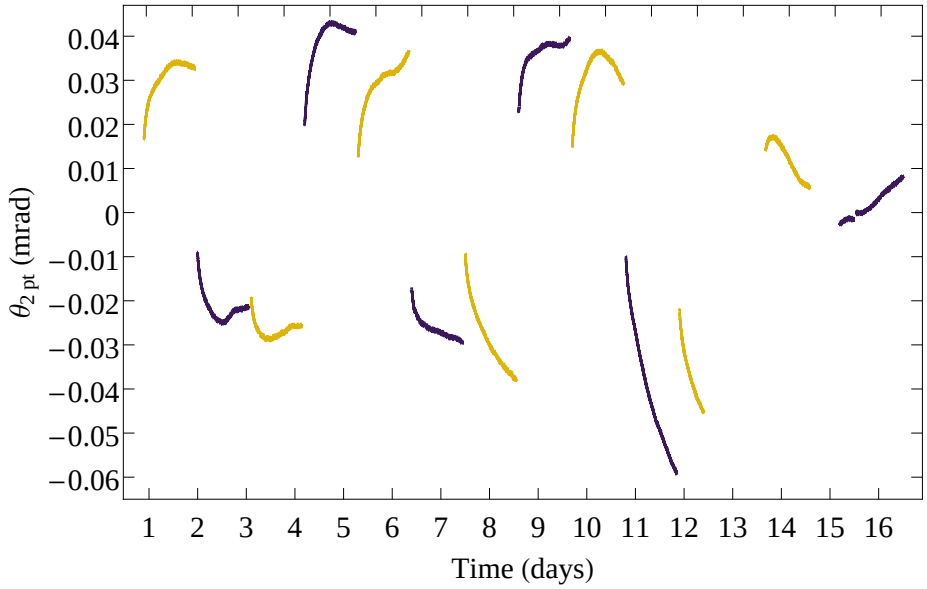

Figure 6.5: Data collected during a two week period with the torsion oscillation removed by the two-point filter. The filtered data was segmented (about 30 segments each day) and each segment fit to harmonics of the rotation frequency. The nonlinear shape of the data comes primarily from fiber relaxation and temperature changes.

period at which the tilt feedback system removed offset drift. The pendulum's four-fold symmetry corresponds to $m = 4$. We suspect that a six-fold bolt-pattern that holds the turntable encoder in place produces the $m = 6$ harmonic. Drift terms c_n modeled movement of the equilibrium point due to fiber anelasticity and thermal effects; however, both the fiber relaxation after pendulum orientation changes and thermal effects were exponential decays [86]. The linear approximation sufficed given the small drifts during the equivalence principle measurements (see figure 6.6) and relatively long time constants of the exponential functions compared to the turntable rotation period.

The Fourier components of the torque $\tilde{\tau}_s$ and $\tilde{\tau}_c$ were obtained without incorporating the pendulum or composition dipole orientation within the apparatus; however, this orientation determines the direction of any signal. To transform from the pendulum (or composition dipole) orientation (defined by equation 5.1) to the laboratory frame we used the following

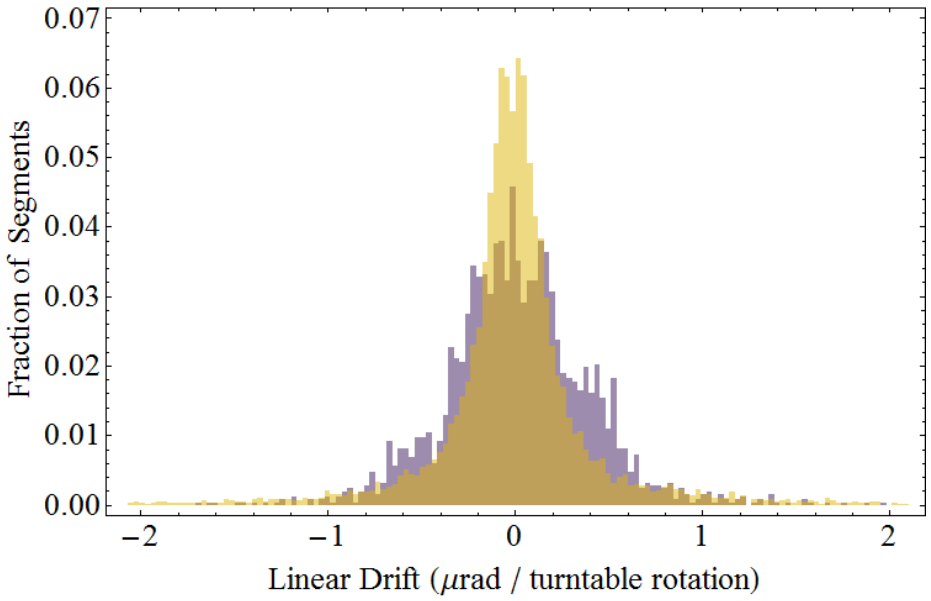

Figure 6.6: The fraction of segments with different rates of linear drift for the beryllium-aluminum pendulum (purple) and earth-moon pendulum (gold). Segments during transient pressure and tilt disturbances were excluded.

transformation:

$$\begin{pmatrix} \tilde{\tau}_{\mathrm{N}} \\ \tilde{\tau}_{\mathrm{W}} \end{pmatrix} = \begin{pmatrix} \cos\phi_{\mathrm{f}} & -\sin\phi_{\mathrm{f}} \\ \sin\phi_{\mathrm{f}} & \cos\phi_{\mathrm{f}} \end{pmatrix} \begin{pmatrix} \tilde{\tau}_{s} \\ \tilde{\tau}_{c} \end{pmatrix} \tag{6.12}$$

6.4 Differential Acceleration

The conversion from torque to differential acceleration of the test bodies using equation 3.4 and the symmetry of our pendulums ($\mathbf{r}_A = -\mathbf{r}_B$ and $m_A = m_B$) results[1] in

$$\Delta a = (n_{\mathrm{TB}} m s)^{-1} \tau_z = \tau_z \begin{cases} 2720 \text{ m s}^{-2} \text{ (N m)}^{-1} & \text{Eight Test-Body} \\ 2030 \text{ m s}^{-2} \text{ (N m)}^{-1} & \text{Earth-Moon} \end{cases} \tag{6.13}$$

where n_{TB} is the number of test bodies of each composition, m is the mass of each test body, and s is the horizontal displacement of each composition's center of mass from the

[1]For estimating the conversion between pendulum twist θ and differential acceleration using $\tau = \kappa\theta$, the conversion was 6.5 fm s^{-2} (nrad)$^{-1}$ for the eight-test-body pendulum and 4.9 fm s^{-2} (nrad)$^{-1}$ for the earth-moon pendulum. This simplified conversion does not include the pendulum's frequency response.

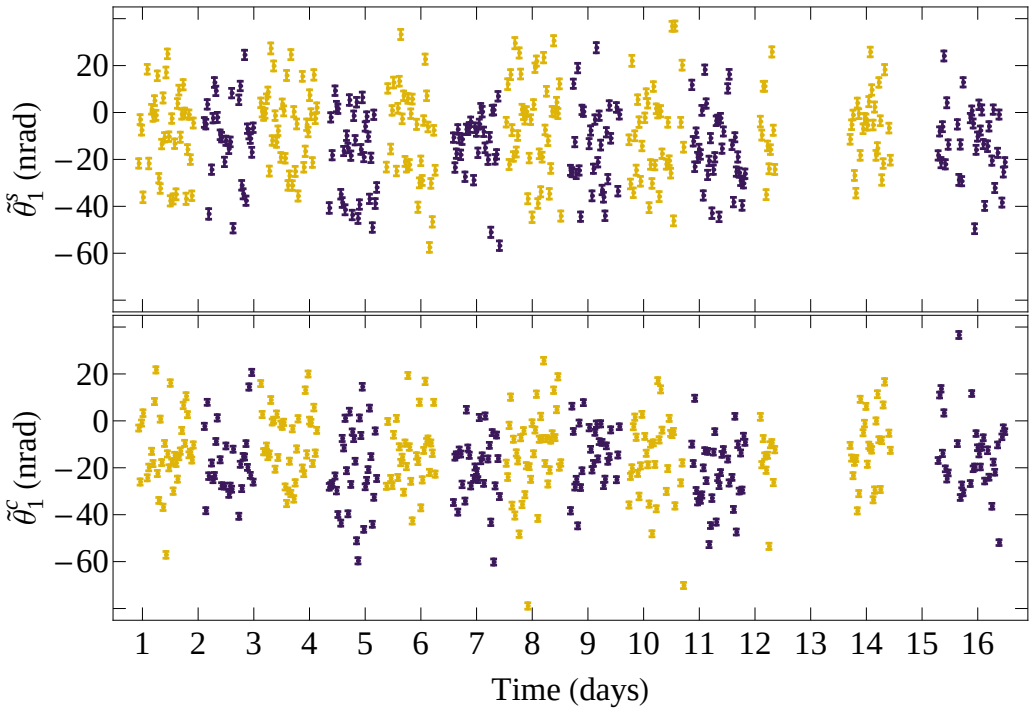

Figure 6.7: Fourier coefficients for $m = 1$ from fits to the segmented twist data during group Be-Al 3.

pendulum's vertical axis. In our pendulum design s is equal to the horizontal radius to each test body's center of mass divided by $\sqrt{2}$.

6.5 Segment Exclusions

Our apparatus's sensitivity to very weak torques required that we exclude data when tilt and pressure disturbances occurred. Temperature changes could also have required data exclusions, but in practice the temperature remained stable compared to the turntable rotation rate. We made efforts to minimize disturbances; however, 12% of the beryllium-aluminum data and 33% of the earth-moon data were excluded due to transient disturbances. The earth-moon pendulum experienced larger twist excursions than the eight-test-body pendulum from transient pressure events. We rebuilt the vacuum chamber to reduce the

frequency of transient pressure events during the earth-moon pendulum data collection: 46% of segments were excluded prior to improvements and only 12% after. Both pressure and tilt disturbances were typically transient events that occurred quickly compared to the turntable period. We identified specific segments where transient events occurred and excluded them from further analysis.

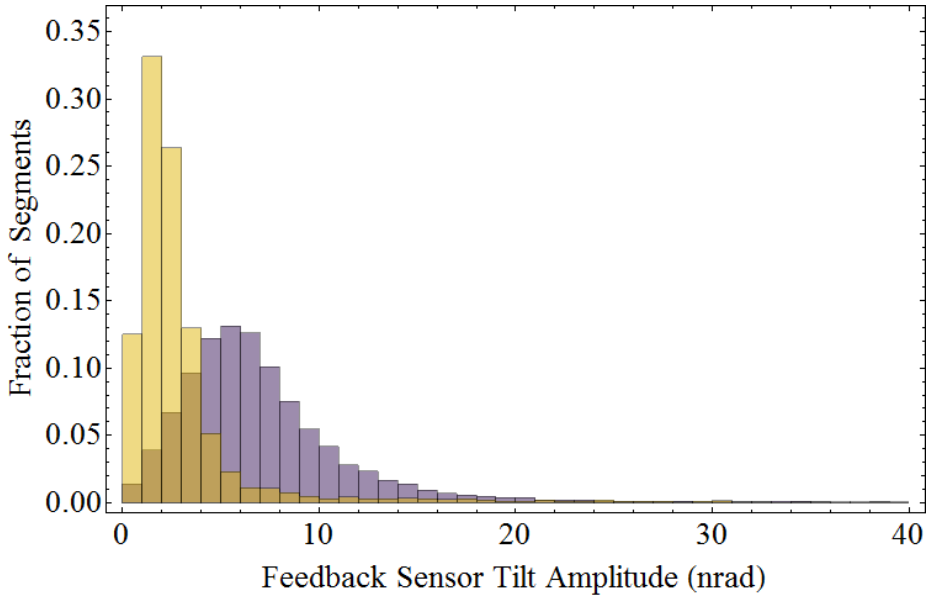

Figure 6.8: Improvements to the tilt leveling feedback loop reduced the residual tilt and tilt variance at the feedback sensor. Purple bars are from before feedback improvements during the beryllium-aluminum configuration. Gold bars are from after tilt feedback improvements during the aluminum-beryllium configuration. The earth-moon distribution is very similar to the aluminum-beryllium, even after the vacuum column changes.

We identified and excluded tilt disturbances using 2 criteria: First, the feedback sensors' tilt amplitudes were smaller than 12 nrad (31 nrad before feedback improvements) when the leveling feedback loop was effective. Between the collection of the beryllium-aluminum and aluminum-beryllium configuration data we improved the tilt feedback loop. Figure 6.8 shows how the improvements reduced the residual tilt at the feedback sensors. Second, the variance of the tilt sensor segment fits served as a proxy to detect transient events. Zero adjustments by the leveling feedback (see figure 6.12) and earthquakes (see the event shown in figure 6.13) were the most common transient tilt events. About 10% of beryllium-aluminum segments

and 13% of the earth-moon segments were excluded due to tilt disturbances. We estimated exclusion thresholds by examining the distribution of tilt sensor fit variances for all segments. During most segments there were not any transient events. Visual estimates using plots of the variance distribution, such as that in figure 6.9, agreed well with values determined by fitting the distribution using the extreme value distribution and solving for the maximum expected value based on the total number of segments [39]. The tilt disturbances were similar for all pendulum configurations, so we used the threshold value of 2×10^3 nrad^2 for all of the analysis.

Pressure disturbances, such as the burst shown in figure 6.11, were identified using pressure sensor segment fit variances following the same method used for tilt transient events. Figure 6.10 shows a correlation between the fit variance for the pressure sensor and twist for the earth-moon pendulum. We used a threshold value of 1.4 μPa^2 on the pressure sensor fit variance to exclude pressure disturbances. The pressure exclusion threshold value was selected to exclude fits that were likely to disturb the pendulum, while allowing fits that mostly fall within the typical distribution. The earth-moon pendulum was more sensitive to pressure disturbances than the eight-test-body pendulum. We rebuilt the vacuum chamber with fewer and redesigned seals to reduce pressure bursts during the earth-moon data collection to address the greater sensitivity.

6.6 Local Source Analysis

The equivalence-principle-violating torque $\tilde{\tau}_{\rm EP}$ makes up only part of the measured torque $\tilde{\tau}$ at the turntable rotation frequency $\omega_{\rm TT}$. The measured torque also includes systematic effects that may be apparatus-fixed $\tilde{\tau}_a$ or fixed to the pendulum frame and suspension $\tilde{\tau}_p$. For runs taken with the pendulum rotated by 180° with respect to the apparatus, $\tilde{\tau}_{\rm EP}$ (and $\tilde{\tau}_p$) follows the pendulum orientation and receives a sign change, but $\tilde{\tau}_a$ remains unchanged. Our data collection process alternated between orientations 1 and 3 or 2 and 4 for successive runs (as shown in figure 5.2). The difference between the two orientations removes $\tilde{\tau}_a$:

$$\begin{aligned} \tilde{\tau}_0 - \tilde{\tau}_{180} &= (\tilde{\tau}_{\rm EP} + \tilde{\tau}_a + \tilde{\tau}_p) - (-\tilde{\tau}_{\rm EP} + \tilde{\tau}_a - \tilde{\tau}_p) \\ &= 2\,(\tilde{\tau}_{\rm EP} + \tilde{\tau}_p) \end{aligned} \tag{6.14}$$

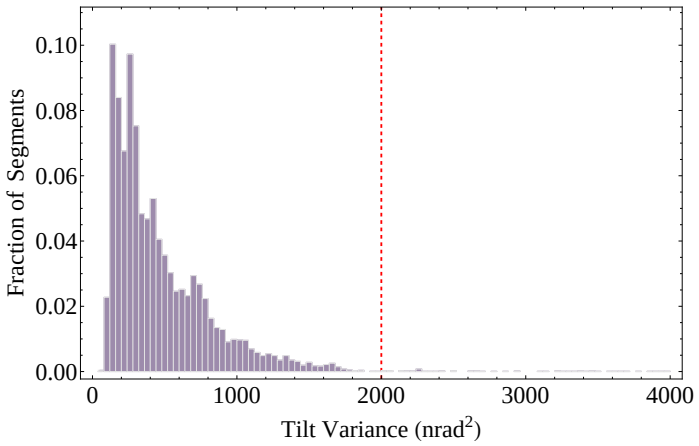

Figure 6.9: The distribution of feedback tilt sensor segment fit uncertainties during the beryllium-aluminum configuration. The histogram shows the fraction of segments for each fit uncertainty and the solid line shows the cut value above which we excluded data. The earth-moon pendulum distribution is similar.

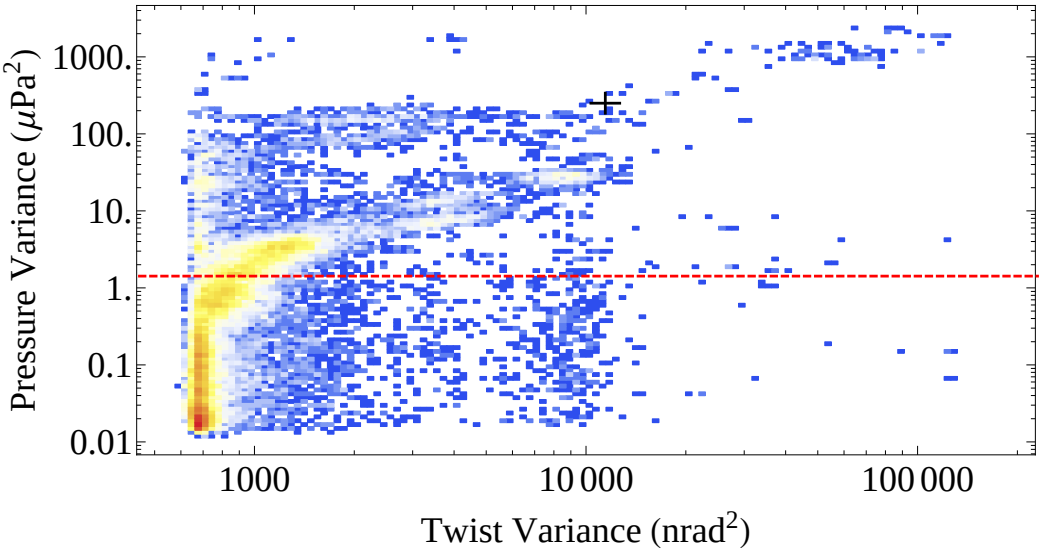

Figure 6.10: The twist fit variance and pressure fit variance were correlated when a pressure disturbance occurred. The plot shows the earth-moon pendulum fits using the original vacuum column. The red dashed line indicates our cut on pressure fit variance, which we determined using the data shown along with data taken using the redesigned column. The black cross shows the fit variance for the segment in figure 6.11.

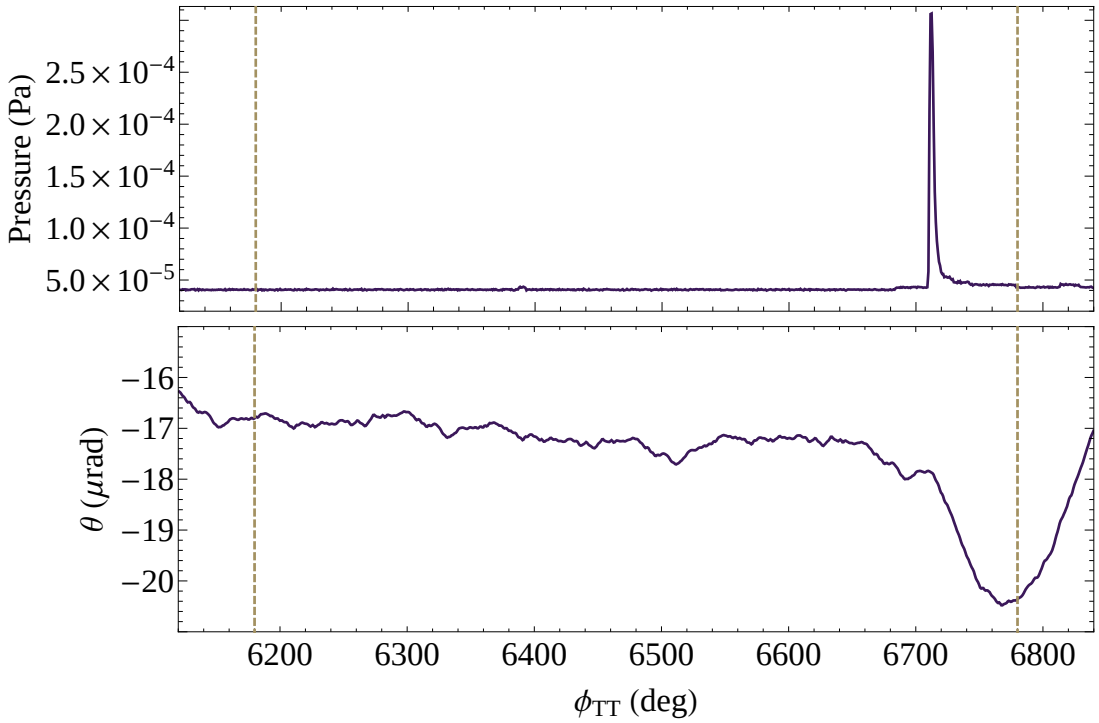

Figure 6.11: A pressure burst disturbed the pendulum. The vertical gold lines indicate the region of correlation with the adjacent segment due to the two-point filter. The pressure burst resulted in a pressure fit variance of 2.5×10^{-10} Pa^2. The corresponding pendulum twist excursion resulted in a twist fit variance of 1.1×10^4 nrad^2.

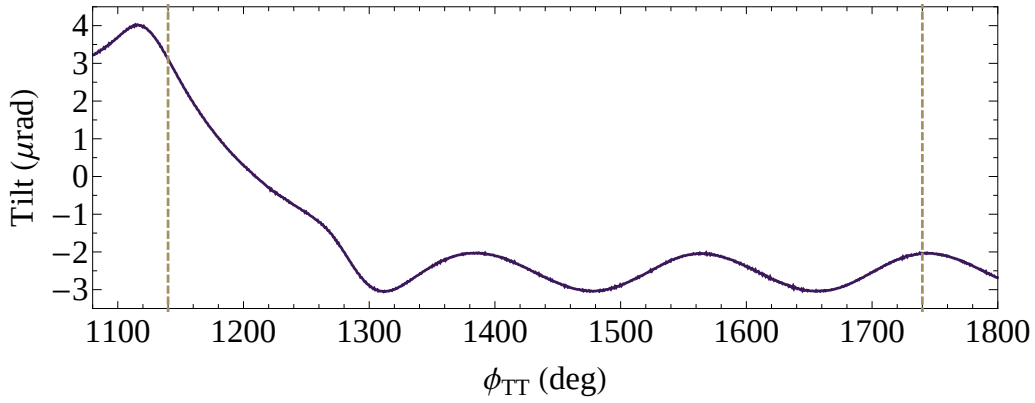

Figure 6.12: The tilt feedback loop adjusted its zero-point over a half turntable rotation. The level adjustment resulted in a tilt fit variance of 4.6×10^4 nrad^2. The vertical gold lines indicate the region of correlation with the adjacent segment due to the two-point filter.

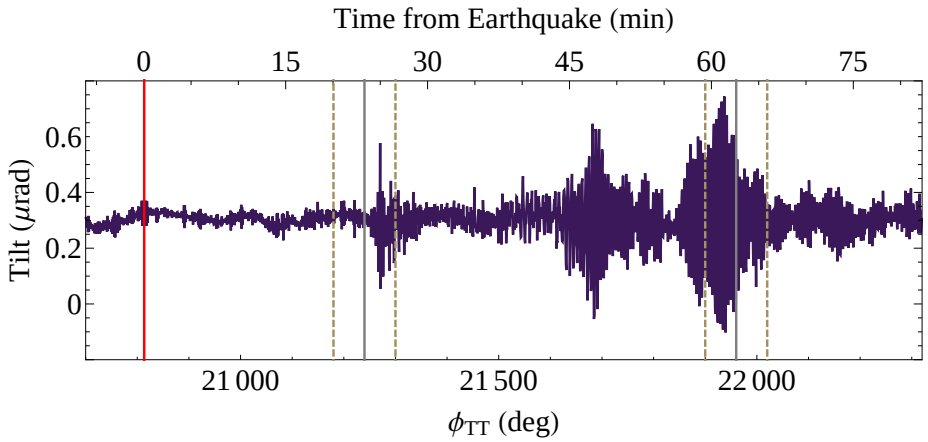

Figure 6.13: A magnitude 6.7 earthquake near Papua New Guinea (6° S, 151° E) on October 17, 2006 disrupted the apparatus as shown by a tilt sensor. The red vertical line indicates the time the earthquake occurred. The seismic waves began arriving at the apparatus about 25 minutes later. The gray vertical lines indicate segment boundaries. The dashed gold lines indicate the region of correlation between adjacent segments due to the two-point filter. The earthquake resulted in a tilt fit variance of 1.2×10^4 nrad^2.

Similarly, the two composition dipole orientations (beryllium-aluminum and aluminum-beryllium) change the sign of $\tilde{\tau}_{\mathrm{EP}}$ relative to $\tilde{\tau}_p$, so the difference between the two configurations removes systematic effects associated with the pendulum's suspension or frame.

We determined the lab-fixed torques from a weighted mean $\bar{\tau}$ and variance $\sigma^2(\tau)$ using weights w computed from the two-point-filter covariance U [34]:

$$w_i = \frac{\sum_{j=1}^{N} (U^{-1})_{ij}}{\sum_{k,\ell=1}^{N} (U^{-1})_{k\ell}} \tag{6.15}$$

$$\bar{\tau} = \sum_{i=1}^{N} w_i \tilde{\tau}_i \tag{6.16}$$

$$\sigma^2(\tau) = \sum_{i,j=1}^{N} w_i U_{ij} w_j \tag{6.17}$$

The weights w incorporated the correlation from the two-point-digital filter through the covariance matrix U (see appendix B) for the N segments of a run. The weighted average due to the two-point filter increased the variance by 4.4% from an equal-weight mean. The

variance of a run's segment fits was greater than expected from the individual segment fit uncertainties as figure 6.7 shows, so we used the variance of the segment fits in each run to determine the standard error for that run. The mean torques were rotated to a consistent orientation of the composition dipole using equation 6.12. Figure 6.14 shows the data points for runs within a data group from the beryllium-aluminum configuration. The difference in the horizontal lines gives $\tilde{\tau}_0 - \tilde{\tau}_{180}$. The inclusion of linear or quadratic drift terms common to both orientations could parametrize slow mechanical drifts, but inclusion of drift terms did not substantially affect the equivalence principle results. Table 6.4 includes the lab-fixed torques determined for each group during the beryllium-aluminum measurement along with the final equivalence-principle-violating torque from the difference between the two configurations.

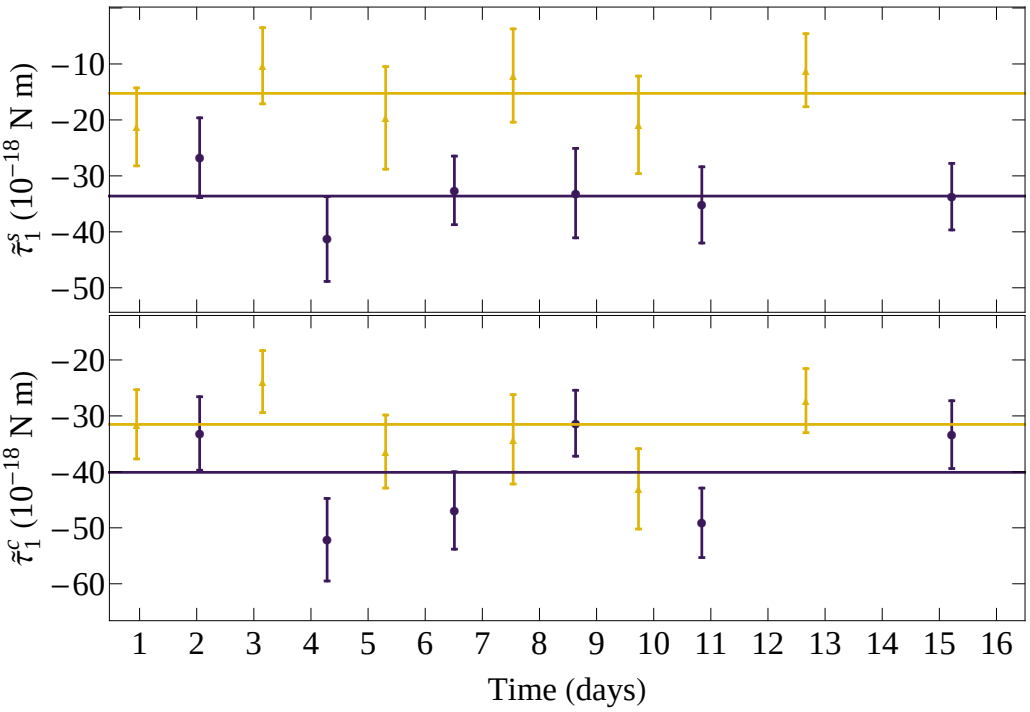

Figure 6.14: The offsets from the opposite pendulum orientations were fit to the data points resulting from the two week data collection group Be-Al 3. Any equivalence-principle-violating signal is in the difference of the offsets.

Table 6.4: The uncorrected lab-fixed torque Fourier components were determined for each eight-test-body pendulum data group. The uncertainties are 1-σ statistical.

Set	$\tilde{\tau}_N$ (10^{-18} N m)	$\tilde{\tau}_W$ (10^{-18} N m)
Be-Al 1	-10.4 $\pm$ 3.0	-0.8 $\pm$ 3.3
Be-Al 2	-2.7 $\pm$ 2.2	-0.9 $\pm$ 2.3
Be-Al 3	-9.2 $\pm$ 2.1	-4.3 $\pm$ 1.8
Be-Al 4	-10.8 $\pm$ 2.8	-3.4 $\pm$ 2.3
Be-Al 5	-5.2 $\pm$ 2.4	-6.2 $\pm$ 2.3
Be-Al 6	-2.9 $\pm$ 2.6	-1.3 $\pm$ 2.6
Be-Al Subtotal	-6.3 $\pm$ 1.0	-3.3 $\pm$ 1.0
Al-Be 1	-5.1 $\pm$ 1.7	-5.5 $\pm$ 1.4
Al-Be 2	2.0 $\pm$ 2.4	-5.4 $\pm$ 2.1
Al-Be 3	-4.5 $\pm$ 1.5	-4.9 $\pm$ 1.8
Al-Be 4	-2.8 $\pm$ 2.2	-6.6 $\pm$ 2.5
Al-Be Subtotal	-3.4 $\pm$ 0.9	-5.5 $\pm$ 0.9
Be-Al Total	-0.7 $\pm$ 0.7	1.7 $\pm$ 0.7

We corrected for tilt and gravity gradient systematic effects on the pendulum twist. Our data acquisition system recorded the output of tilt sensors along with the pendulum twist, so we individually corrected each segment based upon the measured tilt as described in section 7.2. We corrected each data group using the gravity gradient fields (measured with the gradiometer pendulum) and the measured equivalence principle pendulum gravity gradient moments (see section 7.1). The apparatus's insulation gave temperature effects time constants of many hours and active temperature control limited temperature variations as described in section 5.6. The effect of temperature changes were primarily slow drifts of the pendulum's equilibrium position, which we fit using a linear drift term for each segment. Temperature gradient effects exhibited a complex behavior that made corrections

impractical and no magnetic response was resolved, so temperature and magnetic systematic effects were each assigned an overall uncertainty for each data group without any correction.

6.7 Astronomical Source Analysis

An equivalence-principle-violating interaction between the test bodies and an astronomical source would produce a torque signal that follows the position of the source projected onto the horizontal pendulum plane. We fit the pendulum torque towards the sun, galactic center and cosmic microwave background (CMB) dipole direction projected onto the pendulum's horizontal plane to search for equivalence-principle violations related to ordinary matter, dark matter, and preferred frames, respectively. The local horizontal coordinates of each astronomical object were computed using the Naval Observatory Vector Astrometry Software (NOVAS) library [69] or the Solar Position Algorithm (SPA) [104]. Each source was assumed to be the only source of equivalence-principle violation in the fitting process. We estimated tilt and temperature systematic uncertainties by fitting each sensor to the source modulation. For magnetic and gravity gradients, which were not continuously measured, we estimated the systematic uncertainty based on the daily modulation of the source. We assumed the dominant modulation of systematic effects would occur due to human and environmental effects that vary over a solar day.

We wrote an interface to the NOVAS and SPA libraries for Mathematica [140] that accepted planetary body designations or equatorial coordinates and returned the zenith and azimuthal direction toward the specified body at our apparatus's location. The NOVAS library provides accurate solar system coordinate transformations. It also interprets planetary ephemeris data and stellar catalogs to determine the position of any astronomical object. Solar system objects, including the sun, were included through the use of the DE421 ephemeris from the Jet Propulsion Laboratory [53]. The directions to the galactic center [12] and the CMB dipole [65] were transformed from equatorial coordinates to the pendulum's local coordinates using the NOVAS library. The SPA library exclusively provides the sun's position. We verified that the sun's position using our interface to the SPA [104] and NOVAS libraries agreed. The SPA has a stated uncertainty of $\pm 0.0003^\circ$ in the azimuth and zenith angles [104]. NOVAS produced values with estimated computational uncertainties of

$\lesssim 1$ μas [69]. The DE 421 ephemeris technical document estimates sub-kilometer accuracy for earth's orbit [53].

The position $\mathbf{r}_{ast}$ in the laboratory horizontal reference frame of an astronomical object with an azimuth ξ (measured east from north), a zenith angle ζ, a radial orbital variation from circular δr, and an average orbital distance of $\bar{r}$ is

$$\frac{\mathbf{r}_{ast}(t)}{\bar{r}} = \left(1 + \frac{\delta r(t)}{\bar{r}}\right) \sin\left(\zeta(t)\right) \left(\cos\left(\xi(t)\right) \widehat{\mathbf{N}} - \sin\left(\xi(t)\right) \widehat{\mathbf{W}}\right), \tag{6.18}$$

where $\widehat{\mathbf{N}}$ and $\widehat{\mathbf{W}}$ are unit vectors in the local north and west directions. For objects outside our solar system, the ratio $\delta r/\bar{r}$ is effectively zero and was not included in our fits towards the CMB or galactic center. The fit toward astronomical objects included parameters a and b for the pendulum orientation, c for a signal and d quadrature term from the projection of the object's position onto the local horizontal plane, and independent offsets o_s and o_c for each data group.

$$\begin{aligned}\tilde{\tau}^{\mathrm{s}}_{\ell m} = {} & a \sin\left(\phi_{\mathrm{f}}\right) + b \cos\left(\phi_{\mathrm{f}}\right) \\ & + \left[1 + \frac{\delta r(t)}{\bar{r}}\right] \sin\left[\zeta(t)\right] \left\{c \cos\left[m\left(\pm\phi_{\mathrm{f}} - \xi\right)\right] + d \sin\left[m\left(\pm\phi_{\mathrm{f}} - \xi\right)\right]\right\} \\ & + \sum_j o_{s,j} \Theta\left(t - t_j\right)\end{aligned} \tag{6.19}$$

$$\begin{aligned}\tilde{\tau}^{\mathrm{c}}_{\ell m} = {} & a \cos\left(\phi_{\mathrm{f}}\right) - b \sin\left(\phi_{\mathrm{f}}\right) \\ & + \left[1 + \frac{\delta r(t)}{\bar{r}}\right] \sin\left[\zeta(t)\right] \left\{c \sin\left[m\left(\pm\phi_{\mathrm{f}} - \xi\right)\right] - d \cos\left[m\left(\pm\phi_{\mathrm{f}} - \xi\right)\right]\right\} \\ & + \sum_j o_{c,j} \Theta\left(t - t_j\right)\end{aligned} \tag{6.20}$$

The "+ ϕ_{f}" and "- ϕ_{f}" in the c and d parameter terms correspond to the two orientations of the composition dipole with respect to the pendulum frame. The unit step function $\Theta(x)$ controlled the times that the various offsets for different data groups applied.

6.8 Auxiliary Analysis

During our investigation of ion-pump pressure spike effects on the earth-moon pendulum, we found that non-linear drifts in the pendulum twist signal affected the fit Fourier coefficients depending on the segmentation choice. We re-performed our statistical analysis using 10

Table 6.5: The equivalence-principle-violating signal and quadrature for each astrophysical source. Uncertainties are 1-σ statistical. No systematic corrections have been applied.

Source	$\tilde{\tau}_{\rm sig}$ (10^{-18} N m)	$\tilde{\tau}_{\rm quad}$ (10^{-18} N m)
Be-Al Sun	-1.44 $\pm$ 0.82	0.01 $\pm$ 0.82
Be-Al Galaxy	-0.84 $\pm$ 0.91	-1.10 $\pm$ 0.91
Be-Al CMB	1.23 $\pm$ 0.81	-0.62 $\pm$ 0.81
EM Sun	1.02 $\pm$ 0.95	0.78 $\pm$ 0.95

random starting angles for the turntable angle from the interval [0, 1440] with segmentation proceeding from that angle each 720°. To reduce the impact of different data being excluded by our sensor cuts, we required that a continuous group of segments covered a multiple of 720° and a minimum of 1440°. Angles greater than 720° removed the first segment from each run. Comparing fits with a starting angle in the interval [0, 720] to those with a starting angle in the interval [720, 1440] provides a gauge for the statistical effect of different segments being included compared to the effect of the non-linear drifts on the twist signal. Figure 6.15 shows the results for the beryllium-aluminum pendulum local analysis and figure 6.16 for the earth-moon pendulum sun analysis. We conclude that the statistical effect is small compared to the estimated error, but that efforts to reduce the drift in torsion balance experiments would likely improve the measurements.

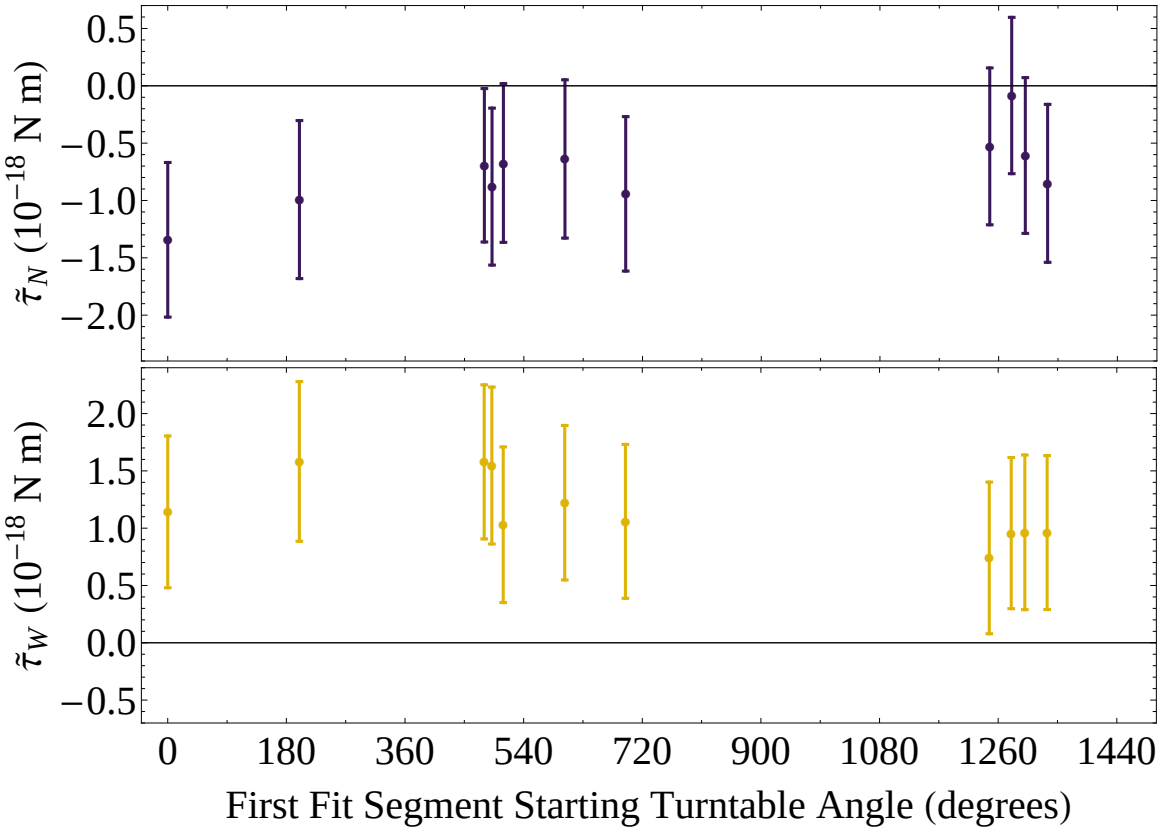

Figure 6.15: Lab-fixed analysis for beryllium and aluminum test bodies performed for 10 random starting segment angles plus 0°.

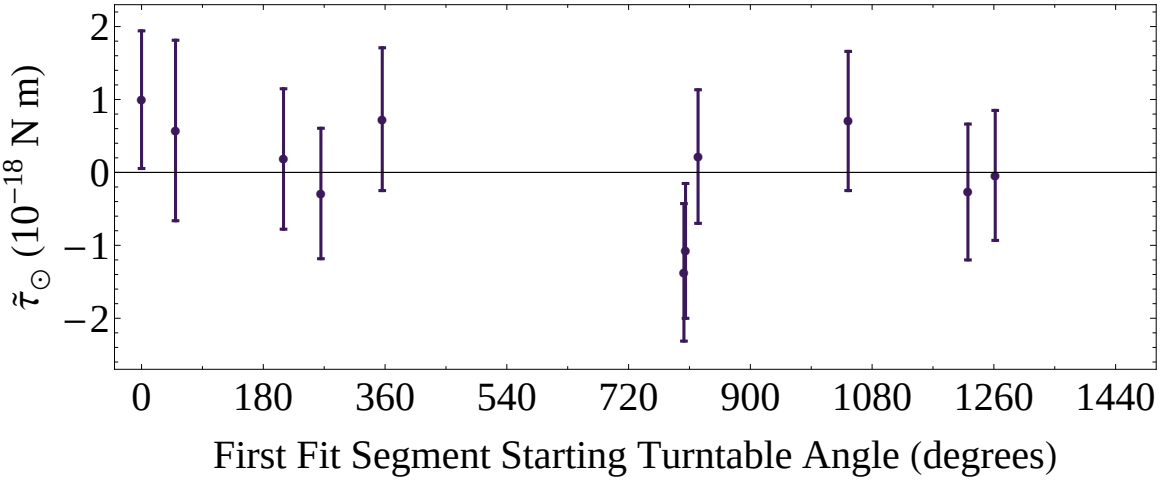

Figure 6.16: Analysis towards the sun for the earth-moon pendulum performed for 10 random starting segment angles plus 0°.

Chapter 7

SYSTEMATIC EFFECTS

Systematic uncertainties arise from the apparatus's interaction with the environment and produced observed effects on our apparatus due to temperature, tilts, gravity gradients, and magnetic fields. We attempted to both reduce the impact of systematic effects through passive shielding or active environmental control and to characterize each effect by exaggerating its source. For gravity gradients and tilts the systematic measurements matched our models, so we applied a correction to the equivalence principle measurements. Thermal and magnetic effects were both attenuated with passive layers of shielding, and any magnetic effect was unresolved. In addition to characterizing specific systematic effects, the test bodies were interchanged on the pendulum frame for eight-test-body pendulum data. The test body exchange removed time-independent systematic effects associated with the pendulum frame or suspension. Changing the pendulum orientation within the apparatus performed a similar function in removing systematic effects related to the apparatus's orientation. Tables 7.1, 7.2, and 7.3 present the lab-fixed and astronomical systematic effects for the different pendulums.

7.1 Gravity Gradients

An uniform gravitational force acts equally on all the pendulum test bodies such that no twist occurs, but gravity gradients produce forces on the different test bodies that act in different directions. We analyzed the torques on the pendulums using the multipole formalism described in section 3.2. Ambient gravity gradients produce a twist of the pendulum modulated at integer multiples of the rotation frequency, with the first harmonic (due to $m = 1$ moments) occurring at the same frequency as an equivalence-principle-violating signal. We designed each equivalence principle pendulum to minimize its sensitivity to gravity gradients (see section 5.1), but imperfections in constructing and suspending the pendulums

Table 7.1: 1-σ systematic corrections and uncertainties for the lab-fixed measurements with the eight test-body pendulum configured with the beryllium-titanium composition dipole. Gravity gradient couplings and tilt were corrected. Temperature gradients and magnetic systematics were not corrected.

	Beryllium - Titanium	
Systematic Effect	$\Delta a_N (10^{-15}\,\mathrm{m\,s^{-2}})$	$\Delta a_W (10^{-15}\,\mathrm{m\,s^{-2}})$
Gravity gradients	1.6 ± 0.2	0.3 ± 1.7
Tilt	1.2 ± 0.6	-0.2 ± 0.7
Magnetic	0 ± 0.3	0 ± 0.3
Temperature gradients	0 ± 1.7	0 ± 1.7
Total systematic	1.8 ± 1.8	0.1 ± 2.5

Table 7.2: 1-σ systematic corrections and uncertainties for the lab-fixed measurements with the eight test-body pendulum configured with the beryllium-aluminum composition dipole. Gravity gradient couplings and tilt were corrected. Temperature gradients and magnetic systematics were not corrected.

	Beryllium - Aluminum	
Systematic Effect	$\Delta a_N (10^{-15}\,\mathrm{m\,s^{-2}})$	$\Delta a_W (10^{-15}\,\mathrm{m\,s^{-2}})$
Gravity gradients	0.04 ± 0.27	0.25 ± 0.67
Tilt	-0.36 ± 0.10	-1.71 ± 0.15
Magnetic	0 ± 0.20	0 ± 0.20
Temperature gradients	0 ± 0.59	0 ± 0.58
Total systematic	-0.32 ± 0.69	-1.46 ± 0.92

Table 7.3: 1-σ systematic uncertainties for the astronomical source measurements. Tilt was corrected on the individual segments. Gravity gradient, temperature gradient, and magnetic systematic effects were not corrected. The improvements to the temperature and tilt systematic uncertainties for the earth-moon pendulum was from increased insulation, active temperature control for the enclosure, and improved tilt feedback.

	Beryllium - Aluminum			Earth - Moon
Systematic Effect	$\Delta a_{\odot}$ (10^{-15} m s^{-2})	Δa_{gal} (10^{-15} m s^{-2})	Δa_{CMB} (10^{-15} m s^{-2})	$\Delta a_{\odot}$ (10^{-15} m s^{-2})
Gravity gradients	0.04	0.08	0.04	0.12
Tilt	0.17	0.19	0.17	0.09
Magnetic	9×10^{-5}	9×10^{-5}	9×10^{-5}	2×10^{-4}
Temperature gradients	1.42	1.54	1.36	0.33
Total systematic	1.43	1.56	1.37	0.36

within the apparatus produced small gravity gradient moments. The leading q_{21} moment was reduced using the tuning screws each time the pendulum was installed in the apparatus (see section 5.1). We measured the environmental gravity gradient fields using the gradiometer pendulum configured with a large specific moment (q_{21}, q_{31}, or q_{41}). Compensating masses near the apparatus reduced the Q_{21}, Q_{22}, and Q_{31} fields at the pendulum's location. A $\approx$1% seasonal variation limited our ability to fully compensate for the environmental gravity gradients. As we only measured the gravity gradient fields periodically, we increased the systematic uncertainty of our gravity gradient field measurements to include the seasonal changes to the environmental gravity gradients during our equivalence principle measurements. We subtracted corrections (see table 7.4) from our laboratory-fixed results for residual gravity gradients based on our measurements of the environmental fields and the pendulums' moments. We did not resolve a significant daily signal in the gravity gradient fields, so we estimated the gravity gradient systematic uncertainty for astronomical sources (see table 7.5) based on the 68.3% confidence level limit on the maximum daily variation of the gravity gradient fields and did not apply any correction.

Table 7.4: The laboratory-frame gravity-gradient torque corrections for the Be-Al and Al-Be configurations of the eight test body pendulum.

Set	21-Torque (10^{-19} Nm)		31-Torque (10^{-19} Nm)	
	τ_1^S	τ_1^C	τ_1^S	τ_1^C
Be-Al	1.0 ± 1.7	2.4 ± 2.6	-0.21 ± 0.36	0.5 ± 2.7
Al-Be	1.08 ± 0.32	5.49 ± 0.45	-0.23 ± 0.50	-1.6 ± 1.5

7.1.1 Gravity gradient analysis

We measured the twist due to gravity gradient coupling between a pendulum and the ambient gradient fields by taking many measurements, each with the gravity gradient compensators rotated to a different azimuthal angle $\alpha_{\ell m}$. All the measurements were fit to a circle (based on equation 3.20) with a radius proportional to the pendulum moment coupling with the compensator field $\left|Q_{\ell m}^{\mathrm{comp}}\right| |q_{\ell m}|$ and a center proportional to the pendulum moment coupling with the environmental field (excluding the compensator) $|Q_{\ell m}^{\mathrm{env}}| \, |q_{\ell m}|$:

$$\tilde{\tau}_{\ell m}^{\mathrm{s}} = a \sin\left(m\phi_{\mathrm{f}}\right) + b \cos\left(m\phi_{\mathrm{f}}\right) - c \sin\left[m\left(\alpha_{\ell m} - \phi_{\mathrm{f}}\right)\right] + d \cos\left[m\left(\alpha_{\ell m} - \phi_{\mathrm{f}}\right)\right] + o_s \tag{7.1}$$

$$\tilde{\tau}_{\ell m}^{\mathrm{c}} = a \cos\left(m\phi_{\mathrm{f}}\right) - b \sin\left(m\phi_{\mathrm{f}}\right) + c \cos\left[m\left(\alpha_{\ell m} - \phi_{\mathrm{f}}\right)\right] + d \sin\left[m\left(\alpha_{\ell m} - \phi_{\mathrm{f}}\right)\right] + o_c \tag{7.2}$$

$$a = 8\pi G \frac{m}{2\ell + 1} \left[\mathrm{Re}\left(Q_{\ell m}^{\mathrm{env}}\right) \mathrm{Im}\left(q_{\ell m}\right) + \mathrm{Im}\left(Q_{\ell m}^{\mathrm{env}}\right) \mathrm{Re}\left(q_{\ell m}\right)\right] \tag{7.3}$$

$$b = 8\pi G \frac{m}{2\ell + 1} \left[\mathrm{Re}\left(Q_{\ell m}^{\mathrm{env}}\right) \mathrm{Re}\left(q_{\ell m}\right) - \mathrm{Im}\left(Q_{\ell m}^{\mathrm{env}}\right) \mathrm{Im}\left(q_{\ell m}\right)\right] \tag{7.4}$$

$$c = 8\pi G \frac{m}{2\ell + 1} \left[\mathrm{Re}\left(Q_{\ell m}^{\mathrm{comp}}\right) \mathrm{Im}\left(q_{\ell m}\right) + \mathrm{Im}\left(Q_{\ell m}^{\mathrm{comp}}\right) \mathrm{Re}\left(q_{\ell m}\right)\right] \tag{7.5}$$

$$d = 8\pi G \frac{m}{2\ell + 1} \left[\mathrm{Re}\left(Q_{\ell m}^{\mathrm{comp}}\right) \mathrm{Re}\left(q_{\ell m}\right) - \mathrm{Im}\left(Q_{\ell m}^{\mathrm{comp}}\right) \mathrm{Im}\left(q_{\ell m}\right)\right] \tag{7.6}$$

The fixed offsets o_s and o_c were incorporated to account for the turntable offset. The two Fourier coefficients $\tilde{\tau}_{\ell m}^{\mathrm{s}}$ and $\tilde{\tau}_{\ell m}^{\mathrm{c}}$ were fit simultaneously, since the fit parameters a, b, c, and d are the same for both. Ideally, the fit circle would pass through the origin, which indicates that the compensator exactly cancels the environmental gradient field for that compensator

Table 7.5: The astronomical-source gravity-gradient torque systematic uncertainties based on gravity gradient daily variation. We used a 68.3% confidence limit on the daily gravity gradient torque because we did not resolve a daily gravity gradient signal.

Measurement	Multipole (ℓ, m)	Torque (10^{-20} N m)	68.3% CL Limit on Torque (10^{-20} N m)
Be-Al	(2, 1)	0.28 ± 0.18	0.37
Al-Be	(2, 1)	0.29 ± 0.18	0.38
EM Dec 2007	(2, 1)	4.5 ± 2.7	5.8
EM Feb 2008	(2, 1)	4.5 ± 2.7	5.8
EM Apr 2008	(2, 1)	4.7 ± 2.8	6.0
EM May 2008	(2, 1)	4.9 ± 3.0	6.3
EM Jul 2008	(2, 1)	5.9 ± 3.6	7.6
EM Oct 2008	(2, 1)	5.7 ± 3.5	7.4
EM Nov 2008	(2, 1)	5.7 ± 3.5	7.4
EM Feb 2010	(2, 1)	2.0 ± 1.3	2.6
EM May 2010	(2, 1)	1.7 ± 1.0	2.2
EM Aug 2010	(2, 1)	1.4 ± 0.88	1.8
EM Sep 2010	(2, 1)	1.8 ± 1.1	2.3
Be-Al	(3, 1)	1.19 ± 0.92	1.6
Al-Be	(3, 1)	1.19 ± 0.92	1.6
EM Jan 2008	(3, 1)	4.6 ± 3.6	6.3
EM May 2008	(3, 1)	4.5 ± 3.5	6.2
EM May 2008	(3, 1)	4.6 ± 3.6	6.3
EM Aug 2010	(3, 1)	4.4 ± 3.4	6.0

orientation. Figures 7.1 and 7.4 show fits using the the q_{21} and q_{31} gradiometer pendulum configurations, respectively.

Our model included only four independent fit parameters (plus an offset for each component), while the environmental and compensator fields and the pendulum moment had a total of six components. We calculated the compensator gravity gradient field using measurements taken during its construction, which provided a fixed reference common to all our measurements and allowed us to extract the pendulum moments and environmental gravity gradient field from the fit parameters:

$$\begin{aligned} q_{\ell m} = \frac{1}{8\pi G}\frac{2\ell+1}{m}\Bigg[& \frac{\left(c\,\mathrm{Im}\left(Q^{\mathrm{comp}}_{\ell m}\right) + d\,\mathrm{Re}\left(Q^{\mathrm{comp}}_{\ell m}\right)\right)}{\left|Q^{\mathrm{comp}}_{\ell m}\right|^2} \\ & + i\frac{\left(c\,\mathrm{Re}\left(Q^{\mathrm{comp}}_{\ell m}\right) - d\,\mathrm{Im}\left(Q^{\mathrm{comp}}_{\ell m}\right)\right)}{\left|Q^{\mathrm{comp}}_{\ell m}\right|^2}\Bigg] \end{aligned} \tag{7.7}$$

$$\begin{aligned} Q^{\mathrm{env}}_{\ell m} = & \frac{(bc-ad)\,\mathrm{Im}\left(Q^{\mathrm{comp}}_{\ell m}\right) + (ac+bd)\,\mathrm{Re}\left(Q^{\mathrm{comp}}_{\ell m}\right)}{c^2+d^2} \\ & + i\frac{(ac+bd)\,\mathrm{Im}\left(Q^{\mathrm{comp}}_{\ell m}\right) + (ad-bc)\,\mathrm{Re}\left(Q^{\mathrm{comp}}_{\ell m}\right)}{c^2+d^2} \end{aligned} \tag{7.8}$$

Fits using the gradiometer pendulum determined the environmental gravity gradient fields and fits using the equivalence principle pendulums determined the pendulum moments. The sum of the compensator field for $\alpha_{\ell m} = 0^\circ$ and the environmental field gives the residual field $Q_{\ell m}$ used for corrections.

We corrected the equivalence principle data using the predicted signal due to the measured equivalence principle pendulum moment and the corresponding residual field according to equation 3.20. Note that while the compensator field enters these equations, the final result does not depend on the value of the compensator so long as the *same* value was used in all the calculations. In essence, the gradiometer pendulum measures the residual signal compared to the compensator and the equivalence principle pendulum correction is the gradiometer ratio times the signal due to the compensator for the equivalence principle pendulum.

7.1.2 Gravity gradient field measurements

The gravity gradient fields were measured with the gradiometer pendulum configured for a large q_{21}, q_{31} or q_{41} moment. The Q_{41} field was measured only once and shown to be negligible, while the Q_{21} and Q_{31} were measured at the beginning and end of each equivalence principle pendulum configuration. Limits on the daily variation of the gravity gradient fields were estimated with gradiometer pendulum measurements over about a week each for the Q_{21} and Q_{31}.

The gradiometer pendulum q_{21} was sufficiently large ($\sim$900 μrad) that the full signal produced by rotating the compensator to the 180° position was larger than the dynamic range of the readout. The compensator was moved to angles of $\leqslant 15°$ from the fully compensated position, which produced signals that remained on the detector. Figure 7.1 shows a fit using the q_{21} gradiometer configuration with the Q_{21} compensator at 5 different angles. Data points for each mirror fall on an individual circle rotated by the mirror angle. For clarity in the plot, the data points were rotated to the 0° pendulum orientation, so that all data points have the same position relative to the circle.

We measure the environmental Q_{21} to a few parts per thousand. However, we observe seasonal variations of $\sim$1% due to changes in the moisture content of the soil behind our laboratory and the Army Core of Engineers' adjustments to the water level in Lake Washington. The seasonal changes limit our ability to fully compensate and correct for gravity gradients. Figure 7.2 shows seasonal changes in the Q_{21} field (the values are listed in table 7.6).

The Q_{31} configuration of the Q_{21} compensator masses (see section 5.10) was used to measure the equivalence principle pendulum q_{31} moment. Figure 7.4 compares gradiometer pendulum measurements using the Q_{31} compensator and using the Q_{21} compensator arranged to produce a large Q_{31} field. The Q_{31} compensator measurement found the gradiometer pendulum q_{31} moment to be 105.73 ± 0.34 g cm^3, in agreement with the value determined using the Q_{21} compensators in the Q_{31} configuration of 106.01 ± 0.07 g cm^3. For comparison, our model calculation was 104.92 g cm^3. Our measurements of the Q_{31} are listed in table 7.6.

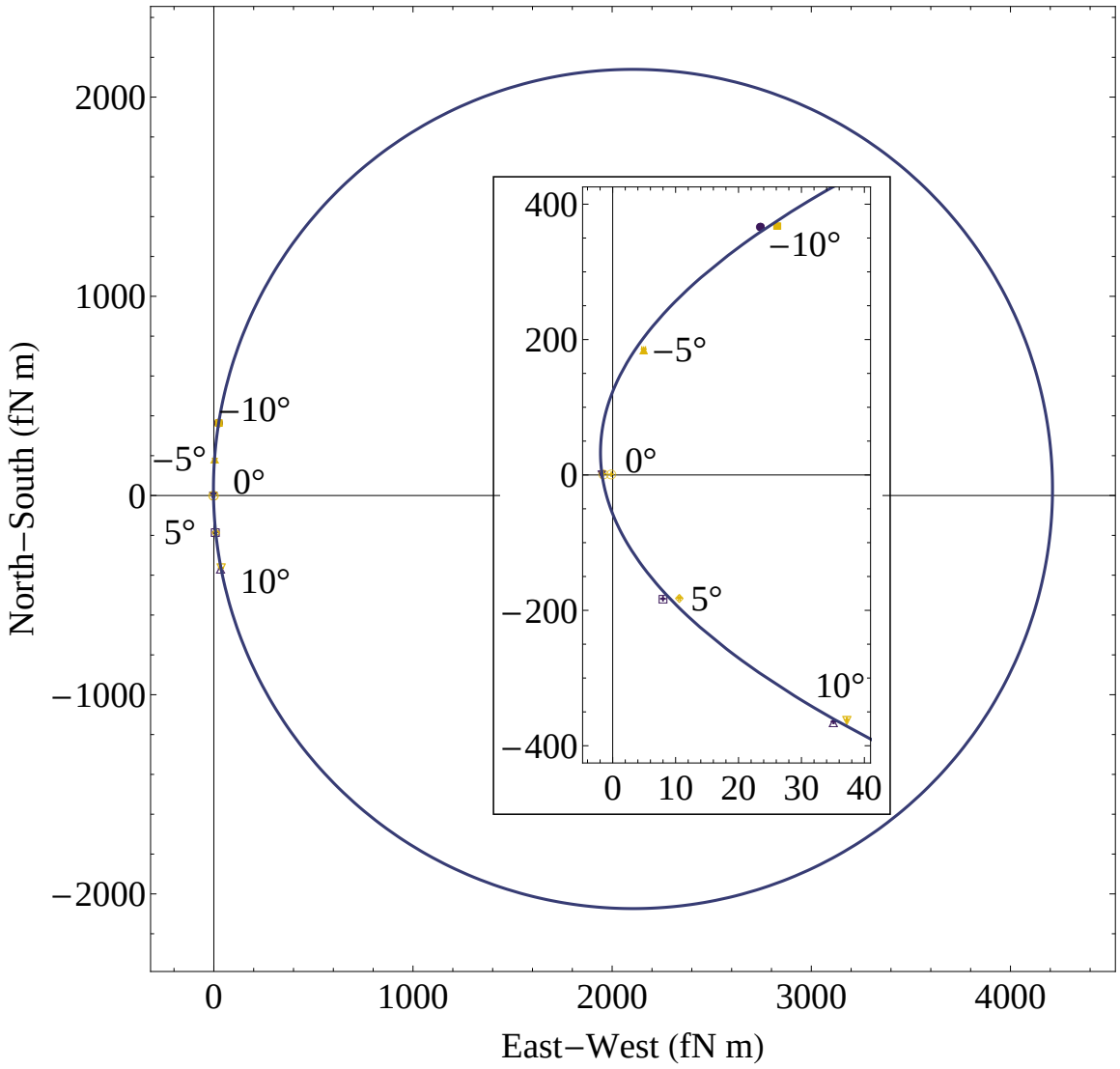

Figure 7.1: A typical measurement of the Q_{21} moment of the ambient gravity gradient. The torque on the gradiometer pendulum was measured for all four pendulum orientations. The measurements for each pendulum orientation lie on a circle (with the data points for each orientation rotated to the 0° pendulum orientation). The Q_{21} compensator was positioned at 5 different angles. The center of the circle determines Q_{21}^{env} and the radius $|Q_{21}^{\mathrm{comp}}|$.

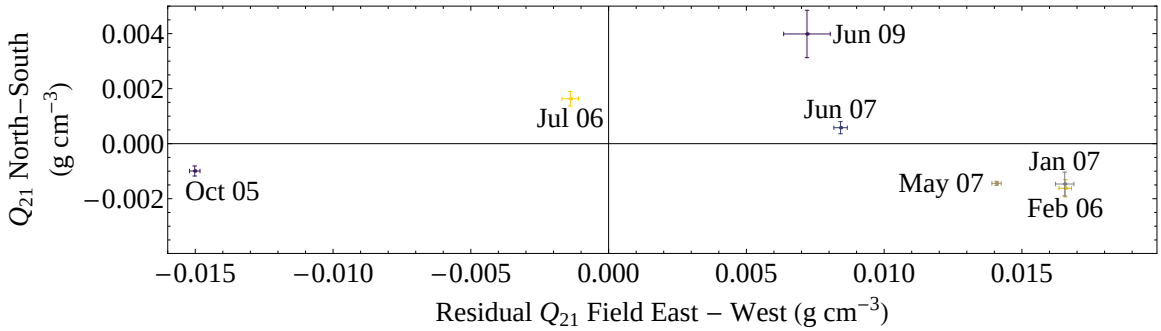

Figure 7.2: The Q_{21} moment of the environmental gravity gradient field varies due to seasonal changes of water levels. The residual environmental Q_{21} field is shown for measurements taken with the gradiometer pendulum in the q_{21} configuration.

To determine the daily variation of the gravity gradient fields, we recorded data with the gradiometer pendulum over a longer time frame in each of the q_{21} and q_{31} configurations. We collected data in the q_{21} gradiometer configuration for about 5 days each in May and June 2007, and we used the q_{31} configuration for about 10 days between the two q_{21} measurements. We fit a daily signal to the Fourier components for the turntable rotation rate (see section 6.7). The daily variation of $|Q_{21}|$ was $(8.0 \pm 4.9) \times 10^{-5}$ g cm^{-3} in May and $(2.5 \pm 5.9) \times 10^{-5}$ g cm^{-3} in June. The daily variation of $|Q_{31}|$ was $(1.2 \pm 1.0) \times 10^{-6}$ g cm^{-4}. We used 68.3% confidence level limits on the magnitude of the daily variation to estimate the systematic uncertainty for astronomical sources because the measurement do not show a significant daily variation.

7.1.3 Equivalence principle pendulum moments

The equivalence principle pendulum moments were designed to be zero, but mounting and machining tolerances resulted in small moments. We adjusted each equivalence principle pendulum's q_{21} moment with tuning screws near the top and bottom of the pendulum (see figures 5.3 and 5.4) each time we installed an equivalence principle pendulum. The tuning screws allowed adjustments of the q_{21} by $\lesssim 0.1$ g cm^2 using copper set screws in the bottom holes for coarse tuning. Fine tuning was performed with titanium set screws, which allowed us to reduce the $|q_{21}| \leqslant 2 \times 10^{-3}$ g cm^2 (about 1/10th of a screw turn). Reducing the

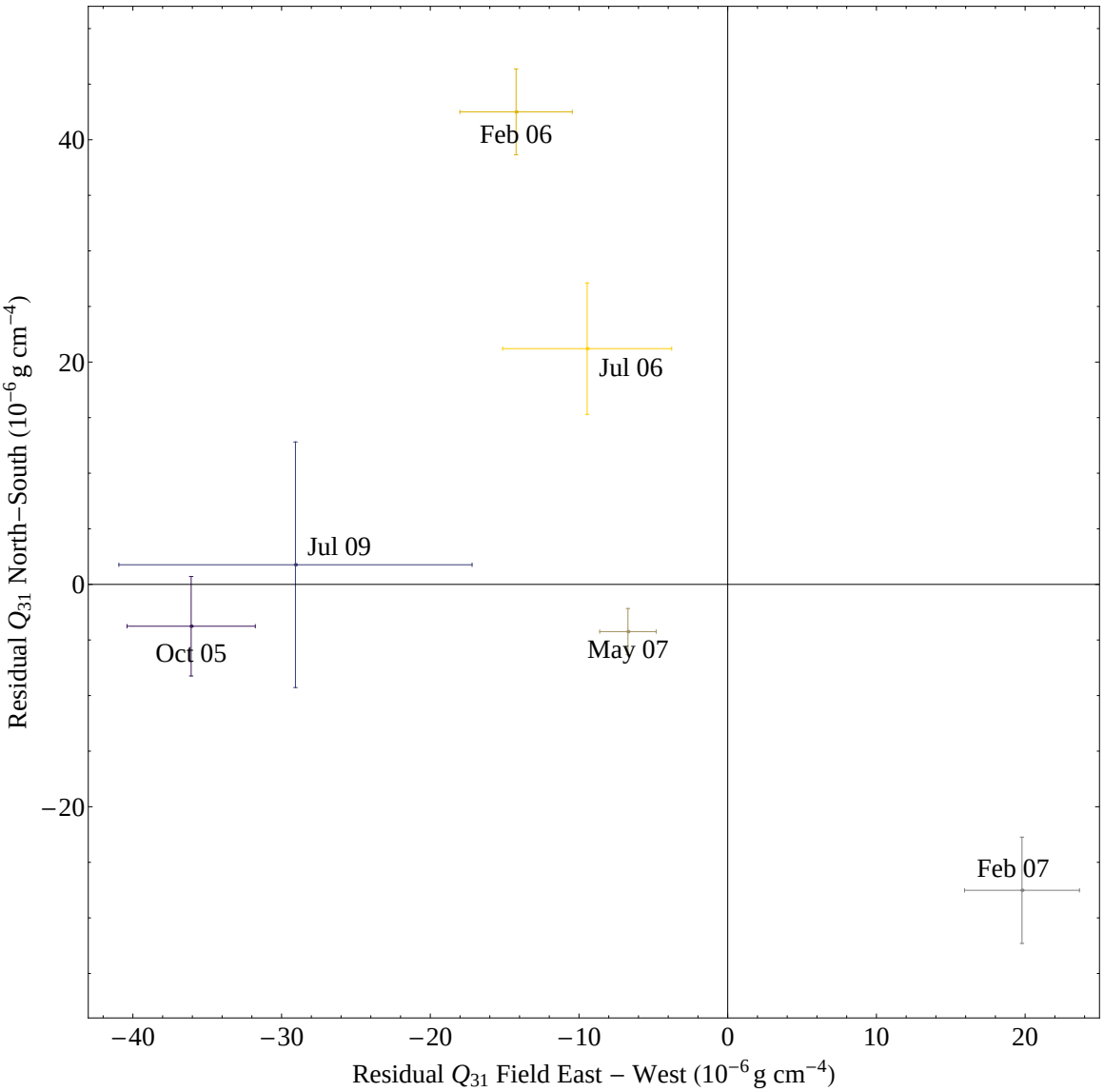

Figure 7.3: The Q_{31} moment of the environmental gravity gradient field varies due to seasonal changes of water levels. The residual environmental Q_{31} field is shown for measurements taken with the gradiometer pendulum in the q_{31} configuration.

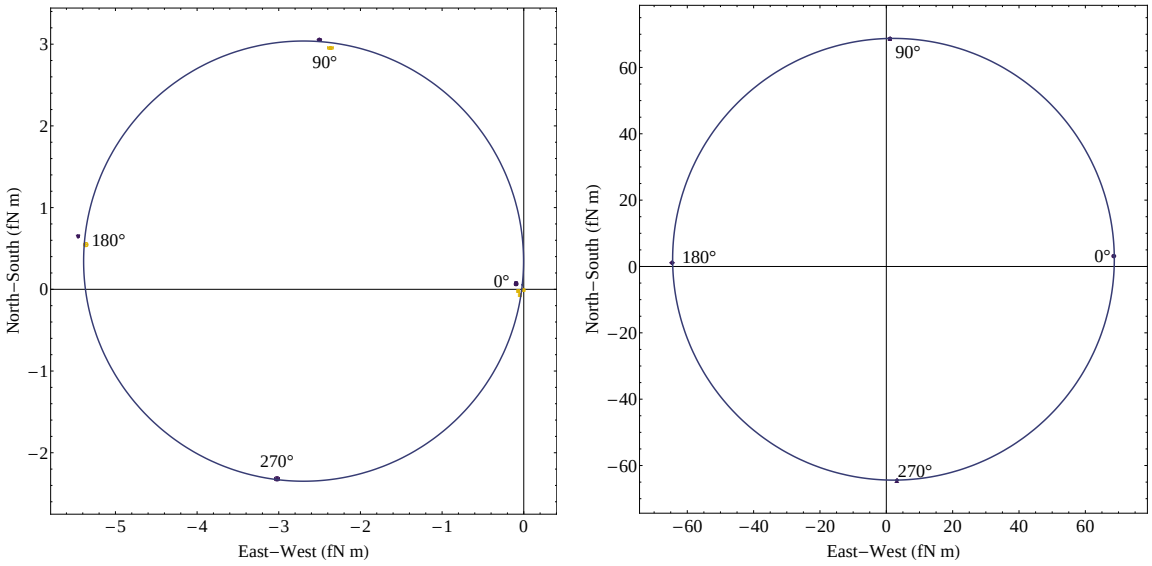

(a) Q_{31} compensator

(b) Q_{31} by Q_{21} compensator

Figure 7.4: A typical measurement of the Q_{31} moment of the environmental gravity gradient using the Q_{31} compensator (left panel) and the Q_{21} compensator in a Q_{31} configuration (right panel). The torque on the gradiometer pendulum was measured for all four pendulum orientations. The measurements for each pendulum orientation lie on a circle (with the data points for each orientation rotated to the 0° orientation for clarity). The center of the circle determines $Q_{31}^{\rm env}$ and the radius $|Q_{31}^{\rm comp}|$. For the measurement with the Q_{21} compensator, the Q_{31} compensator was in the maximally compensating position.

q_{21} moment was an iterative process: Based on the measured moment, the screws were moved and the procedure repeated. One iteration required 3-5 days, since we baked the vacuum system for a full day each time to achieve reliable results. Typically 3 iterations were required to reduce the q_{21} moment to an acceptable level. After minimizing the q_{21} moment, we made final measurements of the q_{21} and q_{31} moments, which we repeated after data collection. Tables 7.7 and 7.8 list the q_{21} and q_{31} moments for the eight-test-body and earth-moon pendulums, respectively.

Table 7.6: The Q_{21}, Q_{31}, and Q_{41} moments of the environmental field were each measured with the gradiometer pendulum. The Q_{21} and Q_{31} were measured before and after each data set, while the Q_{41} was measured only once and shown to be negligible.

Date	$(\ell,\ m)$	$\mathrm{Re}\,(Q_{\ell m})$	$\mathrm{Im}\,(Q_{\ell m})$	Units
Oct 2005	(2, 1)	$(-9.9 \pm 1.8) \times 10^{-4}$	$-1.72283 \pm (1.9 \times 10^{-4})$	g cm^{-3}
Feb 2006	(2, 1)	$(-16.0 \pm 3.3) \times 10^{-4}$	$-1.75448 \pm (2.3 \times 10^{-4})$	g cm^{-3}
Jul 2006	(2, 1)	$(16.4 \pm 2.8) \times 10^{-4}$	$-1.73638 \pm (3.2 \times 10^{-4})$	g cm^{-3}
Jan 2007	(2, 1)	$(-14.6 \pm 4.3) \times 10^{-4}$	$-1.75440 \pm (3.3 \times 10^{-4})$	g cm^{-3}
May 2007	(2, 1)	$(-14.4 \pm 0.7) \times 10^{-4}$	$-1.75193 \pm (1.7 \times 10^{-4})$	g cm^{-3}
Jun 2007	(2, 1)	$(5.9 \pm 1.9) \times 10^{-4}$	$-1.74623 \pm (2.1 \times 10^{-4})$	g cm^{-3}
Jun 2009	(2, 1)	$(39.9 \pm 8.6) \times 10^{-4}$	$-1.74505 \pm (8.5 \times 10^{-4})$	g cm^{-3}
Oct 2005	(3, 1)	$(-3.7 \pm 4.5) \times 10^{-6}$	$(1099.3 \pm 4.3) \times 10^{-6}$	g cm^{-4}
Feb 2006	(3, 1)	$(42.5 \pm 3.9) \times 10^{-6}$	$(1077.41 \pm 3.8) \times 10^{-6}$	g cm^{-4}
Jul 2006	(3, 1)	$(21.2 \pm 5.9) \times 10^{-6}$	$(1072.63 \pm 5.7) \times 10^{-6}$	g cm^{-4}
Feb 2007	(3, 1)	$(-27.5 \pm 4.8) \times 10^{-6}$	$(1043.39 \pm 3.9) \times 10^{-6}$	g cm^{-4}
May 2007	(3, 1)	$(-4.2 \pm 2.1) \times 10^{-6}$	$(1069.89 \pm 1.9) \times 10^{-6}$	g cm^{-4}
Feb 2007	(4, 1)	$(-1.8 \pm 1.4) \times 10^{-4}$	$(-5.4 \pm 1.5) \times 10^{-4}$	g cm^{-5}

Table 7.7: The measured values of the eight-test-body pendulum's moments.

Composition Dipole	Date	Multipole $(\ell,\ m)$	$\mathrm{Re}\,(q_{\ell m})$	$\mathrm{Im}\,(q_{\ell m})$
Be-Al	Aug 2006	(2, 1) g cm^2	$(-9.0 \pm 2.1) \times 10^{-4}$	$(3.9 \pm 2.1) \times 10^{-4}$
Be-Al	Dec 2006	(2, 1) g cm^2	$(-9.2 \pm 1.4) \times 10^{-4}$	$(3.8 \pm 1.6) \times 10^{-4}$
Al-Be	Feb 2007	(2, 1) g cm^2	$(10.8 \pm 0.9) \times 10^{-4}$	$(-1.1 \pm 0.8) \times 10^{-4}$
Al-Be	May 2007	(2, 1) g cm^2	$(7.4 \pm 2.1) \times 10^{-4}$	$(-1.2 \pm 1.6) \times 10^{-4}$
Be-Al	Aug 2006	(3, 1) g cm^3	$(-24.2 \pm 2.3) \times 10^{-2}$	$(-31.8 \pm 2.1) \times 10^{-2}$
Be-Al	Dec 2006	(3, 1) g cm^3	$(-23.8 \pm 0.5) \times 10^{-2}$	$(-35.4 \pm 0.5) \times 10^{-2}$
Al-Be	Mar 2007	(3, 1) g cm^3	$(-19.5 \pm 1.7) \times 10^{-2}$	$(-32.7 \pm 1.3) \times 10^{-2}$
Al-Be	May 2007	(3, 1) g cm^3	$(-20.3 \pm 1.5) \times 10^{-2}$	$(-30.7 \pm 1.5) \times 10^{-2}$
Al-Be	May 2008	(4, 4)† g cm^4	980 ± 40	—

† The magnitude of the q_{44} is shown including 5% uncertainty on the Q_{44} model, which corresponds to $\approx$3 mm in the radial placement of the blocks.

Table 7.8: The measured values of the q_{21} and q_{31} moments of the earth-moon pendulum.

Composition Dipole	Date	Multipole $(\ell,\ m)$	$\mathrm{Re}\,(q_{\ell m})$	$\mathrm{Im}\,(q_{\ell m})$	Units
Earth-Moon	Dec 2007	(2, 1)	$(-65.9 \pm 2.0) \times 10^{-4}$	$(-152.4 \pm 1.8) \times 10^{-4}$	g cm^2
Earth-Moon	Feb 2008	(2, 1)	$(-68.5 \pm 1.2) \times 10^{-4}$	$(-153.2 \pm 0.8) \times 10^{-4}$	g cm^2
Earth-Moon	Apr 2008	(2, 1)	$(-70.8 \pm 2.7) \times 10^{-4}$	$(-158.3 \pm 2.7) \times 10^{-4}$	g cm^2
Earth-Moon	May 2008[†]	(2, 1)	$(-50.9 \pm 4.3) \times 10^{-4}$	$(-174.1 \pm 3.9) \times 10^{-4}$	g cm^2
Earth-Moon	May 2008	(2, 1)	$(-55.5 \pm 2.4) \times 10^{-4}$	$(-173.4 \pm 3.1) \times 10^{-4}$	g cm^2
Earth-Moon	Jul 2008	(2, 1)	$(-42.7 \pm 1.3) \times 10^{-4}$	$(-213.6 \pm 1.2) \times 10^{-4}$	g cm^2
Earth-Moon	Oct 2008	(2, 1)	$(-42.7 \pm 6.7) \times 10^{-4}$	$(-207.0 \pm 5.9) \times 10^{-4}$	g cm^2
Earth-Moon	Nov 2008	(2, 1)	$(-31.2 \pm 1.0) \times 10^{-4}$	$(-211.2 \pm 0.9) \times 10^{-4}$	g cm^2
Earth-Moon	Sep 2009	(2, 1)	$(-24 \pm 15) \times 10^{-4}$	$(22 \pm 19) \times 10^{-4}$	g cm^2
Earth-Moon	Feb 2010	(2, 1)	$(-27.3 \pm 9.9) \times 10^{-4}$	$(68 \pm 14) \times 10^{-4}$	g cm^2
Earth-Moon	May 2010	(2, 1)	$(-30.5 \pm 1.7) \times 10^{-4}$	$(53.6 \pm 1.4) \times 10^{-4}$	g cm^2
Earth-Moon	Aug 2010	(2, 1)	$(-30.4 \pm 2.2) \times 10^{-4}$	$(43.9 \pm 2.0) \times 10^{-4}$	g cm^2
Earth-Moon	Sep 2010	(2, 1)	$(-50.2 \pm 6.9) \times 10^{-4}$	$(46.8 \pm 7.4) \times 10^{-4}$	g cm^2
Earth-Moon	Jan 2008	(2, 2)	$(310.3 \pm 1.6) \times 10^{-4}$	$(-262.6 \pm 1.1) \times 10^{-2}$	g cm^2
Earth-Moon	Jan 2008	(3, 1)	$(1.30 \pm 1.7) \times 10^{-2}$	$(-83.2 \pm 2.1) \times 10^{-2}$	g cm^3
Earth-Moon	May 2008	(3, 1)	$(1.29 \pm 0.8) \times 10^{-2}$	$(-81.4 \pm 1.4) \times 10^{-2}$	g cm^3
Earth-Moon	May 2008	(3, 1)	$(1.29 \pm 3.4) \times 10^{-2}$	$(-85.1 \pm 3.5) \times 10^{-2}$	g cm^3
Earth-Moon	Feb 2010[‡]	(3, 1)	$(4.2 \pm 1.8) \times 10^{0}$	$(-3.8 \pm 2.2) \times 10^{0}$	g cm^3
Earth-Moon	Aug 2010[‡]	(3, 1)	$(14.0 \pm 2.9) \times 10^{-1}$	$(-5.8 \pm 3.0) \times 10^{-1}$	g cm^3
Earth-Moon	Aug 2010	(3, 1)	$(-120.1 \pm 2.3) \times 10^{-2}$	$(87.3 \pm 2.9) \times 10^{-2}$	g cm^3

[†] This measurement was taken with the turntable follower for the electrical feed-through wound one complete revolution.

[‡] This measurement used the Q_{31} compensator.

7.2 Tilt Feed-through

Tilts produce a signal at the turntable rotation frequency by changing the stress on the fiber and the relative position of the pendulum and apparatus as the turntable rotates. For example, a tilt will induce a twist for a fiber that is not perfectly round. The optical readout design was insensitive to tilts and translations, but imperfections may create a systematic signal at the frequency of interest. Our measurements of the tilt systematic effect showed the twist was proportional to the tilt and depended on the pendulum orientation. We corrected our equivalence principle results for the tilt systematic signal based on the measured tilt.

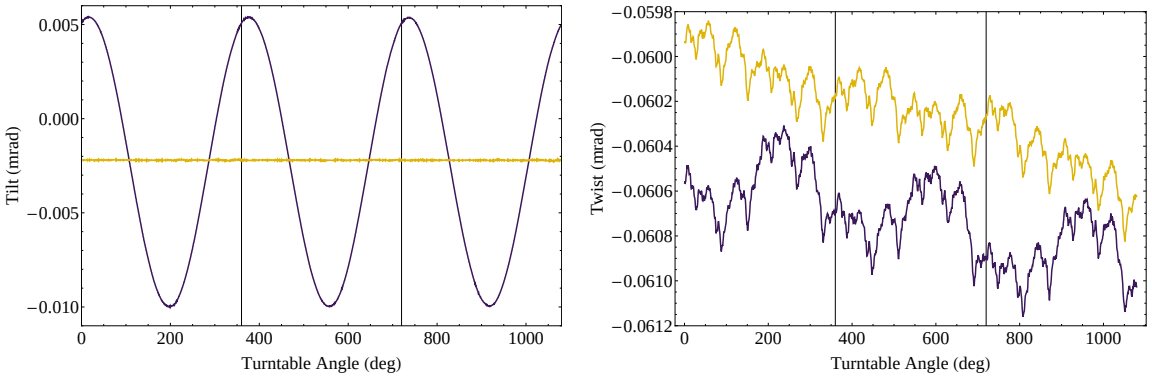

(a) Tilt signal

(b) Pendulum twist

Figure 7.5: The left frame (a) compares the tilt with the leveling loop off (purple) and on (gold) for three rotations of the turntable. The right frame (b) shows the corresponding pendulum twist. The pendulum mode has been removed using a 2-point digital filter.

The tilt sensors have sensitivity to temperature, which we estimate to be small compared to the measurement uncertainty. The tilt sensor manufacturer specifies a temperature related scale factor adjustment with $\kappa_{TC} = -0.25\%/\text{ K}$:

$$\gamma(V,T) = \frac{kV}{1+\kappa_{TC}(T-T_{cal})} \tag{7.9}$$

where γ is the tilt, k is the calibration from voltage to tilt, and T and T_{cal} are the current and calibration temperature respectively. The temperature change at the tilt sensors over the course of a data set is $\lesssim$ 200 mK, which corresponds to a -0.05% change in the scale factor. For a typical signal of 60 nrad this is 0.03 nrad, which is much less than the statistical

uncertainty of ∼1 nrad for a run. Temperature gradient induced thermal expansion within the apparatus produces larger effects.

To measure the tilt sensitivity, we measured the differences in tilt and twist between runs with the tilt feedback enabled and disabled. The tilt is usually ∼10 μrad with the feedback off. Figure 7.5 shows three turntable rotations from two runs used to determine the twist induced by a tilt. The tilt induced systematic twist signal is typically $\lesssim 5\%$ of the tilt. The Fourier coefficients for the pendulum twist and tilt sensor were treated as vectors to calculate a transformation matrix U for each mirror that gives the linear twist response θ for the measured tilt γ:

$$\theta_i = U_{ij}\gamma_j \tag{7.10}$$

$$U = \frac{1}{|\Delta\gamma|}\begin{pmatrix} \Delta\theta_s\Delta\gamma_s + \Delta\theta_c\Delta\gamma_c & \Delta\theta_c\Delta\gamma_s - \Delta\theta_s\Delta\gamma_c \\ -(\Delta\theta_c\Delta\gamma_s - \Delta\theta_s\Delta\gamma_c) & \Delta\theta_s\Delta\gamma_s + \Delta\theta_c\Delta\gamma_c \end{pmatrix} \tag{7.11}$$

For the equivalence principle data, we subtracted the value of θ_i due to the measured tilt γ_j in each segment. Figure 7.6 compares the in-phase $U_{11} = U_{22}$ and quadrature $U_{12} = -U_{21}$ terms of the tilt matrices for the eight-test-body and earth-moon pendulums. The change in the two earth-moon pendulum measurements was due to a new fiber and rebuild of the vacuum system. Each fiber has a unique response to tilts.

We computed the tilt systematic error by propagating the segment twist corrections through our data analysis process. The tilt systematic correction and error for each data group are collected in table 7.9. We imposed a cut on equivalence principle data when the fit variance for the feedback tilt sensors exceeded 2×10^{-9} mrad^2 or any feedback tilt sensor amplitude exceeded 12 nrad (31 nrad prior to tilt feedback improvements). The cut value corresponds to the modeled tilt matching the measured tilt with an uncertainty of 3 nrad per turntable rotation.

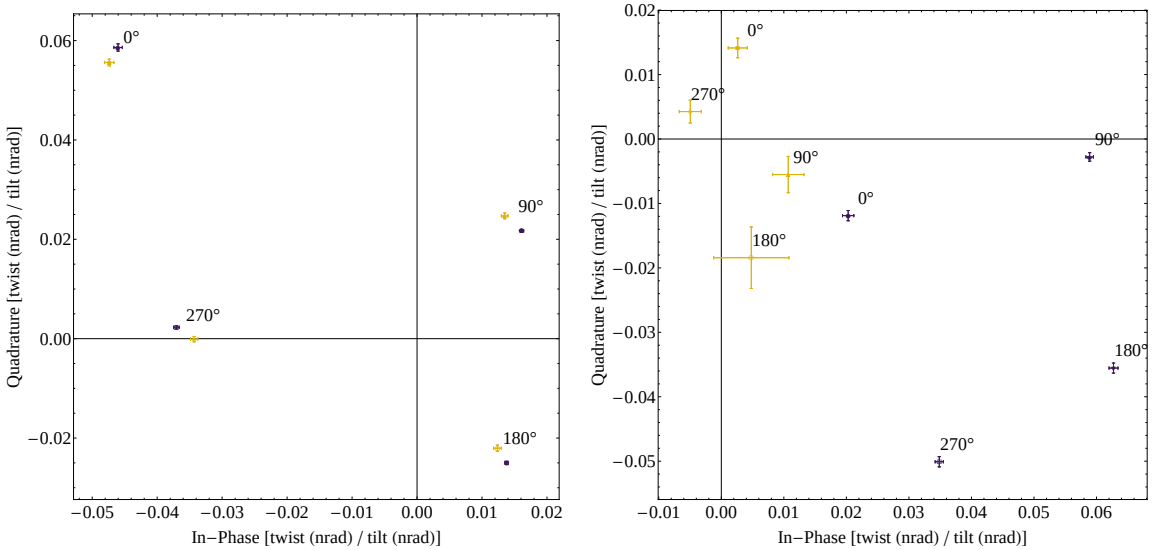

(a) Eight-test-body tilt response

(b) Earth-moon tilt response

Figure 7.6: The left frame (a) compares the tilt-feed-through for the Be-Al (purple) and Al-Be (gold) composition dipoles. The similar tilt matrices illustrate that the pendulum reproducibly attached to the fiber and exchanging the test bodies had a small impact the tilt-feed-through. The right frame (b) compares the tilt-feed-through for the earth-moon pendulum with old column (purple) and new column (gold). The substantial change was due to a major apparatus rebuild (see text).

Table 7.9: The local analysis tilt systematic correction and uncertainty from each data collection group using beryllium and aluminum test bodies.

Set	$\tilde{\tau}_N$ (10^{-18} N m)	$\tilde{\tau}_W$ (10^{-18} N m)
Be-Al 1	-1.7 $\pm$ 0.04	-3.2 $\pm$ 0.04
Be-Al 2	-2.4 $\pm$ 0.03	-3.0 $\pm$ 0.03
Be-Al 3	-2.8 $\pm$ 0.05	-6.5 $\pm$ 0.06
Be-Al 4	-4.5 $\pm$ 0.07	-7.4 $\pm$ 0.09
Be-Al 5	-2.9 $\pm$ 0.06	-6.5 $\pm$ 0.07
Be-Al 6	-2.5 $\pm$ 0.04	-3.0 $\pm$ 0.04
Be-Al Subtotal	-2.8 $\pm$ 0.05	-5.4 $\pm$ 0.06
Al-Be 1	-2.5 $\pm$ 0.04	-6.7 $\pm$ 0.06
Al-Be 2	-2.6 $\pm$ 0.06	-6.7 $\pm$ 0.08
Al-Be 3	-2.2 $\pm$ 0.03	-3.3 $\pm$ 0.03
Al-Be 4	-2.1 $\pm$ 0.05	-3.4 $\pm$ 0.05
Al-Be Subtotal	-2.3 $\pm$ 0.03	-5.3 $\pm$ 0.05

Table 7.10: The astronomical-source tilt systematic uncertainty for beryllium-aluminum and earth-moon pendulums. The extra daily modulation of an astronomical source resulted in statistically unresolved tilt corrections, so we report only the 1-σ systematic uncertainties.

Set	$\tilde{\tau}_\odot$ (10^{-20} N m)	$\tilde{\tau}_g$ (10^{-20} N m)	$\tilde{\tau}_{\mathrm{CMB}}$ (10^{-20} N m)
Be-Al 1	4.9	5.6	5.0
Be-Al 2	3.6	4.1	3.6
Be-Al 3	6.2	6.9	6.1
Be-Al 4	12.6	13.4	12.0
Be-Al 5	8.2	8.6	7.6
Be-Al 6	5.1	5.3	4.7
Al-Be 1	6.1	6.9	6.1
Al-Be 2	9.5	10.6	9.3
Al-Be 3	3.7	4.1	3.7
Al-Be 4	5.6	6.3	5.6
Be-Al Total	6.3	7.0	6.2
EM 1	7.4	—	—
EM 2	23.5	—	—
EM 3	34.2	—	—
EM 4	22.7	—	—
EM 5	7.3	—	—
EM 6	4.8	—	—
EM 7	7.9	—	—
EM 8	23.3	—	—
EM 9	4.1	—	—
EM 10	1.4	—	—
EM 11	4.3	—	—
EM Total	12.0	—	—

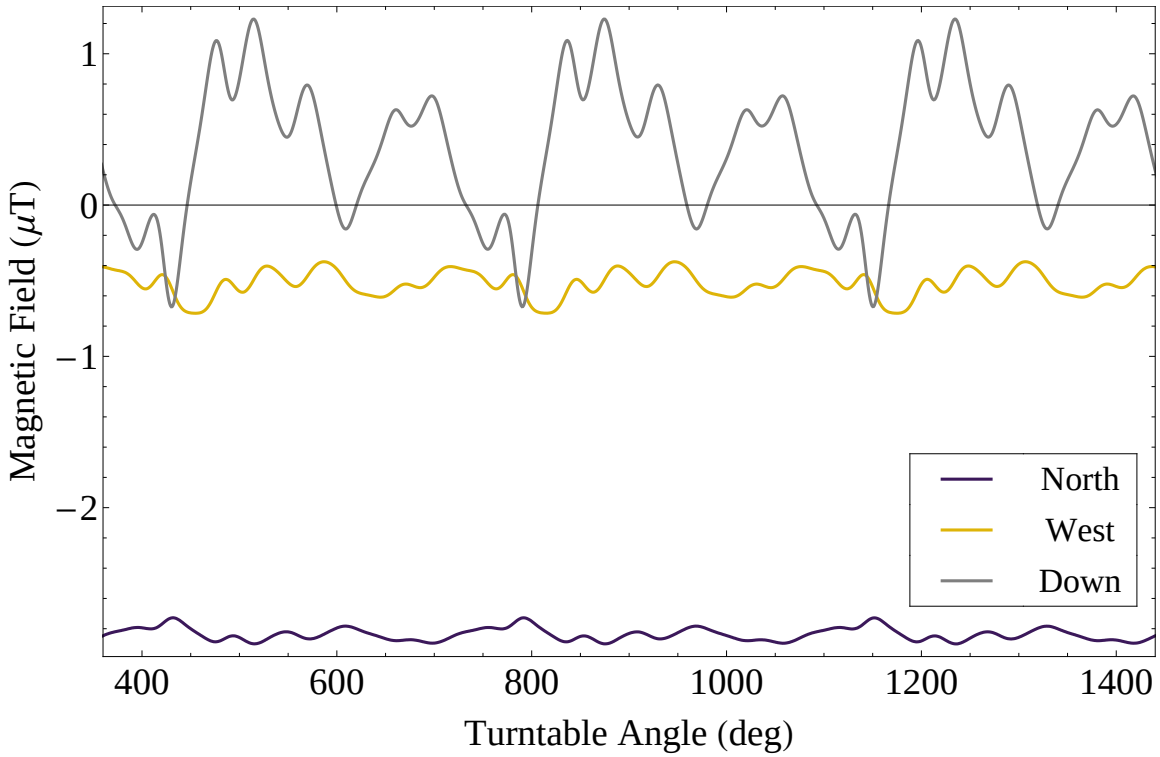

Figure 7.7: Output of a 3-axis magnetometer inside the stationary magnetic shield with the turntable rotating. Screws in the rotating shield that passed near the magnetometer as the turntable rotated were the primary source of the variation with angle.

7.3 Magnetic Effects

Magnetic impurities on a pendulum or residual magnetization of an earth-core test body (made of stainless steel) would produce a torque due to the ambient laboratory magnetic field. As the turntable rotates in the laboratory magnetic field, it modulates the the magnetic interaction at the turntable rotation frequency. We minimized magnetic systematic effects by using non-magnetic materials, demagnetizing each earth-core test body, and surrounding the pendulum with four layers of high magnetic permeability metal (see section 5.8). We measured the magnetic response of the pendulum by placing a strong permanent magnet near the apparatus with the outermost, stationary magnetic shield removed and used the magnitude of the magnetic field within the outermost, stationary magnetic shield to determine the magnetic systematic uncertainty.

For the earth-moon pendulum we took extra care to measure the magnetic field within the stationary shield due to the iron content of the earth-core test bodies. A fluxgate magnetometer measured the magnetic field between the bottom of the rotating shield and the inside of the bottom of the stationary shield near the turntable rotation axis. Due to equipment sharing with other experiments, the magnetometer was only installed for about 150 days out of 381 total days of data taking. Figure 7.7 shows a representative plot of the magnetometer signal, which remained very consistent over all runs. We fit the magnetometer data for all three axes to find the daily variation of the signal at the turntable rotation frequency. No daily variation was resolved as shown in table 7.11, so we added the uncertainties in quadrature to obtain a 1-σ limit on the daily variation of 0.93 nT. The expected atmospheric daily variation is $\sim$20 nT at our laboratory's location [60], which is consistent with a shielding factor of $\sim$30 for the stationary magnetic shield.

Table 7.11: Amplitude of the daily variation of the magnetic field within the stationary magnetic shield.

Direction	Magnetic field daily variation (nT)
North	0.02 ± 0.05
West	0.09 ± 0.16
Down	0.25 ± 0.91

We measured each pendulum's response to a magnetic field using a strong permanent magnet mounted near the outer rotating surface of the apparatus (26 cm from the center of the magnet to the center of the pendulum). A holder fixed the magnet in position and oriented either the north or south pole face of the magnet towards the apparatus. The difference in observed twist signal between the north and south orientations of the magnet determined the magnetic response. The magnet's field at the pendulum's position was 1.7×10^{-4} T. No difference in twist was observed within the measurement uncertainty, so the 68.3% confidence level bound on the magnitude was used to determine the magnetic

Table 7.12: The twist response due to a strong permanent magnet placed near the apparatus at the pendulum's height.

Pendulum	Magnetic response (nrad μT^{-1})
Be-Al	0.01 ± 0.01
Al-Be	0.01 ± 0.01
Earth-Moon	0.03 ± 0.04

uncertainty. Table 7.13 lists the magnetic systematics, while table 7.12 gives the magnetic response for each pendulum. We multiplied the magnetic response by the residual magnetic field inside the stationary magnetic field (3×10^{-6} T) to obtain the lab-fixed magnetic systematic uncertainty and by the daily magnetic field variation (0.93×10^{-9}) T to obtain the astronomical source systematic uncertainty.

Table 7.13: 1-σ magnetic systematic uncertainty for laboratory-fixed and astronomical sources. No correction was applied for magnetic effects. The earth-moon pendulum was only analyzed for astronomical sources. The astronomical uncertainties are negligible compared to other uncertainties.

Pendulum	Lab-fixed (10^{-18} N m)	Astronomical (10^{-18} N m)
Be-Al	0.10	2.9×10^{-5}
Earth-Moon	—	2.3×10^{-4}

7.4 Temperature Effects

Thermally induced mechanical movement and stress affect most parts of the apparatus: we observed temperature effects on the fiber and its suspension, the turntable tilt, and the autocollimator. Our thermal management efforts (see section 5.6) limited the absolute temperature change of the apparatus to a slow drift with a time constant much longer than that of the turntable rotation frequency. Small differences ($\sim$10 mK) in temperature across the apparatus remained and produced a thermally induced twist at the turntable rotation frequency. We estimated the temperature gradient systematic response by creating large horizontal temperature differences across the apparatus and measuring the change to the twist at the turntable rotation frequency.

The layers of insulation and thermal shields surrounding the apparatus attenuated temperature gradients from $\sim$50 mK m^{-1} across the outermost rotating shield to $\lesssim$5 mK m^{-1} across the fiber positioning stage. To examine the effects of a temperature gradient on the pendulum signal, we installed a pair of independently temperature controlled copper panels in place of the the outer, stationary thermal and magnetic shielding to create a large temperature difference across the apparatus (see figure 7.8). Each panel consisted of tubing sandwiched between two copper plates in a cylindrical section covering approximately 45°. Foam $\approx$1 cm thick insulated the outer side of each panel. Each panel's temperature was controlled by water pumped through the tubing from an independent constant temperature bath (Neslab RTE-221). We set temperature differences as large as 7 K between the two temperature panels. The panels were more effective at heating than cooling the enclosure, so we tried to maintain a consistent enclosure temperature by setting the mean temperature of the two panels below the typical enclosure temperature.

Both the temperature gradient and pendulum twist changed in a linear manner. We found that the magnitude of the change in the pendulum's twist coefficients had a linear relationship to the temperature gradient change as illustrated in figure 7.9. With large induced temperature gradients, the linear relationship between changes in twist and changes in temperature gradients existed for temperature sensors on the autocollimator, vacuum column, fiber positioning stage, and across the outermost rotating shields and the phase

Figure 7.8: Independent temperature control of two cylindrical panels placed near the apparatus creates a large horizontal temperature difference that we use to determine the twist induced by temperature gradients.

relationship of each temperature sensor maintained a consistent relationship to the induced gradient. Unfortunately, during equivalence principle data collection, when the apparatus temperature was stabilized, the phase relationship between different temperature sensors was inconsistent with simple heat flow models for the apparatus. We used the largest temperature gradient, across the outermost rotating shield, to estimate the systematic uncertainty and applied the total equally to both Fourier components of the pendulum torque at the turntable rotation frequency.

Inducing a large horizontal temperature gradient also raised the enclosure temperature. The changing enclosure temperature affected the tilt feedback stability and increased drift of the pendulum equilibrium position. These temperature-induced effects made many runs unusable and increased the twist scatter between runs (including those taken with the same temperature panel difference). During later measurements, we reduced the enclosure temperature change by setting the mean temperature of the panels lower than the enclosure temperature; however, the overall enclosure temperature still changed by several degrees between measurements with different temperature gradients. It remains to be explored if temperature panel differences can be found that closely maintain the enclosure temperature.

A horizontal temperature gradient produces a signal at the turntable rotation frequency as the temperature sensor rotates through it. We computed the temperature response at the turntable rotation frequency as the ratio of the twist change to the temperature change between two temperature measurements A and B:

$$\zeta = \frac{\sqrt{\left(\theta^s_A - \theta^s_B\right)^2 + \left(\theta^c_A - \theta^c_B\right)^2}}{\sqrt{\left(T^s_A - T^s_B\right)^2 + \left(T^c_A - T^c_B\right)^2}} \tag{7.12}$$

We fit a line to the combined measurements for all mirrors requiring zero temperature response for zero change in temperature. Table 7.14 lists our measurements of twist response to temperature. The earth-moon pendulum measurements using the original vacuum column were taken each time we reinstalled the thermal shields after performing changes to the apparatus, since we were exploring pressure issues. For all the other configurations, we took an initial and final measurement of the temperature response. For the temperature systematic uncertainty, we multiplied the temperature response by the change in temperature ΔT

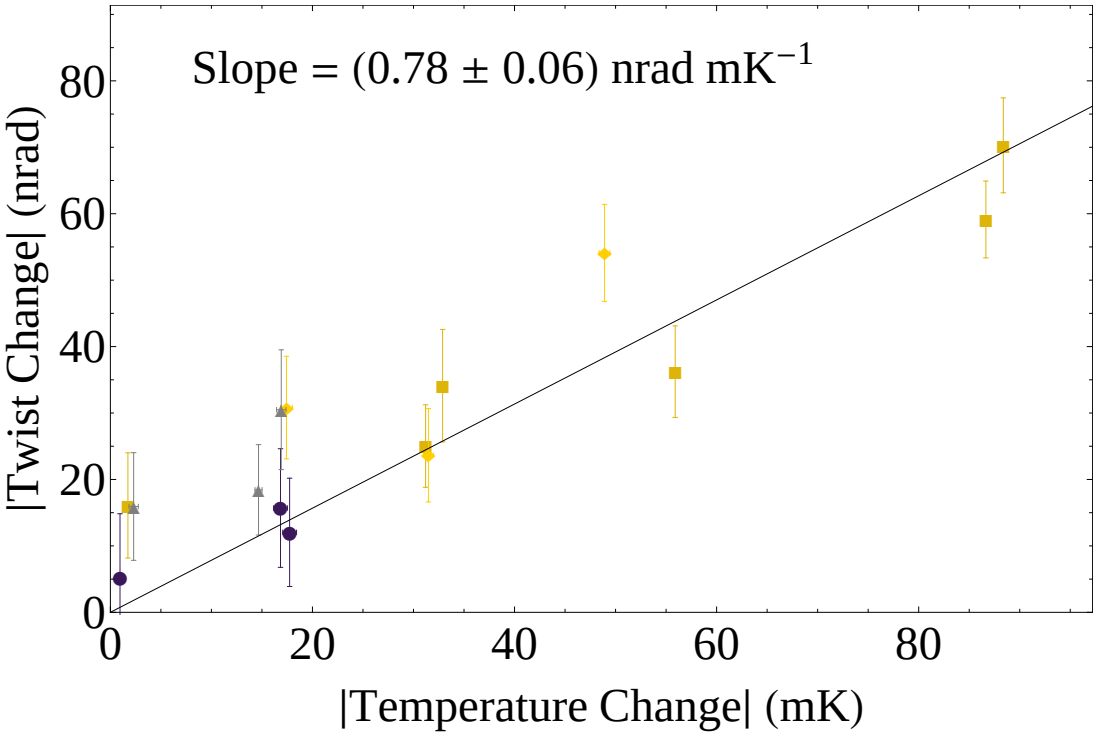

Figure 7.9: The temperature gradient response measured for the beryllium-aluminum configuration. The four pendulum orientations 0°, 90°, 180°, and 270° correspond to purple circles, brown squares, gold diamonds and gray triangles, respectively.

between the two pendulum orientations included in a data set:

$$\tilde{\tau}_{\text{temp}} = \zeta\sqrt{(\Delta T^s)^2 + (\Delta T^c)^2} \tag{7.13}$$

We assigned the total temperature systematic uncertainty to both twist Fourier components because the phase was inconsistent for small temperature gradients. Table 7.15 summarizes the systematic uncertainty due to temperature gradients.

7.4.1 Apparatus Temperature Sensitivity

We performed a detailed investigation of the apparatus's temperature sensitivities between the beryllium-titanium and beryllium-aluminum configurations to reduce temperature-induced systematic effects and further improved insulation between the beryllium-aluminum and aluminum-beryllium configurations. We identified specific locations on the apparatus that

Table 7.14: Twist induced by horizontal temperature differences across the rotating apparatus at ω_{TT}. Insulation and shielding were improved between Be-Al 2 and Al-Be 4 and the thermal mass of the apparatus increased between EM 5 and EM 6.

Measurement	Temperature feed-through (nrad mK^{-1})
Be-Al 1	0.60 ± 0.10
Be-Al 2	0.78 ± 0.06
Al-Be 3	0.22 ± 0.05
Al-Be 4	0.25 ± 0.03
EM 1	0.08 ± 0.02
EM 2	0.17 ± 0.05
EM 3	0.26 ± 0.02
EM 4	0.49 ± 0.05
EM 5	0.40 ± 0.03
EM 6	0.09 ± 0.02
EM 7	0.07 ± 0.02

resulted in the largest induced twist due to an applied temperature gradient. As a result of our investigation we added passive insulation in the most sensitive locations. We had been measuring a different twist response to temperature gradients each time the rotating temperature shields were installed, which we determined was mostly due to variations in the size of the smallest gap between the rotating shield and apparatus. The upper section of the rotating thermal shield closes around the apparatus like a clam shell and rests upon a plate that forms the bottom of the electronics enclosure. The position of greatest temperature sensitivity is where the rotating shield nearly touches the upper support plate for the vacuum can, which supported the fiber positioning stage prior to installing the new column

Table 7.15: Horizontal-temperature-gradient systematic uncertainty for the two beryllium and aluminum configurations.

Group	Temperature gradient systematic effect (10^{-18} N m)			
	Local	Sun	Galaxy	CMB
Be-Al 1	3.10	1.06	1.39	1.11
Be-Al 2	0.03	0.04	0.05	0.04
Be-Al 3	0.05	2.63	3.25	2.63
Be-Al 4	0.18	0.28	0.24	0.23
Be-Al 5	0.31	0.08	0.09	0.08
Be-Al 6	0.47	0.28	0.28	0.28
Al-Be 1	0.09	0.04	0.04	0.03
Al-Be 2	0.39	0.04	0.04	0.02
Al-Be 3	0.06	0.05	0.07	0.05
Al-Be 4	0.07	0.08	0.09	0.05

during the earth-moon data. Heat transfer for small temperature differences across a vertical air gap exponentially decay with the gap size for gaps less than 2 cm [110]. Additional recommendations for future improvements are in section 8.5.

We investigated the apparatus's heat sensitivity at different points with a light bulb. A 50 W light bulb in a steel sheet metal reflector was mounted to a stand so that the height could be changed while keeping the bulb 10 cm from the rotating thermal shields. We measured the difference in $\tilde{\tau}_1^S$ and $\tilde{\tau}_1^C$ with the light on and off with the light positioned at different heights. The maximum change in the twist coefficients was at the support plate for the fiber rotation stage, which is the location of the smallest clearance between the apparatus and the inner thermal shields. The apparatus also experienced a tilt that was order-of-magnitude consistent with a simple model of thermal expansion in the triangular

Table 7.16: Horizontal-temperature-gradient systematic uncertainty for the earth-moon configuration.

Group	Temperature gradient systematic effect Sun (10^{-18} N m)
EM 1	0.09
EM 2	0.09
EM 3	0.21
EM 4	1.61
EM 5	0.60
EM 6	0.33
EM 7	0.09
EM 8	1.10
EM 9	0.01
EM 10	0.03
EM 11	0.16

vacuum column supports.

7.5 Turntable Irregularities

Feedback to a center-less optical encoder maintained a constant turntable rotation rate; however, small variations in the turntable rotation rate affect the measurement. We modeled the turntable orientation in the lab frame as

$$\phi_{\mathrm{TT}}(t) = \omega_{\mathrm{TT}} t + \sum_{m=1}^{\infty} \Phi_m^S sin(m\omega_{\mathrm{TT}} t) + \Phi_m^C cos(m\omega_{\mathrm{TT}} t), \tag{7.14}$$

where Φ_m^S and Φ_m^C are the Fourier coefficients that describe the harmonic deviation of the turntable from the orientation obtained at a constant rotation rate. The largest effect of variations in the turntable rotation rate was a constant offset in the harmonic coefficients

independent of the pendulum orientation. Since the offset did not depend on the orientation of the pendulum, combining data taken with the composition dipole in two different orientations rotated by 180° with respect to the turntable removes the offset. However, due to small drifts, which are correlated with the temperature of the turntable and encoder, a residual systematic effect exists. We account for these drifts by fitting a linear drift to each run segment.

Reproducible variations of the turntable rotation rate, *e.g.*, due to variations in the encoder grating or the 6-fold bolt pattern, can be written as a Fourier series

$$\omega_{\mathrm{TT}}(t) = \omega_c + \sum_m \omega_m e^{-im\omega_c t}, \tag{7.15}$$

where ω_c represents the desired constant turntable rate and ω_m the coefficients of the harmonics describing the variations from the desired constant rate. Inserting the turntable rotation variations as a driving term in equation 3.8 for an undamped torsion balance yields the following pendulum twist:

$$\theta_{TT}(t) = \frac{-im\omega_c}{\omega_0^2 - (m\omega_c)^2}\omega_m e^{-im\omega_c t}. \tag{7.16}$$

We determined the turntable variations by measuring the pendulum twist signal for different turntable rotation speeds. When the turntable rotation speed is fast compared to the pendulum period, the pendulum should be inertial with any variations due only to variations in the turntable rotation rate. The turntable rotation variations had a stable component, which we corrected for using a map in the turntable feedback loop. However, repeated measurement and correction iterations failed to entirely remove the turntable rotation variation despite our science data showing a stable, orientation independent contribution to the twist Fourier components.

Chapter 8

RESULTS

Our equivalence principle experiments have the best differential acceleration sensitivity of any laboratory test, and our strong limits apply to a broad selection of charges. We used three separate test body combinations: beryllium and titanium, beryllium and aluminum, and test bodies that mimic the composition of earth's core and the moon and earth's mantle. At least two different test body pairs and two different sources must be used to create strong limits for all possible charges $\tilde{q}$ (see equation 2.10) because each test body pair (or source) is insensitive at a particular charge parameter $\tilde{\psi}'$. Rotating our torsion balance on a turntable enables us to set the best limits on unknown Yukawa interactions over terrestrial distance scales and permits a detailed investigation of systematic effects. In addition to using earth as a source, we searched for equivalence-principle violations toward the sun, dark matter in the Milky Way, and the direction of the CMB dipole. Careful examination and understanding of systematic effects improves our ability to make measurements limited primarily by the thermal motion of the fiber. The primary results of our equivalence principle experiments are collected in table 8.1.

8.1 Yukawa Interactions

Modern equivalence principle experiments are often interpreted as searches for new forces. We parametrize a hypothetical new force using a Yukawa potential to set limits on the strength $\tilde{\alpha}$ of the interaction between our test bodies and a source based on a chosen interaction range λ and charge $\tilde{q}$ (see section 2.2). We further parametrize the charge with $\tilde{\psi}$ in equation 2.10 to distinguish whether protons and electrons or neutrons carry the charge. Figure 8.1 illustrates the necessity of using multiple sources and composition dipoles to constrain equivalence-principle violations for any possible charge because a single composition dipole or source has a value $\tilde{\psi}'$ for which it is insensitive because the charge

Table 8.1: Horizontal differential accelerations in the lab-fixed frame (Δa_N and Δa_W) and toward the sun, galactic center, and cosmic microwave background dipole ($\Delta a_\odot$, Δa_g, and $\Delta a_{\rm CMB}$). The Eötvös parameters $\eta_\oplus$, $\eta_\odot$, and $\eta_{\rm DM}$ were calculated using the horizontal gravitational accelerations of Earth, Sun, and galactic dark matter of 1.7×10^{-2}, 5.9×10^{-3}, and 4.8×10^{-11} m s^{-2}, respectively. Uncertainties are 1-σ statistical and systematic added in quadrature. We analyzed the earth-moon pendulum data exclusively towards the sun to complement lunar laser ranging results.

		Be-Ti	Be-Al	Earth-Moon
Δa_N	$(10^{-15}\ \mathrm{m\,s^{-2}})$	0.6 ± 3.1	-2.2 ± 2.0	—
Δa_W	$(10^{-15}\ \mathrm{m\,s^{-2}})$	-2.5 ± 3.5	3.0 ± 2.0	—
$\Delta a_\odot$	$(10^{-15}\ \mathrm{m\,s^{-2}})$	-1.8 ± 2.8	-3.9 ± 2.6	2.1 ± 2.0
Δa_g	$(10^{-15}\ \mathrm{m\,s^{-2}})$	-2.1 ± 3.1	-2.2 ± 2.9	—
$\Delta a_{\rm CMB}$	$(10^{-15}\ \mathrm{m\,s^{-2}})$	-2.1 ± 3.1	3.4 ± 2.6	—
$\eta_\oplus$	(10^{-13})	0.3 ± 1.8	-1.3 ± 1.2	—
$\eta_\odot$	(10^{-13})	-3.1 ± 4.7	-6.5 ± 4.5	3.6 ± 3.3
$\eta_{\rm DM}$	(10^{-5})	-4.2 ± 6.2	-4.6 ± 6.1	—
$\eta_{\rm CD}$	(10^{-13})	—	—	1.2 ± 1.1
$\eta_{\rm grav}$	(10^{-4})	—	—	4.5 ± 3.8

is zero. The topography and geology of the Pacific Northwest act as a source for possible interactions with ranges λ down to a meter, while we use earth's large-scale structure and the sun as sources for $\lambda \to \infty$.

Figure 8.2 shows the best limits on the magnitude of $\tilde{\alpha}$ for an infinite range interaction $\lambda \to \infty$ as a function of the charge parameter $\tilde{\psi}$ and compares our combined results with those from Lunar laser ranging[137] and Braginsky [19]. Figure 8.3 shows the greatest and least lower limits of all $\tilde{\psi}$ at each λ (i.e., the maximum and minimum of the combined limits found on figure 8.2 but for each value of λ). For the combined limits in figure 8.3 we incorporate our beryllium-aluminum and beryllium-titanium [113] measurements with a short-range equivalence principle measurement using copper-lead test-bodies towards a

^{238}U attractor [115].

We use the beryllium-titanium and beryllium-aluminum composition dipoles with the earth and sun as sources to set limits on the strength $\tilde{\alpha}$ of a hypothetical new Yukawa interaction (equation 2.5) as a function of the interaction range λ for selected charges of interest $\tilde{q}/\mu = (B - L/\mu)$, (B/μ), and (L/μ) shown in figures 8.4, 8.5, and 8.6, respectively. The combined results in this section's plots use two test body pairs (Be-Ti and Be-Al) and three sources (the earth in the east-west direction, the earth in the north-south direction, and the sun) to set constraints for any charge $\tilde{q}$. The two lunar laser ranging lines come from an inverse-square gravitational force test using the precession of the earth-moon system [127] resulting in the V-shaped limit and a search for polarization of the earth-moon system towards the sun for the longest-range limit [137].

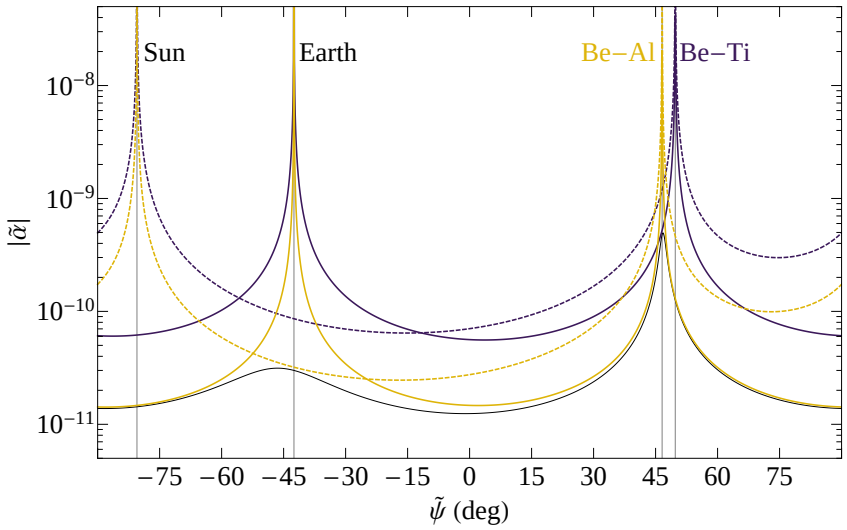

Figure 8.1: Illustration of the necessity of using multiple sources and test-body pairs. The plot shows 95% CL limits on the strength $\tilde{\alpha}$ of a new Yukawa force versus the charge parameter $\tilde{\psi}$ for $\lambda \to \infty$ using two different test-body pairs and two different sources. The vertical lines labeled near the top show the $\tilde{\psi}'$ at which the composition (composition difference) of an object (test-body pair) renders it insensitive. The beryllium-aluminum results are in purple and the beryllium-titanium results are in yellow. Dashed lines use the sun as source and solid lines use the earth. The thin black line shows the combined limit.

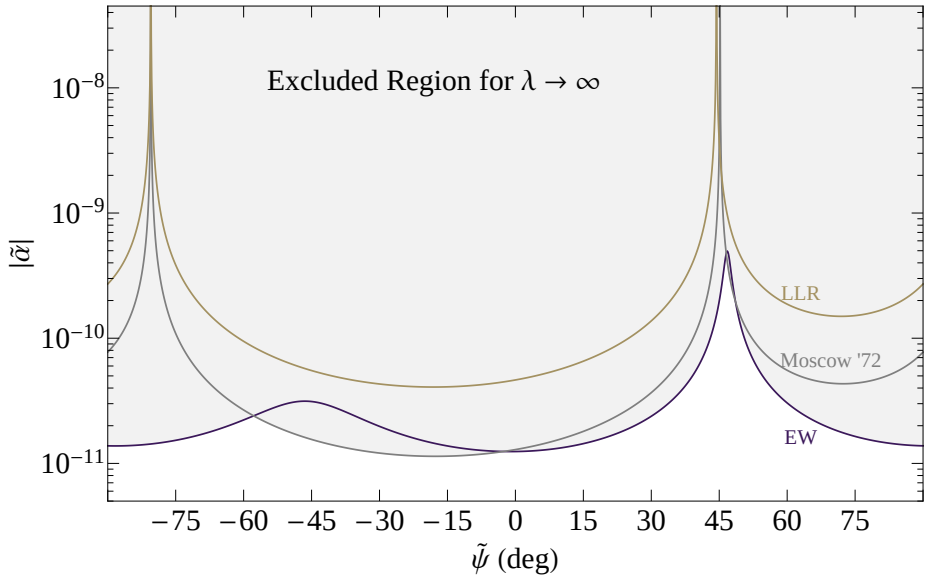

Figure 8.2: 95% CL limits on the strength $\tilde{\alpha}$ of a new Yukawa force for $\lambda \to \infty$. The EW (purple) line is the combined Be-Ti [113] and Be-Al result. Moscow '72 comes from [19] with the sun as a source. The LLR line for the earth and moon falling toward the sun comes from [137].

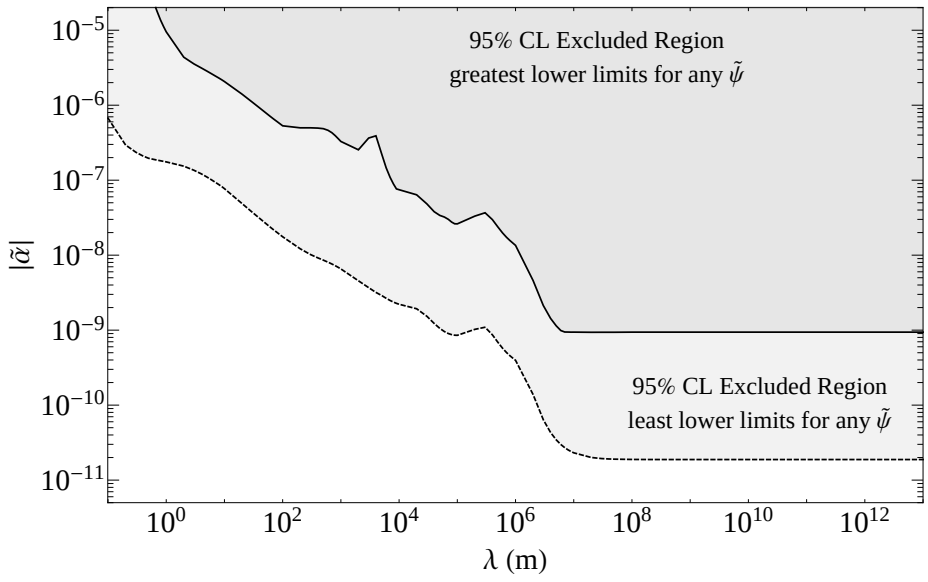

Figure 8.3: 95% CL limits for the greatest lower limit (solid) and least lower limit (dashed) of strength $\tilde{\alpha}$ for any charge $\tilde{q}(\tilde{\psi})$. Both lines are the combined results of the Be-Al, Be-Ti [113], and ^{238}U attractor [115] experiments.

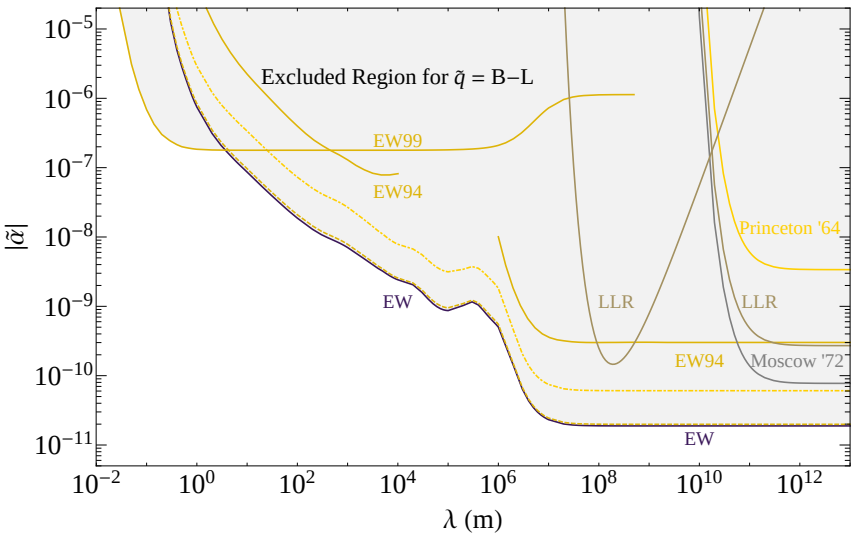

Figure 8.4: 95% CL limits on a new Yukawa force for $\tilde{q} = B - L$. The EW (purple) line is the combined Be-Ti [113] (dot-dashed line) and Be-Al (dashed) result. The EW99, EW94, Princeton '64, and Moscow '72 are from references [115], [124], [109], and [19], respectively. The LLR line with its best limit near $\lambda \sim 10^8$ m is from [127]. The LLR line using the sun as its source comes from [137].

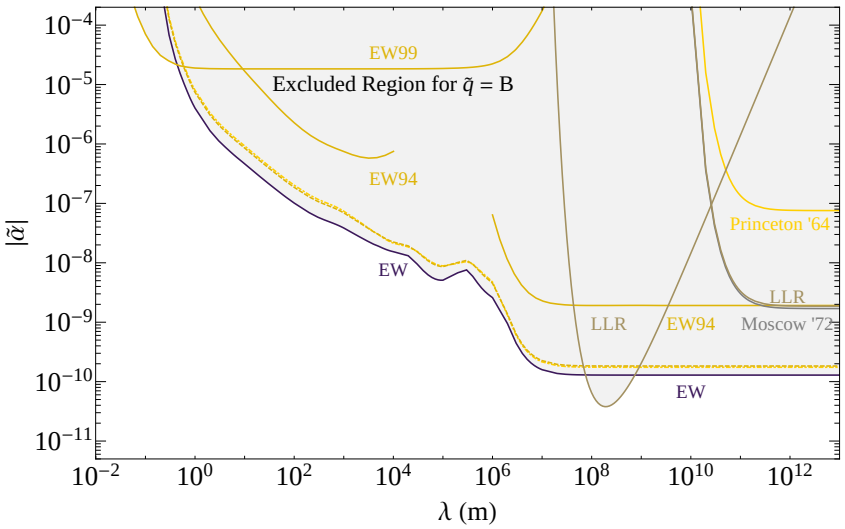

Figure 8.5: 95% CL limits on a new Yukawa force for $\tilde{q} = B$. The EW (purple) line is the combined Be-Ti [113] (dot-dashed line) and Be-Al (dashed) result. The EW99, EW94, Princeton '64, and Moscow '72 are from references [115], [124], [109], and [19], respectively. The LLR line with its best limit near $\lambda \sim 10^8$ m is from [127]. The LLR line using the sun as its source comes from [137].

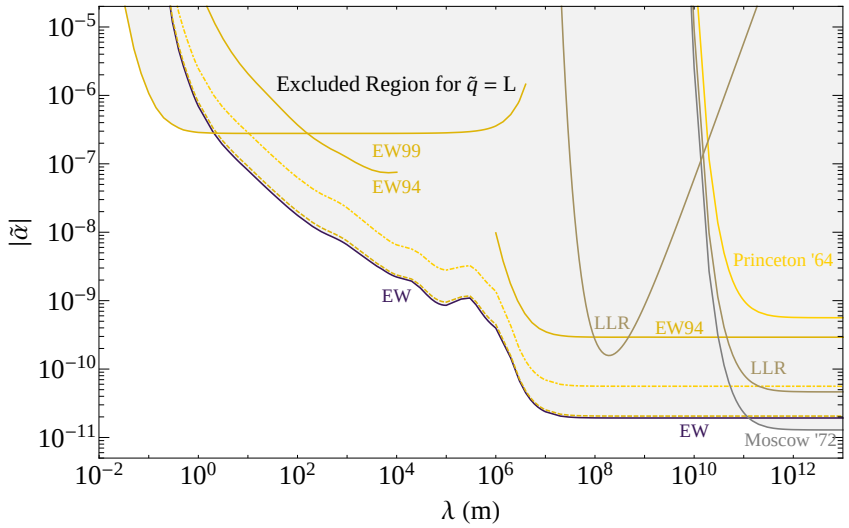

Figure 8.6: 95% CL limits on a new Yukawa force for $\tilde{q} = L$. The EW (purple) line is the combined Be-Ti [113] (dot-dashed line) and Be-Al (dashed) result. The EW99, EW94, Princeton '64, and Moscow '72 are from references [115], [124], [109], and [19], respectively. The LLR line with its best limit near $\lambda \sim 10^8$ m is from [127]. The LLR line using the sun as its source comes from [137].

8.1.1 Antimatter

When considering proposed matter-antimatter equivalence principle experiments (e.g., $H - \bar{H}$ drop experiment [42]), it is useful to compare to the current limits set by torsion balance experiments. The figure of merit for a hydrogen-antihydrogen drop experiment is $\Delta a_{H\bar{H}}/g$, which can be related to torsion balance experiments through equation 4.5:

$$\frac{\Delta a_{H\bar{H}}\left(\tilde{\psi},\lambda\right)}{g} = \tilde{\alpha}\left(\tilde{\psi},\lambda\right)\left[\left(\frac{\tilde{q}_H(\tilde{\psi})}{\mu_H}\right) - \left(\frac{\tilde{q}_{\bar{H}}(\tilde{\psi})}{\mu_{\bar{H}}}\right)\right] a_v\left(\tilde{\psi},\lambda\right) g^{-1}, \tag{8.1}$$

where $\tilde{\alpha}\left(\tilde{\psi},\lambda\right)$ are the existing torsion balance limits and $a_v\left(\tilde{\psi},\lambda\right)$ is the vertical component of the source integration for a given charge parameter $\tilde{\psi}$ and range λ. Figure 8.7 plots limits on $\frac{\Delta a_{H\bar{H}}}{g}$ for a hypothetical hydrogen-antihydrogen equivalence principle experiment performed at our torsion balance's site. Note that while horizontal gravitational acceleration varies dramatically by location, the vertical gravitational acceleration should be relatively similar in different locations.

Our strong constraints on $\tilde{\alpha}$ for all possible charge parameters $\tilde{\psi}$ allows us to transform

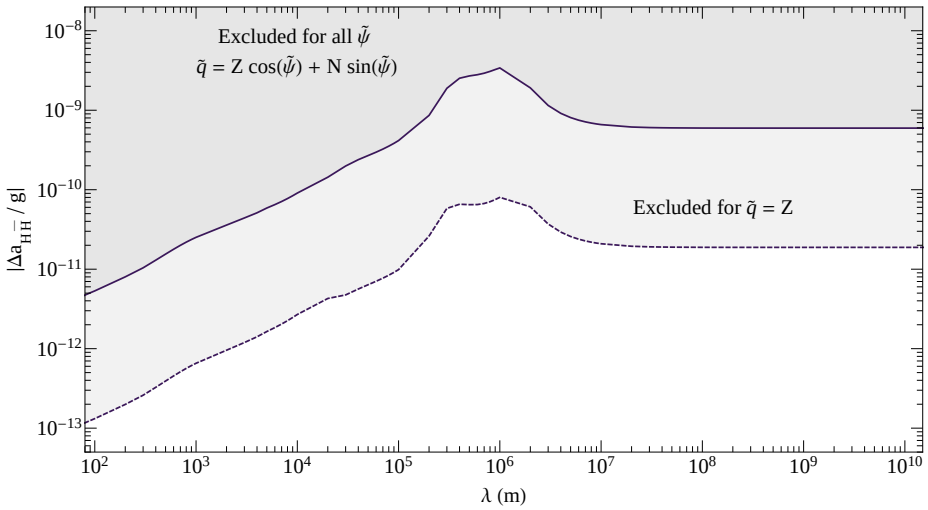

Figure 8.7: 95% CL limits on the ratio of the difference in acceleration of hydrogen and antihydrogen to earth's gravitational field based on our torsion pendulum measurements. The region above the solid line is excluded for all values of $\tilde{q}(\tilde{\psi})$. The dashed line assumes that $\tilde{q} = Z$.

the limits from our composition dipoles to different compositions regardless of the charge $\tilde{q}\left(\tilde{\psi}\right)$ a new interaction may couple to. A hydrogen-antihydrogen experiment clearly is most sensitive to $\tilde{q} = Z$; however, we also look at the signal such an experiment would observe as a function of the charge parameter and present the greatest lower bound for any $\tilde{\psi}$:

$$\frac{\Delta a_{H\bar{H}}(\lambda)}{g} \leqslant \max\left[\tilde{\alpha}\left(\tilde{\psi},\lambda\right) 2\cos\left(\tilde{\psi}\right) a_v\left(\tilde{\psi},\lambda\right) g^{-1}\right] \quad \forall \quad \left(-\frac{\pi}{2} < \tilde{\psi} \leqslant \frac{\pi}{2}\right) \tag{8.2}$$

8.2 Dilaton Constraints

Our experiments constrain the dilaton coupling parameters from the Donoghue and Damour [37] model for equivalence-principle violation by a dilaton field. The dominant dilaton coupling due to gluons was assumed to obey the equivalence principle in the model, but other composition-dependent contributions were parametrized as described in section 2.3. We include the Moscow Al-Pt limit [19] due to the substantially different test body pair composition. Figure 8.8 shows the allowed region for the two largest couplings due to the average light quark mass $D_{\hat{m}}$ and the electromagnetic field strength D_e from equation 2.17. The other couplings $D_{\delta m}$ and D_{m_e} due to differences in light quark masses and to the electron mass were assumed to be zero.

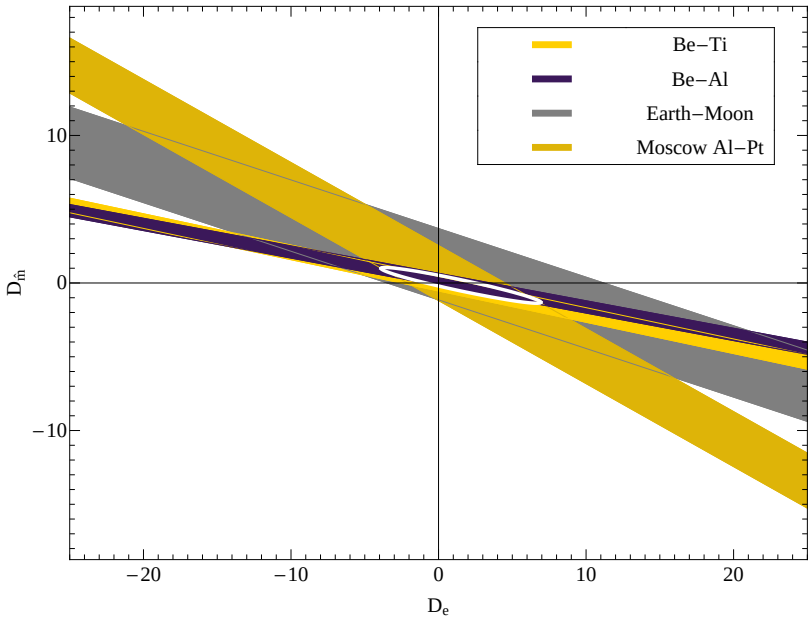

Figure 8.8: 95% CL constraint on the average light quark mass $D_{\hat{m}}$ and electromagnetic field D_e coupling to a long range dilaton field in the Donoghue-Damour model [37] using our beryllium-titanium (yellow), beryllium-aluminum (purple), and earth-moon pendulum (gray) results plus the Moscow aluminum-platinum (gold) limit [19]. The white ellipse shows the combined confidence region.

8.3 Strong Equivalence Principle and Lunar Laser Ranging

Current lunar laser ranging results give $\eta_{\rm LLR} = \Delta a_{\rm LLR}/a_\odot = (-0.8 \pm 1.3) \times 10^{-13}$ [137]. However, millimeter level earth-moon range results due to the APOLLO collaboration will likely improve lunar laser ranging equivalence principle sensitivity by an order of magnitude once newly observed effects are incorporated into models [91]. The exceptional sensitivity of lunar laser ranging presents the opportunity to test the equivalence principle for gravitational binding energy [13]. Lunar laser ranging tests the strong equivalence principle and constrains the combined effects of equivalence-principle violation due to composition and gravitational binding energy. We set a limit on the composition dependent part $\eta_{\rm CD}$ using laboratory test bodies that enhance the composition difference between the earth and moon, but have negligible gravitational binding energy:

$$\eta_{\rm CD} = \eta_\odot^{\rm EM}\,(f_\oplus - f_{\leftmoon}) = (1.2 \pm 1.1) \times 10^{-13}, \tag{8.3}$$

where $\eta_\odot^{\rm EM}$ is our earth-moon pendulum limit towards the sun and $f_\oplus$ and $f_{\leftmoon}$ are the iron content fractions of the earth and moon, respectively. The combined value includes only the effects of gravitational binding energy:

$$\begin{aligned} \eta_{grav} &= \frac{\eta_{\rm LLR} - \eta_{\rm CD}}{\Delta E_{grav}} = (4.5 \pm 3.8) \times 10^{-4}, \text{ or} \\ |\eta_{grav}| &\leqslant 6 \times 10^{-4} \text{ at 1-}\sigma \end{aligned} \tag{8.4}$$

where the difference in fractional gravitational binding energy for the earth-moon system is $\Delta E_{grav} = E_{grav}^\oplus - E_{grav}^{\leftmoon} = -4.4 \times 10^{-10}$. Earth's gravitational binding energy as a fraction of its mass is $E_{grav}^\oplus = -4.6 \times 10^{-10}$ and the moon's is $E_{grav}^{\leftmoon} = -0.2 \times 10^{-10}$.

8.4 Dark Matter

Hydrogen constitutes most of the observable matter in our galaxy. We scale the limits on the differential acceleration of our test bodies towards the dark matter in our galaxy Δa_g by the ratio of our composition dipole charge $\Delta\left(\tilde{q}_p/\mu_p\right)$ to the charge of neutral hydrogen $\tilde{q}_H/\tilde{\mu}$ to produce limits on the acceleration of neutral hydrogen toward galactic dark matter as a function of the charge parameter $\tilde{\psi}$.

$$\frac{\Delta a_H}{a_{\rm DM}} = \frac{\Delta a_g}{a_{\rm DM}} \left(\frac{\tilde{q}_H}{\mu_H}\right) \left[\Delta\left(\frac{\tilde{q}_p}{\mu_p}\right)\right]^{-1}, \tag{8.5}$$

where $a_{\rm DM} = 4.8 \times 10^{-11}$ m s^{-2} is the acceleration towards the dark matter in our galaxy [121]. Figure 8.9 shows that combining lunar laser ranging limits with torsion balance limits on the differential acceleration towards the galactic center limits the non-gravitational acceleration of neutral hydrogen to $\lesssim 5\%$ for any value of $\tilde{\psi}$.

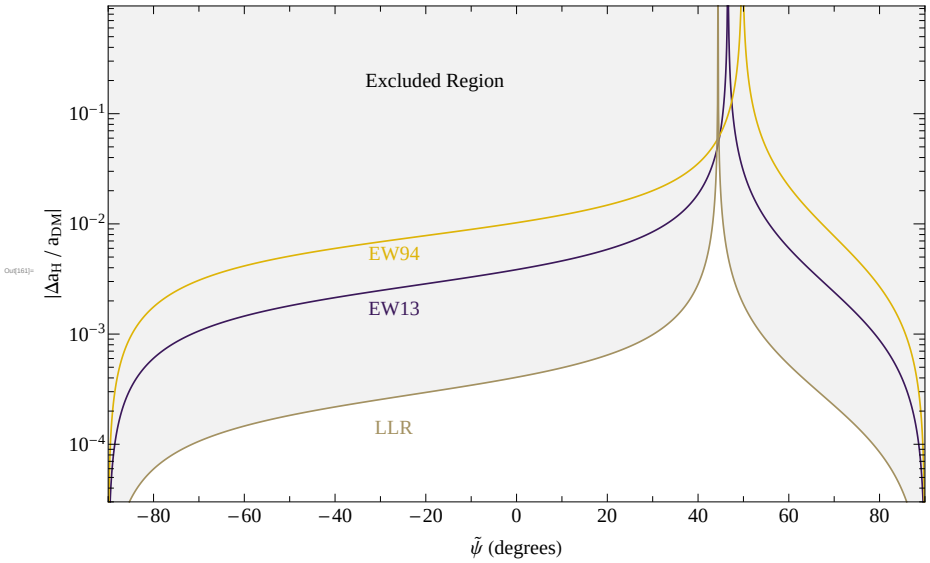

Figure 8.9: 95% CL limits on the ratio of the non-gravitational acceleration of neutral hydrogen to the total acceleration toward galactic dark matter.

8.5 Future Apparatus Improvements

During the course of our measurements several features of the apparatus were identified that could be improved for future experiments.

1. Increase the charge difference of the test bodies using different materials. Some plastic polymers may provide a means of incorporating a hydrogen-rich material.

2. Explore fiber heating and alternative fiber materials. The fibers that were produced using the fiber heating procedure had a larger Q, but were substantially more fragile than the normal tungsten fibers.

3. Develop a method for "continuous" monitoring of the gravitational gradient fields. The change in the gravitation gradient fields during our equivalence principle measurements were a large contribution of the gravitational gradient systematic uncertainty.

4. Reduce non-linear drifts in the fiber due to internal stress and temperature changes:

   (a) The algorithm for rotating the pendulum between mirrors uses the "crane operators trick" — the pendulum attachment is quickly rotated by half the total movement, the pendulum oscillation about the new center results in the movement to the desired mirror, finally the attachment point is quickly rotated to the new position. A new algorithm that minimizes induced fiber stress by adjusting the turntable speed along with the attachment point rotation should reduce the non-linear drift that we observe after pendulum rotations.

   (b) Actively stabilize the autocollimator and fiber attachment point temperatures to minimize thermal drift at the apparatus's most sensitive points. The autocollimator is sensitive to temperature effects through changes in the distances or orientation of optical components and through the inherent temperature sensitivity of the position sensitive photo-detector and of the laser. For example, the UDT SL3-2 photo-detector has a manufacturer specification of typical position drift of 0.06 µm K^{-1} with the beam at the center.

5. The earth-moon pendulum was significantly more sensitive to pressure spikes than the eight-test-body pendulum. Examine the response of various pendulum designs to pressure spikes for improved future designs — the cylindrical symmetry of the eight-test-body pendulum frame may contribute to its reduced sensitivity.

6. The tilt leveling system adjusts the zero point every 2 rotations by linear motion over 180° of turntable rotation. The linear motion has a substantial overlap with the turntable rotation harmonics that we fit.

7. The 4-fold triangular wings that support the vacuum column were observed to produce a thermally induced tilt during the lamp sensitivity tests. A redesigned apparatus

should use cylindrical symmetry.

8. Active temperature control of the apparatus enclosure: An analog control loop was used to test feedback on the apparatus enclosure air temperature. The control loop reduced the weekly low-temperature variation. Add an enclosure temperature control loop to the DAQ. A plastic shroud around the stationary thermal shields may reduce the higher-frequency airflow induced temperature variations from the air circulation fans on the heat exchange radiators.

9. Replace the fiber positioning stage with an improved vacuum feed-through. The existing feed-through uses an O-ring around a rotating shaft. Commercially available ultra-high vacuum rotating feed-throughs may improve the apparatus vacuum and minimize pressure bursts.

10. The magnetic swing damper works remarkably well; however, the design uses nuts on three threaded rods for position adjustments which results in too much adjustment freedom. A redesign should firmly hold the magnet and allow independent horizontal and rotational adjustment.

11. Identify the source of high-frequency $\sim$90-fold and 6-fold turntable rotation effects. The 6-fold effect may be due to the mounting screws for the center-less rotation encoder.

12. Redesign apparatus with fewer O-ring seals or replace with alternative high-vacuum seals.

13. Find temperature panel differences that maintain the enclosure temperature for temperature gradient systematic tests.

BIBLIOGRAPHY

[1] E G Adelberger, J H Gundlach, B R Heckel, S Hoedl, and S Schlamminger. Torsion balance experiments: A low-energy frontier of particle physics. *Prog. Part. Nucl. Phys.*, 62:102–134, 2009.

[2] E G Adelberger, B R Heckel, S Hoedl, C D Hoyle, D J Kapner, and A Upadhye. Particle physics constraints from a recent test of the gravitational inverse-square law. *Phys. Rev. Lett.*, 98:131104, 2007.

[3] E G Adelberger, B R Heckel, and A E Nelson. Tests of the gravitational inverse square law. *Ann.Rev.Nucl.Part.Sci.*, 53:77–121, 2003.

[4] E G Adelberger, B R Heckel, C W Stubbs, and Y Su. Does antimatter fall with the same acceleration as ordinary matter? *Phys. Rev. Lett.*, 66:850–853, 1991.

[5] E G Adelberger, C W Stubbs, B R Heckel, Y Su, H E Swanson, G L Smith, J H Gundlach, and W F Rogers. Testing the equivalence principle in the field of the Earth: Particle physics at masses below 1μeV? *Phys. Rev.*, 42:3267–3292, 1990.

[6] C J Allegre, J-P Poirier, E Humler, and A W Hofmann. The chemical composition of the Earth. *Earth Planet. Sci. Lett.*, 134:515–526, 1995.

[7] D S M Alves, M Jankowiak, and P Saraswat. Experimental constraints on the free fall acceleration of antimatter. *Arxiv pre-print: hep-ph/0907.4110*, 2009.

[8] C Amante and B W Eakins. ETOPO1 1 arc-minute global relief model: Procedures, data sources and analysis. *NOAA Technical Memorandum NESDIS NGDC-24*, page 19, March 2009.

[9] D L Anderson. *Theory of the Earth.* Blackwell Scientific Publications, Boston, Massachusetts, 1989.

[10] G B Andresen et al. Confinement of antihydrogen for 1000 seconds. *Nature Phys.*, 7:558–564, 2011.

[11] M Asplund, N Grevesse, A J Sauval, and P Scott. The chemical composition of the Sun. *Annual Review of Astronomy and Astrophysics*, 47:481–522, 2009.

[12] D C Backer and R A Sramek. Proper motion of the compact, nonthermal radio source in the galactic center, Sagittarius A*. *Astrophys. J.*, 524:805–815, 1999.

[13] S Baeßler, B R Heckel, E G Adelberger, J H Gundlach, U Schmidt, and H E Swanson. Improved test of the equivalence principle for gravitational self-energy. *Phys. Rev. Lett.*, 83:3585, 1999.

[14] J Bardo, G Fiquet, F Guyot, E Gregoryanz, F Occelli, D Antonangeli, and M d'Astuto. Effect of light elements on the sound velocities in solid iron: Implications for the composition of Earth's core. *Earth Planet. Sci. Lett.*, 254:233–238, 2007.

[15] C Bassin, G Laske, and G Masters. The current limits of resolution for surface wave tomography in North America. *EOS Trans. AGU*, 81(81):F897, 2000.

[16] R Bean, Flanagan, I Laszlo, and M Trodden. Constraining interactions in cosmologys dark sector. *Physical Review D*, 78(12):123514, Dec 2008.

[17] J Bovy and G Farrar. Connection between a possible fifth force and the direct detection of dark matter. *Physical Review Letters*, 102(10):1–4, Mar 2009.

[18] V B Braginsky and V I Panov. Verification of the equivalance of inertial and gravitational mass. In *ZhEksp. Teor. Fiz.* [19], pages 873–1272.

[19] V B Braginsky and V I Panov. Verification of the equivalance of inertial and gravitational mass. *JETP*, 34:463, 1971.

[20] T M Brocher. Empirical relations between elastic wavespeeds and density in the Earth's crust. *Bulletin of the Seismological Society of America*, 95(6):2081–2092, December 2005.

[21] H B Callen and R F Greene. On a theorem of irreversible thermodynamics. *Phys. Rev.*, 86(5):702–710, June 1952.

[22] S Carroll. *Spacetime and Geometry: An Introduction to General Relativity.* Addison Wesley, San Francisco, 2004.

[23] S Carroll, S Mantry, M Ramsey-Musolf, and C Stubbs. Dark-matter-induced violation of the weak equivalence principle. *Physical Review Letters*, 103(1):011301, Jul 2009.

[24] S M Carroll, S Mantry, and M J Ramsey-Musolf. Implications of a scalar dark force for terrestrial experiments. *Physical Review D*, 81(6):063507, Mar 2010.

[25] A Cavalleri et al. A new torsion pendulum for testing the limits of free-fall for LISA test masses. *Class. Quantum Grav.*, 26:094017, 2009.

[26] CECW-CE. *Engineering and Design: Control and Topographic Surveying*, 2007.

[27] N Chamoun and H Vucetich. Weak interactions effect on the p-n mass splitting and the principle of equivalence. *arxiv.org*, 2002.

[28] K Y Choi. *A New Equivalence Principle Test Using a Rotating Torsion Balance*. PhD thesis, University of Washington, 2006.

[29] N I Christensen and W D Mooney. Seismic velocity structure and composition of the continental crust: A global view. *JGR*, 100(B7):9761–9788, 1995.

[30] The CDMS Collaboration. website.

[31] The CDMS II Collaboration. Dark matter search results from the CDMS II experiments. *Science*, 327:1619, 2010.

[32] The CoGeNT Collaboration. website.

[33] XENON Collaboration. website.

[34] G Cowan. *Statistical Data Analysis*. Oxford University Press, USA, 1998.

[35] T Damour. Testing the equivalence principle: Why and how? *Class. Quantum Grav.*, 13:A33–A44, 1996.

[36] T Damour and J F Donoghue. Equivalence principle violations and couplings of a light dilaton. *Phys. Rev.*, 82:084033, 2010.

[37] T Damour and J F Donoghue. Phenomenology of the equivalence principle with light scalars. *Class. Quantum Grav.*, 27:202001, 2010.

[38] T Damour and A M Polyakov. String theory and gravity. *Gen. Rel. Grav.*, 26:1171, 1994.

[39] L de Haan and A Ferreira. *Extreme Value Theory: An Introduction*. Springer Science+Business Media, LLC, New York, NY, 2006.

[40] T Dent. Eötvös bounds on coupling of fundamental parameters to gravity. *Phys. Rev. Lett.*, 101:041102, 2008.

[41] J F Donoghue. General relativity as an effective field theory: The leading quantum corrections. *Phys. Rev. D*, 50:3874–3888, Sep 1994.

[42] G Yu Drobychev, P Nedelec, D Sillou, G Gribakin, H Walters, G Ferrari, M Prevedelli, G M Tino, M Doser, C Canali, et al. Proposal for the AEGIS experiment at the CERN antiproton decelerator (Antimatter Experiment: Gravity, Interferometry, Spectroscopy). Scientific Committee Paper CERN-SPSC-2007-017, CERN, Geneva, SPS Experiments Committee, 2007.

[43] A Dupays, E Mass, J Redondo, and C Rizzo. Light scalars coupled to photons and non-Newtonian forces. *Physical Review Letters*, 98(13):131802, Mar 2007.

[44] C D'Urso and E G Adelberger. Translation of multipoles for a 1/r potential. *Phys. Rev. D*, 55(12):7970, 1997.

[45] A M Dziewonski and D L Anderson. Preliminary reference Earth model. *Phys. Earth Planet. Inter.*, 25:297–356, 1981.

[46] B Eakins. Digital Elevation Model (DEM) discovery portal. `http://www.ngdc.noaa.gov/mgg/dem/demportal.html`. retrieved Sept. 24, 2010.

[47] A Einstein. The foundation of the general theory of relativity. In *The Berlin Years: Writings, 1914-1917*, volume 6 of *The Collected Papers of Albert Einstein*, pages 146–200. Princeton University Press, 1997.

[48] Y Enomoto et al. Synthesis of cold antihydrogen in a cusp trap. *Phys. Rev. Lett.*, 105:243401, 2010.

[49] R v Eötvös, D Pekár, and E Fekete. Beiträge zum Gesetze der Proportionalität von Trägheit und Gravität. *Ann. Phys.*, 373(373):11, 1922.

[50] T G Farr et al. The Shuttle Radar Topography Mission. *Rev. Geophys.*, 45(45):RG2004, 2007.

[51] D Finlayson. Combined bathymetry and topography of the Puget Lowland, Washington state. University of Washington website, January 2005. http://www.ocean.washington.edu/data/pugetsound/.

[52] E Fischbach, D Sudarsky, A Szafer, C Talmadge, and S H Aronson. Reanalysis of the Eötvös experiment. *Phys. Rev. Lett.*, 56:3–6, Jan 1986.

[53] W M. Folkner, J G Williams, and D H Boggs. The planetary and lunar ephemeris DE 421. IPN Progress Report 42-178, Jet Propulsion Laboratory, Pasadena, California, 2009.

[54] G T Gillies and R C Ritter. Torsion balances, torsion pendulums, and related devices. *Rev. Sci. Inst.*, 64(2):283–309, 1993.

[55] O W Greenberg. CPT violation implies violation of Lorentz invariance. *Phys. Rev. Lett.*, 89:231602, Nov 2002.

[56] R G Gustafson, W H Lenarz, B B McCain, C C Schmitt, W S Grant, T L Builder, and R D Methot. Status review of Pacific hake, Pacific cod, and walleye pollock from Puget Sound. NOAA Tech. Memo. NMFS-NWFSC-44, Dept. Commer., Washington. U.S., 2000.

[57] M P Haugan. Energy conservation and the principle of equivalence. *Annals of Physics*, 118:156–186, 1979.

[58] W M Haynes, editor. *CRC Handbook of Chemistry and Physics*, chapter Thermal and Physical Properties of Pure Metals. CRC Press/Taylor and Francis, Boca Raton, FL, 94th (internet version 2014) edition, 2013.

[59] B R Heckel, E G Adelberger, C E Cramer, T S Cook, S Schlamminger, and U Schmidt. Preferred-frame and CP-violation tests with polarized electrons. *Phys. Rev.*, 78:092006, 2008.

[60] A P Hitchman, F E M Lilley, and W H Campbell. The quiet daily variation in the total magnetic field: Global curves. *Geophysical Research Letters*, 25(11):98GL51332, 1998.

[61] A W Hofmann. Chemical differentiation of the Earth: The relationship between mantle, continental crust, and oceanic crust. *Earth Planet. Sci. Lett*, 90:297–314, 1988.

[62] C D Hoyle, D J Kapner, B R Heckel, E G Adelberger, J H Gundlach, U Schmidt, and H E Swanson. Submillimeter tests of the gravitational inverse-square law. *Phys. Rev.*, 70:042004, 2004.

[63] National Imagery and Mapping Agency. Department of Defense World Geodetic System 1984: Its definition and relationships with local geodetic systems. NIMA Technical Report 8350.2 Third Edition, National Imagery and Mapping Agency, NIMA (GIMG), Mail Stop L-41, Geodesy and Geophysics Department, National Imagery and Mapping Agency, 3200 South Second Street, St. Louis, MO 63118-3399, 2000.

[64] S B Jacobsen, J E Quick, and G J Wasserburg. A Nd and Sr isotopic study of the Trinity Peridotitie; implications for mantle evolution. *Earth Planet. Sci. Lett.*, 68:361–378, 1984.

[65] N Jarosik, C L Bennett, J Dunkley, B Gold, M R Greason, M Halpern, R S Hill, G Hinshaw, A Kogut, E Komatsu, et al. Seven-year Wilkinson Microwave Anisotropy Probe (WMAP) observations: Sky maps, systematic errors, and basic results. *Astrophysical Journal Supplement Series*, 192(14):15, 2011.

[66] M Javoy, E Kaminski, F Guyot, D Andrault, C Sanloup, M Moreira, S Labrosse, A Jombon, P Agrinier, A Davaille, and C Jaupart. The chemical composition of the Earth: Enstatite chondrite models. *Earth Planet. Sci. Lett.*, 293:259–268, 2010.

[67] K P Jochum, A W Hofmann, M Seufert, and W M White. The composition of mid-ocean ridge basalts, manuscript in preparation. unpublished, 1988.

[68] D B Kaplan and M B Wise. Couplings of a light dilaton and violations of the equivalence principle. *J. High Energy Phys.*, JHEP08:037, 2000.

[69] G Kaplan, J Bangert, J Bartlett, W Puatua, and A Monet. *User's Guide to NOVAS 3.0.* US Naval Observatory, Washington, DC, 2009.

[70] D J Kapner, T S Cook, E G Adelberger, J H Gundlach, B R Heckel, C D Hoyle, and H E Swanson. Tests of the gravitational inverse-square law below the dark-energy length scale. *Phys. Rev. Lett.*, 98:021101, 2007.

[71] Michael Kesden and Marc Kamionkowski. Tidal tails test the equivalence principle in the dark-matter sector. *Physical Review D*, 74(8):083007, Oct 2006.

[72] J Khoury and A Weltman. Chameleon fields: Awaiting surprises for tests of gravity in space. *Physical Review Letters*, 93(17):171104, Oct 2004.

[73] V A Kostelecký and J D Tasson. Matter-gravity couplings and Lorentz violation. *Phys. Rev. D*, 83:016013, Jan 2011.

[74] G Laske, A Dziewonski, and G Masters. Reference Earth model. website, 2011. http://igppweb.ucsd.edu/~gabi/rem.html.

[75] G Laske and G Masters. A global digital map of sediment thickness. *EOS Trans. AGU*, 78(78):F483, 1997.

[76] F G Lemoine, S C Kenyon, J K Factor, R G Trimmer, N K Pavlix, D S Chinn, C M Cox, S M Klosko, S B Luthcke, M H Torrence, Y M Wang, R G Williamson, E C Pavlis, R H Rapp, and T R Olson. The developent of the joint NASA GSFC and the National Imagery and Mapping Agency (NIMA) geopotential model EGM96. NASA Technical Report NASA/TP-1998-206861, National Aeronautics and Space Administration and National Imagery and Mapping Agency, Goddard Space Flight Center, Greenbelt, Maryland, 20771, USA, 1998.

[77] D A Livingstone. *Chemical composition of rivers and lakes.* U.S. Geol. Survey, 1963.

[78] J Longhi. A new view of lunar ferroan anorthosites: Postmagma ocean petrogenesis. *J. Geophys. Res.*, 108:5083, 2003.

[79] J Longhi. Petrogenesis of picritic mare magmas: Constraints on early lunar differentiation. *Geochimica et Cosmochimica Acta*, 70:5919–5934, 2006.

[80] T Lyubetskaya and J Korenaga. Chemical composition of Earth's primitive mantle and its variance. *J. of Geophys. Res.*, 112:B03211, 2007.

[81] S Maaløe and R Steel. Mantle composition derived from the composition of Iherzolites. *Nature*, 285:321–322, 1980.

[82] F T Mackenzie and R M Garrels. Chemical mass balance between rivers and oceans. *Amer. J. Sci.*, 264:507–525, 1966.

[83] D Mattingly. Modern tests of Lorentz invariance. *Living Reviews in Relativity*, 8(5):1, 2005.

[84] W F McDonough. *The Composition of the Earth's Core*. Springer, 2007.

[85] W F McDonough and S-s Sun. The composition of the Earth. *Chemical Geology*, 120:223–253, 1995.

[86] M A Meyers and K K Chawla. *Mechanical Behavior of Materials*. Prentice-Hall, Inc., Upper Saddle River, New Jersey, 1999.

[87] F J Millero. *Physical Chemistry of Natural Waters*. Wiley-Interscience, Danvers, Massachusetts, 2001.

[88] W D Mooney and M K Kaban. The North American upper mantle: Density, composition, and evolution. *J. Geophys. Res.*, 115:B12424, 2010.

[89] J W Morgan and E Anders. Chemical composition of Earth, Venus and Mercury. *Proc. Natl. Acad. Sci.*, 77(12):6973–6977, 1980.

[90] T W Murphy, Jr, E G Adelberger, J B R Battat, L N Carey, C D Hoyle, P LeBlanc, E L Michelsen, K Nordtvedt, A E Orin, J D Strasburg, C W Stubbs, H E Swanson, and E Williams. APOLLO: the Apache Point Observatory Lunar Laser-ranging Operation: Instrument description and first detections. *PASP*, 120:20, 2008.

[91] T W Murphy, Jr, E G Adelberger, J B R Battat, C D Hoyle, N H Johnson, R J McMillan, C W Stubbs, and H E Swanson. APOLLO: Millimeter lunar laser ranging. *Class. Quantum Grav.*, 29:184005, 2012.

[92] National Imagery and Mapping Agency, National Imagery and Mapping Agency, Fairfax, Virginia. *Digital Terrain Elevation Data Level 0*, 1996. Partly in GLOBE Task Team and others, 1999.

[93] M M Nieto and T Goldman. The arguments against 'antigravity' and the gravitational acceleration of antimatter. *Phys. Rept.*, 205:221–281, 1991.

[94] U. S. Coastal Relief Model. `http://www.ngdc.noaa.gov/mgg/coastal/crm.html`, September 2010.

[95] K Nordtvedt. Post-Newtonian gravitational effects in lunar laser ranging. *Phys. Rev. D*, 7:2347–2356, Apr 1973.

[96] K Nordtvedt. Lunar laser ranging and laboratory Eötvös-type experiments. *Phys. Rev. D*, 37:1070–1071, Feb 1988.

[97] K Nordtvedt. Lunar laser ranging: A comprehensive probe of post-Newtonian gravity. *Arxiv pre-print: gr-qc/0301024*, 2003.

[98] K L Nordtvedt, J Müller, and M Soffel. Cosmic acceleration of the Earth and Moon by dark matter. *Astron. Astrophys.*, 293:L73–L74, 1995.

[99] E Okon and C Callender. Does quantum mechanics clash with the equivalence principle - and does it matter? *Arxiv pre-print: 1008.5192v1*, 2010.

[100] H Palme and H S C O'Neill. *Cosmochemical estimates of mantle composition*, volume 2 of *Treatise on Geochemistry*. Elsevier-Pergamon, Oxford, 2003.

[101] R Pegna, A M Nobili, M Shao, S G Turyshev, G Catastini, A Anselmi, R Spero, S Doravari, G L Comandi, and A De Michele. Abatement of thermal noise due to internal damping in 2D oscillators with rapidly rotating test masses. *Phys. Rev. Lett.*, 107:200801, 2011.

[102] J Preskill, M B Wise, and F Wilczek. Cosmology of the invisible axion. *Physics Letters B*, 120(13):127 – 132, 1983.

[103] Professional Instruments Company, Hopkins, MN.

[104] I Reda and A Andreas. Solar Position Algorithm for solar radiation applications. NREL Technical Report TP-560-34302, National Renewable Energy Laboratory, 1617 Cole Blvd, Golden, Colorado 80401, 2003.

[105] M J Reid and A Brunthaler. The proper motion of Sagittarius A*. II. The mass of Sagittarius A*. *The Astrophysical Journal*, 616(2):872–884, Dec 2004.

[106] M J Reid, A C S Readhead, R C Vermeulen, and R N Treuhaft. The proper motion of Sagittarius A*. I. First VLBA results. *The Astrophysical Journal*, 524(2):816, 1999.

[107] A E Ringwood and S Kesson. A dynamic model for mare basalt petrogenesis. *Proc. Lunar Sci. Conf.*, 7:1697–1722, 1976.

[108] A E E Rogers, K A Dudevoir, J C Carter, B J Fanous, E Kratzenberg, and T M Bania. Deuterium abundance in the interstellar gas of the galactic anticenter from the 327 MHz line. *The Astrophysical Journal*, 630(L):L41–L44, 2005.

[109] P G Roll, R Krotkov, and R H Dicke. The equivalence of inertial and passive gravitational mass. *Ann. Phys., NY*, 26:442–517, 1964.

[110] M Rubin. Calculating heat transfer through windows. *Energy Research*, 6:341–349, 1982.

[111] R L Rudnick and S Gao. *Composition of the Continental Crust*, volume 3 of *Treatise on Geochemistry*. Elsevier-Pergamon, Oxford, 2003.

[112] P R Saulson. Thermal noise in mechanical experiments. *Phys. Rev.*, 42:2437–2445, 1990.

[113] S Schlamminger, K-Y Choi, T A Wagner, J H Gundlach, and E G Adelberger. Test of the equivalence principle using a rotating torsion balance. *Phys. Rev. Lett.*, 100:041101, 2008.

[114] I Smid, M Akiba, G Vieider, and L Plöchl. Development of tungsten armor and bonding to copper for plasma-interactive components. *Journal of Nuclear Materials*, 258-263:160–172, 1998.

[115] G L Smith, C D Hoyle, J H Gundlach, E G Adelberger, B R Heckel, and H E Swanson. Short-range tests of the equivalence principle. *Phys. Rev.*, 61:022001, 1999.

[116] Stanford Research Systems, Inc. About lock-in amplifiers. Application Note 3, Stanford Research Systems, Inc., Sunnyvale, California, 2009.

[117] G Steigman and M S Turner. Cosmological constraints on the properties of weakly interacting massive particles. *Nuclear Physics B*, 253(0):375 – 386, 1985.

[118] B Steinberger. Slabs in the lower mantle - results of dynamic modeling compared with tomographic images and the geoid. *Phys. Earth Planet. Inter.*, 118(118):241–257, 2000.

[119] J S Steinhart and S R Hart. Calibration curves for thermistors. *Deep Sea Research and Oceanographic Abstracts*, 15(4):497–503, 1968.

[120] W J Stephenson. Velocity and density models incorporating the Cascadia subduction zone for 3D earthquake ground motion simulations, version 1.3. Open-File Report 2007-1348, U.S. Geological Survey, Earthquake Hazards Ground Motion Investigations, 2007.

[121] C W Stubbs. Experimental limits on any long range nongravitational interaction between dark matter and ordinary matter. *Phys. Rev. Lett.*, 70:119–122, 1993.

[122] C W Stubbs et al. Search for an intermediate-range interaction. *Phys. Rev. Lett.*, 58:1070, 1987.

[123] Y Su. *A New Test of the Weak Equivalence Principle*. PhD thesis, University of Washington, 1992.

[124] Y Su, B R Heckel, E G Adelberger, J H Gundlach, M Harris, G L Smith, and H E Swanson. New tests of the universality of free fall. *Phys. Rev.*, 50:3614–3636, 1994.

[125] C Talmadge, J-P Berthias, R W Hellings, and E M Standish. Model-independent constraints on possible modifications of Newtonian gravity. *Phys. Rev. Lett.*, 61:1159–1162, 1988.

[126] S R Taylor. *Planetary Science: A Lunar Perspective*. Lunar and Planetary Institute, 3303 NASA Road 1, Houston, TX 77058, 1982.

[127] S G Turyshev and J G Williams. Space-based tests of gravity with laser ranging. *Int. J. Mod. Phys.*, 16:2165–2179, 2007.

[128] US Army Corps of Engineers. Lake Washington summary hydrograph. website, 2004. http://www.nwd-wc.usace.army.mil/nws/hh/basins/lwscsh.html.

[129] USGS. Seismic Hazards Investigations in Puget Sound (SHIPS). website, 2011. http://earthquake.usgs.gov/regional/pacnw/ships/.

[130] R C Weber, P-Y Lin, E J Garnero, Q Williams, and P Lognonné. Seismic detection of the lunar core. *Science*, 331(6015):309–312, 2011.

[131] J M Weisberg, D J Nice, and J H Taylor. Timing measurements of the relativistic binary pulsar PSR B1913+16. *The Astrophysical Journal*, 722(2):1030, 2010.

[132] C M Will. *Theory and Experiment in Gravitational Physics*. Cambridge University Press, 1993.

[133] C M Will. The confrontation between general relativity and experiment. *Living Reviews in Relativity*, 9(3):1, 2006.

[134] C M Will and K Nordtvedt, Jr. Conservation laws and preferred frames in relativistic gravity. I. Preferred-frame theories and an extended PPN formalism. *The Astrophysical Journal*, 177:757, Nov 1972.

[135] J G Williams, S G Turyshev, and D H Boggs. Progress in lunar laser ranging tests of relativistic gravity. *Phys. Rev. Lett.*, 93:261101, 2004.

[136] J G Williams, S G Turyshev, and D H Boggs. Lunar laser ranging tests of the equivalence principle with the Earth and Moon. *Int. J. Mod. Phys. D*, 18:1129–1175, 2009.

[137] J G Williams, S G Turyshev, and D H Boggs. Lunar laser ranging tests of the equivalence principle. *Class. Quantum Grav.*, 29:184004, 2012.

[138] J G Williams, S G Turyshev, and T W Murphy, Jr. Improving LLR tests of gravitational theory. *Int. J. Mod. Phys. D*, 13(3):567–582, 2004.

[139] F C Witteborn and W M Fairbank. Experiments to determine the force of gravity on single electrons and positrons. *Nature*, 220:437–440, 1968.

[140] Wolfram Research, Inc. Wolfram Mathematica 7.0.

Appendix A

EARTH SOURCE MODEL

A.1 Numerical Integration

The source acceleration was defined as the source related part of the gradient of the Yukawa potential:

$$\mathbf{F}_{AB} = -\nabla \tilde{V}_{12}(\mathbf{r}) = \alpha \underbrace{\left(\frac{\tilde{q}_1}{\mu_1} m_1\right)}_{pendulum} \underbrace{\left(-G\,\nabla\left(\frac{\tilde{q}_2}{\mu_2} m_2\right)\frac{e^{-|\mathbf{r}|/\lambda}}{|\mathbf{r}|}\right)}_{source}, \tag{A.1}$$

where $|\mathbf{r}|$ is the distance from the pendulum to the source and the gradient is evaluated with respect to the pendulum coordinate $\mathbf{r}_0$. Section 4.1 illustrates the integration using one dimension. For the actual integration of the earth source model, we used a full three dimensional model. For distances $|\mathbf{r}| \lesssim 100$ km, a rectangular grid using an East-North-Up coordinate system with the origin at the pendulum's location was used. For the global models, a spherical coordinate system was used. The following subsections detail the specific equations used for each of these coordinate systems. All three components of the source acceleration were computed.

The numerical integration was performed using the Mathematica [140] numerical integration function NIntegrate. The AccuracyGoal option was utilized as necessary to require at least 10^{-12} accuracy of individual integrations, though greater accuracy was utilized when it did not excessively increase the time to complete integrations. Some zero or near zero values failed to meet this criteria.

Table A.1: The complete earth source acceleration model for charges of $\tilde{q} = B$ and $\tilde{q} = L$.

λ (m)	East (m s^{-2})		North (m s^{-2})		Up (m s^{-2})	
	$\tilde{q} = B$	$\tilde{q} = L$	$\tilde{q} = B$	$\tilde{q} = L$	$\tilde{q} = B$	$\tilde{q} = L$
0.1	-1.417×10^{-11}	-7.063×10^{-12}	3.374×10^{-13}	1.701×10^{-13}	0	0
0.2	-3.438×10^{-9}	-1.663×10^{-9}	1.044×10^{-10}	5.254×10^{-11}	0	0
0.3	-2.494×10^{-8}	-1.237×10^{-8}	8.424×10^{-10}	4.222×10^{-10}	0	0
0.4	-6.313×10^{-8}	-3.143×10^{-8}	2.188×10^{-9}	1.096×10^{-9}	0	0
0.5	-1.097×10^{-7}	-5.469×10^{-8}	3.982×10^{-9}	1.996×10^{-9}	0	0
0.6	-1.633×10^{-7}	-8.147×10^{-8}	6.197×10^{-9}	3.108×10^{-9}	0	0
0.7	-2.239×10^{-7}	-1.118×10^{-7}	8.835×10^{-9}	4.433×10^{-9}	0	0
0.8	-2.904×10^{-7}	-1.451×10^{-7}	1.185×10^{-8}	5.947×10^{-9}	0	0
0.9	-3.569×10^{-7}	-1.783×10^{-7}	1.495×10^{-8}	7.508×10^{-9}	0	0
1.	-4.222×10^{-7}	-2.11×10^{-7}	1.81×10^{-8}	9.093×10^{-9}	-2.15×10^{-12}	-1.063×10^{-12}
2.	-1.013×10^{-6}	-5.079×10^{-7}	5.091×10^{-8}	2.561×10^{-8}	-2.961×10^{-9}	-1.465×10^{-9}
3.	-1.497×10^{-6}	-7.507×10^{-7}	7.932×10^{-8}	3.99×10^{-8}	-3.752×10^{-8}	-1.856×10^{-8}
4.	-1.886×10^{-6}	-9.446×10^{-7}	1.016×10^{-7}	5.11×10^{-8}	-1.434×10^{-7}	-7.097×10^{-8}
5.	-2.238×10^{-6}	-1.12×10^{-6}	1.153×10^{-7}	5.801×10^{-8}	-3.357×10^{-7}	-1.661×10^{-7}
6.	-2.563×10^{-6}	-1.281×10^{-6}	1.199×10^{-7}	6.042×10^{-8}	-6.106×10^{-7}	-3.021×10^{-7}
7.	-2.861×10^{-6}	-1.429×10^{-6}	1.154×10^{-7}	5.833×10^{-8}	-9.582×10^{-7}	-4.74×10^{-7}
8.	-3.134×10^{-6}	-1.565×10^{-6}	1.03×10^{-7}	5.224×10^{-8}	-1.367×10^{-6}	-6.764×10^{-7}
9.	-3.396×10^{-6}	-1.695×10^{-6}	8.84×10^{-8}	4.513×10^{-8}	-1.828×10^{-6}	-9.043×10^{-7}

Table A.1: The complete earth source acceleration model for charges of $\tilde{q} = B$ and $\tilde{q} = L$. (continued)

λ (m)	East (m s^{-2})		North (m s^{-2})		Up (m s^{-2})	
	$\tilde{q} = B$	$\tilde{q} = L$	$\tilde{q} = B$	$\tilde{q} = L$	$\tilde{q} = B$	$\tilde{q} = L$
10.	-3.655×10^{-6}	-1.823×10^{-6}	7.51×10^{-8}	3.864×10^{-8}	-2.332×10^{-6}	-1.154×10^{-6}
20.	-5.926×10^{-6}	-2.947×10^{-6}	-1.119×10^{-7}	-5.328×10^{-8}	-8.715×10^{-6}	-4.311×10^{-6}
30.	-7.798×10^{-6}	-3.873×10^{-6}	-2.999×10^{-7}	-1.46×10^{-7}	-1.613×10^{-5}	-7.977×10^{-6}
40.	-9.421×10^{-6}	-4.676×10^{-6}	-4.7×10^{-7}	-2.3×10^{-7}	-2.4×10^{-5}	-1.187×10^{-5}
50.	-1.089×10^{-5}	-5.404×10^{-6}	-6.161×10^{-7}	-3.021×10^{-7}	-3.202×10^{-5}	-1.584×10^{-5}
60.	-1.226×10^{-5}	-6.079×10^{-6}	-7.353×10^{-7}	-3.61×10^{-7}	-4.016×10^{-5}	-1.987×10^{-5}
70.	-1.35×10^{-5}	-6.694×10^{-6}	-8.277×10^{-7}	-4.067×10^{-7}	-4.835×10^{-5}	-2.392×10^{-5}
80.	-1.462×10^{-5}	-7.247×10^{-6}	-8.953×10^{-7}	-4.401×10^{-7}	-5.658×10^{-5}	-2.799×10^{-5}
90.	-1.569×10^{-5}	-7.778×10^{-6}	-9.48×10^{-7}	-4.661×10^{-7}	-6.482×10^{-5}	-3.207×10^{-5}
$1. \times 10^2$	-1.672×10^{-5}	-8.287×10^{-6}	-9.883×10^{-7}	-4.86×10^{-7}	-7.303×10^{-5}	-3.613×10^{-5}
$2. \times 10^2$	-2.425×10^{-5}	-1.201×10^{-5}	-6.314×10^{-7}	-3.094×10^{-7}	-1.574×10^{-4}	-7.788×10^{-5}
$3. \times 10^2$	-2.896×10^{-5}	-1.434×10^{-5}	3.101×10^{-7}	1.561×10^{-7}	-2.418×10^{-4}	-1.196×10^{-4}
$4. \times 10^2$	-3.188×10^{-5}	-1.579×10^{-5}	1.664×10^{-6}	8.251×10^{-7}	-3.267×10^{-4}	-1.616×10^{-4}
$5. \times 10^2$	-3.397×10^{-5}	-1.682×10^{-5}	3.084×10^{-6}	1.527×10^{-6}	-4.086×10^{-4}	-2.021×10^{-4}
$6. \times 10^2$	-3.56×10^{-5}	-1.762×10^{-5}	4.51×10^{-6}	2.231×10^{-6}	-4.871×10^{-4}	-2.41×10^{-4}
$7. \times 10^2$	-3.693×10^{-5}	-1.828×10^{-5}	5.897×10^{-6}	2.916×10^{-6}	-5.625×10^{-4}	-2.783×10^{-4}
$8. \times 10^2$	-3.807×10^{-5}	-1.884×10^{-5}	7.224×10^{-6}	3.57×10^{-6}	-6.35×10^{-4}	-3.141×10^{-4}
$9. \times 10^2$	-3.908×10^{-5}	-1.934×10^{-5}	8.484×10^{-6}	4.191×10^{-6}	-7.055×10^{-4}	-3.49×10^{-4}

Table A.1: The complete earth source acceleration model for charges of $\tilde{q} = B$ and $\tilde{q} = L$. (continued)

λ (m)	East (m s^{-2})		North (m s^{-2})		Up (m s^{-2})	
	$\tilde{q} = B$	$\tilde{q} = L$	$\tilde{q} = B$	$\tilde{q} = L$	$\tilde{q} = B$	$\tilde{q} = L$
$1. \times 10^3$	$-4. \times 10^{-5}$	-1.978×10^{-5}	9.681×10^{-6}	4.781×10^{-6}	-7.746×10^{-4}	-3.832×10^{-4}
$2. \times 10^3$	-4.593×10^{-5}	-2.267×10^{-5}	2.098×10^{-5}	1.034×10^{-5}	-1.486×10^{-3}	-7.352×10^{-4}
$3. \times 10^3$	-4.764×10^{-5}	-2.352×10^{-5}	3.339×10^{-5}	1.646×10^{-5}	-2.304×10^{-3}	-1.14×10^{-3}
$4. \times 10^3$	-4.653×10^{-5}	-2.3×10^{-5}	4.669×10^{-5}	2.302×10^{-5}	-3.224×10^{-3}	-1.595×10^{-3}
$5. \times 10^3$	-4.37×10^{-5}	-2.165×10^{-5}	5.733×10^{-5}	2.828×10^{-5}	-4.226×10^{-3}	-2.091×10^{-3}
$6. \times 10^3$	-3.969×10^{-5}	-1.972×10^{-5}	6.876×10^{-5}	3.393×10^{-5}	-5.293×10^{-3}	-2.618×10^{-3}
$7. \times 10^3$	-3.482×10^{-5}	-1.736×10^{-5}	7.857×10^{-5}	3.877×10^{-5}	-6.424×10^{-3}	-3.178×10^{-3}
$8. \times 10^3$	-2.923×10^{-5}	-1.464×10^{-5}	8.675×10^{-5}	4.282×10^{-5}	-7.618×10^{-3}	-3.769×10^{-3}
$9. \times 10^3$	-2.3×10^{-5}	-1.16×10^{-5}	9.345×10^{-5}	4.614×10^{-5}	-8.875×10^{-3}	-4.391×10^{-3}
$1. \times 10^4$	-1.62×10^{-5}	-8.266×10^{-6}	9.887×10^{-5}	4.882×10^{-5}	-1.019×10^{-2}	-5.044×10^{-3}
$2. \times 10^4$	6.963×10^{-5}	3.396×10^{-5}	1.152×10^{-4}	5.693×10^{-5}	-2.568×10^{-2}	-1.271×10^{-2}
$3. \times 10^4$	1.534×10^{-4}	7.524×10^{-5}	1.128×10^{-4}	5.576×10^{-5}	-4.245×10^{-2}	-2.101×10^{-2}
$4. \times 10^4$	2.174×10^{-4}	1.067×10^{-4}	1.134×10^{-4}	5.608×10^{-5}	-5.883×10^{-2}	-2.911×10^{-2}
$5. \times 10^4$	2.615×10^{-4}	1.282×10^{-4}	1.192×10^{-4}	5.896×10^{-5}	-7.466×10^{-2}	-3.695×10^{-2}
$6. \times 10^4$	2.898×10^{-4}	1.419×10^{-4}	1.286×10^{-4}	6.359×10^{-5}	-9.016×10^{-2}	-4.462×10^{-2}
$7. \times 10^4$	3.055×10^{-4}	1.493×10^{-4}	1.401×10^{-4}	6.921×10^{-5}	-0.1054	-5.215×10^{-2}
$8. \times 10^4$	3.117×10^{-4}	1.519×10^{-4}	1.521×10^{-4}	7.511×10^{-5}	-0.1204	-5.96×10^{-2}
$9. \times 10^4$	3.11×10^{-4}	1.511×10^{-4}	1.639×10^{-4}	8.086×10^{-5}	-0.1353	-6.699×10^{-2}

Table A.1: The complete earth source acceleration model for charges of $\tilde{q} = B$ and $\tilde{q} = L$. (continued)

λ (m)	East (m s^{-2})		North (m s^{-2})		Up (m s^{-2})	
	$\tilde{q} = B$	$\tilde{q} = L$	$\tilde{q} = B$	$\tilde{q} = L$	$\tilde{q} = B$	$\tilde{q} = L$
$1. \times 10^5$	3.049×10^{-4}	1.475×10^{-4}	1.75×10^{-4}	8.622×10^{-5}	-0.1502	-7.436×10^{-2}
$2. \times 10^5$	1.375×10^{-4}	5.839×10^{-5}	2.272×10^{-4}	1.104×10^{-4}	-0.3012	-0.1491
$3. \times 10^5$	-4.246×10^{-5}	-3.698×10^{-5}	2.202×10^{-4}	1.049×10^{-4}	-0.4602	-0.2278
$4. \times 10^5$	-1.883×10^{-4}	-1.149×10^{-4}	2.004×10^{-4}	9.302×10^{-5}	-0.6271	-0.3104
$5. \times 10^5$	-3.035×10^{-4}	-1.771×10^{-4}	1.82×10^{-4}	8.183×10^{-5}	-0.8005	-0.3962
$6. \times 10^5$	-3.943×10^{-4}	-2.266×10^{-4}	1.71×10^{-4}	7.422×10^{-5}	-0.9798	-0.4848
$7. \times 10^5$	-4.636×10^{-4}	-2.65×10^{-4}	1.716×10^{-4}	7.234×10^{-5}	-1.165	-0.5761
$8. \times 10^5$	-5.152×10^{-4}	-2.942×10^{-4}	1.877×10^{-4}	7.796×10^{-5}	-1.355	-0.6697
$9. \times 10^5$	-5.523×10^{-4}	-3.158×10^{-4}	2.222×10^{-4}	9.244×10^{-5}	-1.55	-0.7653
$1. \times 10^6$	-5.765×10^{-4}	-3.308×10^{-4}	2.778×10^{-4}	1.172×10^{-4}	-1.748	-0.8625
$2. \times 10^6$	-4.96×10^{-4}	-3.085×10^{-4}	1.876×10^{-3}	8.685×10^{-4}	-3.713	-1.819
$3. \times 10^6$	-3.119×10^{-4}	-2.25×10^{-4}	4.215×10^{-3}	1.984×10^{-3}	-5.274	-2.575
$4. \times 10^6$	-1.776×10^{-4}	-1.624×10^{-4}	6.286×10^{-3}	2.976×10^{-3}	-6.378	-3.11
$5. \times 10^6$	-8.721×10^{-5}	-1.2×10^{-4}	7.906×10^{-3}	3.754×10^{-3}	-7.15	-3.484
$6. \times 10^6$	-2.556×10^{-5}	-9.091×10^{-5}	9.141×10^{-3}	4.347×10^{-3}	-7.7	-3.75
$7. \times 10^6$	1.779×10^{-5}	-7.042×10^{-5}	1.008×10^{-2}	4.801×10^{-3}	-8.102	-3.945
$8. \times 10^6$	4.921×10^{-5}	-5.555×10^{-5}	1.081×10^{-2}	5.151×10^{-3}	-8.403	-4.09
$9. \times 10^6$	7.263×10^{-5}	-4.445×10^{-5}	1.138×10^{-2}	5.425×10^{-3}	-8.633	-4.202

Table A.1: The complete earth source acceleration model for charges of $\tilde{q} = B$ and $\tilde{q} = L$. (continued)

λ (m)	East (m s^{-2})		North (m s^{-2})		Up (m s^{-2})	
	$\tilde{q} = B$	$\tilde{q} = L$	$\tilde{q} = B$	$\tilde{q} = L$	$\tilde{q} = B$	$\tilde{q} = L$
$1. \times 10^{7}$	9.05×10^{-5}	-3.598×10^{-5}	1.183×10^{-2}	5.644×10^{-3}	-8.813	-4.289
$2. \times 10^{7}$	1.566×10^{-4}	-4.602×10^{-6}	1.368×10^{-2}	6.537×10^{-3}	-9.518	-4.631
$3. \times 10^{7}$	1.712×10^{-4}	2.344×10^{-6}	1.415×10^{-2}	6.76×10^{-3}	-9.686	-4.713
$4. \times 10^{7}$	1.767×10^{-4}	4.934×10^{-6}	1.433×10^{-2}	6.848×10^{-3}	-9.751	-4.744
$5. \times 10^{7}$	1.793×10^{-4}	6.173×10^{-6}	1.442×10^{-2}	6.891×10^{-3}	-9.783	-4.76
$1. \times 10^{8}$	2.004×10^{-4}	1.658×10^{-5}	1.454×10^{-2}	6.952×10^{-3}	-9.827	-4.781
$2. \times 10^{8}$	2.013×10^{-4}	1.7×10^{-5}	1.458×10^{-2}	6.968×10^{-3}	-9.839	-4.787
$5. \times 10^{8}$	2.016×10^{-4}	1.713×10^{-5}	1.459×10^{-2}	6.973×10^{-3}	-9.842	-4.789
$1. \times 10^{13}$	2.045×10^{-4}	1.856×10^{-5}	1.459×10^{-2}	6.974×10^{-3}	-9.843	-4.789

A.1.1 Integration Equations in Cartesian Coordinates

Equation A.1 is extended from point particles to an integral over an extended body in Cartesian coordinates:

$$\mathbf{a}_s = G \iiint\limits_{source} \left[\frac{\tilde{q}_s}{\mu_s}(\mathbf{r})\rho_s(\mathbf{r}) \right] (\lambda + |\mathbf{r}|) \frac{e^{-|\mathbf{r}|/\lambda}}{\lambda |\mathbf{r}|^3} \left[(x - x_0)\hat{\mathbf{x}} + (y - y_0)\hat{\mathbf{y}} + (z - z_0)\hat{\mathbf{z}} \right] dx\, dy\, dz, \tag{A.2}$$

where $|\mathbf{r}| \equiv \sqrt{(x - x_0)^2 + (y - y_0)^2 + (z - z_0)^2}$ and the coordinate position $\mathbf{r}_0 = (x_0,\, y_0,\, z_0)$ is the pendulum location.

A.1.2 Integration Equations in Spherical Coordinates

Similarly to the Cartesian version, but using the gradient operator in spherical coordinates gives

$$\begin{aligned} \mathbf{a}_s =& G \iiint\limits_{source} \left[\frac{\tilde{q}_s}{\mu_s}(\mathbf{r})\rho_s(\mathbf{r}) \right] (\lambda + |\mathbf{r}|) \frac{e^{-|\mathbf{r}|/\lambda}}{\lambda |\mathbf{r}|^3} \\ & \times \Big\{ \left[r\cos(\theta)\cos(\theta_0) - r_0 + r\cos(\phi - \phi_0)\sin(\theta)\sin(\theta_0) \right] \hat{\mathbf{r}} \\ & + r \left[\cos(\phi - \phi_0)\cos(\theta_0)\sin(\theta) - \cos(\theta)\sin(\theta_0) \right] \widehat{\boldsymbol{\theta}} \\ & + r\sin(\phi - \phi_0)\sin(\theta)\widehat{\boldsymbol{\phi}} \Big\} r^2 \sin(\theta)\, dr\, d\theta\, d\phi, \end{aligned} \tag{A.3}$$

where $|\mathbf{r}| \equiv \sqrt{r^2 + r_0^2 - 2rr_0 \left[\cos(\theta)\cos(\theta_0) + \cos(\phi - \phi_0)\sin(\theta)\sin(\theta_0) \right]}$ and the coordinate position $\mathbf{r}_0 = (r_0,\, \theta_0,\, \phi_0)$ is the pendulum location.

When integrating the elliptically deformed Earth in spherical coordinates, the $\hat{\mathbf{r}}$ component does not correspond to down, so the results obtained using equation A.3 must be rotated to align with local vertical in the laboratory frame. We determined the tangent vector at a latitude ϑ to the ellipse defining the Earth's surface and the normal vector (by rotating the tangent vector 90°). The dot product of the unit vectors for the tangent (North) and normal (up) with the relevant components from the integration give the components in the appropriate frame for the laboratory.

$$\begin{aligned}
\mathbf{r}(\vartheta) &= \frac{b}{\sqrt{1-\varepsilon^2\cos^2(\vartheta)}}\,\hat{\mathbf{r}} \\
&= \frac{b}{\sqrt{1-\varepsilon^2\cos^2(\vartheta)}}\left[\cos(\vartheta)\,\hat{\mathbf{x}} + \sin(\vartheta)\,\hat{\mathbf{z}}\right] \qquad \text{(A.4)} \\
\mathbf{T}(\vartheta) &= \frac{\partial}{\partial\vartheta}\mathbf{r}(\vartheta) \\
&= \frac{b}{(1-\varepsilon^2\cos^2(\vartheta))^{3/2}}\left[-\sin(\vartheta)\,\hat{\mathbf{x}} + (1-\varepsilon^2)\cos(\vartheta)\,\hat{\mathbf{z}}\right] \qquad \text{(A.5)} \\
\hat{\mathbf{T}}(\vartheta) &= \sqrt{\frac{1}{(1-\varepsilon^2)^2\cos^2(\vartheta)+\sin^2(\vartheta)}}\left[-\sin(\vartheta)\,\hat{\mathbf{x}} + (1-\varepsilon^2)\cos(\vartheta)\,\hat{\mathbf{z}}\right] \qquad \text{(A.6)} \\
\hat{\mathbf{N}}(\vartheta) &= \sqrt{\frac{1}{(1-\varepsilon^2)^2\cos^2(\vartheta)+\sin^2(\vartheta)}}\left[-\sin(\vartheta)\,\hat{\mathbf{x}} + (1-\varepsilon^2)\cos(\vartheta)\,\hat{\mathbf{z}}\right] \qquad \text{(A.7)}
\end{aligned}$$

Alternatively, the dot product of the unit normal vector and the unit radial vector can be used to define a rotation matrix where the rotation angle γ is given by

$$\cos(\gamma) = \frac{(1-\varepsilon^2)\cos^2(\vartheta)+\sin^2(\vartheta)}{\sqrt{(1-\varepsilon^2)^2\cos^2(\vartheta)+\sin^2(\vartheta)}}. \qquad \text{(A.8)}$$

Inserting values for the WGS84 reference ellipsoid and the apparatus location gives $\gamma =$ 3.3 mrad.

There are further corrections due to the non-uniformity of the earth, such that the geoid is different from the reference ellipsoid used in this model. The geoid difference from the ellipsoid was not included in our model. The geoid differences are typically meters, which was negligible at the scales considered for the entire earth integration. Any corrections would involve rotations $\lesssim 60$ μrad.

A.2 Coordinate Systems, Map Projections, and Datums

Many different reference datums are in use for both historical reasons and due to their suitability for particular uses (e.g., the North American Datum was designed to remain constant on the North American Plate despite tectonic movements). To properly compute the true distances between points, the origin and model must both be within the same datum. In joining various models from different datums, the boundaries must be properly aligned, so that the entire region is included, but only included once. Furthermore, different datums

may be used for horizontal (map) coordinates and vertical coordinates. As an additional complication, some datums are updated periodically based on current measurements .

Core of Engineers Datum (COE) The vertical datum used by the US Army Corps of Engineers for the water level in Lake Washington.

Earth Gravity Model (EGM) A series of models of earth's potential field used as the basis for the geoid in many global datums.

East-North-Up (ENU) The local coordinate system used for numerical integration of regional ($\lesssim$100 km) model data. The coordinate axes were aligned with East, North, and Up at the pendulum's location.

Mean Lower Low Water (MLLW) A vertical datum typically used for sea level measurements defined by the average of the lower low tide on each tidal day.

North American Vertical Datum (NAVD) The vertical control datum for surveying in the US.

North American Datum (NAD) A datum used for the North American continent. Revised in 1927 and 1983 (NAD27 and NAD83).

Universal Transverse Mercator zone 10N (UTM 10N) Universal Transverse Mercator is a system of projections covering the surface of the earth that allow Pythagorean distance calculations locally. Seattle is located in zone 10 North.

Washington State Plane (WSP) A series of datums for surveying within the state of Washington. The laboratory plans and the PSDEM2005 model both used revisions of the WSP datum. The definition for the PSDEM2005 model is a Lambert conformal conic projection tied to the North American Datum of 1983 using the Geodetic Reference System 1980 ellipsoid.

World Geodetic System (WGS) A global datum for both vertical and horizontal positions. The coordinate origin is designed to be located at earth's center of mass. The 1984 revision (WGS84) is currently one of the most common reference datums for global data. The global crust model was referenced to WGS84.

A.3 Importing Model Files

Digital Elevation Models (DEM) used for the source integration were obtained or located primarily from the NOAA website [46]. DEMs come in many different formats. For this work, three different formats were imported an ASCII text file for the PSDEM2005 model, GRD98 binary files, and DTED Level 0 files. Generic functions within Mathematica and relying on built-in file handling capabilities of Mathematica were used to import the DEMs for visualization and use in the source integration. Due to the advantages of binary data storage, the PSDEM2005 model was converted to the GRD98 format for general analysis work. The DTED level 0 files were similarly consolidated, as they were distributed in files covering 1 square degree (with a 30 arc second grid size). We included datum conversion within the access functions that were called to retrieve data points from the models within the numerical integration process.

A.4 Composition Models

Four different crustal composition models are compared in table A.2. Rudnick and Gao's 2003 [111] model's bulk crust composition was used as the charge for all terrain within the local models and for the crust within the whole earth model. This model's value is well within one standard deviation of the mean value, and as the most recently published, it was assumed to represent the best current knowledge of earth's bulk crustal composition. Hofmann's [61] and Rudnick's [111] models indicate that location dependent differences are 0.1% for Z/μ and N/μ.

In contrast to the crust, where direct measurements of the composition may be made, the mantle composition must be determined indirectly. An initial composition based on some measurable composition is converted to the mantle composition using models of physical and chemical processes that separate elements in a layered earth. The initial composition

Table A.2: Comparison of four models of earth's crustal composition from Anderson [9], Christensen and Mooney [29], Hofmann [61], and Rudnick and Gao [111]. Rudnick and Gao's bulk crust value is used for all source computations relating to earth's crust.

Source	Z/μ	N/μ	B/μ
[9] - Bulk Crust	0.494587	0.506006	1.00059
[29] - Bulk Crust	0.495525	0.505054	1.00058
[61] - Oceanic Crust	0.494129	0.506482	1.00061
[61] - Continental Crust	0.494475	0.506124	1.00060
[111] - Upper Crust	0.495397	0.505183	1.00058
[111] - Middle Crust	0.495186	0.505399	1.00059
[111] - Lower Crust	0.494539	0.506061	1.00060
[111] - Bulk Crust	**0.495005**	**0.505584**	**1.00059**
Bulk Crust Mean†	0.494838	0.505755	1.00059
Bulk Crust Standard Deviation†	0.00056	0.00057	0.000012

† [61] is weighted by surface area for the two crustal components.

is usually some ensemble of meteorite compositions, since meteorites are assumed to be remnants of the material from which the earth formed. Comparing the observed surface minerals, some of which come from mantle melts, with the meteorite derived composition results in differences that must be explained by the chemical and physical processes included in the model. Twelve mantle composition models are compared in table A.3. Most of the models report a value for the bulk silicate earth, which is the combined composition of the mantle and crust. However, since the mass of the crust is about 0.6% that of the mantle, the change in charge from subtracting the crust will be much less than 0.6% and is $\lesssim 10^{-5}$ for the mantle models considered here. This is much less than the 3×10^{-4} uncertainty between different models. Andersen 1989 [9] and Javoy *et al* [66] further separate their models into an upper and a lower mantle with different compositions. For the mantle's source integral, Lyubetskaya and Korenaga's [80] recent model for the mantle composition is adopted due to its robust statistical treatment of the problem.

Table A.3: Comparison of charge from models for earth's mantle's composition from Allegre *et al.* [6], Jacobsen, Quick and Wasserburg [64], Maaløe and Steel [81], Anderson [9], Ringwood and Kesson [107], Jochum *et al.* [67], Javoy *et al.* [66], Lyubetskaya and Korenaga [80], McDonough and Sun [85], McDonough [84], and Morgan and Anders [89]. The source acceleration model uses Lyubetskaya and Korenaga's model [80].

Source	Z/μ	N/μ	B/μ
[6] - Mantle + Crust	0.495541	0.505032	1.00057
[64] in [9]	0.495671	0.504902	1.00057
[81] in [9]	0.49544	0.505133	1.00057
[9]	0.4958	0.504768	1.00057
[107] in [9]	0.495489	0.505085	1.00057
[9] - Mantle + Crust	0.4955	0.505078	1.00058
[9] - Upper Mantle†	0.495289	0.505294	1.00058
[9] - Lower Mantle†	0.495592	0.504984	1.00058
[67] in [61]	0.495634	0.504939	1.00057
[66] - Prim. Upper Mantle	0.495521	0.505053	1.00057
[66] - Prim. Lower Mantle	0.495469	0.505111	1.00058
[80] - Mantle + Crust	**0.495419**	**0.505155**	**1.00057**
[85] - Mantle + Crust	0.495335	0.505242	1.00058
[84] - Mantle	0.495379	0.505198	1.00058
[89] - Mantle + Crust	0.495324	0.505256	1.00058
Mean†	0.4955	0.505075	1.00058
Standard Deviation	0.000159604	0.000163178	4.08696×10^{-6}

† [9] is weighted by 32.5% for the upper mantle and 67.5% for the lower mantle to give a bulk value.

Earth's core is primarily iron, but also contains up to 15% of a lighter element in order to satisfy density and sound propagation constraints. Sulfur, silicon, and oxygen (or some combination of them) are considered the most likely candidates for the light element, but possibilities such as hydrogen would have a much greater effect on the charge. The charges for six likely models of earth's core along with 4 possibilities for a light alloying element that has a large impact on the charge are shown in table A.4. Due to the unknown light element, the mean charges of the proposed core models is adopted for earth's core composition for the source integral. However, if hydrogen and magnesium are allowed as candidates the uncertainty in the charge is $\sim$10%. Restricting choices to sulfur, oxygen and silicon with up to 15% content by weight produces an uncertainty of $\sim$0.5%. Improvements in experiments exploring the high temperature and pressure alloys of iron will likely reduce the uncertainty on this in the future.

Table A.4: Comparison of the charge from composition models for earth's core from Allegre *et al.* [6], Bardo *et al.* [14], Javoy *et al.* [66], McDonough [84], and McDonough and Sun [85]. 5% to 15% of earth's core by weight is due to a light element. The most commonly considered candidates are sulfur, silicon, and oxygen. The silicon and oxygen model of [66] was used for the source acceleration model.

Source	Z/μ	N/μ	B/μ
[6] - Si-S-O Core	0.470691	0.530403	1.00109
[14] - Si-O Core	0.468892	0.532215	1.00111
[66] - Si-O Core	**0.469009**	**0.532113**	**1.00112**
[84] - S-Si Core	0.468728	0.532399	1.00113
[84] - S-O Core	0.468241	0.532881	1.00112
[89] - S Core	0.46784	0.533307	1.00115
Mean	0.468900	0.532220	1.00112
Standard Deviation	0.000981	0.000996	0.000018
[85] - 15% H	0.545639	0.454172	0.999811
[85] - 5% H	0.491971	0.50875	1.00072
[85] - 15% O	0.471333	0.529699	1.00103
[85] - 5% Mg	0.467555	0.533577	1.00113

Appendix B

DIGITAL FILTER CORRELATION

A finite-impulse-response (FIR) digital filter can attenuate unwanted signals or noise using a weighted sum of data points x_i:

$$y_i = \sum_{p \in \{\text{filter points}\}} c_p x_{i+p} \tag{B.1}$$

We use a digital filter to remove the torsion mode of the pendulum. Correlations arise because two or more different y include the same value x_i. The covariance between different y is

$$\begin{aligned} cov[y_k, y_\ell] &\simeq \sum_{i,j} \frac{\partial y_k}{\partial x_i} \frac{\partial y_\ell}{\partial x_j} V_{ij} \\ &= \sigma^2 \sum_{p,q \in \{\text{filter points}\}} |c_p|\,|c_q|\,\delta_{k+p,\ell+q} \end{aligned} \tag{B.2}$$

where V_{ij} is the covariance matrix for the values of x, the sums over i and j are over all points and the sums over p and q are over the points included in the filter. I assume that the values x are uncorrelated random variables recorded at a uniform interval and from the same distribution, i.e., all x have the same uncertainty. These assumptions result in V being diagonal (from the uncorrelated x) and proportional to the identity matrix $V_{ij} = \sigma^2 \delta_{i,j}$.

In our analysis, the data was separated into segments and fit to extract the Fourier coefficients for harmonics of the turntable rotation. The absolute values of the c were used to compute the correlation. The effect of a negative c_j appears through the attenuation correction (see section 6.1). The correlation between different segments was modeled as due solely to the multiple inclusion of the same underlying data points and computed as the

covariance of the mean of two segments:

$$f_k = \frac{1}{M} \sum_{i=k}^{k+M} y_i \tag{B.3}$$

$$\begin{aligned} cov[f_k, y_\ell] &\simeq \sum_{i,j} \frac{\partial f_k}{\partial y_i} \frac{\partial f_\ell}{\partial y_j} cov[y_i, y_j] \\ &= \frac{\sigma^2}{M^2} \sum_{p,q \in \{\text{filter points}\}} |c_p|\,|c_q| \\ &\qquad \times \max\left(0, \min\left(k+M+p, \ell+M+q\right) - \max\left(k+p, \ell+q\right)\right) \end{aligned} \tag{B.4}$$

f_k defines a data segment consisting of M filtered data points y. Data segments f_k and f_ℓ may overlap.

B.1 Two-point Filter

A two-point digital filter designed to remove a sinusoid of period T has $c_p = 1/2 \;\forall\; p \in \{-\beta, \beta\}$, where β corresponds to the number of data points in $T/4$:

$$y_i = \frac{1}{2}(x_{i-\beta} + x_{i+\beta}). \tag{B.5}$$

Define (potentially overlapping) data segments consisting of M filtered data points y

$$\begin{aligned} f_j &= \frac{1}{M} \sum_{i=(j-1)M+1}^{jM} y_i \\ &= \frac{1}{M} \sum_{i=(j-1)M+1}^{jM} \frac{1}{2}(x_{i-\beta} + x_{i+\beta}) \end{aligned} \tag{B.6}$$

where j defines the data segment within a data run of N segments.

Evaluating the partial derivatives in the covariance relationship gives

$$\frac{\partial f_k}{\partial x_i} = \frac{1}{2M} \sum_{p=(k-1)M+1}^{kM} (\delta_{i,p-\beta} + \delta_{i,p+\beta}), \tag{B.7}$$

which results in the following relationship for covariance:

$$\begin{aligned} U_{k\ell} = cov[f_k, f_\ell] =& \sum_{i,j} \Big[\frac{1}{2M} \sum_{p=(k-1)M+1}^{kM} (\delta_{i,p-\beta} + \delta_{i,p+\beta}) \Big] \\ & \times \Big[\frac{1}{2M} \sum_{q=(\ell-1)M+1}^{\ell M} (\delta_{j,q-\beta} + \delta_{j,q+\beta}) \Big] \sigma^2 \delta_{ij} \\ =& \frac{\sigma^2}{M^2} \Big[\delta_{k\ell}(M-\beta) + (\delta_{k,\ell-1} + \delta_{k,\ell+1}) \frac{\beta}{2} \Big] \end{aligned} \tag{B.8}$$

Making use of the correlation due to the filtering increases the uncertainty by about 4.5%, which closely matches the value determined from taking means of even or odd (uncorrelated) data segments and comparing to that of the variance determined by using either the first half or second half of the data segments in a run.

B.2 Four-point Filter

A four-point digital filter to remove a sinusoid with a particular period and to reduce the polynomial order of drift in the manner of a derivative was used in the analysis presented in this thesis and had the form:

$$y_i = x_{i-3\beta} - x_{i-\beta} + x_{i+\beta} - x_{i+3\beta}, \tag{B.9}$$

where $\beta = T/8$.

A four-point filter (functioning as a derivative of the two-point filter) has different signs for the different terms; however, to compute the correlation used to determine a fit to harmonic components (see section 6) all the signs are taken as "+". An approximation to the case of fitting a sine and a cosine term of the same frequency ω is given by the mean of the product of the value of the sine and cosine at each data point with the recorded measurement (effectively a lock-in filter):

$$\frac{1}{M} \sum_{i=1}^{M} y_i(\sin(\omega t_i), \cos(\omega t_i)) \tag{B.10}$$

The relative signs of the filter values will change as a function of the signal frequency ω; however, this effect is accounted for in the attenuation correction. The correlation effect

results from the mapping of multiple data points to each average value, which are then used in the fitting procedure.

Then the covariance between data segments is

$$cov[f_k, f_\ell] \simeq \sum_{i,j} \frac{\partial f_k}{\partial x_i} \frac{\partial f_\ell}{\partial x_j} V_{ij} \tag{B.11}$$

with V_{ij} as the covariance matrix for the values $x_{i,j}$ and is diagonal due to the assumption that the values $x_{i,j}$ are uncorrelated, so that V is the identity matrix times the variance of a data point or in components $V_{ii} = \sigma^2$ and $V_{ij} = 0 \; \forall \; i \neq j$. Evaluating the partial derivatives in the covariance relationship gives

$$\frac{\partial f_k}{\partial x_i} = \frac{1}{2M} \sum_{p=(k-1)M+1}^{kM} (\delta_{i,p-3\beta} + \delta_{i,p-\beta} + \delta_{i,p+\beta} + \delta_{i,p+3\beta}), \tag{B.12}$$

which results in the following relationship for covariance:

$$\begin{aligned} U_{k\ell} = cov[f_k, f_\ell] = & \sum_{i,j} \Big[\frac{1}{2M} \sum_{p=(k-1)M+1}^{kM} (\delta_{i,p-\beta} + \delta_{i,p+\beta}) \Big] \\ & \times \Big[\frac{1}{2M} \sum_{q=(\ell-1)M+1}^{\ell M} (\delta_{j,q-\beta} + \delta_{j,q+\beta}) \Big] \sigma^2 \delta_{ij} \\ = & \frac{\sigma^2}{M^2} \Big[\delta_{k\ell}(M - \beta) + (\delta_{k,\ell-1} + \delta_{k,\ell+1}) \frac{\beta}{2} \Big] \end{aligned} \tag{B.13}$$

B.3 Weighted Mean

The filter covariance matrices can be used to produce a weighted mean of the data segments or used in a generalized least-squares fit to different models.

The weighted mean ξ and variance $V[\xi]$ of all the data segments in a data run is given using a weight

$$w_i = \frac{\sum_{j=1}^{N} (U^{-1})_{ij}}{\sum_{k,\ell=1}^{N} (U^{-1})_{k\ell}}, \tag{B.14}$$

$$\xi = \sum_{i=1}^{N} w_i f_i, \tag{B.15}$$

$$V[\xi] = \sum_{i,j=1}^{N} w_i U_{ij} w_j. \tag{B.16}$$

Additionally, the χ^2 is defined as

$$\chi^2 = \sum_{i,j=1}^{N} (f_i - \xi)(U^{-1})_{ij}(f_j - \xi) \tag{B.17}$$

VITA

Todd Wagner was born and raised in Stillwater, Minnesota. He attended the University of Southern California with a Trustee and a National Merit scholarship, where he concurrently completing his freshman college year and his senior high school year through the Resident Honor Program. After graduation from USC, he worked for Ball Aerospace in San Diego developing software to track rockets during their launch. He moved into a computer security position with Exodus Communications (subsequently purchased by Cable & Wireless) where he developed and operated the back end systems for intrusion detection monitoring of many well known web sites. Todd married his fabulous wife, Michelle Linders Wagner, in 2003 in Beverly Hills, California. Todd and Michelle are the proud parents of two children.